University of Silesia
Faculty of Mathematics, Physics and Chemistry, The August Chełkowski Institute of Physics

Université du Maine
Institute of Molecular Engineering and Functional Materials


**Ph.D. Thesis**

# Structural and physical properties of Fe-Nb-B-RE type of bulk magnetic nanocrystalline alloys

By

**Grzegorz Ziółkowski**

Supervisor: Dr hab. inż. Artur Chrobak

Co-supervisor: Prof. Nirina Randrianantoandro

Supporting-supervisor: Dr Joanna Klimontko

Chorzów, 2015

## Acknowledgments

*I would like to thank Prof. Nirina Randrianantoandro, the Université du Maine in Le Mans as well as the Campus France for all scientific care and administrative support during my stay in France.*

*I also thank Dr Joanna Klimontko for many valuable suggestions and all help.*

*Especially heartfelt, I would like to thank my supervisor Dr hab. inż. Artur Chrobak for several years of pleasant cooperation, all provided knowledge as well as introducing me to the arcana of scientific work.*

# Table of content

# 1. Introduction

In nowadays technologies the so-called hard magnetic materials plays an important role. Such materials are widely used in the energetic, electronic or automotive industry. Also an energy harvesting, based on electric generators, requires cheap and efficient permanent magnets. One may divide the hard magnets into the two groups: with and without the rare earth (RE) metals. The first group of alloys and compounds is considered as the best, accounting their high coercive field and the so-called $|BH|_{max}$ parameters. Unfortunately, the world resources of the rare earth elements are limited and therefore, searching of new materials that reveal hard magnetic properties but with a reduced (or even without) the RE content is of great importance. In this field, researches are focused on i) improvement of coercivity of the classical ALNICO alloys, ii) improvement of magnetic remanence of high-coercive materials by the spring-exchange coupling with magnetically soft phases and iii) introduction of additional magnetic anisotropies using different kinds of nanostructures.

The presented PhD thesis refers to preparation technology, structural and magnetic properties of the Fe-Nb-B-RE type of bulk nanocrystalline alloys. As the technology of the bulk alloys, the so-called vacuum suction casting was chosen. The chemical compositions of the examined alloys is originated from the Fe-Nb-B (NANOPERM) amorphous melt spun ribbons in which niobium, as an alloying addition, slows down crystallization of iron leading to some optimization of magnetic properties. In our case, we expect the two effects. Firstly, magnetic hardening caused by the RE elements (by the $RE_2Fe_{14}B$ hard magnetic phases) and secondly, a formation of nano/micro-structures preferred for the introduction of additional magnetic anisotropies (by a combination of the preparation technology and the Nb content). The idea of this work is to study the possibility of i) improvement hard magnetic characteristics of the title materials and ii) decreasing the RE content without deterioration of the characteristics. From scientific point of view, the goal was supported by numerical analysis and computer simulations referring to disordered nano-magnetic structures.

The thesis is divided into the following main chapters. In the introduction section a theoretical background, used in an analysis of obtained results, as well as measurement techniques are widely described. For clarity, the experimental part is presented separately in the three chapters. The section "Preliminary researches" is concentrated on structural and magnetic properties of Fe-Nb-B-RE alloys in reference to technology parameters as well as type and content of the RE addition. The section "Main researches" refers to magnetic hardening effect observed for the found optimal chemical composition in a combination with optimal preparation conditions. The last chapter consists of numerical analysis and simulations performed in order to explain the magnetization processes of the investigated materials. After the presentation of the obtained results the main discussion was conducted in Chapter 8 and summarized in a form of conclusions in Chapter 9.

The names, quantities and methods were italicized at first mention. Moreover, the all parameters and variables (in a contrast to constants) were also italicized. There is no one common listing for the quantities and symbols, however, each of them is clearly explained at first usage and, if necessary, together with expressions.

Almost all presented results were published in worldwide scientific journals and in a patent application, listed below:

1. A. Chrobak, G. Haneczok, G. Chełkowska, A. Kassiba, G. Ziółkowski. *Numerical analysis of superparamagnetic clusters*. Physica Status Solidi (a) 208, No. 11 (2011) 2692–2698.

2. G. Ziółkowski, A. Chrobak, N. Randrianantoandro, G. Chełkowska. *Numerical analysis of time dependent effects in bulk nanocrystalline hard magnets*. Solid State Phenomena 194 (2012) 62-66.

3. A. Chrobak, G. Ziołkowski, N. Randrianantoandro, J. Klimontko, G. Haneczok. *Phase structure and magnetic properties of Fe–Nb–B–Tb type of bulk*. Journal of Alloys and Compounds 537 (2012) 154–158.

4. G. Ziółkowski, A. Chrobak, J. Klimontko. *Phase structure and magnetic properties of Fe-Nb-B-Nd type of bulk nanocrystalline alloys*. Solid State Phenomena Vol. 203-204 (2013) 302-305.

5. A. Chrobak, J. Klimontko, M. Kubisztal, G. Haneczok, G. Ziółkowski, A. Kachel. *Effect of ball milling on structure and magnetic properties of Fe-Mb-B-Tb bulk nanocrystalline alloys*. Solid State Phenomena Vols. 203-204 (2013) 280-283.

6. G. Ziółkowski, A. Chrobak, N. Randrianantoandro, J. Klimontko. *Phase structure and magnetic properties of Fe-Nb-B-Pt type of bulk nanocrystalline alloys*. Acta Physica Polonica A 126 (2014) 174-175.

7. A. Chrobak, G. Ziółkowski, N. Randrianantoandro. *Phase stability of* $(Fe_{80}Nb_6B_{14})_{0.9}Tb_{0.1}$ *bulk nanocrystalline magnet*. Acta Physica Polonica A 126 (2014) 176-177.

8. A. Chrobak, G. Ziółkowski, G. Haneczok. *Influence of cooling rate on magnetic properties of* $(Fe_{80}Nb_6B_{14})_{1-x}Tb_x$ *type of bulk nanocrystalline alloys*. Acta Physica Polonica A 126 (2014) 178-179.

9. A. Chrobak, G. Ziółkowski, N. Randrianantoandro. *Magnetic hardening of Fe-Nb-B-Tb type of bulk nanocrystalline alloys*. Journal of Alloys and Compounds 583 (2014) 48-54.

10. G. Ziółkowski, A. Chrobak. *Magnetization processes of nanoparticles embedded into ferromagnetic matrix*. Acta Physica Polonica A 127 (2015) 597-599.

11. A. Chrobaka, G. Ziółkowskia, N. Randrianantoandrob, J. Klimontkoa, D. Chrobak, K. Prusikc, J. Rak. *Ultra-high coercivity of* $(Fe_{86-x}Nb_xB_{14})_{0.88}Tb_{0.12}$ *bulk nanocrystalline magnets*. Acta Materialia, Volume 98 (2015) 318-326.

12. Patent application nr P.408634 submited in 2014 entitled "*Metoda wytwarzania materiałów objętościowych o ultra wysokiej koercji typu RE-Fe-B-Nb, gdzie RE to Tb i Dy oraz stop uzyskiwany tą metodą*.".

# 2. Theoretical background

## 2.1. Magnetism – basic principles and materials[1]

### 2.1.1. Basic magnetic quantities

The phenomenon of magnetism at the atomic level is related to the spin and orbital angular momentum of the electron. The energy levels, which can be occupied by the electrons, may be determined based on solution of the *Schrödinger equation*. These states are characterized by four quantum numbers:

1. The size of the orbit and its energy is determined by *the total* (also called *principal*) *quantum number* $n$ = 1, 2, 3, etc. related to the so-called K, L, M, etc. shell, respectively.

2. The angular momentum of the orbital motion is described by *the orbital angular momentum quantum number* $l$ = 0, 1, 2, …, $n$-1 (also marked as s, p, d, f, ...). For a given value of l the module of the orbital angular momentum vector equals $\hbar\sqrt{l(l+1)}$ where $\hbar = \mathrm{h}/2\,\pi$ and h = 6,626 069 57·10$^{-34}$ Js is the *Planck's constant*.

3. *The magnetic quantum number* $m_l$ is associated with the projection of orbital angular momentum on the selected direction (usually along the applied field) and may assume values of -l, -l+1, …, 0, …, l-1, l.

4. The value of the spin angular momentum is determined by *the spin quantum number* s = ½ according to the relationship $\hbar\sqrt{\mathrm{s}(\mathrm{s}+1)}$. The projection of the spin angular momentum vector on the selected direction $s_z$ (eg. z-axis) can take only two values ±ħ/2 and it is associated with *the magnetic spin quantum number* $m_s$ = ±1/2 ($s_z = m_S\hbar$).

[1] This chapter summarizes the most important knowledge in context of presented work base on many books in a topic of magnetism, especially [1], [2], [3], [4] and [5].

The moving electron can basically be considered as a current flowing in a wire that coincides with the electron orbit. An electron with mass *m*, charge *e* and an orbital angular momentum $\hbar\vec{l}$ has an associated magnetic moment:

$$\overrightarrow{\mu_l} = -\frac{|e|}{2m}\hbar\vec{l} = -\mu_B\vec{l} \tag{2.1}$$

where $\mu_B$ is called *the Bohr magneton* and it is equal to $9.27400968 \cdot 10^{-24}$ J/T. Moreover, the absolute value of this magnetic moment and its projection along specific direction are equal to $|\overrightarrow{\mu_l}| = \mu_B\sqrt{l(l+1)}$ and $\mu_{lz} = -m_l\mu_B$, respectively. In the case of the spin angular momentum $\hbar\vec{s}$ the associated magnetic moment is equal to:

$$\overrightarrow{\mu_s} = -g_e\frac{|e|}{2m}\hbar\vec{s} = -g_e\mu_B\vec{s} \tag{2.2}$$

where $g_e$ (=2.002290716) is so-called *the spectroscopic slitting factor*, and the component in the field direction is $\mu_{sz} = -g_e m_s\mu_B$.

The energy of magnetic moment $\vec{\mu}$ in a magnetic field $\vec{H}$ is given by the formula:

$$E = -\vec{\mu}\cdot\mu_0\vec{H} \tag{2.3}$$

where $\mu_0 = 4\pi * 10^{-7}\ \mathrm{TmA^{-1}}$ is *the vacuum permeability*. Due to the fact that the projection of the spin magnetic moment to the direction of the magnetic field can assume only two values, and the lowest energy setting is preferred, so the electrons with $m_s$ = - ½ and + ½ are set parallel and antiparallel to the external field, respectively.

In case of ion or atom, the orbital and spin motions of the all electrons and the interaction between them have to be considered. Usually (see spin-orbit coupling) *the resultant total angular momentum* $\vec{J}$ for atom with $i$ electrons can be expressed by the formula:

$$\vec{J} = \vec{L} + \vec{S} \tag{2.4}$$

where $\vec{L} = \sum_i \vec{l_i}$ is *the total orbital angular momentum*, $\vec{S} = \sum_i \vec{s_i}$ is *the total spin angular momentum* and the components of magnetic moment are equal to $\overrightarrow{\mu_L} = -\mu_B\vec{L}$ and $\overrightarrow{\mu_S} = -g_e\mu_B\vec{S}$, respectively.

The interaction between the $\vec{L}$ and $\vec{S}$ vectors leads to precession around $\vec{J}$ as well as the precession of *the total magnetic moment* $\overrightarrow{\mu_{tot}} = \overrightarrow{\mu_L} + \overrightarrow{\mu_S}$ around the same axis (see Figure

2.1). Note, that due to $g_e > 1$, there is an angle $\theta$ between $\vec{J}$ and $\overrightarrow{\mu_{tot}}$ axes. Moreover, usually the time measurement of the magnetic moment is much larger than the period of $\overrightarrow{\mu_{tot}}$ rotation, therefore its perpendicular (to the axis of rotation) component will be equal to zero. In this situation, the magnetic moment responsible for magnetic properties is expressed as:

$$|\vec{\mu}| = |\overrightarrow{\mu_{tot}}|\cos(\theta) = g_J \mu_B J \tag{2.5}$$

It can be shown that:

$$g_J = 1 + \frac{J(J+1) + S(S+1) + L(L+1)}{2J(J+1)} \tag{2.6}$$

where $g_J$ is Landé spectroscopic $g$-factor. Additionally, $J$ is the total angular momentum quantum number of the atom and it can be determined based on so-called Hund's rules:

1. The value of $S = \sum_i m_{si}$ takes a maximum as far as allowed by the Pauli exclusion principle.
2. The value of $L = \sum_i m_{li}$ also takes a maximum as far as allowed by rule 1.
3. If the shell is less than half filled $J = L - S$, otherwise $J = L + S$.

One can note that only unfilled electron shells can be a source of spin or orbital angular momentum. Figure 2.2 shows the values of $J$, $S$, and $L$ quantum numbers as a function of electrons number for the unfilled *3d* electron shells (characteristic for the iron group) and 4f (characteristic of rare earth elements).

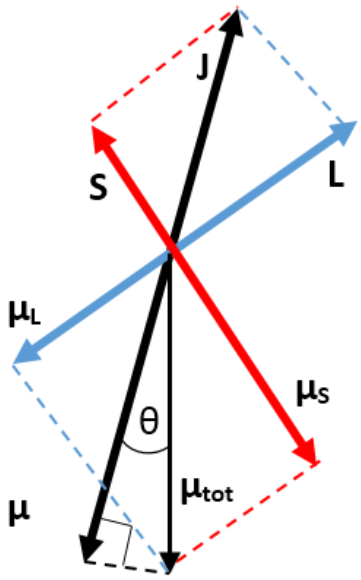


Figure 2.1. The Spin-orbit interaction between the angular momenta $\vec{S}$ and $\vec{L}$.

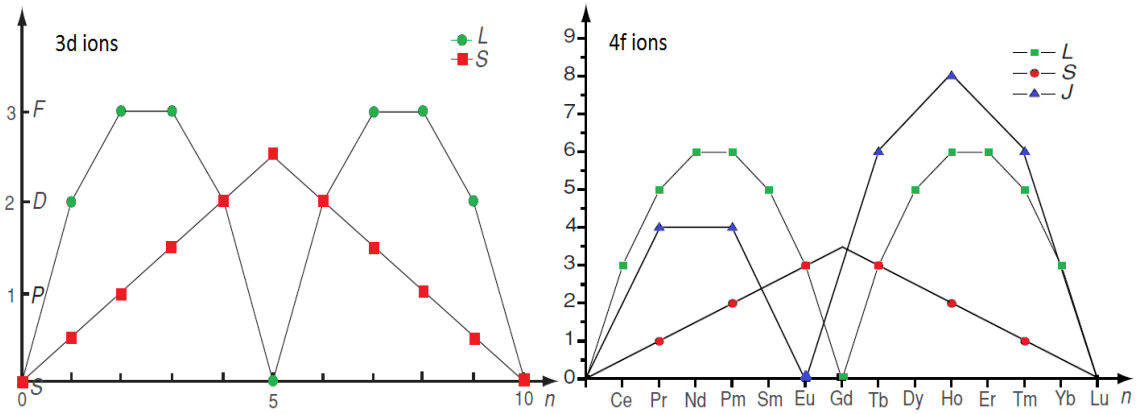


Figure 2.2. The values of the *J*, *S* and *L* quantum numbers as a function of electrons number for the electron shells of *3d* and *4f* (adapted from [2]).

Generally, magnetism in macro scale is a combination of atomic magnetic moments and interactions leading to the formation of different magnetic structures. There are several parameters characteristic for magnetic materials.

The sum of the magnetic moments per unit volume is called Magnetization (A/m in the SI unit system):

$$\vec{M} = \frac{\sum \vec{\mu}}{V} \tag{2.7}$$

Magnetic susceptibility $\chi$ is the ratio of magnetization to the magnetic field strength $\vec{H}$ (without unit):

$$\chi = \frac{|\vec{M}|}{|\vec{H}|} \tag{2.8}$$

Magnetic field in material are described by the magnetic induction (with the unit in SI: Tesla, T):

$$\vec{B} = \mu_0(\vec{H} + \vec{M}) \tag{2.9}$$

Additionally, when $\vec{B}$, $\vec{H}$ and $\vec{M}$ vectors are parallel the magnetic induction can be written as:

$$B = \mu_0(H + M) = \mu_0(1 + \chi)H = \mu_0\mu_r H \tag{2.10}$$

where $\mu_r$ is the relative magnetic permeability (in vacuum) and $\mu_0\mu_r$ is so-called absolute magnetic permeability (H/m). Table 2.1 summarizes the different magnetic parameters and their units in IS and CGS systems.

Table 2.1. Basic quantity for magnetic materials in macro scale with their units (base on [6]).

| Quantity | Symbol | CGS | SI | Conversion |
|---|---|---|---|---|
| **Magnetic induction** | $B$ | G | T | $10^{-4}$ |
| **Magnetic field intensity** | $H$ | Oe | A m$^{-1}$ | $10^3 / 4\pi$ |
| **Magnetization** | $M$ | emu cm$^{-3}$ | A m$^{-1}$ | $10^3$ |
| **Magnetic polarization** | $J$ | - | T | - |
| **Magnetic moment** | $m$ | emu | A m$^2$ | $10^{-3}$ |
| **Susceptibility (volume)** | $\chi$ | - | - | $4\pi$ |
| **Magnetic permeability** | $\mu$ | G/Oe | H m$^{-1}$ | $4\pi \times 10^{-7}$ |
| **Relative permeability** | $\mu_r$ | - | - | 1 |
| **Vacuum permeability** | $\mu_0$ | G/Oe | H m$^{-1}$ | $4\pi \times 10^{-7}$ |

### 2.1.2. Magnetic structures

The magnetic moments of atoms interact with each other that leads to the formation of ordered structures. In context of magnetic systems, there are four typical interactions:

1. *Dipolar interaction*: is an interaction between two magnetic moments by magnetic field generated by the moments. This interaction is relatively weak and usually (at high temperature) not sufficient to provide ordering.

2. *Exchange interaction*: it is provided by overlapping of wave functions of interacting electrons and has a quantum nature. This kind of interaction is stronger than dipolar, however, appears on the short distance and usually is limited to nearest neighbors of spins.

3. *RKKY interaction* (acronym of names - Ruderman, Kittel, Kasuya, and Yosida): it is long range interaction through the conduction electrons. In this case the exchange integral can be expressed by:

$$J_{RKKY}(r) = 6\pi Z J'^2 N(E_F)[\frac{\sin(2k_F r)}{(2k_F r)^4} - \frac{\cos(2k_F r)}{(2k_F r)^3}] \quad (2.11)$$

   where $Z$ is the number of conduction electrons per atom, $J'$ is the exchange integral of *s-f* (for rare earth) or *s-d* electron (in case of a transition metal), $N(E_F)$ is the density of states at the Fermi level, $k_F$ is the wave vector value of the electron on Fermi surface and $r$ is the distance between atoms. It is important to note that for long distance the exchange integral is proportional to $1/r^3$ and has an oscillating character.

4. *Superexchange*: In case of crystal structure where the "magnetic" atoms are separated by "nonmagnetic" atoms, the coupled of spins of *d* electrons (or *f*) through the *p* electron of the "non-magnetic" atoms may occur. This kind of interaction normally leads to antiparallel set of spins of *d* (or *f*) electrons for coupled atoms.

In general, the type of structure is determined by the tendency to minimize of the system energy. Base on the so-called *Heisenberg model* the energy of magnetic system can be expressed as:

$$E = -\sum_{i,j} J_{ex_{ij}}\, \overrightarrow{S_i}\overrightarrow{S_j} - \sum_i K_i\left(\overrightarrow{S_i}\cdot\overrightarrow{n_i}\right)^2 - g\mu_B\mu_0 \sum_i \overrightarrow{H_i}\cdot\overrightarrow{S_i} - D\sum_{i,j}\left[\frac{\overrightarrow{S_i}\cdot\overrightarrow{S_j}}{|\,\overrightarrow{r_{ij}}\,|^3} - \frac{3}{|\,\overrightarrow{r_{ij}}\,|^5}\left(\overrightarrow{S_i}\cdot\overrightarrow{r_{ij}}\right)\left(\overrightarrow{S_j}\cdot\overrightarrow{r_{ij}}\right)\right] \tag{2.12}$$

where presented sums corresponds to *exchange interaction*, *magnetic anisotropy*, *magneto-static energy* and *dipolar interaction*, respectively. In this formula *i* and *j* indexes of spins $\overrightarrow{S_i}$ with easy magnetization axis $\overrightarrow{n_i}$, a distance between spins is expressed by $\overrightarrow{r_{ij}}$. $J_{ex_{ij}}$ , $K_i$ and *D* parameters are related to exchange integral, anisotropy and dipolar interaction, $H_i$ corresponds to external magnetic field acts on the spin *i*.

Typical magnetic structures are the systems of: a) non-interacting magnetic moments called paramagnetism, b) parallel ordered magnetic moments called ferromagnetism (when exchange integral are positive), c) antiparallel ordered magnetic moments i.e. antiferromagnetism (exchange integral are negative) and d) ferrimagnetism when the ordered is also antiparallel but the opposite magnetic sublattices are not equal. At this point it is worth to note that all materials have also diamagnetic properties related to the interaction between an external magnetic field and electrons witch induces the opposite field and the material is pushed out. The diamagnetism effect is very weak and it is often overlapping by a much stronger effect depending on magnetic structures like ferromagnetism. Figure 2.3 summarizes the different types of magnetic structures and their properties.

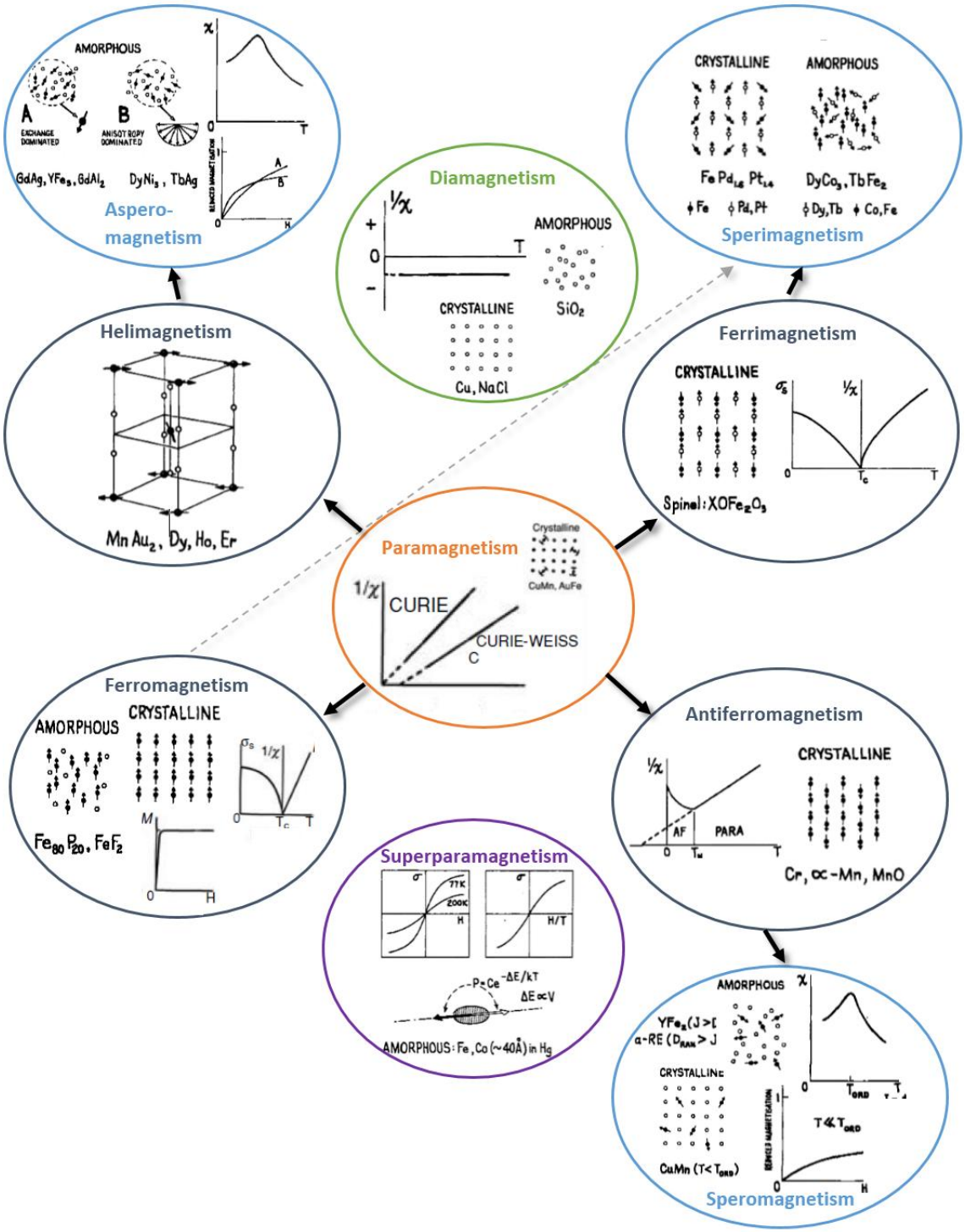


Figure 2.3. The family of magnetic structures (base on [5]).

In case of paramagnetic materials, the magnetic moments do not interact with each other and without external magnetic field they are randomly directed, so, the total magnetization is equal to zero. Otherwise, the interaction between magnetic field and the

magnetic moments (with energy $E_H = -\vec{\mu} \cdot \vec{B}$) leads to ordering along the field direction. However, a thermal vibrations of atoms breaking this ordering and an equilibrium between the interaction with field and the thermal energy is established at a specific temperature. Based on the canonical distribution, the average magnetic moment $\langle \mu_Z \rangle$ along the field direction can be calculated. Finally, the classical approximation of magnetization is equal to:

$$M(T,H) = n \cdot \langle \mu_Z \rangle = n \cdot \mu \cdot \left( \coth x - \frac{1}{x} \right) = n \cdot \mu \cdot L(x), x = \frac{\mu B}{k_B T} \qquad (2.13)$$

where *n* is the number of magnetic moments per unit volume and $L(x)$ is the *Langevin function*. Note, that if $x \ll 1$ (weak field or high temperature), then $L(x) \approx \frac{x}{3}$ and the magnetic susceptibility is described by so-called *Curie law*:

$$\chi = \frac{n\mu_0 \mu^2}{3\mathrm{k}_B T} = \frac{C}{T} \qquad (2.14)$$

More correct quantum approach (including the fact that $m_J = J, (J-1), \ldots, -(J-1), -J$) leads to the magnetization formula expressed by the magnetic saturation $M_S$ and the *Brillouin function* $B_J$:

$$M(T,H) = \mathrm{ng}_J \mu_B \mathrm{JB}_J(x) = M_S B_J(x) \qquad (2.15)$$

$$B_J(x) = \frac{2J+1}{2J} \coth\left( \frac{2J+1}{2J} x \right) - \frac{1}{2J} \coth\left( \frac{x}{2J} \right), x = \frac{g_J \mu_B \mathrm{JB}}{k_B T} \qquad (2.16)$$

Just as before in case of $x << 1$, this expression is simplified to the magnetic susceptibility shown above, except that the magnetic moment is called the *effective moment* and it is equal to:

$$\mu_{eff} = g_J \mu_B \sqrt{J(J+1)} \qquad (2.17)$$

The values of the magnetic moment of paramagnetic ions are usually equal to few $\mu_B$, and therefore a relatively large fields or low temperatures are required to saturate this type of material.

The opposite situation is observed for materials like crystalline iron or gadolinium. In this case, high magnetization is possible at low or even without external magnetic fields. These properties may be explained by the so-called *molecular field* $H_m$ provided by all

magnetic moments (it can be derived from the quantum nature of exchange interaction). The molecular field together with the external magnetic field leads to the ordering of the magnetic moments along some direction:

$$\overrightarrow{H_{tot}} = \vec{H} + \overrightarrow{H_m} = \vec{H} + N_W \vec{M} \tag{2.18}$$

where $N_W$ is the Weiss constant. If $N_W > 0$ then the magnetic susceptibility of the material greatly increases and the magnetic moments set parallel to the external magnetic field which leads to typical ferromagnetic order. The strength of the molecular field is related to the strength of the exchange interactions (direct or RKKY indirect) at the atomic level. Above a specific temperature $T_c$ (called the *Curie temperature*) thermal energy is stronger than these interactions and materials behave like paramagnets following the *Curie-Weiss low*:

$$\chi = \frac{C}{T - \theta_p}, \theta_p = N_W C = \frac{N_W n \mu_0 g_J^2 J(J+1)\mu_B^2}{3k_B} \tag{2.19}$$

where $\theta_p$ is the *paramagnetic Curie temperature*. It can be shown that at a given *J,* the reduced magnetization $M\,(T)/M\,(0)$ as a function of reduced temperature $T/T_c$, where $M(0) = ng\mu_B J$, can be expressed using the *Brillouin function*:

$$\frac{M(T)}{M(0)} = B_J\left(\frac{3J}{J+1}\frac{T_c}{T}\frac{M(T)}{M(0)}\right) \tag{2.20}$$

The so-called *Bethe-Slater curve* (presented in Figure 2.4) shows that there is a relation between the exchange integral and the interatomic distance by the atomic radius ratio $r_{ab}/r_d$. In case of Fe, Co or Ni the exchange integral is bigger than 0 which leads to the ferromagnetic ordering, while for Mn or Cr the energy minimum can be achieved in antiparallel ordering.

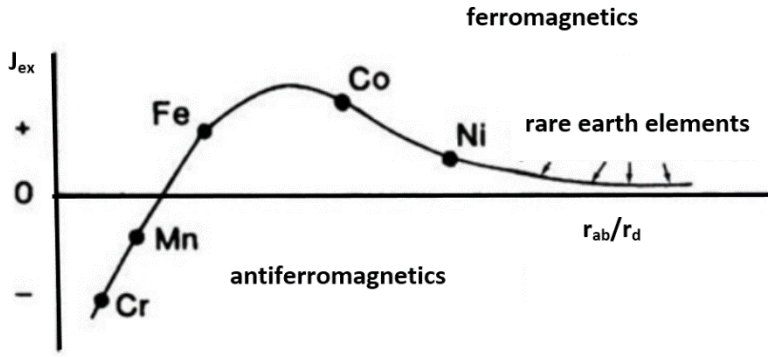


Figure 2.4. The Bethe-Slater curve, the exchange integral ($J_{ex}$ on this picture) as a function of the interatomic distance by the atomic radius $r_{ab}/r_d$ (adapted from [7]).

The exchange integrals may be negative due to the exchange interaction and also the oscillating nature of the RKKY interaction. The antiparallel coupling of the magnetic moments leads to the formation of two ferromagnetic and oppositely directed sub-lattices *A* and *B*. In case of antiferromagnetic, the magnetization of the first lattice $M_A$ is equal to the magnetization $M_B$, at least at $T = 0$. Above the Neel temperature $T_N$ the thermal energy breaking the ordering and the system is paramagnetic with magnetic susceptibility:

$$\chi = \frac{C}{T - \frac{1}{2}C(N_1 + N_2)} = \frac{C}{T - \theta_P}, \theta_p = \frac{1}{2}C(N_1 + N_2) \tag{2.21}$$

where $N_1$ and $N_2$ are the Weiss constant corresponding with the molecular fields provided by the same and the opposite lattice magnetization. Below the Neel temperature the magnetic susceptibility can be expressed as:

$$\chi = \chi_{\parallel}\cos^2\alpha + \chi_{@}\sin^2\alpha \tag{2.22}$$

where $\alpha$ is the angle between the direction of magnetic field and easy magnetization axis. Moreover, the $\chi_{\parallel}$ and $\chi_{@}$ are the magnetic susceptibility related to the parallel and perpendicular magnetic field to the easy magnetization direction:

$$\chi_{\parallel} = \frac{N\mu_0 g^2 J(J+1)\mu_B^2 B_J'(x_0)}{k_B T - \frac{1}{2}C(N_1 + N_2)N\mu_0 g^2 J(J+1)\mu_B^2 B_J'(x_0)}, \qquad \chi_{@} = -\frac{1}{N_2} \tag{2.23}$$

It is worth noting that in case of polycrystalline materials consisting of randomly oriented grains, the magnetic susceptibility can be transformed to the formula:

$$\chi = \frac{1}{3}\chi_{\parallel} + \frac{2}{3}\chi_{@} \tag{2.24}$$

The ferrimagnetic properties are characteristic for the materials with different value of magnetic moments of *A* and *B* sublattice. This situation leads to the different value of $M_A$ and $M_B$. Generally, the total magnetization along the stronger sublattice is equal to:

$$\left|\vec{M}\right| = \left|\left|\overrightarrow{M_A}\right| - \left|\overrightarrow{M_B}\right|\right| \tag{2.25}$$

where:

$$\begin{aligned} \overrightarrow{M_A} &= -n_A\mu_B g_A\langle\overrightarrow{J_A}\rangle = -n_A\mu_B g_A\overrightarrow{J_A}B\left(\frac{g_A J_A H_A}{k_B T}\mu_B\right) \\ \overrightarrow{M_B} &= -n_B\mu_B g_B\langle\overrightarrow{J_B}\rangle = -n_B\mu_B g_B\overrightarrow{J_B}B\left(\frac{g_B J_B H_B}{k_B T}\mu_B\right) \end{aligned} \tag{2.26}$$

The $H_A$ and $H_B$ are magnetic fields acting to the A and B sublattice. At high temperature the magnetic susceptibility is equal to:

$$\begin{aligned} \chi &= \frac{C}{T - T_c}, \\ T_c &= \frac{1}{2}(C_A N_{AA} + C_B N_{BB}) + \frac{1}{2}\sqrt{(C_A N_{AA} - C_B N_{BB})^2 + 4C_A C_B N_{AB} N_{BA}} \end{aligned} \tag{2.27}$$

where $N_{AA}$, $N_{AB}$, $N_{BA}$ and $N_{BB}$ are the Weiss constants related to the combinations of molecular field provided by the magnetization of A and B sublattice. Figure 2.5 shows an example of M(T) curve spited to the $M_A$ and $M_B$ magnetizations. It should be noted that at $T < T_C$, it may happen that the magnetization of both sublattices is the same which is called the compensation point.

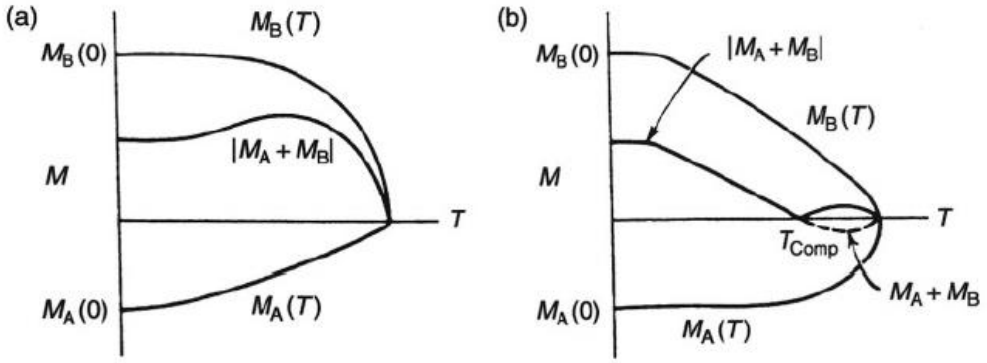


Figure 2.5. Two example of spontaneous magnetization as a function of temperature predicted by the molecular field theory without (a) and with (b) the compensation point [3].

## 2.1.3. Localized and itinerant magnetism

The magnetic moment of $Fe^{3+}$ iron ions is equal to about 4 $\mu_B$ and 2.2 $\mu_B$ for a different ion compounds and the crystalline iron, respectively. This difference is related to the fact, that in the first case the 3d electrons (responsible for magnetism) are well localized, while in the second case there are partially free. Although, the 3d electrons in the metallic iron (or other intermetallic compounds of iron) are not completely free, usually, in order to characterize magnetic phenomena the approximation of free electron gas can be used. At the temperature equal to zero the energy levels up to the Fermi energy will be filled, while at higher temperatures (when the Fermi-Dirac statistics is used) the higher levels by a value of $k_B T$ than $E_F$ can be occupied. Only the electrons with energy close to $E_F$ can give a contribution to the magnetic susceptibility, so the magnetic properties will be determined by the density of states at the Fermi level:

$$g(E_F) = \frac{3n}{2E_F} = \frac{m_e k_F}{\pi^2 \hbar^2} \tag{2.28}$$

where $n$ is the number of electrons per unit volume and $m_e$ is the electron effective mass. In the presence of an external magnetic field the energy bands of spins up and down are split by the value $2\mu_B B$ of energy. Due to the fact that in equilibrium state the Fermi level is the same for both bands, so the amount of electrons with the spins directed along the field is greater than the spins directed opposite and the magnetization is equal to:

$$M = \mu_B(\Delta n_\uparrow - \Delta n_\downarrow) = g(E_F)\mu_B^2 B \tag{2.29}$$

where $\Delta n_\uparrow$ and $\Delta n_\downarrow$ are a change in the electron concentration for the spin up and down

cases. The susceptibility of free electrons is determined by the *M* / *H* ratio and equal to:

$$\chi = \frac{3n\mu_0\mu_B^2}{2E_F} \tag{2.30}$$

In case of the ferromagnetic materials (and $T < T_C$) the 3d bound splitting may occur even without external magnetic field. This phenomenon can be explained by the minimum of electrons system energy. This energy is increasing by the electron transfer from the "down" spins band to the "up" spins band (kinetic energy) and on the other hand can be minimized by the magnetostatics energy of the resultant magnetization in the molecular field:

$$\Delta E = \Delta E_{kin} + \Delta E_M = \frac{1}{2} g(E_F)\delta E^2[1 - Ug(E_F)] \tag{2.31}$$

where $U = \mu_0\mu_B^2 N_W$ described the average delta energy by 3d electron pair during changing of the spin direction. The minimum of the energy can be achieved in case of $[1 - Ug(E_F)] \geqslant 1$ i.e. the Stoner condition for ferromagnetism, while for opposite situation the system is paramagnetic. For example for the fifty first elements of the periodic system only the Fe, Co and Ni satisfy this condition and there are ferromagnetic. Due to the fact that the 3d band is relatively narrow (the 3d electrons are not completely free), the magnetic moments of the 3d metals are usually described as a located with the atoms which are characterized only by the apparent value of $S'$ (spin angular momentum) expressed in the formula:

$$\mu_{3\mathrm{d}} = g_e\mu_B S' = \mu_B\left(\frac{n_\downarrow - n_\uparrow}{n}\right) \tag{2.32}$$

However, this type of magnetism is called itinerant magnetism.

Another kind of situation one can observed for a rare earth metals. In this case, the electrons from partially filled 4f shell are the source of magnetism. These electrons do not participate in conductivity (because 4f is not an external shell) and therefore, magnetism in such materials is called localized. Moreover, the 4f electrons of nearest atoms cannot interact directly due to high distances between them, so, the magnetic coupling is indirect (by a conduction electrons) according to the RKKY model. These interactions are weaker than exchange coupling which is reflected in low values of the Curie temperature.

Especially interesting is the combination of localized magnetism of rare-earth (RE) elements and itinerant magnetism of transition metals (T). From practical point of view the rare earths provides a large magnetic moment, magnetocrystalline anisotropy and a magnetostriction, while the transition metals are caracterized by high Curie temperature (strong exchange interactions). Such combination is a base for many modern magnetic materials. The 5d electrons play important role in the RE magnetic coupling, while the hybridization of 5d (for RE atoms) and 3d (for T atoms) electrons is responsible for the atomic bonds in RE-T compounds. Due to the spontaneous splitting of 3d band, the energy gap between the lower limit of the 5d band and the upper limit of 3d band is lower for the spins "up" sub-band than for the spins "down" sub-band.

Due to this effect and the Pauli principle, the resultant spin of the 5d electrons will be antiferromagnetically directed to the resultant spin of the 3d electrons. The spins coupling of the 4f-3d electron is always antiparallel, but the setting of RE and T magnetic moments is not necessarily antiferromagnetic. Generally, in case of so-called heavy RE elements, upper than Gd in the periodic table (where the 4f band is filled more than half and J=L+S), the magnetic moments of RE and T atoms are coupled antiferromagnetically, while for the opposite situation i.e. light rare earth, the coupled is ferromagnetically.

### 2.1.4. Magnetic anisotropy

All presented in the previous chapters considerations assumed that the magnetic properties are isotropic i.e. directionally independent. In fact, the materials exhibit anisotropic properties and this effect should be taken into account in models describing magnetization processes. There are different types of magnetic anisotropy such as magnetocrystalline, shape, induced, magneto-elastic and surface that are discussed below.

The *magnetocrystalline anisotropy* is correlated with certain crystallographic direction. In some cases, the crystalline field can modify the electron orbitals and consequently the orbital angular momentum. As a result of the spin-orbit coupling, an easy magnetization direction (or directions) corresponding to the minimum of free energy (due to the magnetic moments of the system) is preferred. For materials with a single easy magnetization axis, like a hexagonal rare earth compounds, the energy of uniaxial anisotropy by unit volume can be expressed by the formula:

$$\frac{E_a}{V} = K_0 + K_1 \sin^2\theta + K_2 \sin^4\theta \tag{2.33}$$

Where $K_1$, $K_2$ are so-called anisotropy constants and $\theta$ is an angle between $\vec{M}$ and easy magnetization axis. In more general case, the magnetocrystalline anisotropy is determined by directional cosines of the magnetization to the axis of crystal lattice as shown in Figure 2.6.

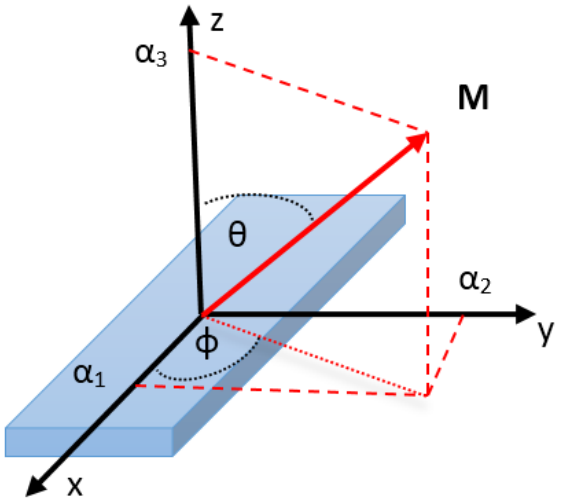


Figure 2.6. Definition of directional cosines to the axis of crystal lattice.

For materials with several easy magnetization axes and directional cosines equal to $\alpha_1$,$\alpha_2$, $\alpha_3$, the energy of anisotropy in case of cubic, tetragonal and hexagonal lattice can be expressed as:

$$\frac{E_a}{V} = K_0 + K_1(\alpha_1^2\alpha_2^2 + \alpha_2^2\alpha_3^2 + \alpha_3^2\alpha_1^2) + K_2(\alpha_1\alpha_2\alpha_3)^2 + \cdots \tag{2.34}$$

$$\frac{E_a}{V} = K_0 + K_1\alpha_3^2 + K_2\alpha_3^2 + K_3(\alpha_1^2 + \alpha_2^2) + \cdots \tag{2.35}$$

$$\frac{E_a}{V} = K_0 + K_1(\alpha_1^2 + \alpha_2^2) + K_2(\alpha_1^2 + \alpha_2^2)^2 + K_3(\alpha_1^2 + \alpha_2^2)^3 + \cdots \tag{2.36}$$

respectively. For example, anisotropy constants of bcc-Fe are equal to $K_1 = 5.48 * 10^4\ J/m^3$ $(4.02 * 10^{-6}\ eV/atom)$ and $K_2 = 1.96 * 10^2\ J/m^3$ $(1.44 * 10^{-8}\ eV/atom)$.

The *shape anisotropy* is associated with the macroscopic shape and size of the object. The finite size of the sample leads to the interaction between magnetic field produced by

magnetization of the material with its magnetic moments and an external magnetic field. This phenomenon (called *demagnetization*) is related with demagnetization field $H_D$ and magnetostatic energy $E_D$. The minimum of this energy leads to the favored direction. Generally, the magnetostatic energy can be expressed as:

$$E_D = -\frac{1}{2}\int \mu_0 \vec{M} \cdot \overrightarrow{H_D} dV \tag{2.37}$$

where $H_D$ depends on object geometry. For example, the final formula of $E_D$ by the unit volume for sphere object, infinite cylinder (along z axis) and infinite plain (xy) is equal to:

$$\frac{E_D}{V} = \frac{1}{6}\mu_0 M^2 \tag{2.38}$$

$$\frac{E_D}{V} = \frac{1}{4}\mu_0 M^2 \sin^2\theta \tag{2.39}$$

$$\frac{E_D}{V} = K_0 + K_S \sin^2\theta \tag{2.40}$$

respectively. In the case of spherical symmetry, this energy does not depend on the direction, while for an infinite cylinder the energy minimum occurs when the magnetization is parallel (or antiparallel) to the z-axis. The third case is the equivalent of thin films where the perpendicular magnetization to the plane is preferred. Moreover, the $K_S$ parameter is proportional to the $M^2$ and its typical value in case of thin films can be even 100 times more than magnetocrystalline anisotropy constant.

The *induced anisotropy* is provided by an external magnetic field and it is characteristic for amorphous or structural disordered materials. Assume that the fully disordered system consists of two types of atoms with strong magnetic coupling between nearest neighbors (high $T_C$). In presence an external field and at high (but < $T_C$) temperature, the positions of atoms can be change according to the binding energy between them:

$$E_{bind} = al(\cos^2\phi - 1/3) \tag{2.41}$$

where $a$ is a constant, $l$ a parameter depending on the type of atoms and $\Phi$ is the angle between the magnetization and the vector connecting to the position of a pair of atoms. The optimal positions of the atoms will be frozen during culling with external field and

leads to a preference for a particular direction. Finally, the energy of induced anisotropy is equal to:

$$E_{ind}\frac{1}{aV} = -K_{ind}\cos^2(\theta - \theta_{ann}) \tag{2.42}$$

where $K_{ind}$ is anisotropy constants, $(\theta - \theta_{ann})$ is the angle between the direction of cooling field and the measuring field. This type of anisotropy can be also induced, for instance, by a deformation in the presence of an external magnetic field.

The *magneto-elastic anisotropy* is associated with magnetostriction of the material. The deformation of the material and consequently a change of interatomic distances can lead to the magnetic effects and vice versa. This phenomena (related to the spin-orbit interaction) is the so-called *magneto-elastic coupling*. Magnetostriction coefficient $\lambda$ is defined as the relative change of linear sample dimension:

$$\lambda = \frac{\delta l}{l} = \frac{l - l_0}{l} \tag{2.43}$$

In case of the cubic crystal lattice the energy of magneto-elastic coupling is expressed by the formula:

$$\frac{E_{me}}{V} = \frac{3}{2}\lambda_s \sigma \sin^2\theta \tag{2.44}$$

where $\lambda_s$ is the magnetostriction coefficient in magnetic saturation, $\sigma$ is the stress, and $\theta$ is the angle between the direction of magnetization and measured magnetostriction.

The *surface anisotropy* is related with the difference of the magnetic properties inside the material and for the surface or interfacial areas. Breaking of the translational symmetry leads to the development of the anisotropy energy formula. Generally, the energy (by unit volume) of magnetocrystalline anisotropy can be expressed as:

$$\frac{E_S}{V} = K_{eff}\sin^2\theta \tag{2.45}$$

where $\theta$ is the angle between the magnetization and the normal to the surface, which is also the easy magnetization axis. The effective anisotropy coefficient $K_{\text{eff}}$, including participation of the volume ($K^{\text{V}}$) and the surface ($K_{\text{S}}$) anisotropy, is equal to:

$$K_{eff} = K^{V} + \frac{1}{d} K_{S} \tag{2.46}$$

where $d$ is the linear size of the object (eg. a thickness of thin film or nanograins diameter). Note, that measurements of $M(H)$ for a deferent field direction to the surface provides the information about $K_{\text{eff}}$ coefficient and based on the graph of $d\,K_{\text{eff}}$ as a function of $d$, the $K^{\text{V}}$ and $K_{\text{S}}$ can be also determined.

## 2.1.5. Selected magnetic characteristics and parameters

It is difficult to imagine the development of many fields of technology without the modern magnetic materials. Scale of applications is very wide including electrical and energy engineering, computer sciences and environmental protection technology. The most popular are ferromagnetic materials ($J_{ex} > 0$) with application potential related to parameters of the so-called *magnetic hysteresis loop* (Figure 2.7a shows a typical example) such as:

a) *saturation magnetization*, i.e. the state reached when an increase in applied external magnetic field $H$ cannot further increase the magnetization of the material,

b) *coercive field* (or *coercivity*) is a value of magnetic field that causes demagnetization of a material after magnetic saturation,

c) *magnetic remanence* is the magnetization left after an external magnetic field is removed,

d) *permeability*, is the relation between the magnetizing field $H$ and the magnetic field $B$ i.e. $\mu = B / H$ which is not constant for ferromagnetic materials,

e) *maximum energy product* $|BH|_{\text{max}}$ calculated in the second quadrant of the hysteresis loop (in the $B/H$ representation) coordinate system (the highest $BH$

product) which determines the maximum of magnetic energy realted to a stray field produced by the material.

f) *maximum energy product* $|JH|_{max}$ (where $J$ is the magnetic polarization, equal to $\mu_0 M$). The values of $|JH|_{max}$, determined from $M(H)$ loops in the second quadrant, describe magnetic energy density stored into material which means also the energy required for demagnetization (see Figure 2.7b).

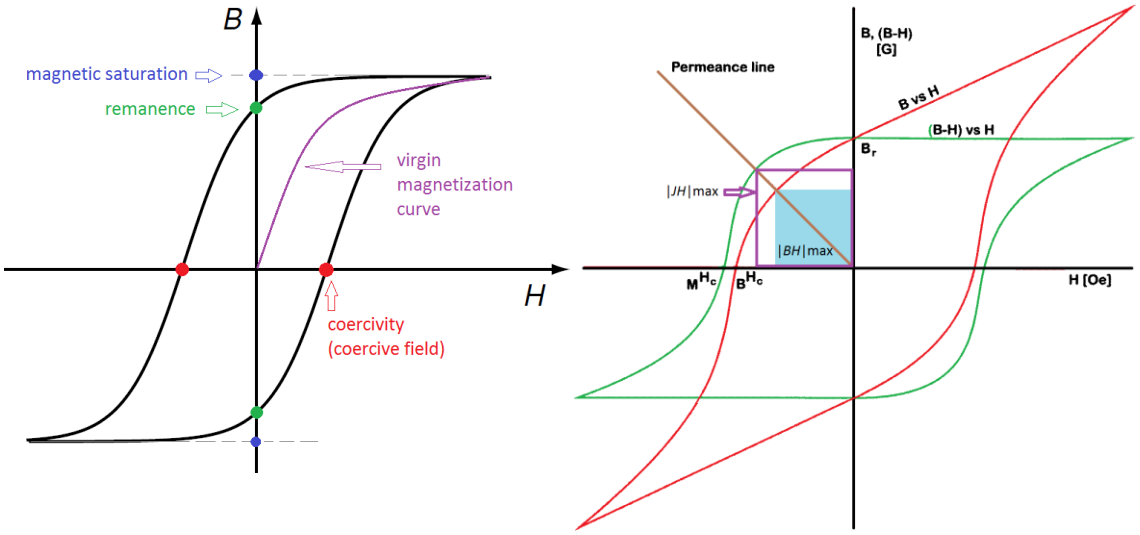


Figure 2.7. A typical curve of the hysteresis loop for ferromagnetic materials with their parameters (a); comparison of the hysteresis loop in the $B/H$ and $M/H$ representation as well as $|BH|_{max}$ and $|JH|_{max}$ parameter (b).

The basic division of ferromagnetic materials distinguishes the so-called *soft* and *hard magnets* depending on the value of coercive field. Generally, the materials with the coercive field less than $10^3$ A/m are magnetically soft, while materials with coercivity more than $10^4$ A/m are classified into hard magnetic group.

From application point of view and in the case of soft magnetic materials, the aim is to maximize the value of the magnetic permeability (initial as well as maximum) and minimize the energy losses associated with a full cycle of remagnetization (i.e. the area of the hysteresis loop). Such parameters can be achieved when the magnetic structure consists of ferromagnetic coupled atoms with high magnetic moment like Fe or Co, and a microstructure characterized by a low energy of the magnetocrystalline anisotropy. The domain structure, or more precisely, the ability to move of the domain walls is also

important. In the case of internal stress, which usually occurs during the production of materials, the magneto-elastic coupling plays an important role. Therefore, the soft magnetic material should have a magnetostriction coefficient close to zero, and the final step of a preparation process should reduce the stress. In a group of so-called conventional soft magnetic materials there are known iron-based with different magnetic and non-magnetic elements. An example is a silicon steel FeSi (with a few percent of silicon), which is used to produces a magnetic cores of transformers. Other examples are alloys of Fe-Ni (78% Ni and 22% Fe), Fe-Co (50% Fe and 50% Co), Fe-Ni-Co, Fe-Si-Al etc. Currently, the most promising magnetic materials (not only soft) are amorphous and nanocrystalline alloys based on iron. Figure 2.8 shows a comparison of the soft magnetic properties for different kind of amorphous and nanocrystalline materials. First discovered ferromagetic nanocrystalline alloys are called *FINEMET* with Fe as the main element and Si, B, P as additions. The saturation induction and initial magnetic permeability are equal to about $10^4$ and 1 T, respectively. In the so-called *NANOPERM* type alloys the Si addition is eliminated which leads to increasing of saturation induction. Subsequently, for *HITPERM* type alloys the iron is partially replaced by cobalt in order to increase the Curie temperature.

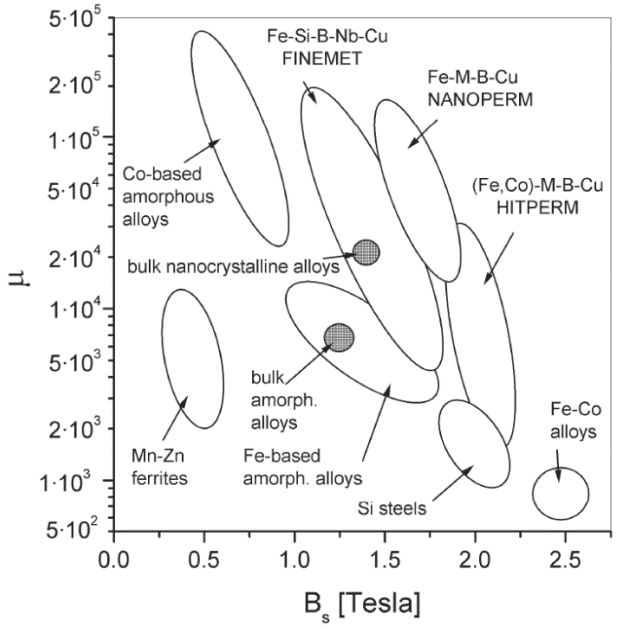


Figure 2.8. Comparison of soft magnetic properties for different type of amorphous and nanocrystalline materials [8].

Hard magnetic materials have also many applications. Generally, there are used to produce a magnetic field, which is necessary for power generators, electric motors, sensors and data storage devices, without which it is difficult to imagine the modern development of information technology and in almost every area of human activity. Magnetically hard materials should be characterized by a high value of the coercive field, a large value of saturation magnetization and remanence. Moreover, the maximum energy product is also very important. Thus, any kind of magnetic anisotropy (understood as the energy barrier standing in the way to changing of magnetic moment direction), will be useful for magnetic hardening - starting from magnetocrystalline anisotropy at the atomic scale up to the shape and surface anisotropies related to the size and form of the sample as a whole. In addition, all factors which slows down the movement of domain walls, such as structural defects, internal stresses and grain boundaries are also desired. Examples of well-known hard magnetic materials are strontium and barium ferrites ($SrO{\cdot}6Fe_2O_3$, $BaO{\cdot}6Fe_2O_3$), alnico alloys (Al-Ni-Co) as well as Pt-Co and Pt-Fe alloys. Moreover, some compounds of transition metals and rare earths elements are very promising. Hard magnetic materials are especially important for this work and there are described in detail in the third chapter.

## 2.2. Nanomagnetism

### 2.2.1. Impact of sizes on the electronic structure

In recent years, a rapid development of low-dimensional physical systems can be observed ([9], [10], [11], [12]), i.e. the structures which are at least in one dimension less than 1 μm (so-called mesoscopic systems), or less than 100 nm (nano systems). Smaller systems, where specific number of atoms can modify the properties are called clusters. Depending on how many dimensions are not limited to the nanoscale, one can be distinguished:

a) a thin films (2D systems), if there is just one dimension in nanoscale;

b) a nanowire (1D systems), if there are two dimensions in nanoscale;

a) nanoparticles (0D systems), if all dimensions are in nanoscale.

It should be noted that there are many currently known low-dimensional systems like fullerenes, nanotubes, graphene etc. with characteristic structures and properties related to their dimentions.

Unique properties of low-dimensional structures have several reasons. The main feature of such systems is a significant contribution of surface [6]. Figure 2.9a presents the percentage of surface contribution vs. average size of particle (assuming 2 Å of lattice constant). One can note that for object less than 10nm in diameter, significant number of atoms are placed on the surface. The second difference, in comparison to the bulk materials, is that the size of such objects are close to the values of certain characteristic parameters, such as range of RKKY interaction or even exchange interaction, domain size, thickness of domain wall, critical single domain size and so on. Therefore, the interaction between magnetic moments and consequently the nature of magnetic ordering are modified. The typical values of selected parameters are summarized in Table 2.2. Another reason is a breaking of translational symmetry, which involves a reduction of the coordination number (nearest neighbors), broken bonds at the surface and frustrations. In case of magnetic properties, the limited size at least in one direction, leads to strong magnetic anisotropy, which also must be taken into account for description of the

magnetization process. Recent studies have shown that both soft as well as hard magnetic properties can be controlled by appropriate nanostructure and optimized for specific applications.

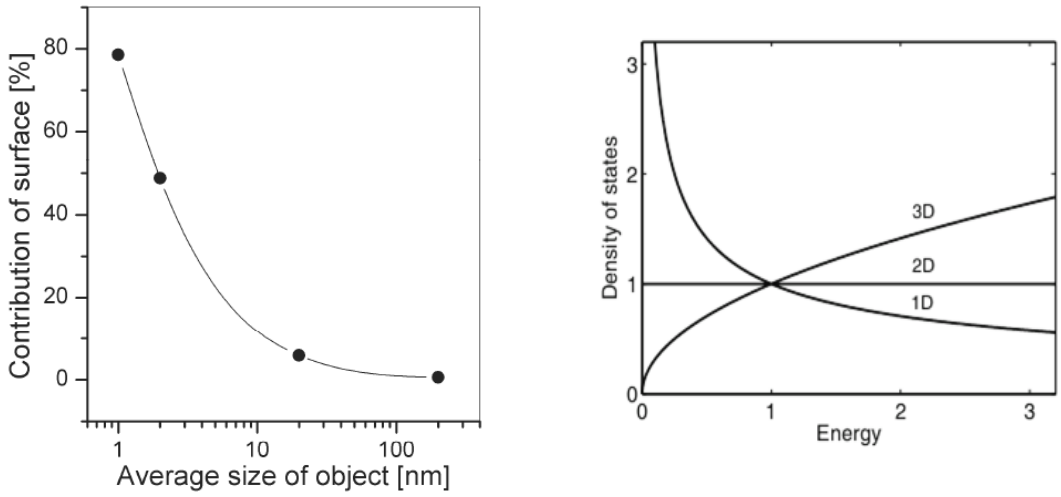


Figure 2.9. (a) Contribution of surface (in %) as a function of average size of the object with lattice constant equal to 2 Å. (b) Density of states of the electrons in the potential well with different dimensionality.

Table 2.2. Typical values of length for selected parameters (based on [6]).

| Length | Symbol | Typical magnitude [nm] |
|---|---|---|
| **Interatomic distance (Fe)** | $d_a$ | $2.5 \times 10^{-1}$ |
| **Range of exchange interaction** | $d_{ex}$ | $\sim 10^{-1}$ - $\sim 1$ |
| **Range of RKKY interaction** | $d_{RKKY}$ | $\sim 10^{-1}$ - $\sim 10$ |
| **Domain size** | $d_c$ | $10 - 10^4$ |
| **Superparamagnetic critical diameter** | $D_{cr}^{spm}$ | $\sim 1$ - $\sim 10^2$ |
| **Critical singe-domain size** | $D_{cr}$ | $\sim 10$ - $\sim 10^3$ |
| **Domain wall width** | $\delta_0$ | $\sim 1$ - $\sim 10^2$ |
| **Exchange length** | $l_{ex}$ | $\sim 1$ - $\sim 10^2$ |
| **Spin diffusion length** | $l_{sd}$ | $\sim 10$ - $\sim 10^2$ |
| **Electron mean free path** | $\lambda_{mfp}$ | $\sim 1$ - $\sim 10^2$ |
| **Superconducting coherence length** | $\zeta$ | $\sim 1$ - $\sim 10^3$ |
| **Fermi wavelength/metal** | $\lambda_F$ | $\sim 10^{-1}$ |
| **Fermi wavelength/semiconductor** | $\lambda_F$ | $\sim 10^2$ |

Reduction of dimensional solid structure leads to quantization of the electron states density function, even without taking into account the surface effects. The density of state function, for the electrons in the potential well with three, two and one dimension in nanoscale are presented in Figure 2.9b. The free electron situation can be applied as an approximation to analyze the impact of the size of the object on its electronic structure. In case of 0D structure, the electron energy is equal to [6]:

$$E = \frac{\hbar^2 \pi^2}{2m}\left(3\frac{n^2}{L^2}\right) \tag{2.47}$$

where $n$ = 1, 2, 3,… and $L$ is a size in each dimensions. If $L$ = 1 nm then $\Delta E \approx 1$ eV and energy levels are separated like for atoms. Therefore, decreasing the size of the object leads to a change of the density of states from quasi-continuous function (for macroscopic systems) to the discrete function with forbidden energy gaps. On the other hand, in case of 2D structures, with dimensions $L_x$ and $L_y$ in nanoscale, while $L_z = L$ is much bigger than other, the electron energy can be expressed as [6]:

$$E = \frac{\hbar^2 \pi^2}{2m}\left(\frac{n_x^2}{L_x^2} + \frac{n_y^2}{L_y^2} + \frac{n_z^2}{L^2}\right) \tag{2.48}$$

Due to the number $n_x$ and $n_y$ (in nanoscale) the gap between energy levels is big, but due to the number $n_z$ the energy value are essentially continuous ($L / L_x \approx 10^9$). Therefore, the density of states function has a stepped shape and between the steps the function of $g(E) \sim E^{-1/2}$ should be expected. In case of 1D structure, the $g(E)$ function between steps is constant. Summary of all discussed situation is shown in Figure 2.10.

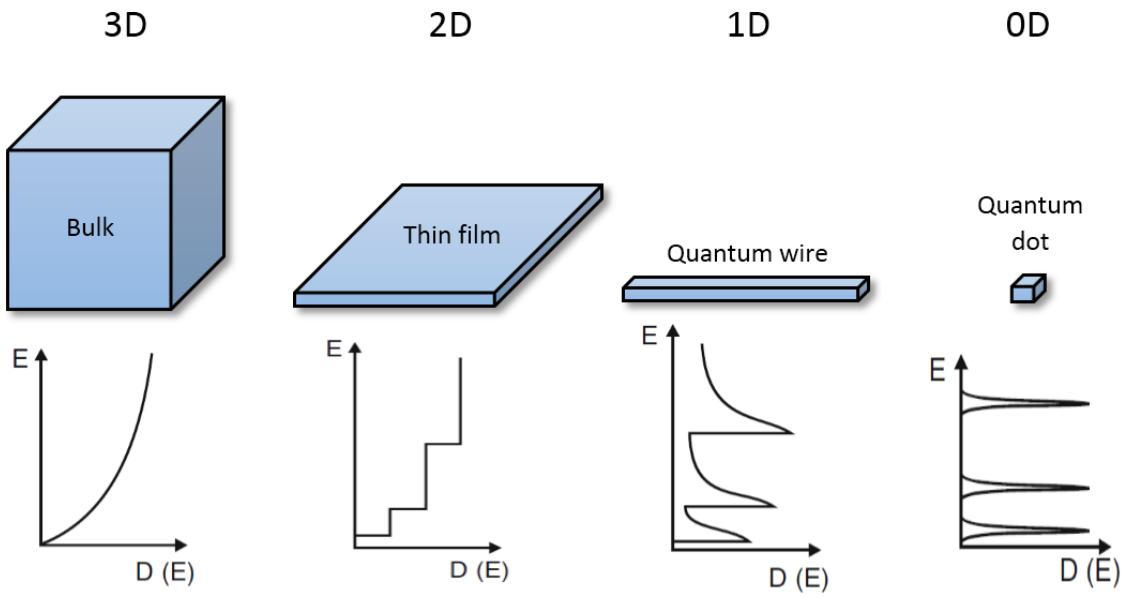


Figure 2.10. Impact of the system size to the density of electron states (adapted from [13]).

It is important to note that many physical properties like the magnetic susceptibility of the conduction electrons (the Pauli paramagnetism), the Stoner ferromagnetism condition or, in the case of 3d metals, the value of the magnetic moment are a function of density of states at the Fermi level. Therefore, the size of the object influences these properties due to the changes of the electronic structure.

### 2.2.2. Domain structure and nanoparticles magnetization process

*The domain structure* is a collection of regions containing coupled magnetic moments with the same magnetization direction. Each region is separated from each other by so-called *domain walls* i.e. the area where spins changes the direction of magnetization between domains. Formation of magnetic domains is caused by the minimization of different types of energy including demagnetization energy (interaction of magnetic moments with magnetic field produced itself by the material), anisotropy and also the energy of domain walls. Therefore, this phenomenon depends on chemical composition, shape and size of the sample.

For the analysis of the nano-objects magnetization process, the behavior of domain walls plays an important role. In case of nanograins, the so-called *Bloch walls* should be

expected. For this situation (presented on Figure 2.11a) there is no space limitation for rotating spins. If rotation of spins is enclosed in specific plane (as it is illustrated on Figure 2.11b) then it is so-called *Neel wall*, characteristic for thin films.

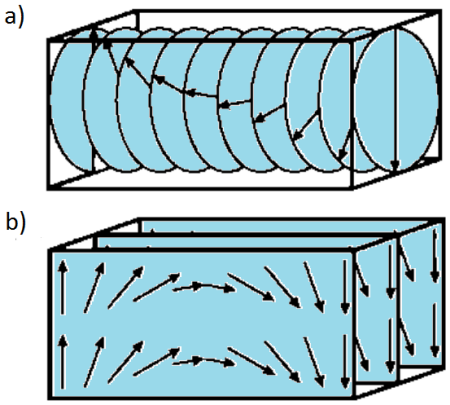


Figure 2.11. Rotation of the spins in the Bloch walls (a) and Neel walls (b).

Let us consider slightly simplified case of material with uniaxial magnetocrystalline anisotropy and anisotropy constant equal to $K_U$. The thickness of domain wall $\delta$ is associated with competition between exchange interaction and anisotropy energy:

$$\delta = Na = \pi\sqrt{\frac{A}{K_U}}, A = \frac{2J_{ex}S^2}{a} \tag{2.49}$$

where $a$ is lattice constant. For example, for iron $\delta$ is equal about 40 nm. If the size of nanograins is less than the domain wall thickness then such material has only one domain. Figure 2.12a andFigure 2.12b show an example of one- and two-domain magnetic particles. In case of spherical nanoparticle the critical diameter can be expected as:

$$D_{cr} = \frac{72\sqrt{AK_U}}{\mu_0 M_s^2} \tag{2.50}$$

Some examples of magnetic materials with value of critical diameter $D_{cr}$ and the domain wall energy $\gamma$ are summarized in Table 2.3.

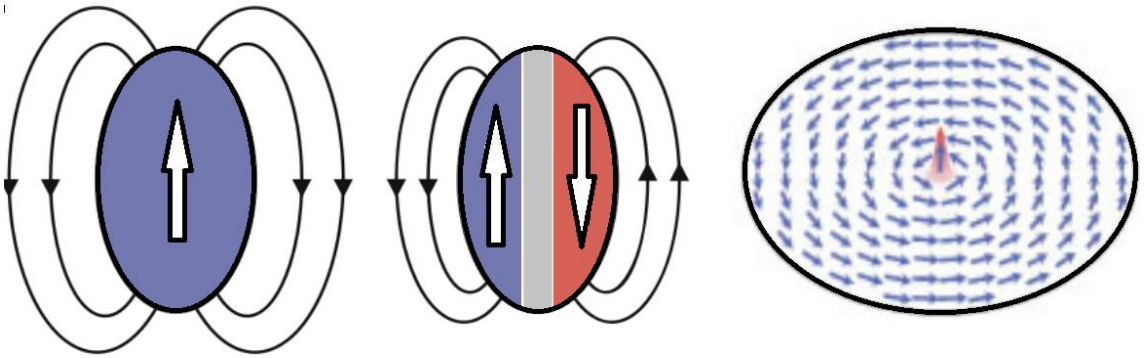

Figure 2.12. Example of single-domain and two-domain particle, as well as vortex structure from left to right, respectively (adapted base on [6]).

Table 2.3. Values of $\mu_0 M_s$, $D_{cr}$ and $\gamma$ parameters for selected magnetic materials.

| Material | $\mu_0 Ms^2$ [$10^6$ $Jm^{-3}$] | $D_{cr}$ [nm] | Domain wall energy $\gamma$ [$10^{-3}$ |
|---|---|---|---|
| **$Fe_3O_4$** | 0.29 | 12.4 | 2 |
| **$CrO_2$** | 0.2 | 180 | 2 |
| **MnBi** | 0.45 | 480 | 12 |
| **$Nd_2Fe_{14}B$** | 2.06 | 210 | 24 |
| **$SmCo_5$** | 0.88 | 1,170 | 57 |
| **$Sm_2Fe_{17}$** | 1.33 | 420 | 31 |
| **FePt** | 1.44 | 340 | 32 |
| **$BaFe_{12}O_{19}$** | 0.183 | 62 | 6.3 |
| **Fe** | | 19 | 3.9 |
| **Co** | | 96.4 | 13.6 |
| **Ni** | | 53.6 | 0.878 |
| **$Ni_{0.8}Fe_{0.2}$** | | 4.66 | 0.215 |

As can be seen from the above analysis, the magnetic properties of ferro- or ferri-magnetic nanoparticle will strongly depend on their size. Small particle exhibits superparamagnetic properties. Due to thermal excitations, the magnetic moments of the particle are free to change the magnetization direction and the average magnetization is equal to zero. In this case, the magnetization process is well described by the classical Langevin function.

Slightly larger particles (but smaller than $D_{cr}$) consist only a single domain which can be described by the Stoner-Wohlfarth model (described later). When the particle size is larger than the range of exchange interaction but smaller than the width of the domain wall, then the so-called *vortex structure* can occur. This situation is presented in Figure 2.12c. Moreover, it is worth to compare the typical hysteresis loop for a single domain particle (Figure 2.13a) and the vortex structure (Figure 2.13b). In second case, the increasing external magnetic field destroys the vortex ordering and leads to the formation of a single domain which is observed as a growing of magnetization. When external magnetic field is switched off, the vortex structure will be reconstructed which leads to a sudden drop of magnetization.

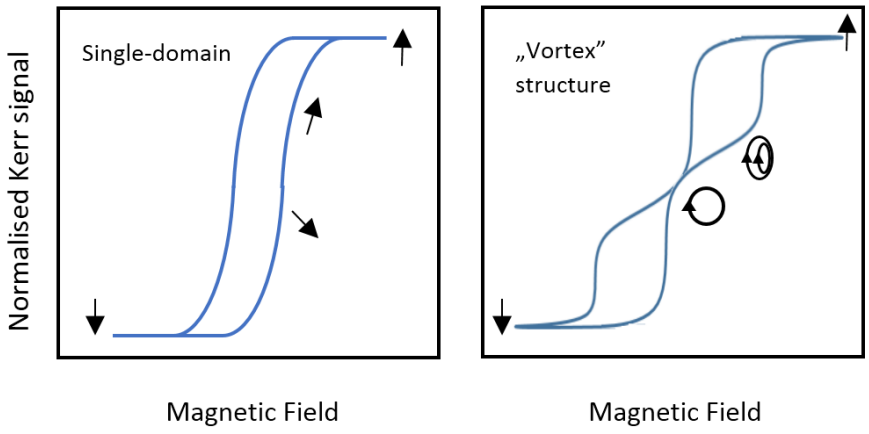


Figure 2.13. Typical hysteresis loops for single-domain particle and "vortex" structure.

## 2.2.3. Interacting and no-interacting nanoparticles

The magnetic properties of the no-interacting nanoparticles describes *Stoner-Wohlfarth model* elaborated (after developed) in 1948 [14]. In this model it is assumed that temperature is equal to zero and the single domain particle is an ellipsoid with the main axis as well as the one easy magnetization axis along the z-direction. This situation is presented in Figure 2.14 with an external field axis $H$, magnetization axis $M$ and angles $\Psi$, $\varphi$ and $\theta$. Moreover, the coherent rotation of all magnetic moments (uniform magnetization in whole volume) is also assumed.

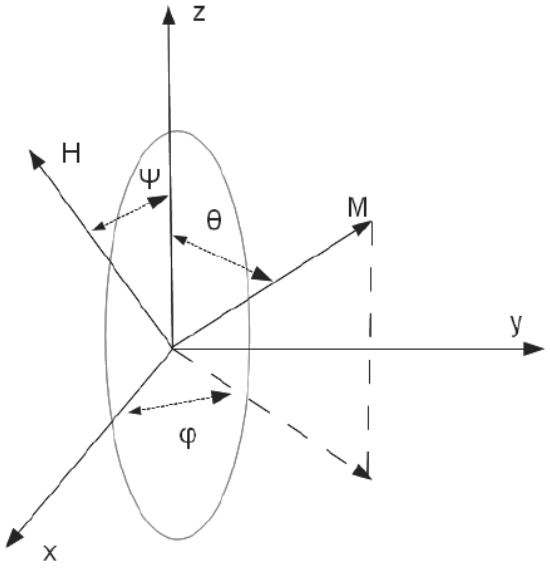


Figure 2.14. Presentation of $H$ and $M$ directions as well as $\Psi$, $\varphi$ and $\theta$ angles for ellipsoidal particle in the frame of Stoner-Wohlfarth model (see the text).

In case of $\Psi = 0$, the total energy of such system can be expressed as:

$$\frac{E}{V} = K_1 \sin^2\theta - \frac{1}{2}\mu_0 M^2 N_{\parallel} \cos^2\theta - \frac{1}{2}\mu_0 M^2 N_{@} \sin^2\theta - \mu_0 M_S H(\cos\theta\cos\Psi + \sin\theta\sin\Psi\cos\phi) \tag{2.51}$$

where the first term is related to the magnetocrstalline anisotropy ($K_1$ is a coefficient of uniaxial anisotropy), the second and third corresponding to the shape anisotropy of ellipsoid and the last one express the magnetic energy ($M_S$ is magnetic saturation, $N_{\parallel}$ and $N_{@}$ are the demagnetization factors parallel and perpendicular to the main axis). After simplification of $\varphi = 0$ (based on symmetry), the problem can be reduced to the x-z plane, and then:

$$\frac{\partial E}{\partial \theta} = 2K_1 \sin\theta\cos\theta - \mu_0 M_S^2 \sin\theta\cos\theta (N_{@} - N_{\parallel}) - \mu_0 M_S H \sin\theta \tag{2.52}$$

Moreover, based on minimum condition the nucleation field $H_N$, needed to revert magnetization from parallel to antiparallel direction, can be directly calculated.

Let us assume a spherical shape of particle i.e. $N_{\parallel} = N_{@}$ and external magnetic field along z direction. Figure 2.15a presents some examples of $E(\theta)$ for different ratio of $\mu_0 M_S H$ / $K_1$. One can note that without magnetic field there are two equivalent minima at $\theta$=0 and $\theta$=π, while increasing of H leads to decreasing of energy barrier.

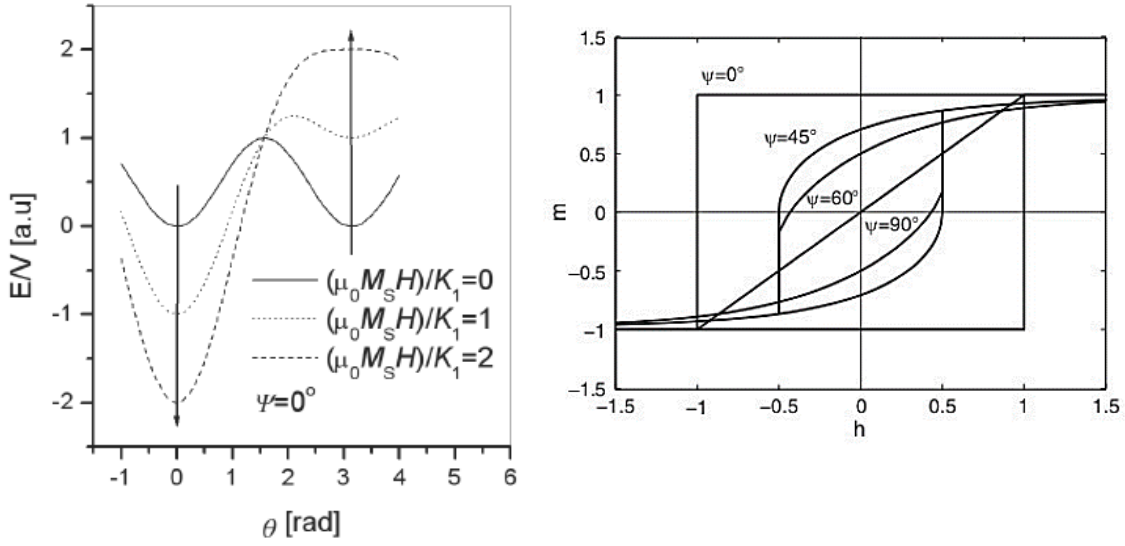


Figure 2.15. (a) E(θ) dependences with different ratio of magnetic energy vs. anisotropy (Ψ=0) as well as (b) the magnetic hysteresis loops (Ψ=0º - 90º) calculated in a frame of the Stoner-Wolfarth model.

The height and position of energy barrier as well as anisotropy field $H_A$ when the barrier disappear are equal to:

$$\Delta E = K_1 V(1-\frac{H}{H_A})^2, \qquad \theta_{max} = arccos\left(-\frac{\mu_0 M_S H}{2K_1}\right) \text{ and } H_A = \frac{2K_1}{\mu_0 M_S} \qquad (2.53)$$

respectively. At temperature above absolute zero, the thermal excitation energy and consequently the possibility of spontaneous jumping by the energy barrier (changing the magnetization direction) should be also taken into account. Such approach is described in the section 2.3.2. The Stoner-Wohlfarth model allows determinate the total magnetization as a function of magnetic field (magnetic hysteresis loops) for any angle $\Psi$. The examples of such hysteresis at $T = 0$ for $\Psi = 0º$, 45º,60º and 90º are presented in Figure 2.15b.

Presented S-W model describing the magnetization process of a single particle or non-interacting system. However, if the distance between the particles are sufficiently small then the exchange or RKKY interactions are expected. The analysis of the interaction between the magnetic particles can be done based on the so-called. *Henkel plot* [15], [16] i.e. a comparison of the two magnetic remanence curves: $M_{DC}$ and $M_R$ as a function of magnetic field $H$. In order to measure the $M_{DC}(H)$ curve, the material should be saturated in field $H$, next the field is reverted to the value of $-H$ and switch to zero. The remanence

after such procedure is the $M_{DC}(H)$ value. The curve of $M_R(H)$ can be measured in classical way i.e. it is the remanence without field after magnetization in a field $H$ (starting from demagnetised material). In case of non-interacting magnetic particles, the following equation should be satisfied:

$$M_{DC}(H) = M_R(\infty) - 2M_R(H) \tag{2.54}$$

On the other hand, for the system with interacting particles the above formula is not fullfilled, and then the measure of coupling can be expressed as:

$$\Delta m_h(H) = m_{DC}(H) - [1 - 2\mathrm{m}_r(H)] \tag{2.55}$$

where $m_{DC}(H) = M_{DC}(H)/M_R(\infty)$ and $m_r(H) = M_r(H)/M_R(\infty)$. The $\Delta m_h(H)$ function is the Henkel plot and it can be used to determine the presence of particles interaction. An alternative approach is to analyze the hysteresis loop with virgin magnetization curve [17], [18]. Similar as before, in case of system without interaction the formula should be true:

$$M_{vir}(H) = \frac{1}{2}[M_{up}(H) - M_{down}(H)] \tag{2.56}$$

where $M_{vir}$ is a virgin magnetization curve and $M_{up}$ as well as $M_{down}$ are the upper and bottom (in comparison to $M_{vir}$) curve at the same magnetic field. Any deviation from this formula is a measure of interaction between particles.

### 2.2.4. Spring magnetism

Especially interested group of magnetic materials are the alloys and nanocomposites containing grains of two phases - magnetically soft and hard. In cases when both phases are magnetically coupled at the atomic level (exchange interactions) and moreover, the hard phase is dominant, such system may be characterized by high coercivity (related to the hard magnet phase) and simultaneously, high magnetic moments provided by the soft magnet phase [19], [20], [21]. This situation is called *spring magnetism* and is expected for permanent magnets, because it can lead to a high value of maximum energy product. Let us compare the hysteresis loops presented on Figure 2.16.

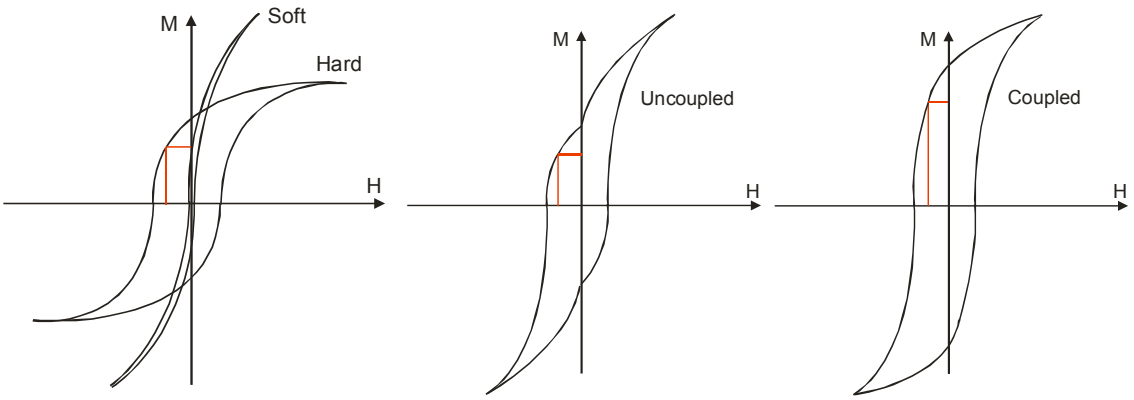


Figure 2.16. (a) A typical soft and hard magnet hysteresis loops, (b) standard uncoupled hysteresis, and (c) result of spring-magnet effect.

The first illustration shows two hysteresis curves typical for soft and hard magnetic phases. Without strong exchange interactions between magnetic moments associated with the different phases, a classic uncoupled superposition of this hysteresis is expected (Figure 2.16b). However, if exchange energy between two phases is dominant, then (as it is shown on Figure 2.17) the "soft" magnetic moments are freezing in specific direction with nearest "hard" moment neighbors, even in presents of external magnetic field. In other words, the magnetic moments of soft magnet phase will change their magnetization progressively according to increasing of external field and some part of them will stay associated with magnetization direction of hard magnet phase. This situation leads to coupled hysteresis loop as shown on Figure 2.16c.

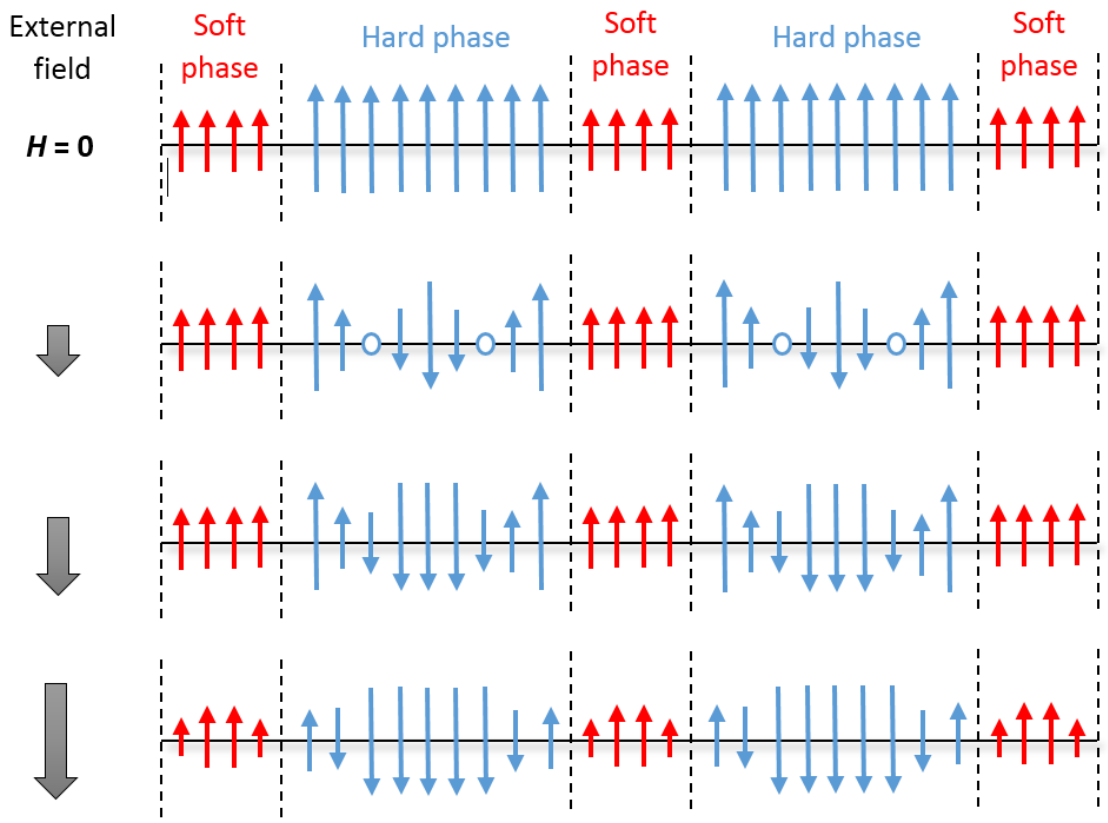


Figure 2.17. Kneller and Hawig's idea of exchange coupling hard and soft phases.

## 2.2.5. Magnetism in disordered materials

Many types of materials such as amorphous, nanocrystalline alloys and so-called *diluted magnetic materials* may be characterized by some kind of disorder: in structure, interaction between magnetic moments or magnetic anisotropy parameters. Even in polycrystalline samples, some anomalies related to the area between the grains can be observed. Both, structural as well as magnetic disorder implies a change of magnetic properties and should be included during modeling of such systems.

Let us assume the spin system $S_i$ with direct exchange coupling described by the parametetr $J_{ij} = J(|\vec{r_i} - \vec{r_j}|)$ and magnetic anisotropy attributed to each site. Hamiltonian of such system can be written as:

$$H = -\sum_{i,j} J_{ex_{ij}} \overrightarrow{S_i} \cdot \overrightarrow{S_j} - \sum_i K_i (\overrightarrow{S_i} \cdot \overrightarrow{z_i})^2 - g\mu_B \mu_0 \sum_i \overrightarrow{H_i} \cdot \overrightarrow{S_i} \qquad (2.57)$$

where $K_i$ is the anisotropy constant, $z_i$ is the easy magnetization axis on $i$ site and and $H_i$ is the magnetic field applied to the spin on site $i$.

The firs sum is usually limited to the nearest neighbors and it is related to the energy of spins interactions. The second sum expresses magnetocrystalline anisotropy while the third one corresponds to the magnetic energy. Generally, there are three ideas to introduce various types of disorder into such model:

1. A distribution of $H_i$ (magnetic field) leads to the so-called *random field Ising model* (RFIM), developed in 1975 by Imry and Ma as an extension of basic ferromagnetic Ising model [22], [23], [24].
2. The approach which provides a distribution of $J_{ij}$ parameter was presented by Scott Kirkpatrick with David Sherington and is called *S-K model* or *random bond model* (RBM) [25].
3. Both anisotropy parameters can be replaced by a distribution (but random axis $z_i$ is more realistic approach), which is called *random anisotropy model* (RAM). This situation is typical for amorphous and nanocystaline materials.

A particularly important type of disorder for amorphous and nanocrystalline systems is the anisotropy disorder, described in details in references [26], [27], [28] and [29]. This kind of disorder can be provide by the distribution of anisotropy constant $K_i$ and also (which is more realistic) the random easy magnetization axis $z_i$. With the assumption of $K_i = K$, $J_{ex_{ij}} = J_{ex}$, as well as $z_i$ distributed randomly and in two dimensional space, the free energy and magnetization can be analytically calculated [30]. However, the other approach to the disorder provided by random anisotropy axis requires computer simulations methods to solve the three-dimensional problem of the Hamiltonian and generate the curve of magnetization vs. temperature and applied field. The values of magnetic coercive $H_C$ and reduced remanence $M_R/M_S$ as a function of $K/J_{ex}$ ratio for simulated hysteresis loops are shown in Figure 2.18a and Figure 2.18b, respectively. It turns out that $H_C$ strongly increasing in range $2 < K/J_{ex} < 10$, while $M_R/M_S$ slightly decreasing from 0.8 to 0.55 for the same interval.

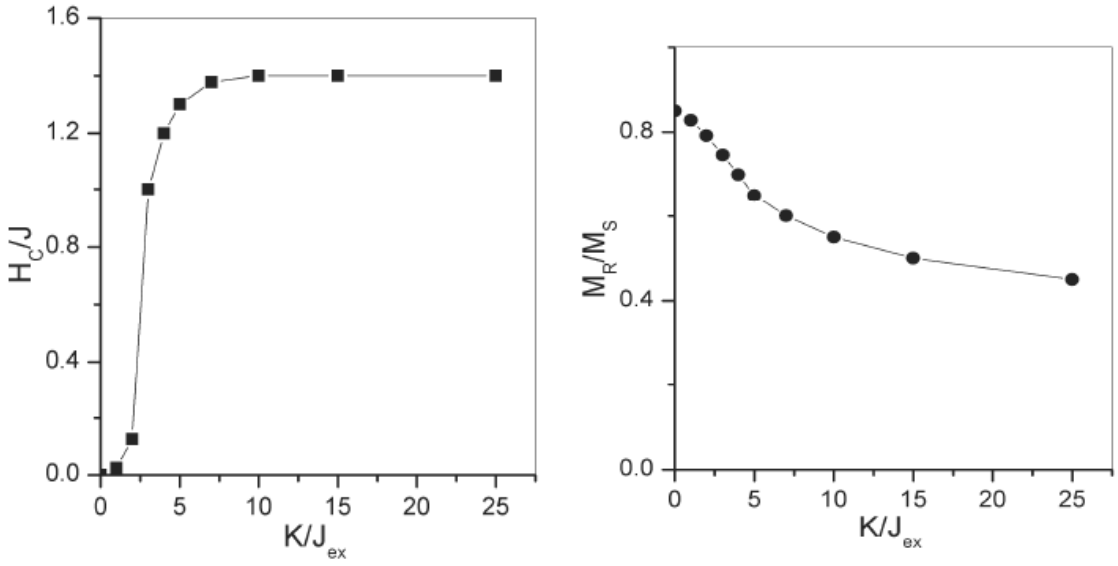


Figure 2.18. The magnetic coercive $H_C$ and reduced remanence $M_R/M_S$ as a function of $K/J_{ex}$ ratio based on hysteresis simulations with random anisotropy axis.

In case of nanocrystalline materials, many nanograins may be included in the range of magnetic correlation. This means that many randomly generated easy magnetization axes (associated with each nanograins) should be taken into account in the range of exchange interaction. In such case, the average anisotropy coefficient is equal to [31]:

$$\langle K \rangle = \frac{1}{\varphi^6} \frac{K_{loc}^4 D^6}{A^3} = K_{loc} (\frac{D}{L_0})^6 \tag{2.58}$$

where $D$ is a diameter and $K_{loc}$ is local anisotropy of the particles and $A$ is the exchange stiffness constant of crystalline phase. Moreover, $\varphi = 1$ for so-called *Herzer model* (more details in [32], [33], [34]) or $\varphi = (4/3)^{1/2}$ for *Alben model*. Note, that the average anisotropy coefficient is proportional to $D^6$ and also it is included in two important soft magnetic quantities: coercivity $H_C$ and initial magnetic permeability $\mu_i$:

$$H_C = p_C \frac{\langle K \rangle}{M_S} \approx p_C \frac{K_{loc}^4}{M_S A^3} D^6 \tag{2.59}$$

$$\mu_i = p_\mu \frac{M_S^2}{\langle K \rangle} \approx p_\mu \frac{M_S^2 A^3}{K_{loc}^4} \frac{1}{D^6} \tag{2.60}$$

where $p_C$ and $p_\mu$ are a constants close to unity. An example of dependence of $\langle K \rangle$ as a function of $D$ for FeSi (bcc) nanograins is shown in Figure 2.19a. In this case, the soft magnetic properties are significantly improved for $D < 10$ nm due to decreasing of $\langle K \rangle$

to almost zero. Figure 2.19b presents some other examples of $H_C$ and $\mu_i$ for Fe-based nanocrystalline compounds.

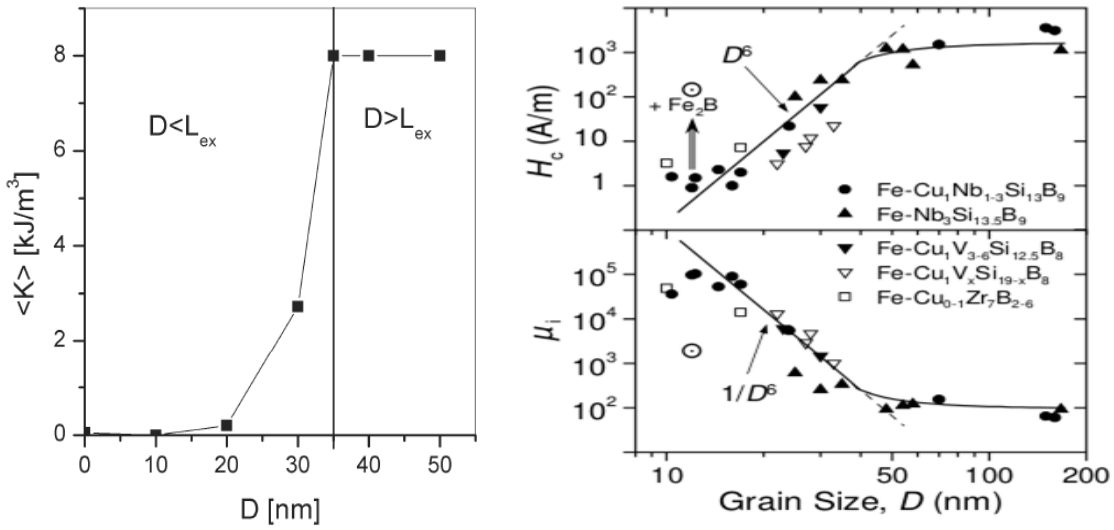


Figure 2.19. (a) The average anisotropy coefficient vs. diameter of particles for FeSi (bcc) nanograins [34] and (b) coercivity as well as low-field magnetic permeability for several nanocrystalline Fe-based compounds [35].

## 2.3. Modeling of magnetization processes in hard magnetic systems

### 2.3.1. Monte Carlo simulations

Monte Carlo simulation is a numerical method which allows determining properties of some phenomenon by repeating deterministic calculations for many random inputs. Generally, the deterministic problem is solving using a probabilistic analog.

According to the *law of large numbers* the frequency of a random event will be close to the probability of this event for a large number of trials and will tend to become closer as more trials are performed:

$$\lim_{n\to\infty} P\left(\left|\frac{S_n}{n} - p\right| \leq \varepsilon\right) = 1 \tag{2.61}$$

where $S_n$ is a number of success for Bernoulli trial and $n$ is a total number of trials, $p$ is a success probability in one trial and $\varepsilon$ is any positive number. Base on this assumption the Monte Carlo simulation can be performed. Firstly, a domain of possible inputs should be defined. The main simulation generates the random inputs (with probability distribution over the domain) and applies deterministic calculations for each of them. At the end the obtained results are aggregated.

The common example of Monte Carlo method is a calculation the value of π number. In this case, the starting point is drawing the square with a circle inside. Next, the random point in the square is chosen (random inputs) and the value of $P_o$ is increasing if the point belongs to circle (deterministic calculations). The $P_o$ / $n$ ratio is an estimate of the ratio of the two areas, which is equal to π / 4 (results aggregation). The Monte Carlo method is a common technique that can be used to solve mathematical, statistical as well as physical problems. First application in this field, concerned radiation shield, was performed by Stanislaw Ulam.

Generally, there are three common approaches to computer simulation in physics: deterministic (molecular dynamics), stochastic (Monte Carlo) and hybrid (Brownian dynamics). In equilibrium statistical mechanics, a classic system at temperature $T$, which

can exchange energy with the environment, can be described by so-called *Boltzmann equation* (*canonical ensamble*):

$$P(x)=\frac{1}{Z}\exp(-\frac{U(x)}{k_B T}) \tag{2.62}$$

where $U(\mathbf{x})$ is a potential energy, $k_B$ is Boltzmann constant and $Z$ is equal to:

$$Z=\int \exp\left(-\frac{U(x)}{k_B T}\right)dx \tag{2.63}$$

In this case a physical quantity $A(\boldsymbol{x})$ can be calculated by formula:

$$<A>=\frac{1}{Z}\int A(x)\exp\left(-\frac{U(x)}{k_B T}\right)dx \tag{2.64}$$

The so-called *Metropolis algorithm* base on random walks on the state space, such that the relative probabilities of the stay are in agreement with Boltzmann equation. In case of canonical ensemble the so-called *detailed balance condition* can be expressed as:

$$\frac{T(x\rightarrow x')}{T(x'\rightarrow x)}=\exp(-\frac{\left[U(x')-U(x)\right]}{k_B T}) \tag{2.65}$$

where $x \rightarrow x'$ represents transition between any two states $x$ and $x'$. One of the solution (usually called *Metropolis algorithm*) is:

$$T(x\rightarrow x')=\min[1,\exp\left(-\frac{\left[U(x')-U(x)\right]}{k_B T}\right)] \tag{2.66}$$

In context of magnetism important role plays the *Ising model* consisting of a set of $N$ spins $S_i=\pm 1$ localized in nodes of lattice. The energy of such system in external magnetic field $h_i$ is equal to:

$$H=-\frac{1}{2}\sum_{<i,j>}^{N} J_{ij}S_i S_j-\sum_i h_i S_i \tag{2.67}$$

where $J_{ij}$ is the exchange integral and $<i,j>$ means the nearest neighbors. One of the most interesting quantities is magnetization of the system:

$$m=\frac{1}{N}\sum_{i=1}^{N}<S_i> \tag{2.68}$$

The quintessence of Metropolis algorithm is random initialization state and iterations. Each iterations consist of random choosing of spin, changing its value and calculation the changing of energy $\Delta U$. The new state will be accepted if $\exp(-\Delta U/k_B T) > r$ where $0 < r < 1$ is a random value.

## 2.3.2. Numerical analysis of magnetization processes based on the two-level model

In some cases, magnetization processes can be considered as a kind of competition between magnetostatic and anisotropy energies. If in a material the so-called pinning of magnetic moments over an energetic barrier is a dominant mechanism one may modeling the magnetization process in a frame of the two-level model, as shown in Figure 2.20.

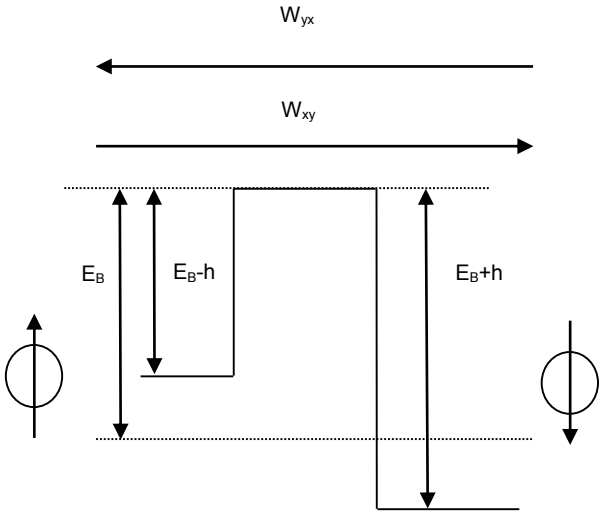


Figure 2.20. Schematic diagram of the two-level model.

The two-level statement means two states of a magnetic moment align parallel (let say Y) and anti-parallel (let say X) to an external magnetic field. These two states are separated by an energetic barrier which reflects the competition between magnetostatic energy

$h=\mu_0\mu H$ and anisotropy energy $E_B$. In such approach the resulting apparent energy barrier equals $E_B$- $\mu_0\mu H$. In temperatures $T > 0$ thermal excitations allow spontaneous jumping over the barrier leading to non-equilibrium occupation of the states X and Y. Dynamics of the system is described by the following equations:

$$\begin{aligned} \frac{dn_X}{dt} &= W_{YX} n_Y - W_{XY} n_X \\ \frac{dn_Y}{dt} &= W_{XY} n_X - W_{YX} n_Y \end{aligned} \tag{2.69}$$

where $n_X$ is the number of objects in state X, $n_Y$ is the number of objects in state Y, $W_{XY}$ and $W_{YX}$ is the transition frequency from X to Y, and from Y to X, respectively.

The quantities $W_{XY}$ and $W_{YX}$ may be written as:

$$\begin{aligned} W_{XY} &= W_0 \exp\left(-\frac{E_B - h}{k_B T}\right) \\ W_{YX} &= W_0 \exp\left(-\frac{E_B + h}{k_B T}\right) \end{aligned} \tag{2.70}$$

where $W_0$ is the jump frequency for $T \to \infty$. Solution of the equation system is:

$$n_X = n\tau W_{YX} + \left(n_{X0} - n\tau W_{YX}\right)\exp\left(-\frac{t}{\tau}\right) \quad , \quad \tau = \frac{1}{W_{XY} + W_{YX}} \tag{2.71}$$

where $n=n_X+n_Y$, $n_{X0}=n_X(t=0)$ and $\tau$ is the time constant.

Magnetization of the considered system can be defined as:

$$M = \mu(n_Y \cos\theta_Y - n_X \cos\theta_X)/V \tag{2.72}$$

where $\theta_Y$ and $\theta_X$ are the angles between magnetic field $H$ and magnetization of the object in state Y and X, respectively.

The analyzed magnetic moment can be related to single atoms or magnetically coupled atomic clusters. In real materials an appearance of a distribution of magnetic objects characterized by different magnetic moments and energetic barriers is expected. For non-interacting systems the magnetization can be calculated as a superposition of all magnetic objects contributing to magnetization process. In the case of interacting objects the

situation is more complex and the barrier can be considered as an apparent quantity including magnetic anisotropy energy as well as energy of the interactions.

Based on the described above model one may solve two problems. The first one is a simulation of magnetization curve (e.g. hysteresis loop) assuming some distribution of magnetic objects with different magnetic moment, energetic barrier and space alignment. Using the above equations the simulation is not so complicated. Figure 2.21 shows examples of hysteresis loops calculated for the following non-interacting systems (at 300K in ±1T range of magnetic field): a) single magnetic phase, b) two magnetic phases with different contribution of anisotropy constant.

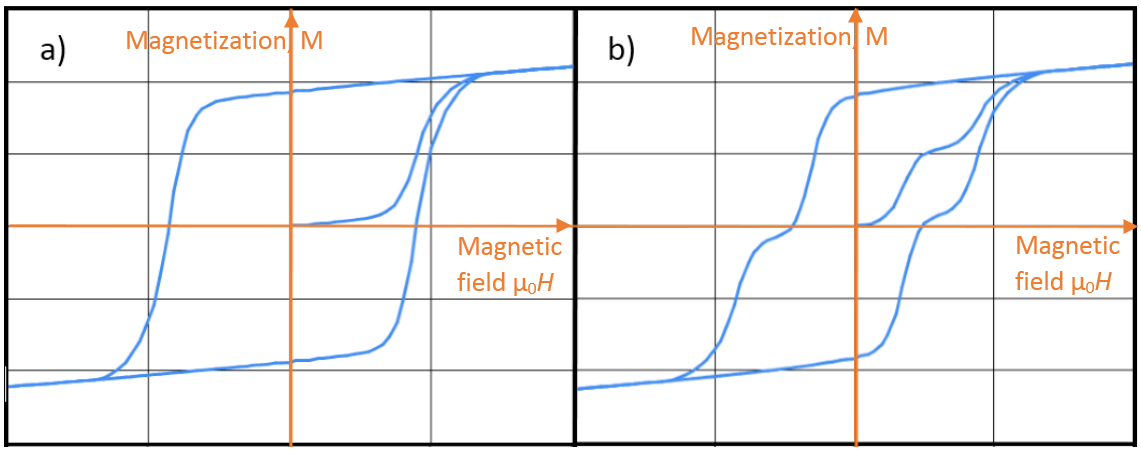


Figure 2.21. Examples of simulated hysteresis loops calculated based on the two-level model (see in text).

The second problem is opposite, i.e. determination of magnetic moment and energetic barrier (or their distribution) based on magnetization curve. The main difficulty is caused by some indistinguishably of two kind on magnetic objects, let say α and β, for which $E_B^{\alpha} - \mu_0 \mu^{\alpha} H = E_B^{\beta} - \mu_0 \mu^{\beta} H$. Furthermore, one can assume that for a typical measurement time 100 s, without external magnetic field and at a given temperature $T$ all objects that satisfy the condition $E_B < 25 k_B T$ change their magnetization over the barrier $E_B$. Accounting the above the indistinguishably of magnetic objects is expressed by the line $25 k_B T = E_B - \mu_0 \mu H$, called $H$-line. In $E_B$-$\mu$ space all objects with parameters below the $H$-line contribute to change of magnetization, see Figure 2.22. Let us analyze the experiment consisting in reversal magnetization after saturation.

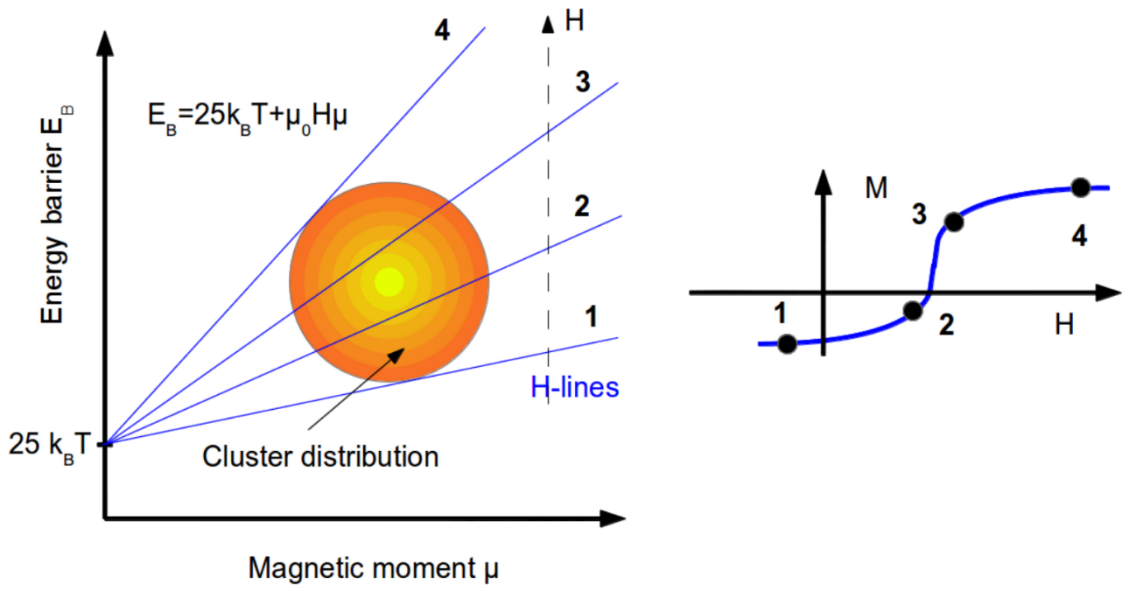


Figure 2.22. "Activation" of magnetic objects as a function of *H* at a given *T*. The circle represents distribution of magnetic objects.

Increasing field caused that more magnetic objects jump over the energetic barrier changing overall magnetization of the measured sample. This pinning effect is schematically depicted in Figure 2.23.

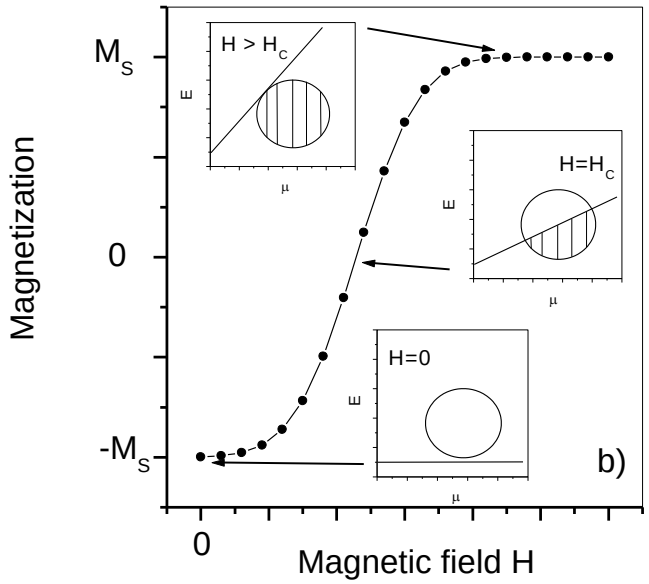


Figure 2.23. *M*(*H*) curve simulated by the pinning effect.

Determination of distribution of magnetic objects in $E_B$-$\mu$ space needs to overcome the described indistinguishability along the *H*-lines. The solution is to determine of the *H*-lines related to some homological points of the distribution at two different temperatures and calculate the parameters (i.e. magnetic moment and energetic barrier) from their intersection using simple geometric relation, as shown in Figure 2.24.

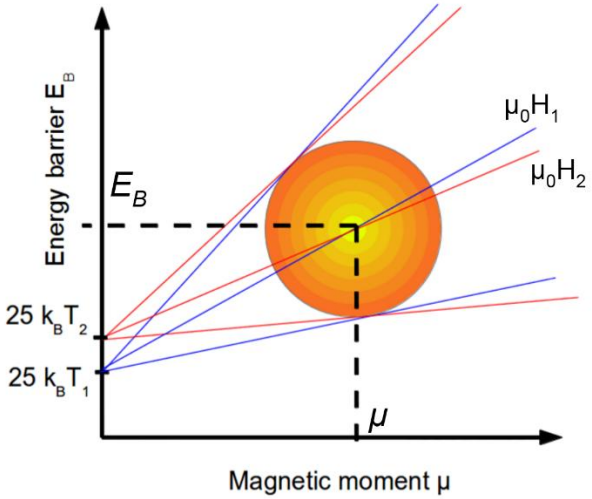


Figure 2.24. Determination of magnetic moments and energetic barriers of magnetic objects using H-lines.

In a simple case, parameters of the *H*-lines can be determined form derivative of magnetization d*M*/d*H* vs. magnetic field. Thus, the intercept is $25k_BT$ and slope is $\mu_0 H$, where *H* is a field related to some homological point. From a shift of this field determined at $T_1$ and $T_2$, one may calculate a real position in $E_B$-$\mu$ space using the equations:

$$\mu = 25k_B(T_2 - T_1)/(\mu_0 H_1 - \mu_0 H_2) \tag{2.73}$$

$$E_B = 25k_B T_1 + \mu\mu_0 H_1 \tag{2.74}$$

## 2.3.3. Magnetic viscosity and time depending effects

The phenomenon of so-called time depending effects (magnetic viscosity) [36], [37], [38] is related to the fact that two direction of magnetization can be separated by and energy barrier $\Delta E$. Thermal excitations can provide the energy needed to jumping the barrier with probability proportional to $exp(-\Delta E/k_BT)$, wherein $\Delta E$ is related to anisotropy energy and interaction between external magnetic field and particle magnetization. Generally, in case

of real materials the response of magnetization during time is a complex phenomenon and can be expressed as:

$$M(t) = \sum_i M_{Si}\left[1 - exp\left(\frac{-t}{\tau_i}\right)\right] \tag{2.75}$$

where the summation is over all magnetic objects characterized by time constant $\tau_i$ and magnetization $M_{Si}$ at $t = \infty$. In more general approach the $\tau_i$ constants can be expressed by a distribution characterizing magnetic objects inside the material. Figure 2.25 presents some examples of $M(t)$ curves obtained based on formula (2.75) and assumed Gaussian distributions of $\tau_i$ for one narrow and one wide component as well as a combination of the both.

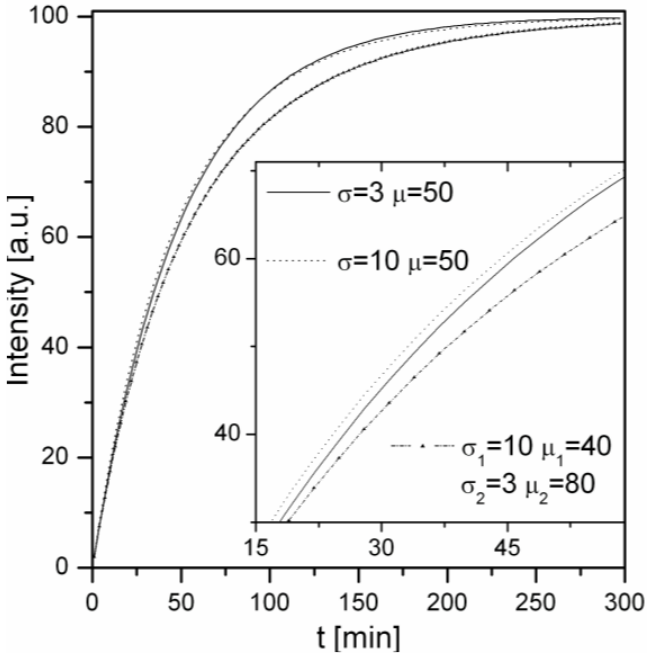


Figure 2.25. M($t$) curves generated from assumed different Gaussian distributions of relaxation time (see the text) [39].

After the assumptions that the magnetic objects have equal energy barrier $E_B$, the magnetization is produced equally be all magnetic objects, one can calculate an analytical expression of $M(t)$ [40]:

$$M(t) - M(t_0) = m' E_B k_B T ln(t - t_0) + const \tag{2.76}$$

where the quantity $E_B k_B T$ is so-called magnetic viscosity and m' is the saturation magnetization of the object. Note, that the slope of $M(\ln t)$ curve is a measure of magnetic viscosity.

### 2.3.4. Simulated annealing and others optimization methods

A common problem performing simulations is to find the energy minimum of the system. On the other hand, a typical task during the numerical analysis of experimental data is to find the parameters of the theoretical model which lead to same results as obtained during measurements. The compatibility of experimental $y_i$ and theoretical $f(x_i)$ data (for $n$ points) can be expressed using the so-called chi-square test:

$$\chi^2 = \sum_{i=1}^{n} \left( \frac{y_i - f(x_i)}{\sigma_i} \right)^2 \tag{2.77}$$

where $\sigma_i$ is an error of point $i$.

Both tasks, finding the minimum of energy as well as the minimum of $\chi^2$ are a classical optimization problem which can be solve by many type of numerical methods. However, in real applications, the well-known so-called *gradient algorithms* and *greedy algorithms* often stuck in a local minimum, and does not lead to global best state. On the other hand, systematic checking of each possible solution takes too much time and it is not possible to perform from practical point of view. Another class of optimization algorithms are *non-deterministic methods* [41] and so-called *evolution algorithms* [42]–[44] in particular. There are several types of such methods like *Particle swarm optimization* [45], *Genetic algorithm* [46], *Ant colony optimization* [47] and their ideas usually based on the behavior of animals, insects, natural phenomenon or evolution processes.

Especially important from this work point of view is the so-called *Simulated annealing algorithm* (SA) presented on Figure 2.26 [48], [49]. Generally, this method is similar to the greedy algorithm i.e., in a single step processes only one state of the system and always accept the change leading to energy minimization. However, the additional parameter of temperature $T$ is included and any new state of system with higher energy can be also accepted with probability proportional to:

$$\exp\left(\frac{-\Delta E}{T}\right) \tag{2.78}$$

Moreover, the temperature $T$ starting from high value and it decreases after some set of steps according to formula: $T_{i+1} = \alpha\ T_i$ where α is the algorithm parameter (usually very near to 1). In practice, during the initial stages of annealing, the system changes randomly (so-called exploration phase) and after some time, only solutions close to lower energy states will be promoted (exploitation phase). Note, that in this paragraph the energy can be understood as any parameter that should be optimized, for example $\chi^2$ formula.

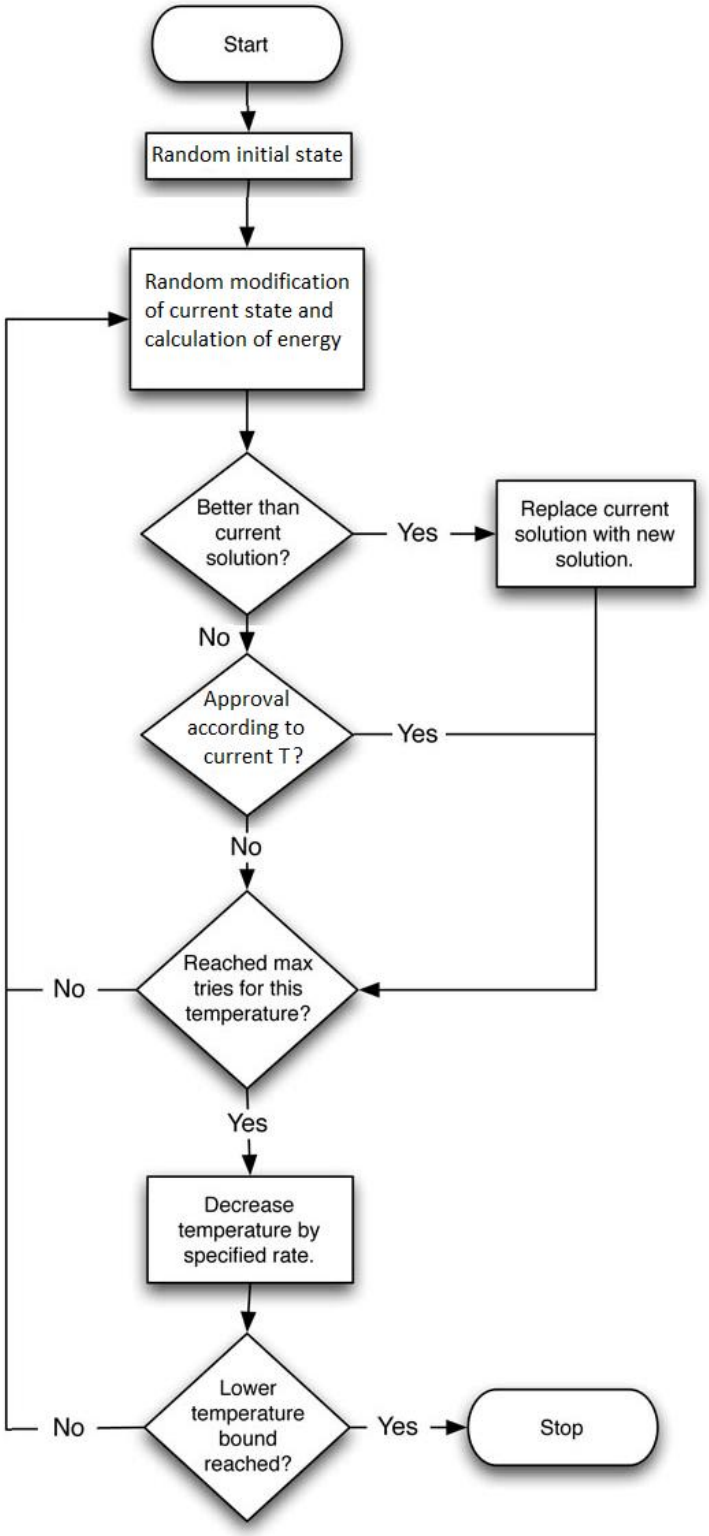


Figure 2.26. Diagram of Simulated annealing algorithm.

## 2.4. Selected technology of hard magnetic materials

### 2.4.1. Casting mold technique

*Casting,* known for thousands years, is a method of manufacturing by pouring liquid metal into a cavity with predetermined shape in a mold and then cooling down that leads to solidification. One of the common types of magnets, produced in this way, are the so-called *Alnico magnets*. In this case, the main element is iron with additions of 8-12% Al, 15-26% Ni, 5-24% Co, up to 6% Cu and up to 1% Ti. All elements are put into an induction furnace and melted at temperatures about 1750°C. The melted material is poured into a sand mold with a cavity corresponding to a desired shape of the final magnet. The volumes for the material inside the mold are linked by horizontal and vertical tubes, so that the liquid can easily displace all the air to fill up all the voids. The mold with the alloy is quickly cooled to prevent gamma second phase forming. The resulting magnet is heat treated in the presence of an external magnetic field which forms its final properties. Casting enables the production of large magnets, even over tens of kilograms.

### 2.4.2. Vacuum suction technique

An aperture of *the vacuum suction technique* [50] consists of sample chamber with an electrode and a mold connected to a vacuum reservoir and a vacuum pump. Especially important element is the casting mold (usually cooper) with cylindrical hole in the center. The sample preparation is performed in two steps. Firs, the material, paced on the top of the mold and consists of appropriate chemical elements, is melting in electric art according to melting procedure and in presents of neutral gas. Typically, the melting current and melting time are one of the technology parameters. After a few seconds the melted material is sucked by the vacuum into the hole in the mold. Such procedure leads to rapid solidification of the liquid material in a form appropriate to dimensions of the hole inside the casting mold. One may note that the cooling rate obtained by vacuum suction technique is lower than in case of *melt spinning* and depending on sample diameter. Nevertheless, from application point of view a big advantage of this method is

a production of bulk nanocrystalline alloys with dimension in order of several mm and in different forms like rods, ingots, etc.

Due to the fact that the vacuum suction technique plays important role in presented work, a detailed description of example of such apparatus will be perform in section 4.3.

### 2.4.3. Melt spinning

Amorphous alloys can be synthesized by several method of rapid solidification processing like *splat quenching, gas atomization and condensation* or the most common *melt spinning* [4]. The high cooling rate, typically greater than $10^4$ K/s, associated with this methods suppresses crystallization. Melt-spinning apparatus is schematically shown in Figure 2.27. A rotating wheel is cooled by water or liquid nitrogen. A thin stream of liquid material is dripped onto the wheel and rapid cooled which leads to the solidification process. The amorphous metallic ribbons prepared by melt spinning have about 20μm in thickness.

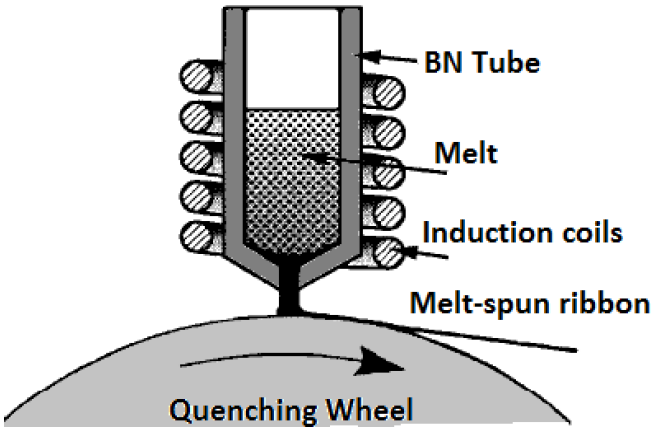


Figure 2.27 Diagram of melt spinning technique (base on [4]).

Note that the amorphous state is less stable than the crystalline state and this causes amorphous alloys to spontaneously crystallize upon heating. One of the important technology parameters is melt temperature which affects the ribbon thickness and final nanocrystal size distribution after nanocrystallization. The magnetic properties of FINEMET alloys depending on melt temperature parameter were investigated by Lim et al. in positions [51], [52].

## 2.4.4. Powders technology: milling and sintering

A typical production process for the so-called *sintered neodymium magnets* is composed of several steps and it is shown in Figure 2.28. The main elements: Fe, Nb, B and in some cases, small additions of Nb, Al, Dy, Gd, Co or Cu are melted using a *vacuum induction furnace* to form an alloy. In this method an induction furnace containing a refractory lined crucible surrounded by an induction coil is located inside a vacuum chamber. The induction furnace is connected to an AC power source at a frequency precisely correlating to the furnace size and material being melted. Cooled alloy in the form of ingots is milling in argon atmosphere by *hydrogen decrepitation* or *hydrogenation disproportionation desorption and recombination* (*HDDR*) process.

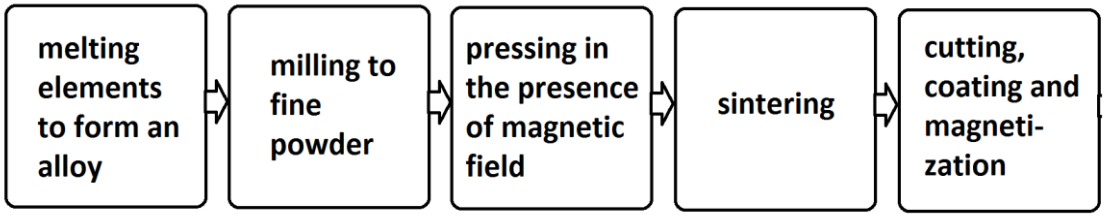


Figure 2.28 Typical production process of sintered neodymium magnets.

The resulting powder with a grain size less than 3μm is pressing in the presence of an external magnetic field. At this stage, the size of a press container for the powder is slightly larger than the expected size of the final magnet. The applied magnetic field is parallel to the compacting force (so-called *axial pressing*) or perpendicular to the direction of compaction (*transverse pressing*). The best magnetic properties can be obtained using the so-called *isostatic pressing*. In this method, the powder is closed in rubber mold and placed inside the large fluid container. The material is compacted from all sides by increasing of fluid pressure. Applying of the external field (by a solenoid coil set either side of the compacting powder) causes anisotropy i.e. the direction of magnetisation is locked in place and only one is preferred. Note that the easy axis of magnetisation for $Nd_2Fe_{14}B$ alloy is c-axis of the tetragonal structure and alignment along this axis allows fully magnetic saturation with high coercivity. In the case of the *bonded magnets*, no external field may be used but then the magnetic properties are worse.

The magnets in this form are easy to crush, therefore the next step is sintering process by applying the appropriate temperature function in an atmosphere without oxygen (all oxides degrades the properties). At the end of this process the material is rapidly cooled.

During the sintering, the material shrinks unevenly and the additional treatment is required to obtain final dimensions. Due to the very high hardness of FeNbB magnets, a diamond tools are used. In the case of production on a mass scale, large blocks of material can be press and there are cutting to smaller magnets at this stage. In order to protection (e.g. corrosion), a final magnet is coated by Ni-Cu-Ni, Zn, Au, Ag, Ti, PTFE or other layers. The plating has about 15-30μm in thickness.

Finally, the prepared Neodymium magnet is magnetized by applying a field at least 3 times larger than the material coercivity. It is worth noting that more than 95% of rare earth elements and approximately 76% based on these alloys magnets are produced by China [53]. A similar production method is also used for the manufacture of *Samarium–Cobalt magnets*.

## 2.5. Measurement methods of magnetic and related properties

### 2.5.1. Measurement of magnetization

It is known that applying inhomogeneous magnetic field causes force acting on a magnetic material which is proportional to its magnetic susceptibility. This property is the basis for different kinds of magnetic balances like *Weiss-Farrer*, *Gouy*, *Sucksmith*, *Cahn* or *Faraday magnetic balance* [54] which is schematically illustrated in Figure 2.29a. In this case, a special shape of the electromagnet pole pieces provides inhomogeneous magnetic field. The sample is attached to the balance which can measure the force or the voltage needed to compensate of deflection by the coils on the other side of balance (Cahn method). The sample can be placed inside a cryostat or heater which allows performing measurements as a function of temperature.

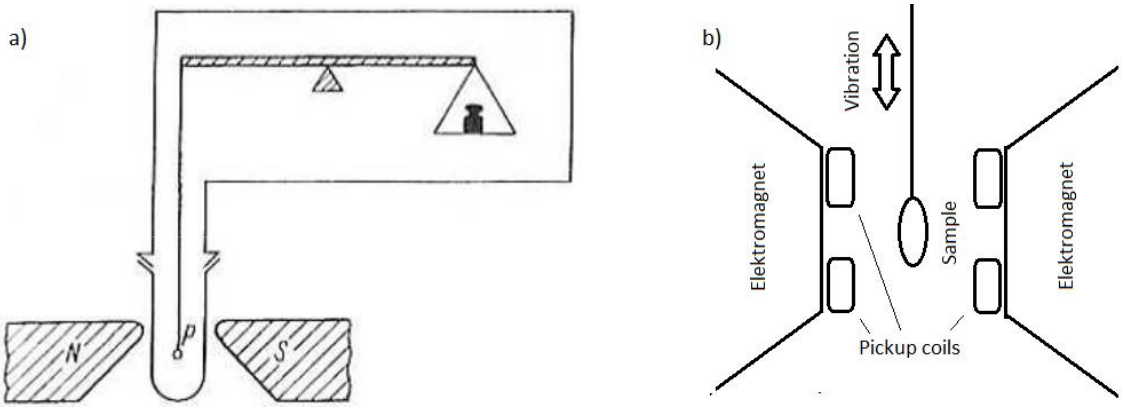


Figure 2.29 Diagram of Faraday magnetic balance [54] (a) and VSM (b).

Another approach to measurements of magnetization are so-called *dynamic methods* based on the electromagnetic induction phenomenon like *Vibrating Sample Magnetometer* (*VSM*) [55]. A sample is placed inside a uniform magnetic field and vibrates between pick-up coils as shown in Figure 2.29b. The induced voltage in the pickup coil is proportional to the sample's magnetic moment and parameters of vibration (amplitude, frequency), but it does not depend on the strength of the applied magnetic field. Commercial magnetometers provide measurements of magnetization as a function

of the external magnetic field (using superconducting magnets even up to several Tesla), temperature and time.

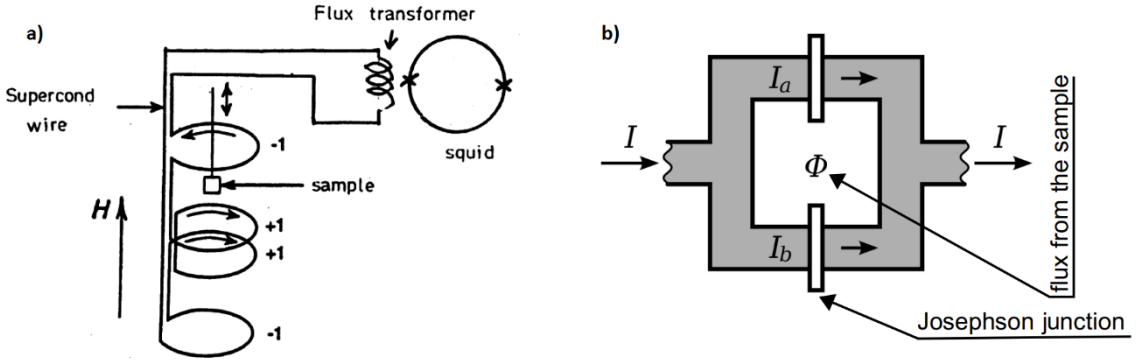


Figure 2.30 Diagram of SQUID magnetometer (a) and DC SQUID superconducting loop (b).

Some kind of extended version of VSM is *SQUID magnetometer* [56], [57]. The superconducting quantum interference device (SQUID) can be used as a flux to voltage converter in the VSM technique. There are two types of SQUIDs, named according to the applied bias: (a) *RF* (working on an AC with radio frequency) and (b) *DC SQUID* which is schematically illustrated in Figure 2.30a. The main part of a DC SQUID is the dual Josephson junction (Figure 2.30b) mounted on a superconducting loop and coupled inductively with the coils. Magnetic flux modulates the current passing through the junction which is detected and amplified by some feedback electronics. The magnetometers with SQUID are the most sensitive magnetic devices and they can measure field as low as $10^{-14}$ T which is less even than fields associated with human brain activities.

## 2.5.2. Mössbauer spectroscopy

Atomic nucleus is a system of quantized energy levels which can be excited by absorption of gamma radiation. High-energy states are temporary and excess energy will be emitted in a quantum form. In the case of free atoms, can be observed a recoil of nucleus due to the high energy of gamma radiation. This means that the energy of the emitted photon is equal to:

$$E = E_w - E_p - E_0 \text{ and } E_0 = \frac{E^2}{2Mc^2} \tag{2.79}$$

where $E_0$ is recoil energy, $E_\omega$, $E_p$ corresponds with low and high energy state of the nucleus, respectively and M is its mass. However, for some part of the atoms inside in a crystal lattice, the recoil may not occur and the emitted energy is sufficient to excite another nucleus. A contribution of *the recoilless fraction* depends on a temperature (higher temperature - higher recoil probability) properties of the crystal lattice and radiation energy. This effect was discovered by *R.L. Mössbauer* in 1957 (the Nobel Prize in 1961) and it is observed for a limited number of isotopes such as Fe, Ru, Sn, Sb, Te, I, W, Ir, Au, Eu, Gd, Dy, Er, Yb, Np and others. For example, in case of a solid states which crystallizing to the regular system, the ratio of recoilless emitted photons to the all of them can be expressed as:

$$f = exp\left\{-\frac{3E_R}{2k\theta}\left[1 + 4\left(\frac{T}{\theta}\right)^2 \int_0^{\theta/T} \frac{xdx}{e^x - 1}\right]\right\} \tag{2.80}$$

where $E_R = E_\omega - E_p$, $\theta$ is Debye'a temperature and $x = \frac{h\omega}{kT}$. In case of $^{57}$Fe in crystal lattice at room temperature $f = 0.75$.

The Mössbauer spectrometer [58], [59] (using absorption geometry) consists of three main elements: moving radiation source, sample and detector. Due to the Doppler effect, the sample receives a wider spectrum of energy $\Delta E = v/c\ E$ (where $\upsilon$ is the source speed relative to the sample) and absorbs selected wavelengths. The resulting graph shows the number of counts (gamma radiation received by detector) as a function of speed (usually in $mm/s$), which represents the source energy. Based on the fitted model the main parameters such as *isomer shift* (IS), *quadrupole splitting* (QS) and *hyperfine splitting* (MS) can be determined. The energy levels of nucleus (absorption peaks) are split and shifted depending on its environment like Coulomb interaction (charge of electrons and nucleus), hyperfine interaction, gradient of the electric field and nucleus quadrupole moment interaction etc. For example, the energy levels of $^{57}$Fe nucleus in case of: a) - mono and -quadrupole interaction and b) Zeeman splitting are shown in Figure 2.31.

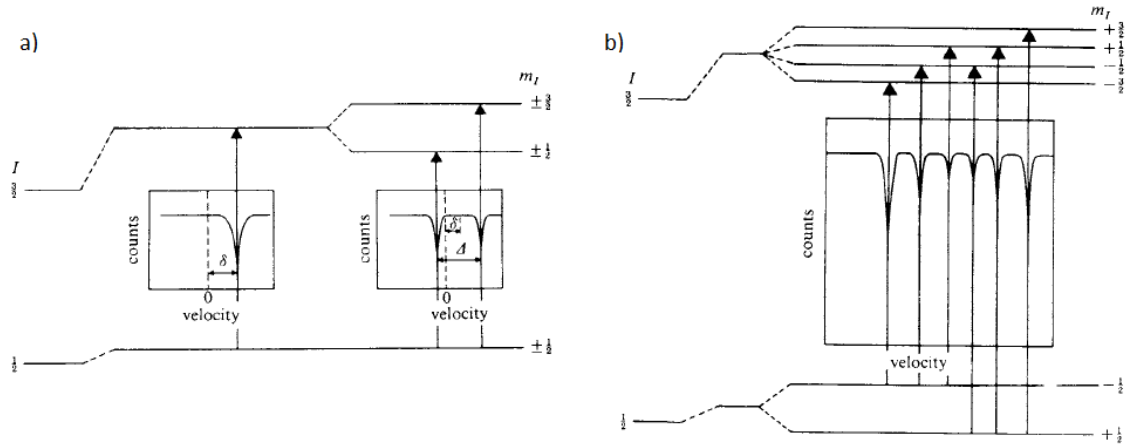


Figure 2.31 Diagram of the energy levels for $^{57}Fe$ nucleus in case of: a) mono and quadrupole interaction and b) Zeeman splitting (base on [60]).

Table 2.4 Application of Mössbauer spectroscopy (base on [54]).

| Field | Isomer shift $\delta$ | Quadrupole effect | Hyperfine field $H$ | Recoilless fraction and the second row Doppler shift | Line width $\Gamma$ |
|---|---|---|---|---|---|
| **Analysis** | Chemical, structural and phase identification | | | | |
| **Nuclear** | Nucleus radius | Nuclear moments | | | Lifetime |
| **Solid State** | Electron structure | Local symmetry of the electron configuration | Magnetic structures, spin orientation, magnetic ions configuration | Phonons soft mods, binding anisotropy | Relaxation phenomena |
| **Chemistry** | Covalent bond order | Ligands symmetry, binding orbitals | Magnetic ions configuration | Binding anisotropy | Defects and stoichiometry |

| | | | | | |
|---|---|---|---|---|---|
| **Metallurgy** | Electron structure | Order-disorder transition, phase identification | Phase precipitation, phase transitions | Constant force, an harmonic binding | Atomic transport |
| **Biology** | Valence changing | Ligand system | | Free or boundary complexes | |

The Mössbauer spectroscopy has many applications (some of them are listed in Table 2.4) and can provide information about oxidation, chemical bonds, phase structure, temperature of a magnetic transitions, the geometric and magnetic structure of crystals, amorphous materials, electron spin relaxation time in paramagnetic substances, superparamagnetism phenomenon and others. A detailed description of the Mössbauer spectroscopy can be found in [58]–[60].

### 2.5.3. X-ray diffraction

The X-rays wavelength is the order of distances between the atoms in solid state structures (about $10^{-10}m = 1Å$). The beam of X-rays directed into the sample interacts with the electron clouds of the atoms in crystal lattice as was shown in Figure 2.32.

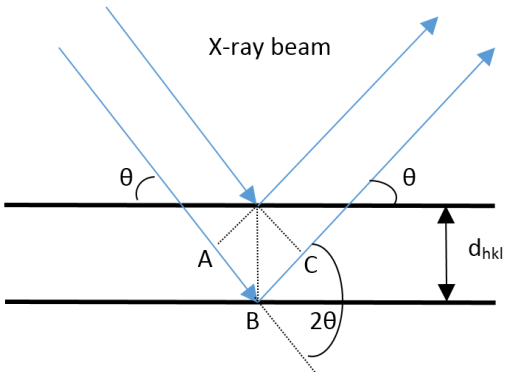


Figure 2.32. X-ray beam reflected by the successive (*hkl*) planes.

The scattered waves can interfere constructively or destructively which leads to interference patterns. The *Bragg equation*:

$$n\lambda = 2d_{hkl}sin\theta \tag{2.81}$$

determines conditions for interference maximum, where $\lambda$ is the wavelength of incident wave, $d_{hkl}$ is the spacing between the planes in the atomic lattice, $\theta$ is the angle between the incident ray and the scattering planes and $n$ is an integer. By measuring the angles and intensities of diffracted beams various information about mean positions of the atoms, their chemical bonds and disorder can be determined.

The resultant amplitude of the scattered electromagnetic waves at the $N$ atoms of the unit cell is equal to:

$$F_{hkl} = \sum_{j=1}^{N} f_j e^{2\pi i(u_j h + v_j k + w_j l)} \tag{2.82}$$

where $f_j$ is the amplitude of the scattering radiation on the *j*-th atom, $u_j, v_j, w_j$ are the coordinates of the *j*-th atom and $hkl$ are so-called *Miller indices*. The total intensity of the reflex is proportional to the square of the amplitude, i.e. $J_{hkl} \sim |F_{hkl}|^2$. Registration of multiple reflections for different $hkl$ allows determining the atomic positions in the unit cell.

There are several methods to perform the described type of measurements. The *Laue method* consists in continuous radiation of a static single crystal. The ray's angles and the distances between the planes are fixed, so the reflexes depend on changing the wavelength. This technique is useful to study symmetry and orientation of the examined crystal. In studies of single crystal the *rotating crystal method* is also commonly used. In this approach, the radiation is monochromatic, however a continuous change of angles between the incident ray and the crystallographic axes is applied. This technique allows determining the crystallographic parameters with high accuracy (6 digits after the decimal point [54]). Other technique, the *Debye-Scherrer* method is useful in research of polycrystalline materials. In this case, the monochromatic radiation incidents on a sample powder. Among many of the powder grains with statistical orientation in space, there are also the grains with some family of crystallographic planes sufficient to satisfy the Bragg condition. Especially useful technique from this work point of view is the *powder diffraction method*. In this case the powdered sample is placed in a sample holder into a

goniometer of the diffractometer. The reflected beam is recorded by a detector (e.g. scintilltion, proportional, CCD, etc.).

It is important to note, that one of the common method of crystallite size calculation is based on the X-ray diffraction and the so-called *Scherrer equation*:

$$D = \frac{K \times \lambda}{\beta \times cos\theta} \tag{2.83}$$

where $D$ is the crystallite size, λ is the X-ray wavelength, β (in radians) is the width of the peak (full width at half maximum, FWHM) after correcting for instrumental peak's broadening, $\theta$ is the Bragg angle and $K$ is the Scherrer constant. The $K$ value depends on the method of definition of peak's breadth, the crystallite shape, the crystallite size distribution and the indexes of diffraction line (Langford and Wilson [61]). Typically a value of $K$ varies from 0.62 and 2.08, however in the absence of any information about a crystal shape it is commonly accepted to use $K$ = 0.89 - 1.

The X-ray diffraction is a very important technique in crystallography and chemistry which is commonly used to study phase structure, unit cell, chemical bonds and structure disorder. More information about it can be found in the literature, eg. [62], [63].

### 2.5.4. Atomic and magnetic force microscopy

*Atomic force microscopy* (*AFM*) [64] is a type of scanning probe microscopy with demonstrated resolution in the order of atomic scale (Å). A sample is placed on a movable table (usually using piezoelectric actuators) and scanned by sharp tip (probe) attached to elastic cantilever. The principle of this kind of measurements is schematically shown in Figure 2.33.

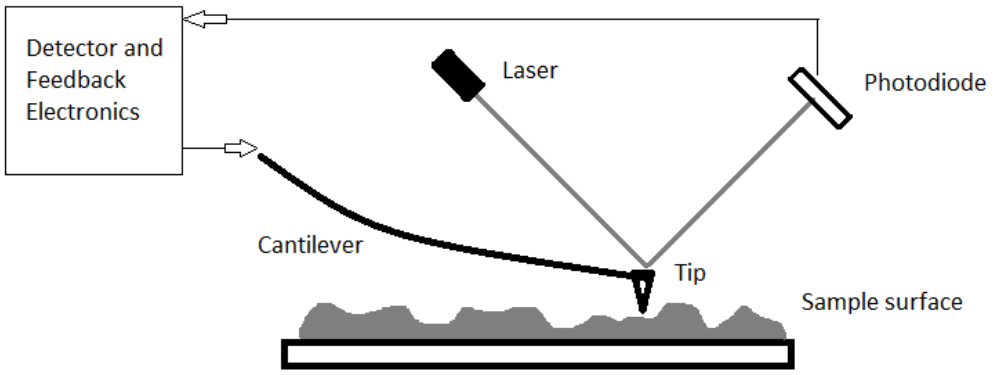


Figure 2.33 Diagram of Atomic Force Microscopy.

Forces between the tip and the sample lead to a deflection of the cantilever what is detected by reflection of laser beam and photodiodes system. Other technique of cantilever deflection measuring like *Scanning Tunneling Microscope*, *optical interferometry* or *capacitive detection* also can be used. The measured forces for set of points on the sample are converted to the surface image. It is possible to measure the different kinds of forces such as mechanical contact force, electrostatic forces, van der Waals forces, chemical bonding, capillary forces etc.

One of the varieties of AFM is *the magnetic force microscope* (*MFM*). In this case, the tip is magnetized and the magnetic interaction (including magnetic dipole-dipole interaction) between the sample and the tip are measured. The magnetic force between the tip and the sample is equal to:

$$\vec{F} = \mu_0(\vec{m} \cdot \nabla)\vec{H} \tag{2.84}$$

where $\mu_0$ is the vacuum permeability, $\vec{m}$ is the magnetic moment of the tip and $\vec{H}$ is the magnetic stray field from the sample surface. Note, that when the tip is close to the sample surface, both - magnetic, as well as atomic and electrostatic forces are measured. Due to this fact, first the topographic profile is carried out, next the magnetized tip is lifted from the sample surface and the magnetic signal is extracted during the second pass. In case of the *static mode*, the measurement base on the cantilever deflection perpendicular to the surface by distance $\Delta z = F_z/k$ where $k$ is a cantilever spring constant in $z$-direction. During the measurement in *dynamic mode* the cantilever is approximate as a damped

harmonic oscillator. The forces acting on the tip leads to the shift of natural resonance frequency $f_n$, which can be expressed as:

$$\Delta f = f'_n - f_n \approx -\frac{f_n}{2k}\frac{\partial F_z}{\partial z}, \quad f'_n = f_n\sqrt{1-\frac{\partial F_z/\partial z}{k}} \qquad (2.85)$$

where $f_n = \omega_n/2\pi$. Typical measured forces are as low as $10^{-14}$ N, with the spatial resolutions as low as 20 nm, so the MFM can be used to image domain walls, closure domains and other magnetic structures.

## 2.5.5. Differential scanning calorimetry

*The differential scanning calorimetry* (*DSC*) [65] is one of the *thermal analysis method* based on keeping the same temperature for tested and reference sample placed in two thermally insulated containers. Scheme of DSC device is shown on Figure 2.34. The experiment is carried out under isothermal or increasing / decreasing temperature conditions. The device measures the difference between the amount of heat delivered to both samples (second one is the reference). Depending on type of reaction (endothermic or exothermic), the tested sample needs more or less heat energy than reference one to keep the same temperature. Accounting the amount of heat, absorbed or released during the measurement as a function of temperature, the kind of transitions can be determined. Using the DSC method, it is possible to study phase transitions, crystallization, melting, oxidation, glass transition as well as other chemical reactions.

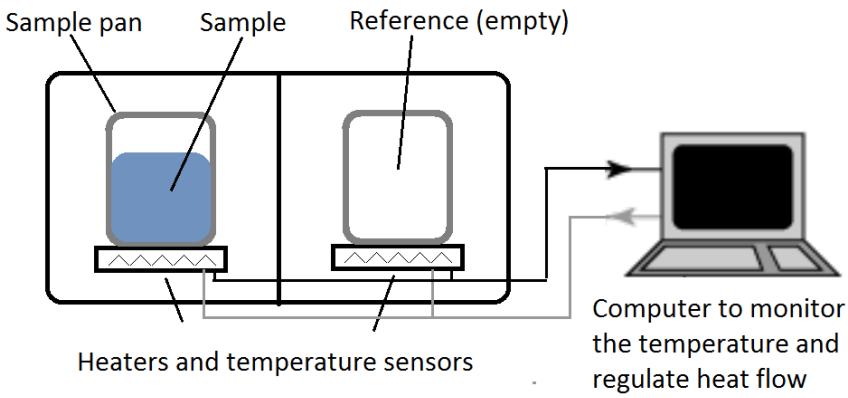


Figure 2.34 DSC equipment schematic.

## 2.5.6. Scanning Electron Microscopy

The *scanning electron microscope* (*SEM*) [66] technique makes a profit of the focused electron beam to scanning a sample surface and based on various signals provides the images of topography as well as chemical composition. The main advantage of electros in comparison to optical microscopy is that the used wave length is about $10^5$ times smaller than the wavelength of light which leads to much better resolution. Generally, the electrons, accelerated by the electric field, correspond to the *de Broglie wavelength* according to the relationship (without relativistic effects):

$$\lambda = \frac{\mathrm{h}}{\sqrt{2\mathrm{m_e}eV}} \tag{2.86}$$

where $V$ is the voltage electric field, h is the Planck constant and $\mathrm{m_e}$ as well as e are electron mass and charge, respectively. Interaction of electron beam with surface of the sample provides several kinds of signals like *secondary electrons* (*SE*), *backscattered electrons* (*BSE*), *Auger electrons* (*AE*) and *X-rays*. Figure 2.35 shows some examples of radiations from the material (in response to electron beam) as a function of sample depth, including simple schematic explanation of its origin.

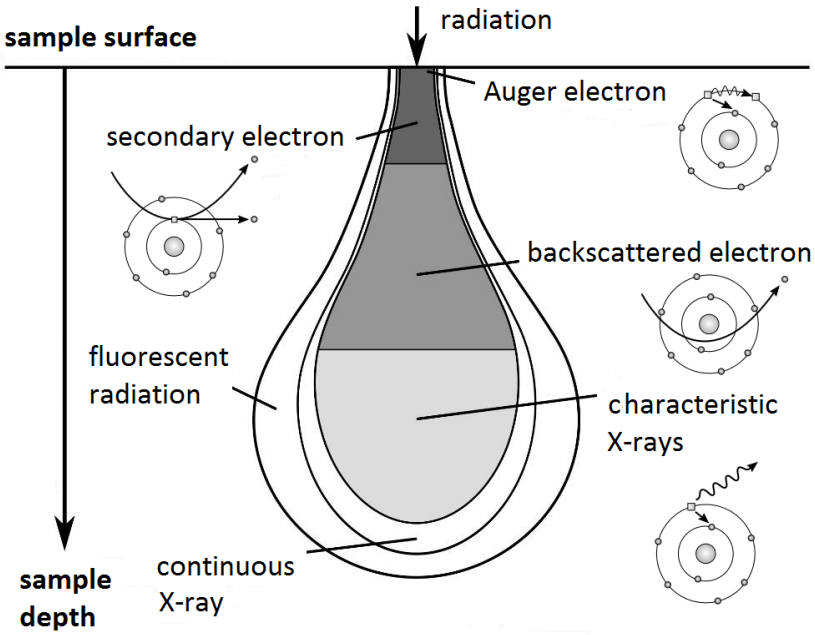


Figure 2.35 Simple diagram of the electron-sample interaction.

The secondary electrons are derived from the sample near the surface (knocked out from material) as well as the primary beam (which lost most of energy and escaped). This kind of signal is very sensitive to the surface topography. On the other hand, the high energy backscattered electrons, which left the material after elastic reflection with no loos of kinetic energy, correspond to the chemical composition of the surface. The amount of BSE is much smaller than SE and increases with increasing atomic number.

# 3. Review of resent achievements in the field of hard magnetic materials

In the 21st century, a rapid development of modern technologies requires superb permanent magnets. Such materials are essential components in many electric and electronic devices. Typical applications are computers (data storage), laboratory and medical equipment (e.g. magnetic resonance imaging), as well as renewable energy and motorization (wind turbines, electrical vehicles). Moreover, permanent magnets are key element of many sensors and actuators, therefore new kinds of such materials are necessary in order to make electric devices smaller, lighter and more energy efficient.

Historically, the first permanent magnet was $Fe_3O_4$ compound, which naturally occurs in rocks. This material is known for more than thousand years and it founds the application in navigation devices. Figure 3.1 presents an extraordinary development in the field of permanents magnets during the last century. At the end of 19th century the iron-based tungsten steel magnets were developed, however the first big discovered (in 1931) were the so-called *Alnico* magnets based on aluminum-nickel-cobalt-iron elements. This material consists small elongated ferromagnetic FeCo particles precipitated in a weakly magnetic Al-Ni matrix. They have strong shape anisotropy, and superior properties compared with the steel magnets. In 1950 the hexagonal hard *ferrrites* of (Ba/Sr)$Fe_{12}0_{19}$ ceramic magnets were discovered. This material has larger coercively due to large magnetocrystalline anisotropy, however low magnetization and Curie temperature are disadvantages of such magnets. The next big step took place in 1960s when the *rare-earth permanent magnets* were developed. First generation of such magnets, based on $SmCo_5$ compound, has high maximum energy product in comparison with previously known materials. Moreover, increasing of Co content ($Sm_2Co_{17}$) and small additions of Fe, Cu and Zr lead to increase of magnetization which was the base for second generation of such magnets. Since 1970s, many investigations were made to remove Co due to high prices and replace it by Fe-base compound without deterioration of magnetic properties. The most significant breakthrough took place in 1984 when Sagawa et al [67] and Croat et al [68] discovered good hard magnetic properties for sintered and rapidly quenched

magnets (called third generation) base on ternary $Nd_2Fe_{14}B$ phase. Due to very high maximum energy product and thermal stability in room temperature this kind of permanent magnets found many applications in modern technologies during last decades. Moreover, the Curie temperature (about 300 ºC) as well as coercivity can be increased by doping of heavy rate-earth elements (like Dy and Tb). In the other hand, high price of RE (especially heavy RE) are the cause of a lot of research in order to decreasing such elements content without degeneration of magnetic properties base on different kind of preparation methods.

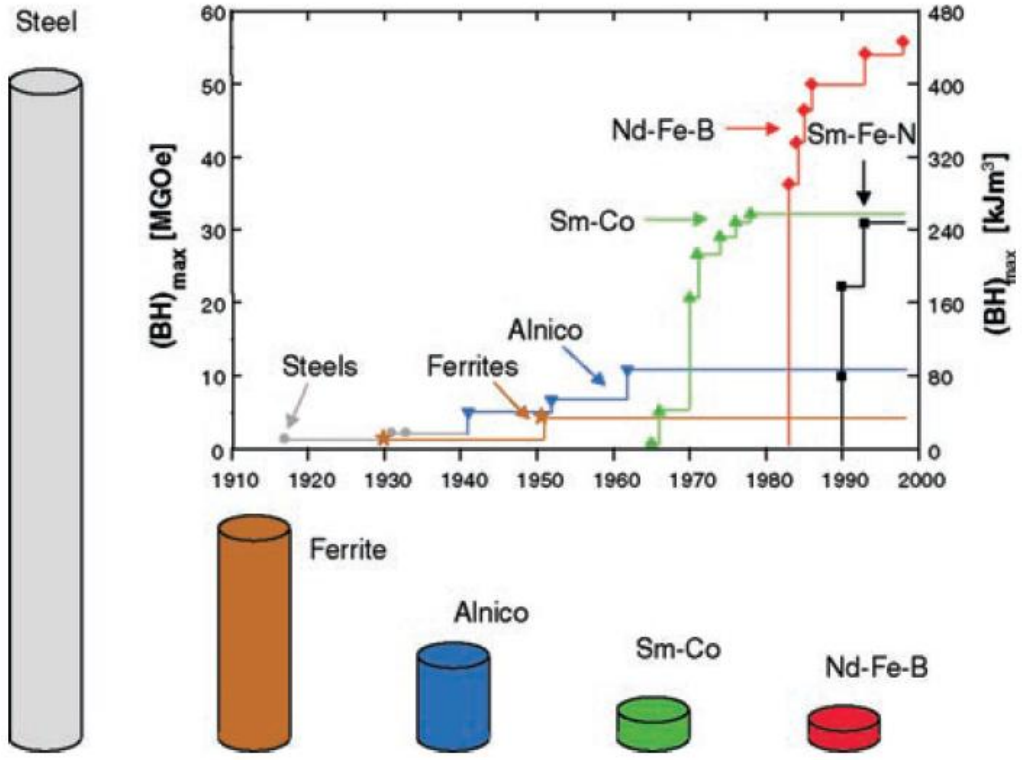


Figure 3.1 Development of hard magnetic materials and the energy density $|BH|_{max}$ in the 20th century as well as presentation of different types of materials with comparable energy densities [69].

Many researches indicate that in area of hard magnetic materials very attractive are classical and nanostructured alloys and compounds based on transition (T) and rare earth (RE) elements. Generally, the atoms of transition metals (Fe, Co) are the source of a large

magnetic moment, while the rare earth metal atoms are the source of magnetocrystalline anisotropy [3]. The most interesting of RE-T compounds are tetragonal structure of $RE_2Fe_{14}B$ and hexagonal structure of $RECo_5$ (or $RECo_7$). An example of $Nd_2Fe_{14}B$ crystal structure in $P4_2/mnm$ space group is presented on Figure 3.2. However, strong magnetocrystalline anisotropy in such structures depends on sign of anisotropy constant $K_1$. In case of $K_1 < 0$ the magnetization vector belongs to surface which is perpendicular to c-axis of crystal lattice. Unfortunately, this surface has no energy barrier which prevents changes of magnetization direction, therefore only compound with positive anisotropy constant can be used to produce permanent magnets. For example, in case of ternary $RE_2Fe_{14}B$ phases [3]:

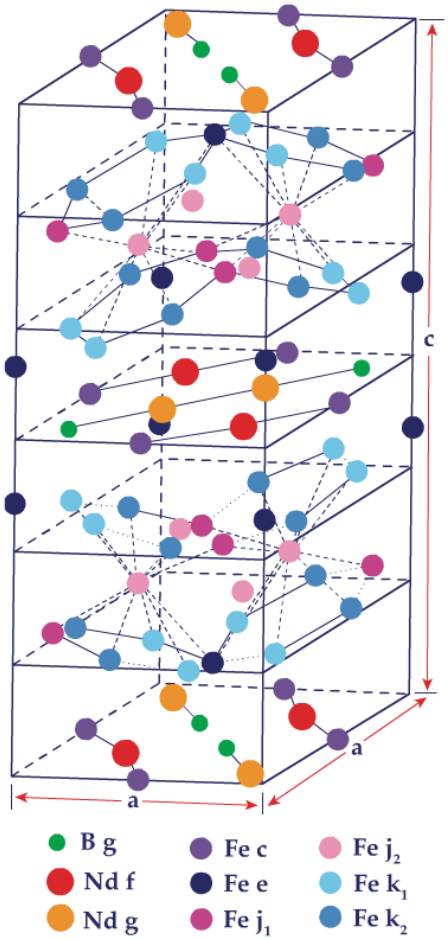


Figure 3.2 Crystal structure of $Nd_2Fe_{14}B$ phase.

- K1 > 0 for RE = Ce, Pr, Nd, Tb, Dy, Ho
- K1 < 0 for RE = Sm, Er, Tm, Yb,

and in case of $RECo_5$ as well as $RCo_7$:

- K1 > 0 dla RE = Sm, Er, Tm, Yb,
- K1 < 0 dla RE = Ce, Pr, Nd, Tb, Dy, Ho.

Second important factor is the type of magnetic coupling between RE and Fe elements. According to the Hund roles the magnetic moments of atoms of RE with less than half-full 4f shell, will be ferromagnetically coupled with iron magnetic moment. This situation leads to high value of saturation magnetization that is preferred in case of permanent magnets. On the other hand, in case of rare earth elements with 4f shell filled more than half, the coupling is antiferromagnetic, so, the total magnetic moment will be smaller than in the previous case. Therefore, for $RE_2Fe_{14}B$ as well as Sm for $RECo_5$, Pr and Nd (preferred due to lower price), are the best candidates to produce low cost and effective permanent magnets. Table 3.1 summarizes lattice parameter as well as magnetic properties of several $RE_2Fe_{14}B$ type phases.

Table 3.1 Lattice parameter (a, c) as well as magnetic properties of $RE_2Fe_{14}B$ compounds family (ρ - dencity, $B_s$ - saturation induction, μ - magnetic moment, $H_a$ – anisotropy field and $T_c$ - The Curie temperature) [70].

| Compound | a | c | ρ | $B_s$ | μ | $H_a$ | $T_c$ |
|---|---|---|---|---|---|---|---|
| | nm | nm | g/cm$^3$ | T | $\mu_B$/f.u. | MA/m | K |
| **$Ce_2Fe_{14}B$** | 0.877 | 1.211 | 7.81 | 1.16 | 22.7 | 3.7 | 424 |
| **$Pr_2Fe_{14}B$** | 0.882 | 1.225 | 7.41 | 1.43 | 29.3 | 10 | 564 |
| **$Nd_2Fe_{14}B$** | 0.882 | 1.224 | 7.55 | 1.57 | 32.1 | 12 | 585 |
| **$Sm_2Fe_{14}B$** | 0.880 | 1.215 | 7.73 | 1.33 | 26.7 | - | 612 |
| **$Gd_2Fe_{14}B$** | 0.879 | 1.209 | 7.85 | 0.86 | 17.3 | 6.1 | 661 |
| **$Tb_2Fe_{14}B$** | 0.877 | 1.205 | 7.93 | 0.64 | 12.7 | 28 | 639 |
| **$Dy_2Fe_{14}B$** | 0.875 | 1.200 | 8.02 | 0.65 | 12.8 | 25 | 602 |
| **$Ho_2Fe_{14}B$** | 0.875 | 1.199 | 8.05 | 0.86 | 17.0 | 20 | 576 |
| **$Er_2Fe_{14}B$** | 0.874 | 1.196 | 8.24 | 0.93 | 18.1 | - | 554 |
| **$Tm_2Fe_{14}B$** | 0.874 | 1.195 | 8.13 | 1.09 | 21.6 | - | 541 |
| **$Y_2Fe_{14}B$** | 0.874 | 1.204 | 6.98 | 1.28 | 25.3 | 3.1 | 565 |

Another significant element that can strongly improve hard magnetic properties and model them for specific applications is nanostructure. A nanocrystalline alloys containing grains of the hard magnetic phases combines different types of magnetic anisotropy, like grains magnetocrystalline anisotropy, shape anisotropy as well as surface anisotropy associated with grain boundaries areas. In addition, the grain boundaries are a source of internal stress that cause a slowing down of the domain wall motion. All of these elements provide an energy barrier which blocks the magnetic moments and leads to magnetic hardning effect (high coercivity and remanence). Moreover, due to the fact that the interaction energy between magnetic moment $\mu$ of field $H$ is proportional to the product of $\mu H$, the small one-domain particles (but not superparamagnetic) i.e. with low magnetic

moment are preferred. Another interesting idea is a nanocomposite of soft and hard magnetic phases. When the grains of both phases are magnetically coupled in atomic level and the hard phase is dominant, according to spring exchange model, the maximum energy product will be significantly improved.

Different kind of permanent magnets including their most-important parameters are summarized in Table 3.2. Moreover, important role in the field of applications may be confirmed by a large number of patents in the United States and around the world. The most important in the context of presented work during last two decade are summarized in Table 3.3.

Table 3.2. Selected type of permanents magnets and their properties (maximum energy product $BH_{MAX}$, remanenence induction $B_R$ as well as coercivity $H_C$) [40].

| Material | $BH_{MAX}$ | $B_R$ | $H_C$ |
|---|---|---|---|
| | $KJ/m^3$ | mT | kA/m |
| **31/2% Cr Steel** | 1.03 | 1030 | 56 |
| **3% Co Steel** | 3.02 | 970 | 13 |
| **17% Co Steel** | 5.49 | 1070 | 18 |
| **38% Co Steel** | 7.79 | 1040 | 191 |
| **Ceramic 2** | 14.3 | 290 | 224 |
| **Ceramic 6** | 19.5 | 320 | 57 |
| **Alnico 4** | 10.7 | 560 | 318 |
| **PtCo** | 71.6 | 645 | 20 |
| **Vicalloy 1** | 6.36 | 750 | 20 |
| **Remalloy** | 7.95 | 970 | 42 |
| **Cunife 1** | 11.1 | 550 | 202 |
| **MnAlC** | 39.8 | 545 | 358 |
| **$SmCo_5$** | 160 | 900 | 696 |
| **$Nd_2Fe_{14}B$** | 320 | 1300 | 1120 |

Table 3.3. Selected patents in US in subject of permanent magnets during last 20 years.

| US nr of patent | Date | Authors | Topic | Family of materials | Favorable parameters |
|---|---|---|---|---|---|
| **6261387** | Jul., 2001 | Panchanathan | Rare-earth iron-boron magnet containing cerium and lanthanum | $[(Ce_xLa_{1-x})yRE_{1-y}]_z(F_{1-v}B_v)$<br>RE- ziemia rzadka<br>F- Fe, Co | $H_c \approx 0.4$ T |
| **6120620** | Sep., 2000 | Benz et al. | Praseodymium-rich iron-boron-rare earth composition, permanent magnet produced therefrom, and method of making | Pr (13-19 % at.)<br>B (4-20 % at.)<br>Fe (61-83 % at.) | $H_c \approx 0.8$ T<br>$BH_{max} \approx$ 35MgOe |
| **5690752** | Nov., 1997 | Yamamoto et al. | Permanent magnet containing rare earth metal, boron and iron | RE (25-31 % wag.)<br>B (0.5-1.5 % wag.)<br>Fe (reszta) | $H_c \approx 1.5$ T<br>$BH_{max} \approx$ 41MgOe |
| **5449417** | Sep., 1995 | Shimizu et al. | R-Fe-B magnet alloy, isotropic bonded magnet and method of producing same | RE-Fe-B-M<br>RE (12.5 – 15 % At.)<br>B (4 – 8 % At.)<br>M - Nb,W,V,Mo,Ta, (0.05 – 3 % At.) | $H_c \approx 2$ T |

One of the alternative for commonly used Neodymium-base magnets at temperature higher than 500 K are the alnico alloys. However, the coercivity of such compound strongly depends on the nanostructure developed during spinodal decomposition. Zhou et al [71] have carefully investigated three representative alnico alloys using atomic-scale techniques. In case of alnico 5-7 the spinodal phase assembly has a “brick-and-mortar” structure and the $\alpha_1$ phase is faceted on the {100} planes. While, alnico 8 as well as 9 are characterized by “mosaic” structure and $\alpha_1$ phase is faceted on the planes {110} and {100}. The additions of Ti and Cu elements may change microstructure of anico materials. In case of alnico 8 and 9, Cu was pushed out of the $\alpha_2$ phase and resides at corners of two <110> planes of the $\alpha_1$ phase. Moreover, the $\alpha_2$ phase transforms into $L2_1$-ordered structure in alnico 8 and 9 from B2-ordered structure in alnico 5-7 under the influence of the Ti additive. In this paper the calculated and measured $B_r$, $H_c$ and $|BH|_{max}$ for all three kind of alnico materials were compared. For example, alnico 9 is

characterized by $B_r$ = 10.6 kG (calculated 11.5 kG), $H_c$ = 1.5 kOe (calculated 3.89 kOe) and $|BH|_{max.}$= 9 MOe (calculated 21.4 MOe). It is important to note that in all cases the measured coercivity as well as energy product is about 2–3 times below theoretical limits. The authors suggest that the most promising way to improve this parameter is reducing the spatial dimensions of the $\alpha_1$ phase.

Another interesting paper [72] refers the influence of microstructure on magnetic properties of nanocrystalline Fe–Pt–Nb–B permanent magnet ribbons. A good hard magnetic properties ($\mu_0 M_r$ = 0.65 T, $H_c$ = 820 kA/m, $|BH|_{max}$ = 70 kJ/m$^3$) were obtained for $Fe_{52}Pt_{28}Nb_2B_{18}$ melt-spun ribbon after annealed at 973 K for 1h. Based on $^{57}$Fe Mössbauer spectra, XRD and TEM observation one can say that microstructure consists of $L1_0$-FePt hard-magnetic grains, with diameter about 15–45 nm, dispersed in a soft magnetic medium composed by A1-FePt, $Fe_2B$, and boron-rich $Fe_{52}B_{39}Pt_4Nb_5$ remainder phase. Moreover, strong exchange coupling between hard and soft magnetic phases was detected and attributed to high energy product. In case of this alloy, magnetic properties are relatively stable in temperature range up to 550 K.

Novel exchange-coupled $SmFe_3$/α-Fe nanocomposite magnets have been studied by Li et al [73]. The $Sm_{22}Fe_{78}$ ribbons were prepared by melt spinning technique (50 m/s) and, in some cases, annealed at 723-753 K for 10 min with and without external magnetic field of 5 kOe. In case of annealing with field obtained structure consists hard magnetic $SmFe_3$ phase and soft magnetic α-Fe with grains about 80-100 nm and 3-8 nm, respectively. Moreover, this phases are strongly exchange-coupled which leads to one component hysteresis loops with very high remanent ratio $M_r/M_s$ = 0.93 and energy product equal to 13.0 MGOe (for annealing at 753 K). On the other hand material prepared by non-field annealing is characterized by lower volume fraction α-Fe and larger grains equals 10-30 nm. The critical size for such compound was calculated to about 11.6 nm, therefore, the exchange-coupled was about 40% weaker than in first case.

In 2011, R.M. Liu at al [74] have reported ultrahigh coercivity in ternary $Tb_{14}Fe_{86-x}B_x$ ($x$=5.2–6.8) melt spun ribbons. Phase composition of such materials depends on $x$ parameter and cooling rate. Relatively soft magnetic phase like $TbFe_2$ and FeB exist in low as well as high boron content, however in case of $Tb_{14}Fe_{79.6}B_{6.4}$ ribbon the highest coercivity (1.67 T using 10 m/s of wheel speed) correlated with high $Tb_2Fe_{14}B$ phase

content was detected. Moreover, the coercivity of the ribbons is strongly dependent on the wheel speed and there is only a narrow wheel speed range ($V_s$ = 10.5 – 11.5 m/s) provides appropriate nanostructure to improve hard magnetic properties. Similar behaviors of $RE_2Fe_{14}B$ melt-spun ribbons were also reported by other researchers [75], [76]. On the other hand, magnetization and remanence decrease systematically with increasing $V_s$. In case of material obtained using optimal chemical composition and cooling rate the coercivity, remanence and magnetic saturation in field of 9 T were equal to 77.4 kOe, 24.86 emu/g and 3931 emu/g, respectively. The microstructure of this sample was composed of fine and uniform crystal grains (about 100 nm in average diameter), which was responsible for the ultrahigh coercivity of the ribbons.

Especially interesting for this work is a technique of preparation of magnetic material called vacuum suction casting method. The advantages are quick and relatively simple process and a large sample volume (bulk materials). However, the cooling rate obtained by this method is much smaller than e.g. melt spinning and the obtained structure strongly depends on the chemical composition and technology parameters. Tan et al [77] have investigated the $Fe_{67-x}Co_{10}Nd_3Y_xB_{20}$ ($x$ = 0, 2, 6, 10) alloys prepared by suction casting with form dimensions: 1 mm × 10mm × 50 mm. They found that glass-forming ability (GFA) of such compounds can be effective improved by a small addition of Y (6 at.%) which leads to mostly amorphous phase, while a mixture of several crystal phases for low and high Y content where observed. It is also important to note that, the coercively of as-cast material (for $x$ = 6) increases after annealing at temperature equal to 948 K (indicated as optimal) for 30 min, from 10 kA/m up to 101 kA/m. Moreover, during this process, the remanence increases from 10 $Am^2/kg$ up to 46 $Am^2/kg$. The results are attributed to the strengthening exchange coupling between the soft and hard magnetic phases. Similar materials with Dy additions ($Fe_{67}Co_{9.4}Nd_{3.1}Dy_{0.5}B_{20}$) in a form of rod with 0.5 mm in diameter were investigated by W. Zhang [78]. In this case, the best magnetic properties, $J_r$ = 1.19 T and $H_c$ = 244 kA/m, were obtained after annealing at 913 K for 10 min.

Another interesting work carried out by J. Zhang et al [79] concerns the GFA of the $(Nd,Fe,B)_{96}Nb_4$ system. The best GFA was observed for $Fe_{65.28}B_{24}Nd_{6.72}Nb_4$. Such composition (for the as-cast sample) leads to almost fully amorphous structure and soft magnetic properties. The alloy with higher Nd content ($Fe_{64.32}B_{22.08}Nd_{9.6}Nb_4$) contains amorphous plus $Nd_2Fe_{14}B$ phases which leads to inhomogeneous hysteresis loops with

soft and hard magnetic components. Moreover, annealing at 983 K for 5 min strongly increases the coercivity up to $H_C$ = 1100 kA/m, with remanence $M_r$ = 0.44 T and energy product $|BH|_{max}$ = 33 kJ/m$^3$.

H. Man at al. [80] have studied the relationship between microstructure and magnetic properties of the $Fe_{61-x}Nd_{10}B_{25}Nb_x$ ($x$ = 0, 4) alloy. Samples were prepared by suction casting technique in a form of bulk sheet (1 mm × 10mm × 80 mm). The Nb was chosen for alloying addition due to great GFA enhancement [79], [81]. Base on DSC data, the onset of crystallization as well as multi-step melting behavior temperatures were observed at 955 K and 1300-1400 K, respectively. The optimum hard magnetic properties i.e. $H_C$ = 1191 kA/m, $B_r$ = 0.42 T and $|BH|_{max}$ = 31.7 kJ/m$^3$ were obtained after annealing at 943 K for 20 min, while as-cast sample was magnetically soft. The heat treatment provides crystalline phases including $Nd_2Fe_{14}B$ (attributed to high $H_C$), paramagnetic (in room temperature) $NdFe_4B_4$ phase with the grain size of 370 nm and small amount of NbFeB. The last of the mentioned phases may prohibit the crystall growth, and hence, enhance the desired magnetic properties as reported in [82], [83]. However, it is not expected in this case, therefore, the authors suggest suppressing the precipitation of the NbFeB phase in the as-cast alloy in order to improve hard magnetic properties.

The vacuum suction casting technique can be extended by external magnetic field presents during quenching process which may impact on orientation of magnetic crystalline grains. Dan et al [84] reported inducing anisotropy in bulk $Nd_{55-x}Co_xFe_{30}Al_{10}B_5$ ($x$ = 10, 15, 20) nanocrystalline alloys by quenching in magnetic field with strength equal to 0.25 T. The hysteresis loop measured in parallel orientation to the introduced field presents more square-like shape with higher remanence and energy product (from 8.24 to 11.1 kJ/m$^3$ for $x$ = 20), however, they observed slightly smaller coercivity (1.46 to 1.37 T) than in the case of hysteresis loop measured along the perpendicular direction. Moreover, magnitude of the magnetic anisotropy can be enhanced by a proper concentration of Co. Structural investigations show that nanocrystalline particles with 10-30 nm size consists of mostly $Nd_2(Fe,Co)_{14}B$, $Nd_3Co$, $Nd_3Al$, $NdAl_2$ phases and they are embedded in residual amorphous matrix.

The magnetic properties as well as phase compositions of several bulk Fe-based alloys with good hard magnetic properties obtained by quenching or devitrification annealing

process are summarized in Table 3.4. Typical phase compositions of such materials consist of $Fe_3B$, α-Fe (soft magnetic) and $Nd_2Fe_{14}B$ phases. The highest maximum energy product $|BH|_{max}$ = 92.7 kJ/m$^3$ was reported for $Fe_{67}Co_{9.4}Nd_{3.1}Dy_{0.5}B_{20}$ rod (0.5 mm in diameter), while the $Fe_{61}Nd_{10}B_{25}Nb_4$ sheet (1 mm in thickness) is characterized by the highest coercivity, $H_C$ = 1191 kA/m.

Table 3.4 The magnetic properties, size, conditions and phase composition of various Fe-based bulk permanent alloys [80].

| Alloy | $H_c$ [kA/m] | $M_r$ [T, *Am$^2$/kg] | $\|BH\|_{max}$ [kJ/m$^3$] | The smallest size [mm] | Temp. [K], time [min] | Phase compositions | Ref. |
|---|---|---|---|---|---|---|---|
| **$Fe_{67}Co_{9.4}Nd_{3.1}Dy_{0.5}B_{20}$** | 244 | 1.19 | 92.7 | 0.5, rod | 913, 10 | αFe, $Fe_3B$, $Nd_2Fe_{14}B$, | [78] |
| **$Fe_{75.8}Nd_{4.5}Cu_{0.2}Nb_1B_{18.5}$** | 230 | 0.46 | - | 0.5, rod | 883, 10 | αFe, $Fe_3B$, $Nd_2Fe_{14}B$ | [85] |
| **$Fe_{68}Nd_3Y_3B_{22}Mo_4$** | 364 | - | - | 1.5, rod | - | αFe, $Fe_3B$, $Nd_2Fe_{14}B$, $Y_2Fe_{14}B$,$Nd_2Fe_{23}B_3$ | [86] |
| **$Fe_{64.5}Nd_7Y_{2.5}B_{23}Nb_3$** | 892 | 0.57 | 56.8 | 2, rod | 983, 15 | αFe, $Fe_3B$, $Nd_2Fe_{14}B$, $Fe_2Nb$, $Nd_2Fe_{23}B_3$ | [87] |
| **$Fe_{61}Co_{13.5}Zr_1Pr_{4.5}B_{20}$** | 133 | | 14.6 | 0.2, tube | 903, 30 | αFe, $(FeCo)_3B$, $Pr_2(Fe,Co)_{14}B$ | [88][89] |
| **$Fe_{61}Co_{13.5}Zr_1Pr_{3.5}Dy_1B_{20}$** | 144 | | 22.7 | 0.2, tube | 923, 30 | α(Fe,Co), $(FeCo)_3B$, $(Pr,Dy)_2(Fe,Co)_{14}B$ | [90] |
| **$Fe_{61}Co_{10}Nd_3Y_6B_{20}$** | 101 | 46* | - | 1, sheet | 948, 30 | αFe, $Fe_2Y$, $Nd_2Fe_{14}B$, | [77] |
| **$Fe_{68}Zr_2Y_4B_{21}Nd_5$** | 380 | 49* | 43 | 0.8, sheet | 963, 30 | αFe, $Nd_2Fe_{14}B$, $NdFe_4B_4$, $NdFe_3B_3$ | [91] |
| **$Fe_{43}Co_{27}Zr_3Nd_5B_{22}$** | 179 | 21* | - | 1, sheet | 1033,10 | αFe, $Nd_2Fe_{14}B$, FeB, unknown phase | [92] |
| **$Fe_{71.5}Nd_{9.5}B_{15}Nb_4$** | 1162 | 0.59 | 59 | 0.7, rod | Directly | αFe, $Fe_3B$, $Nd_2Fe_{14}B$, $Nd_2Fe_{23}B_3$ | [93] |
| **$Fe_{64.32}Nd_{9.6}B_{22.08}Nb_4$** | 1100 | 0.44 | 33 | 1.5, rod | 983, 5 | $Nd_2Fe_{14}B$ | [79] |
| **$Fe_{60}Co_{13}Pr_9B_{14}Ti_3Zr_1$** | 780 | - | - | 0.2, tube | Directly | $Pr_2(Fe,Co)_{14}B$ | [94] |
| **$Fe_{61}Nd_{10}B_{25}Nb_4$** | 1191 | 0.42 | 31.7 | 1, sheet | 943, 20 | $Nd_2Fe_{14}B$, $NdFe_4B_4$, NbFeB | [80] |

Bulk permanent magnets are widely used in modern technologies starting from wind generators and sensors up to hybrid-car traction drive motors. Most of these technologies require stable properties at temperature above 180 ºC. The best hard magnetic properties have Nd-Fe-B-based alloys, however, in this case high Dy addition is required to improve the Curie temperature. J.M.D Coey [95] has carried out good analysis of magnetic materials in the context of their price. It is important to note that the elements like Tb and Dy are one of the most expensive (1000 – 10 000 $/kg) in the periodic table. On the other

hand, Nd, Pr, Y and Sm costs below 1000 $/kg, Co or Ni below 100 $/kg, while Fe and Al less than 10 $/kg [95]. Today, the market splits roughly 2:1 between Nd–Fe–B (with $|BH|_{max}$ > 200 kJ/m$^3$) and hard ferrite (with $|BH|_{max}$ < 38 kJ/m$^3$). However, the ratio of theirs cost is more than 25:1. Therefore, especially important challenge in the field of the permanent magnets is to fill the gap between this alloys, i.e. development of materials with energy product about 100-200 kJ/m$^3$ as well as without or with low content of rare earth and thus, a relatively low price.

# 4. Aim, work plan and experimental procedures of the thesis

## 4.1. Aim of the thesis

Based on the review of the papers concerning iron-based hard magnets, one can notice that further progress in the field of modern hard magnetic materials requires investigations related to a proper micro/nano structure of multiphase systems containing interacting hard and soft magnetic phases. So, very important seems to be the preparation technology that allows obtaining nanostructured materials and controlling properties of the nanostructure. It is worth to mention the two main preparation procedures. The first one starts from amorphous precursor (usually obtained by melt-spinning technique in the form of ribbons) and nanostructure is formed during isothermal annealing. The second possibility is a formation of nanostructure directly from liquid state by fast solidification, for example, like in the vacuum suction casting technique. From application point of view, a big advantage of this method is a production of bulk nanocrystalline alloys with dimension in order of several mm and in different forms like rods, ingots, etc.

**The aim of the presented work is to study magnetic and related properties of Fe-NB-B-RE bulk nanocrystalline alloys prepared by vacuum suction technique with the so-called light (like Pr, Nd) or heavy (i.e. Tb, Dy) RE elements**.

The PhD thesis is focused on: i) magnetic interactions in multiphase magnetic materials, ii) magnetism in TM-RE disordered structure, iii) influence of microstructure on selected physical properties and iv) numerical modeling and characterization of the nanomagnetic structures. From application point of view, especially important is a combination of chemical compositions and technology parameters (cooling rate, melting current) of the studied alloys, in order to improve hard magnetic characteristics and / or decrease the RE content without deterioration of their desired properties. The knowledge in this subject will be useful in the field of fundamental magnetism of disordered nano-systems as well as functionalization of the Fe-Nb-B-RE bulk nanocrystalline alloys.

## 4.2. Plan of work and investigated alloys

All work considered in a frame of the presented Ph.D. thesis has been divided in two stages:

I. The preliminary researches (described in Chapter 5) were focused on structural and magnetic characteristics of studied alloys in a large range of variability taking into account chemical composition and technology parameters. The main aim of this stage was estimation the optimal type and content of alloying addition as well as sample diameter in the context of hard magnetic properties. The performed work includes:

   1. Sample preparation based on the $(Fe_{80}Nb_6B_{14})_{1-x}RE_x$ composition, where RE = Tb, Nd, Pr, Er, Pt and $x$ = 0.02 to 0.32. The alloys were produced by the vacuum suction casting with sample diameter $d$ = 0.5 mm, 1 mm, 1.5 mm, 2 mm and melting current $I$ = 25 A.

   2. Measurements of:
      i. structural properties including the x-ray diffraction, the Mössbauer spectroscopy and the scanning electron microscopy,
      ii. magnetic properties by the SQUID magnetometer, the Faraday type magnetic balance, the Kerr microscopy and the AFM/MFM technique,
      iii. structural and magnetic transitions due to thermal treatment (DSC) and milling.

II. The main researches (Chapter 6) were focused on the magnetic hardening effect observed for selected alloys. During this stage the impact of chemical composition, preparation conditions as well as thermal treatment on improvements of hard magnetic properties were carefully exanimated. Moreover, the aim was explanation of the observed phenomena based on performed investigations and numerical analysis. This work consists:

   1. Sample preparation based on the optimal condition estimated in previous stage. In this case the RE = Tb, Dy and Tb/Y with $d$ = 0.5 mm to 1.5 mm

were chosen. The impact of Nb content between 2 and 8 at.% as well as melting current $I$ = 15 A, 25 A, 35 A and 45 A were also studied.

2. Measurements of:
   i. structural properties including the x-ray diffraction, the Mössbauer spectroscopy and the scanning electron microscopy,
   ii. magnetic properties by the SQUID magnetometer (including field annealing investigations), the Faraday type magnetic balance, the Kerr microscopy and the AFM/MFM technique.
3. Numerical analysis of time dependent effects and simulations focused on magnetization process of hard magnetic systems (Chapter 7) including: i) the Monte Carlo simulations in a frame of 3D Heisenberg model as well as ii) the Stoner-Wohlfarth and Two-level models extended by random field.

The full list of chemical compositions and technology parameters for the all studied alloys is presented in Figure 4.1.

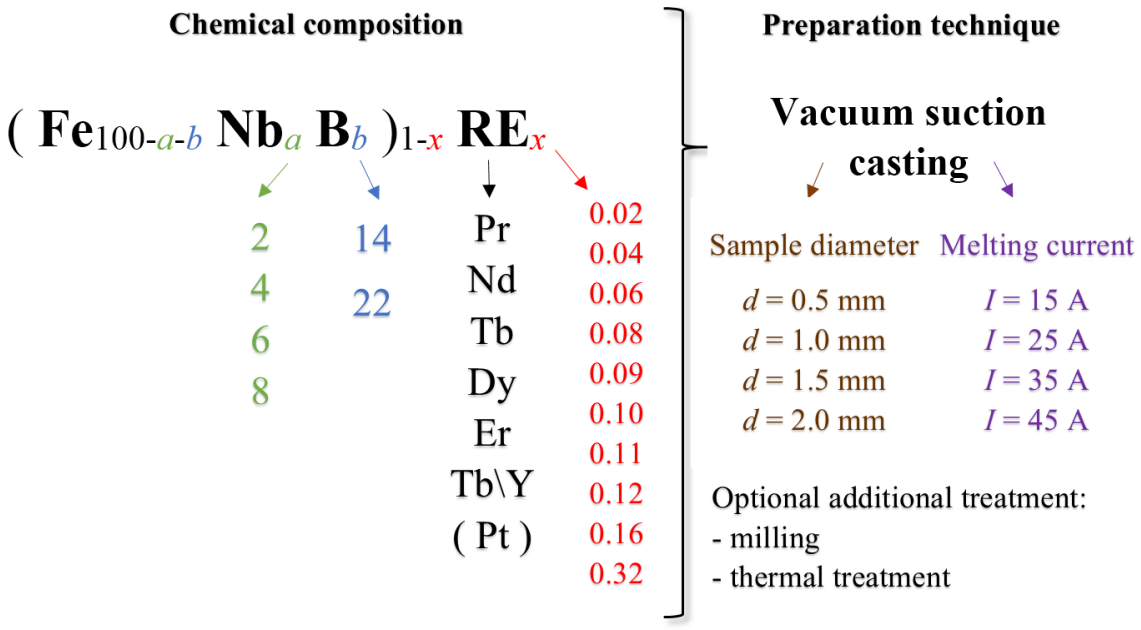


Figure 4.1. Diagram of the all prepared alloys including chemical composition and technology parameters.

## 4.3. Measurement techniques

For the obtained alloys the following measurement techniques and data analysis were performed:

1. Structural measurements:
    a. The X-ray diffraction measurments were carried out on powdered samples (20 sec in one ball agate mill) by Siemens D-5000 diffractometer (θ–θ configuration) with CuKα radiation (1.5418 Å, 40 kV, 30 mA) without monochromator and with nickel filter. The powder diffraction diagrams were measured form 10 to 120 degrees with high resolution. The qualitative and quantitative phase analysis were performed by High Score Plus program with PDF-4 database (Powder Diffraction Data). The size of crystal grains was calculated based on Sherrer equation. The parameters for each lines (i.e. intensity, peak positions, FWHM) were fitted to the experimental data by the least-squares method by means of the computer program the "X-ray Powder Reflection Profiler".
    b. The $^{57}$Fe Mössbauer measurements in transmission geometry with constant acceleration spectrometer, using a $^{57}$Co source diffused in a rhodium matrix. The parameters were fitted to the experimental data by the least-squares method.
    c. Micrographs of the sample surfaces as well as chemical maps were performed using scanning electron microscopy (SEM). Before this measurements the samples were cut and included into a resin. Next, flat surfaces by mechanical polishing were prepared.
2. Magnetic measurements:
    a. The SQUID magnetometer (XL-7, Quantum Design) in the temperature range 2 K – 300 K and magnetic field up to 7 T.
    b. The Faraday type magnetic balance in temperature range from 300 K up to 1100 K.
    c. The magnetic domain observations were performed by the means of Quesant Q-Scope 250 AFM/MFM system, equipped with a 40 μm × 40 μm piezo-scanner. The measurements of polished sample surfaces

performed with the silicon probe coated by 40 nm thick cobalt alloy film. The cantilever resonant frequency were equal to 75 kHz with force constant about 2.8 N $m^{-1}$.

d. The observation of magnetic domain magnetization processes in micro-metric scale and magnetic field range up to 1 T were carried out by magneto-optic Kerr microscopy.

3. Thermal measurements:
    a. Investigation of thermal stability by heating up to 900 K using NETZSCH differential scanning calorimeter with heating rate of 20°C/min (0.33K/s).
4. Numerical analysis:
    a. Time dependent effects of magnetization.
    b. Determination of distribution of magnetic moment of cluster/nanograins near and below blocking temperature region.
    c. Computer simulations of the microstructure obtained from the structural investigations.

## 4.4. Preparation technique

A scheme of the vacuum suction casting technique used to sample preparation is illustrated in Figure 4.2. The main element is the sample chamber with a casting head and tungsten cathode connected to a TIG DC inverter. The head is composed of a copper block cooled by water circulation and the replaceable mold with cylindrical hole in the center. The bottom of casting mold is connected to a vacuum reservoir and a vacuum pump. All valves as well as a current source are managed by the control unit with a microcontroller and a special dedicated program.

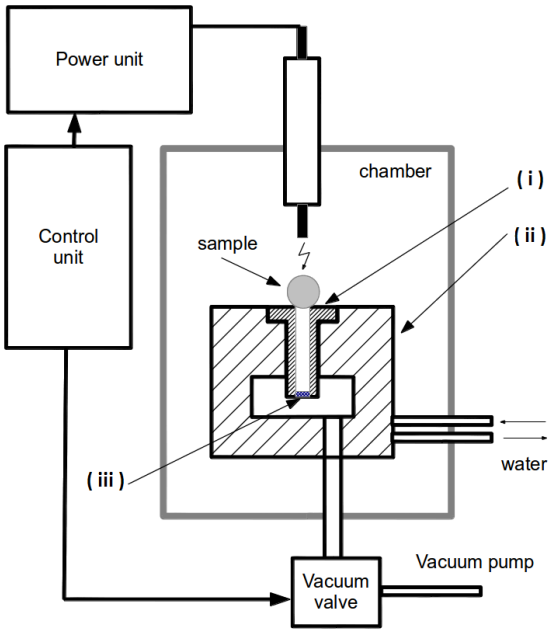


Figure 4.2 Diagram of vacuum suction technique: mold with cylindrical hole (i), copper block (ii) and the net (iii) prevents liquid melt from diffusing out of the mold.

Sample preparation is performed in two stages. Firstly, the precisely weighed amount of chemical elements is melted in an electric arc to form a sphere. The melting process is repeated several times in order to ensure uniform distribution of chemical composition. Next, the preformed material is placed on the top of mold with a cylindrical hole and melted according to the procedure shown in Figure 4.3.

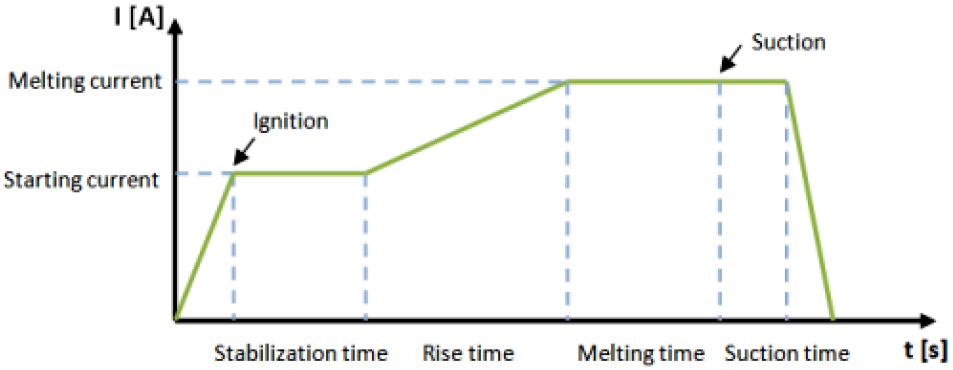


Figure 4.3 Diagram of melting process.

The main melting process consists of several steps: i) the electrical arc ignition using minimum current, ii) a linear current increasing (which prevents splashing of the material), iii) melting of the sample using appropriate high current for a few seconds (technology parameters) and iv) rapid suction of the liquid material by the vacuum into the hole in the mold. The entire melting process is controlled by a driver and carried out under an argon atmosphere (0.2 at. pressure). The final sample has the form of a rod with a length of several cm and a diameter of the order of mm as presented in Figure 4.4.

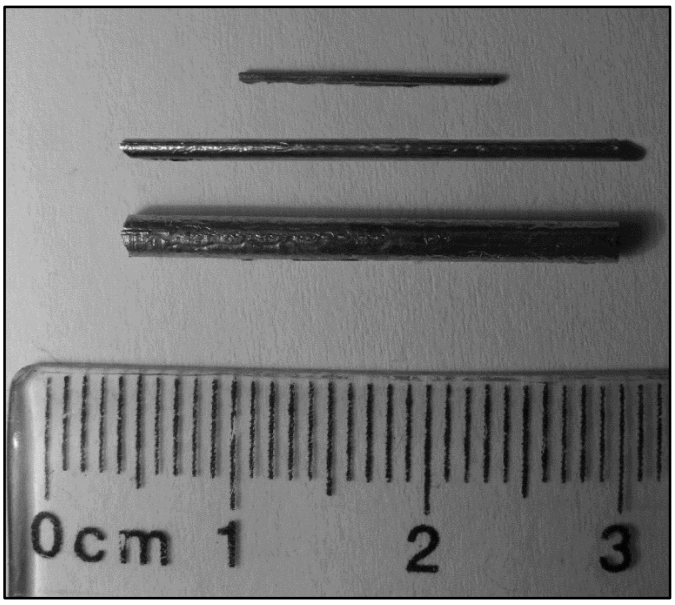


Figure 4.4. Typical picture of the sample prepared by vacuum suction casting technique: 2, 1 and 0.5 mm in diameter on the bottom, middle and top, respectively [96].

Note, that the most important parameters of described technology are: i) the cooling rate of the melted material controlled by the diameter *d* of the hole in the mold (small diameter - high cooling rate) and ii) the melting temperature of the material corresponding with applied melting current *I*.

# 5. Preliminary researches

This chapter refers to preliminary researches, in which some studies were carried out in order to test an influence of technology parameters and chemical compositions on structural and magnetic properties of the Fe-Nb-B-RE bulk alloys. The idea of this part of the PhD work was formulated accounting the both predictions based on the present state of art as well as some trial and error method, leading to an effective way for controlling of magnetic properties of the alloys tested.

In the frame of the preliminary researches the following problems were studied and discussed:

1. An influence of Tb content on structural and magnetic properties. In our case, hard magnetic properties are surely related to the $Tb_2Fe_{14}B$ phase, therefore, a change in phase structure i.e., a balance between the hard and other possible soft phases, is expected.
2. An influence of the cooling rate during casting, controlled by the different mold diameters. This aspect of the researches should reveal a change in microstructure of the alloys and, in a consequence, its impact on magnetic hardening.
3. Phase stability of a selected representative alloy. It is known that the fast-cooling alloys can be thermodynamically unstable. For possible high-temperature or long-term applications, this part can give some important information.
4. Effect of a pulverization degree on structural and magnetic properties. These studies were carried out in order to reveal a role of direct interactions between the magnetic phases. Moreover, the hard magnetic powders are widely used as a component in many magnetic composites, therefore, this subject seems to be interesting.
5. An influence of selected alloying additions on magnetic properties of the Fe-Nb-B-X type of bulk alloys. The variation of the X parameter allows us to make a decision which composition is promising and which is not, taking into account the aim of the thesis.

The performed steps, sometimes in bad directions, were very useful for the broad characterization and final designing of the alloys in question.

# 5.1. Influence of Tb content on structural and magnetic properties of the $(Fe_{80}Nb_6B_{14})_{1-x}Tb_x$ bulk alloys.

In order to investigate the influence of Terbium alloying addition content on structural and magnetic properties, the series of samples of $(Fe_{80}Nb_6B_{14})_{1-x}Tb_x$ (x = 0.02, 0.04, 0.06, 0.08, 0.09, 0.1, 0.12, 0.16, 0.32) were prepared by means of the vacuum suction casting technique. All materials obtained using melting form with **1.5mm** in inner diameter and melting current equal to **25A**. Next, the X-ray diffraction, Mössbauer spectroscopy, magnetic balance and SQUID magnetometer measurements were carried out.

## 5.1.1. Structural properties

Figure 5.1 presents a selected part of XRD patterns ($x$ = 0.02, 0.04, 0.06, 0.09, 0.1 and 0.12). The well-defined sets of Bragg's peaks corresponding to different crystal phases can be found. The patterns consist mainly of ternary $Tb_2Fe_{14}B$ and binary $TbFe_2$ phases as well as some peaks that cannot be attributed to any known structures. In the case of $x$ = 0.12 a contribution of intermediate or disordered phases was observed. In addition, the average size of crystallites in order of tens nm were calculated, using the Sherrer equation. Detailed analysis of the phase composition, supported by the XRD results, was carried out based on the Mössbauer spectra.

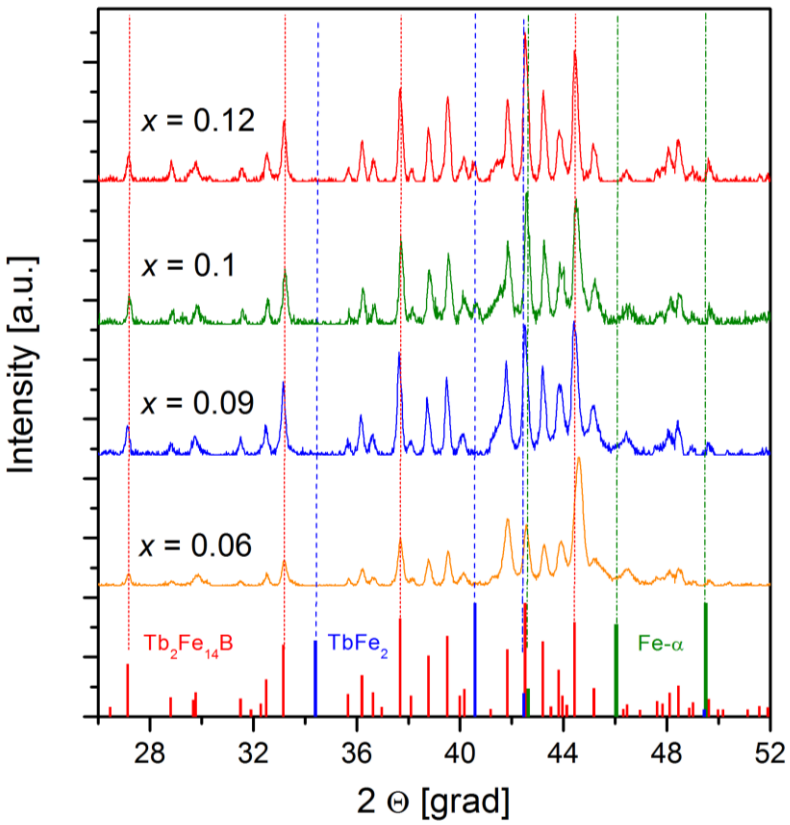


Figure 5.1. Part of X-ray diffraction patterns obtained for $(Fe_{80}Nb_6B_{14})_{1-x}Tb_x$ alloys.

Figure 5.2 presents the $^{57}Fe$ Mossbauer results obtained for selected alloys ($x = 0.04$, 0.06, 0.1, 0.12) with set of deconvoluted Zeeman sextets corresponding to detected phases. Obtained spectra are complex and consist of many components associated with ternary $Tb_2Fe_{14}B$, binary $TbFe_2$, as well as $Fe_\alpha$ and $Tb_{1.1}Fe_4B_4$ phases. The full phase compositions for all investigated alloys were summarized in Table 5.1. Generally, the contribution of hard magnetic phase $Tb_2Fe_{14}B$ increases with Tb content up to 76% for $x = 0.12$ and then decreases. Simultaneously, the binary phase $TbFe_2$ (relatively soft magnetic) starting from 27% for $x = 0.04$, has a minimum for $x = 0.12$ and then increases. Moreover, higher content of $Fe_\alpha$ (maximum 21%) and $Tb_{1.1}Fe_4B_4$ (maximum 24%) for the alloys with low Tb addition ($x = 0.04$, 0.06) can be observed. Is should be also noted that in the case of $x = 0.04$ the detected phases are only like to the ordered structure which suggests a contribution of crystal disorder within formed grains (the values in brackets in Table 5.2).

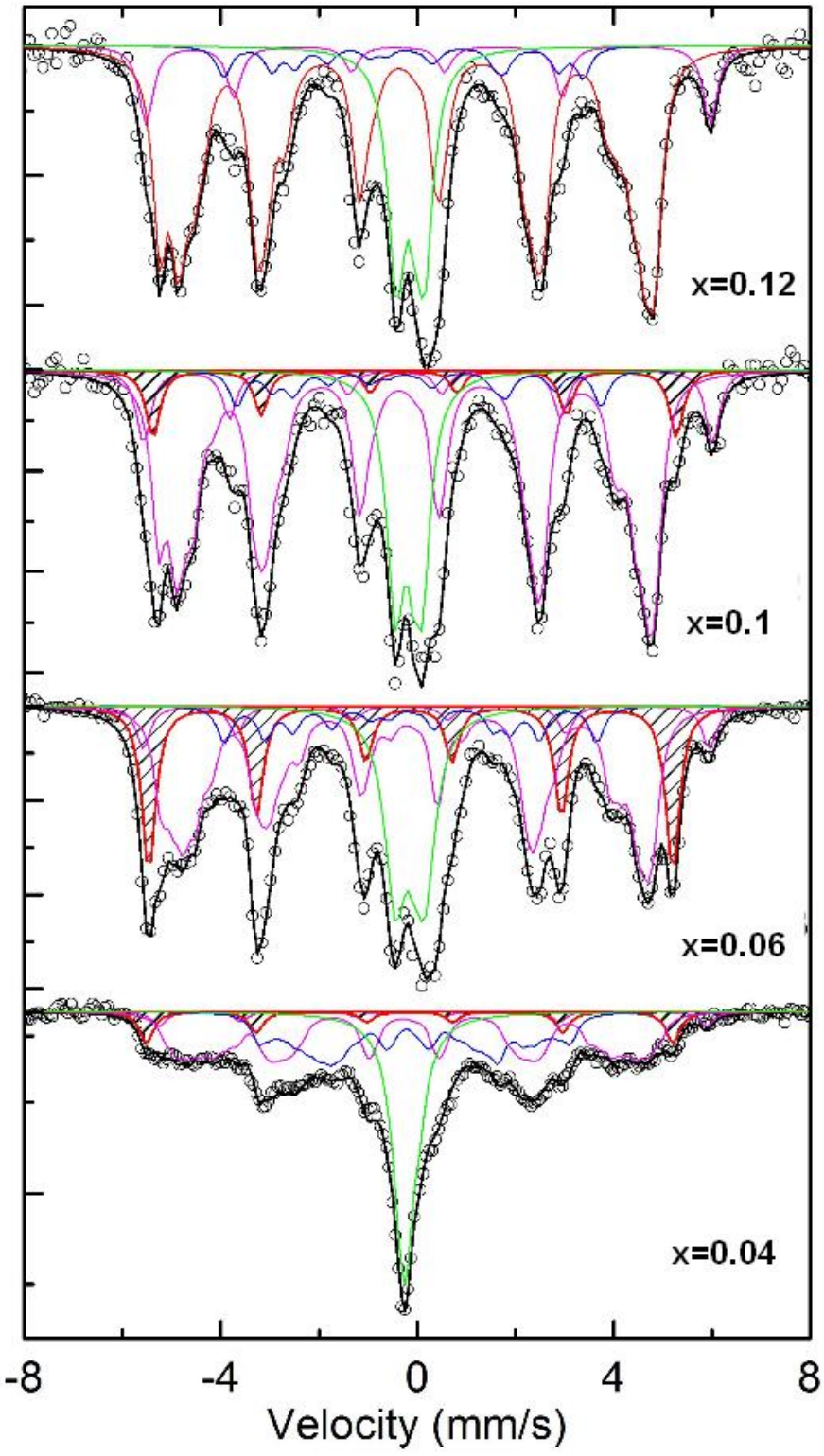


Figure 5.2. The $^{57}Fe$ Mössbauer spectra for the $(Fe_{80}Nb_6B_{14})_{1-x}Tb_x$ alloys with sets of Zeeman sextets attributed to different phases [97].

Table 5.1. The $^{57}$Fe Mössbauer parameters for each detected component of the $(Fe_{80}Nb_6B_{14})_{1-x}Tb_x$ alloys.

| *x* | Phase | I.S. (mm/s) ± 0.01 | 2ε / QS (mm/s) ± 0.01 | $B_{hf}$ (T) ± 0.02 | Area (%) ± 2 | Sum |
|---|---|---|---|---|---|---|
| **0.06** | $Fe_\alpha$ | 0.01 | 0.03 | 32.8 | 21 | 21 |
| | $Tb_2Fe_{14}B$ | 0.09 | 0.51 | 35.5 | 6 | 52 |
| | $Tb_2Fe_{14}B$ | -0.13 | 0.18 | 30.8 | 1 | |
| | $Tb_2Fe_{14}B$ | -0.05 | 0.33 | 28.9 | 11 | |
| | $Tb_2Fe_{14}B$ | -0.02 | 0.32 | 27.5 | 10 | |
| | $Tb_2Fe_{14}B$ | 0 | -0.72 | 27.3 | 8 | |
| | $Tb_2Fe_{14}B$ | 0 | 0.27 | 25.6 | 6 | |
| | $TbFe_2$ | -0.07 | 0.18 | 23.2 | 5 | 9 |
| | $TbFe_2$ | -0.04 | -0.2 | 17 | 4 | |
| | $Tb_{1.1}Fe_4B_4$ | 0.01 | 0.5 | 0 | 18 | 18 |
| **0.1** | $Fe_\alpha$ | 0.09 | 0.02 | 32.8 | 8 | 8 |
| | $Tb_2Fe_{14}B$ | 0.04 | 0.67 | 35.7 | 9 | 69 |
| | $Tb_2Fe_{14}B$ | -0.13 | 0.16 | 31.1 | 18 | |
| | $Tb_2Fe_{14}B$ | -0.06 | 0.23 | 29.5 | 17 | |
| | $Tb_2Fe_{14}B$ | -0.08 | 0.34 | 27.6 | 13 | |
| | $Tb_2Fe_{14}B$ | -0.1 | -0.28 | 26.9 | 8 | |
| | $Tb_2Fe_{14}B$ | -0.11 | 0.39 | 25.9 | 4 | |
| | $TbFe_2$ | 0 | 0.38 | 22.7 | 4 | 6 |
| | $TbFe_2$ | 0.07 | 0.03 | 17.5 | 2 | |
| | $Tb_{1.1}Fe_4B_4$ | -0.02 | 0.44 | 0 | 17 | 17 |
| **0.12** | $Tb_2Fe_{14}B$ | 0.07 | 0.6 | 35.3 | 10 | 76 |
| | $Tb_2Fe_{14}B$ | -0.12 | 0.15 | 31 | 23 | |
| | $Tb_2Fe_{14}B$ | -0.09 | 0.26 | 29.2 | 17 | |
| | $Tb_2Fe_{14}B$ | -0.08 | 0.33 | 27.5 | 12 | |
| | $Tb_2Fe_{14}B$ | -0.06 | -0.23 | 27.2 | 7 | |
| | $Tb_2Fe_{14}B$ | -0.1 | 0.04 | 25.1 | 7 | |
| | $TbFe_2$ | -0.15 | 0.07 | 22.4 | 4 | 7 |
| | $TbFe_2$ | 0.08 | 0.08 | 17.8 | 3 | |
| | $Tb_{1.1}Fe_4B_4$ | 0.02 | 0.48 | 0 | 17 | 17 |

Table 5.2. The mean diameter D of the main phase (calculated based on XRD) and contribution of each phase (obtained from Mössbauer spectra in %) for the investigated materials. The values in brackets means "phase like".

| $(Fe_{80}Nb_6B_{14})_{1-x}Tb_x$ | D [nm] ±10 | $Tb_2Fe_{14}B$ [%] ±2 | $TbFe_2$ [%] ±2 | $Fe_\alpha$ [%] ±2 | $Tb_{1.1}Fe_4B_4$ [%] ±2 |
|---|---|---|---|---|---|
| ***x* = 0.04** | 25 | (41) | (27) | (7) | 24 |
| ***x* = 0.06** | 28 | 52 | 9 | 21 | 18 |
| ***x* = 0.08** | 28 | 64 | 14 | (8) | 12 |
| ***x* = 0.10** | 29 | 69 | 6 | 8 | 17 |
| ***x* = 0.12** | 32 | 76 | 7 | 0 | 17 |
| ***x* = 0.16** | 28 | 59 | 28 | 0 | 13 |
| ***x* = 0.32** | 27 | (7) | 83 | 0 | 10 |

## 5.1.2. Magnetic properties

The magnetic properties of investigated materials were measured by Faraday magnetic balance and SQUID magnetometer. Figure 5.3 presents magnetization dependences as a function of temperature up to 1100 K for $x$ = 0.04, 0.09, 0.12 and 0.16. In case of all studied alloys ~~a~~ two magnetic transitions (drop of $M(T)$) around temperature equal to $T_C$ = 620 K and $T_C$ = 1070 K were observed. Moreover, for $x$ = 0.04, 0.09, 0.12 one can see an increase of magnetization with temperature starting from 300 K up to 620 K, and also for all of this (including x = 0.04), increasing of magnetization after first transition up to around 850 K.

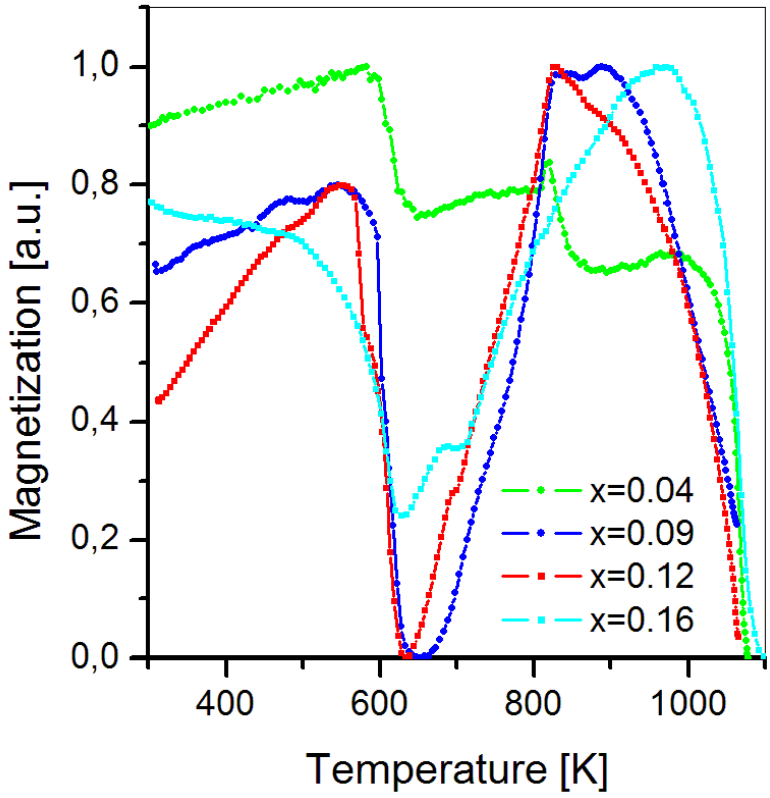


Figure 5.3. The M($T$) curves obtained by magnetic balance for series of the $(Fe_{80}Nb_6B_{14})_{1-x}Tb_x$ materials [97].

The magnetic hysteresis loops were obtained using SQUID magnetometer in the temperature range 2 K – 300 K and magnetic field up to 7 T. Figure 5.4 - Figure 5.11 depict M($H$) dependences measured at $T$ = 300 K, 200 K, 100 K, 50 K, 10 K for all alloys. It can be seen that alloys with low Tb content ($x$ = 0.02, 0.04) exhibits relatively soft

magnetic properties with high magnetic saturation ($M_S$ = 137 emu/g for $x$ = 0.02). However, increasing of Tb contribution leads to a strong increase of magnetic coercivity with maximum equal to 1.46 T (at $T$ = 300 K) for $x$ = 0.1. Further increase of the $x$ parameter causes the observed decrease of coercivity $H_C$. Moreover, one can note that for the materials with 2 and 4 at. % of Tb the presented hysteresis loops are almost temperature-independent, while for the highest Tb addition the increase of coercivity with decreasing temperature was observed. Selected magnetic properties of the exanimated samples including low and room temperature coercivity, magnetic saturation, magnetic remanence as well as $|JH|_{max}$ and $|BH|_{max}$ are listed in Table 5.3.

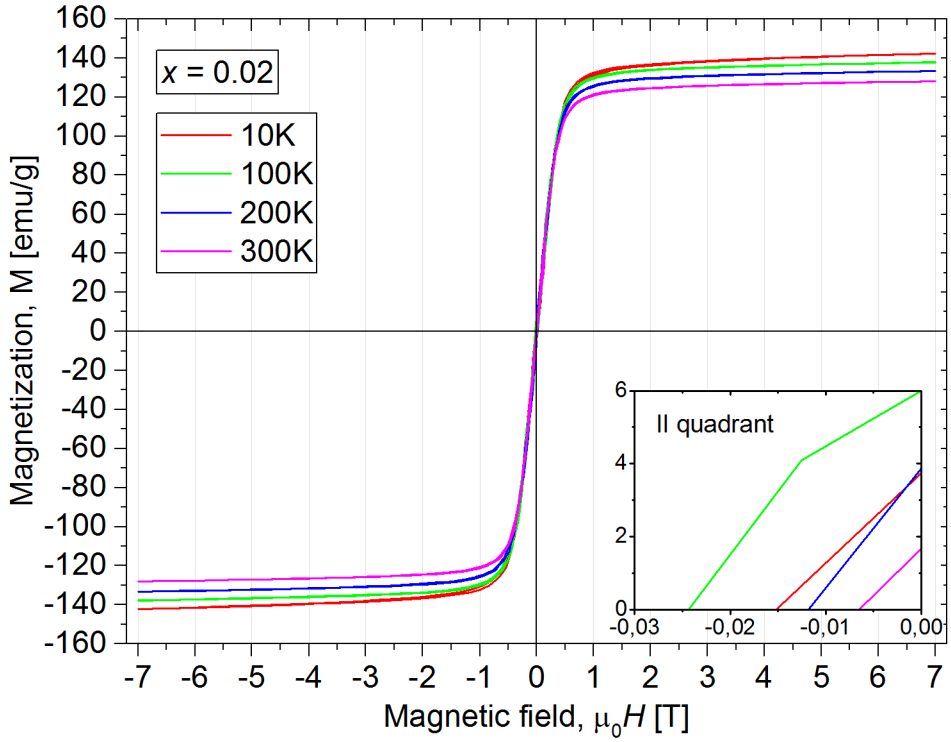


Figure 5.4. The magnetic hysteresis loops obtained for the $(Fe_{80}Nb_6B_{14})_{0.98}Tb_{0.02}$ alloys at temperature range from 10 K up to 300 K.

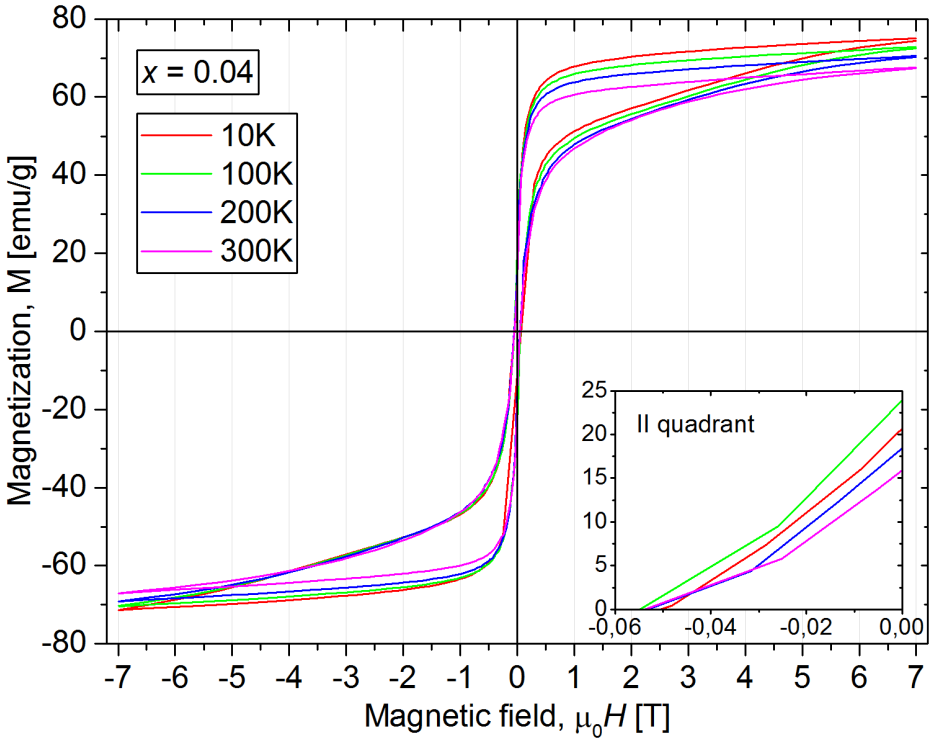


Figure 5.5. The magnetic hysteresis loops obtained for the $(Fe_{80}Nb_6B_{14})_{0.96}Tb_{0.04}$ alloys at temperature range from 10 K up to 300 K.

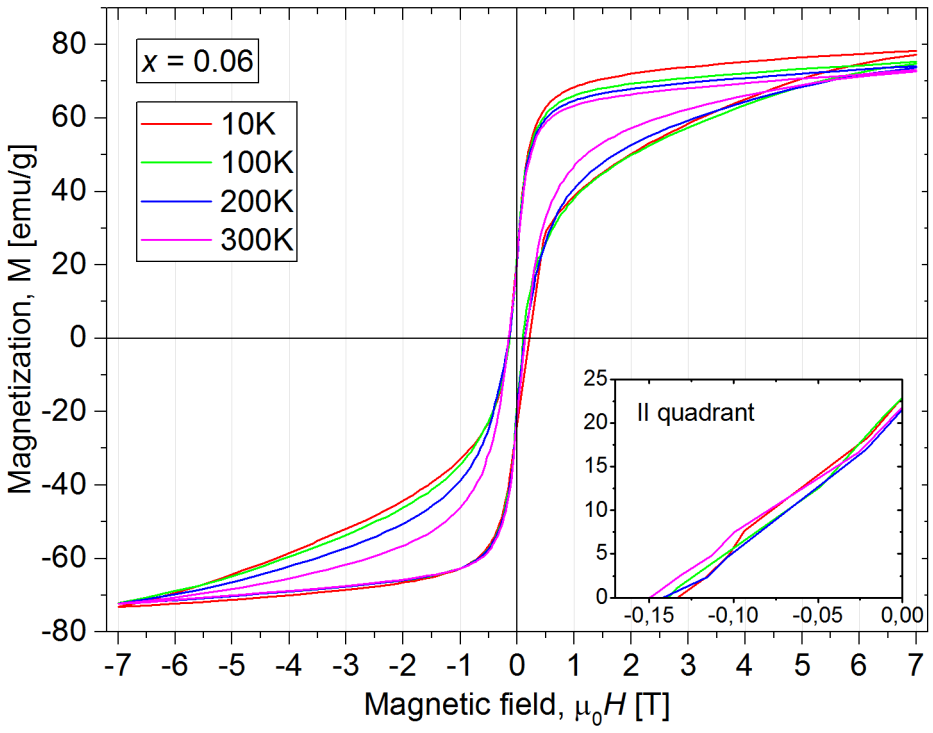


Figure 5.6. The magnetic hysteresis loops obtained for the $(Fe_{80}Nb_6B_{14})_{0.94}Tb_{0.06}$ alloys at temperature range from 10 K up to 300 K.

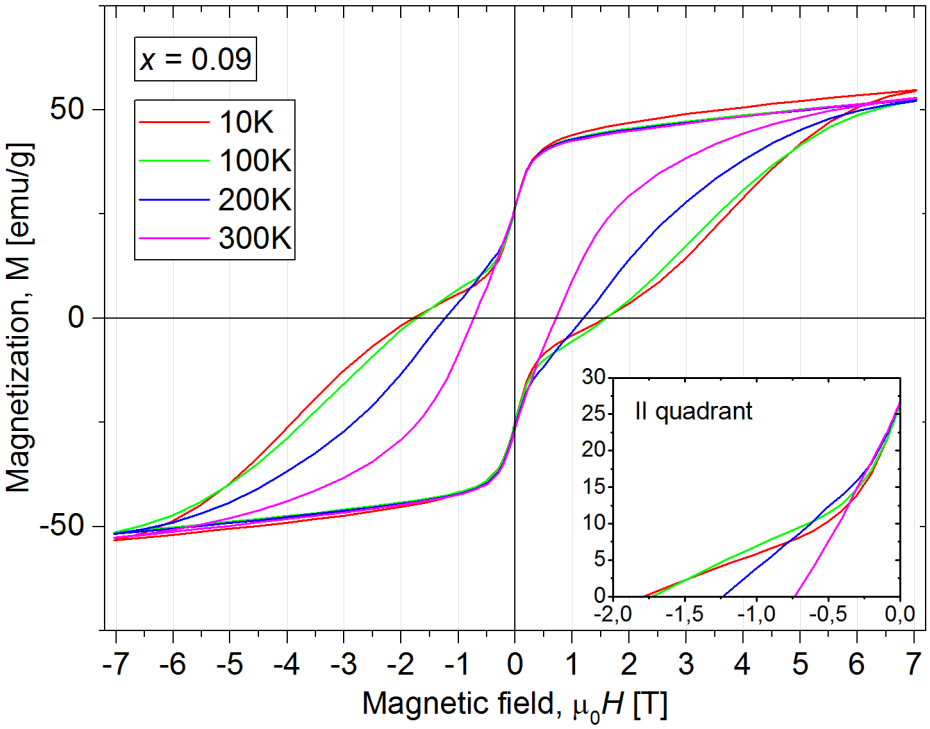


Figure 5.7. The magnetic hysteresis loops obtained for the $(Fe_{80}Nb_6B_{14})_{0.91}Tb_{0.09}$ alloys at temperature range from 10 K up to 300 K.

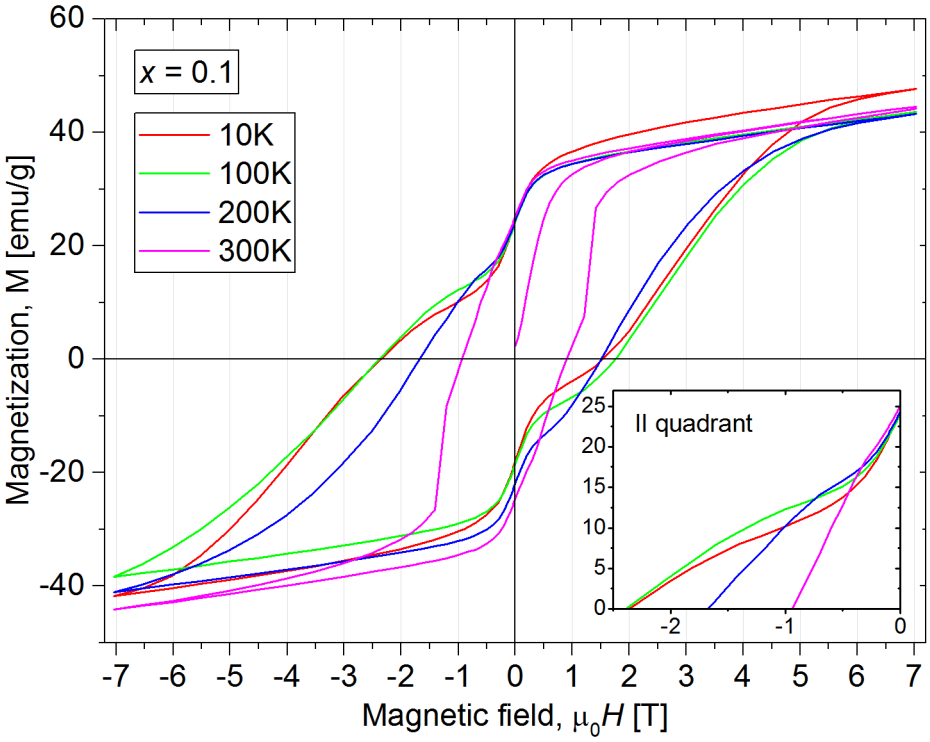


Figure 5.8. The magnetic hysteresis loops obtained for the $(Fe_{80}Nb_6B_{14})_{0.9}Tb_{0.1}$ alloys at temperature range from 10 K up to 300 K.

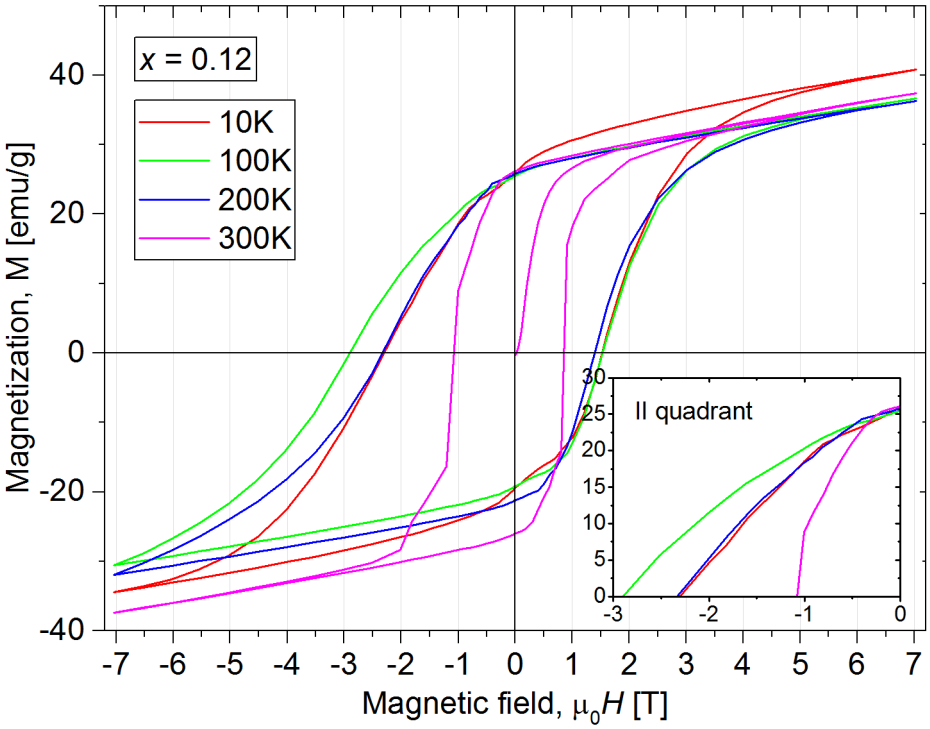


Figure 5.9. The magnetic hysteresis loops obtained for the $(Fe_{80}Nb_6B_{14})_{0.88}Tb_{0.12}$ alloys at temperature range from 10 K up to 300 K.

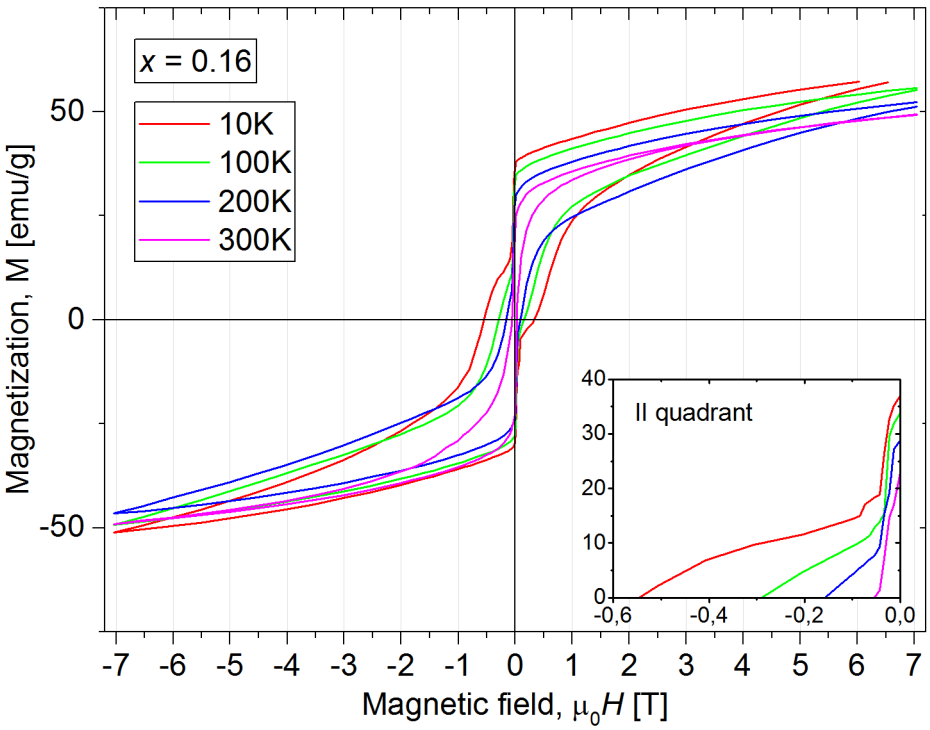


Figure 5.10. The magnetic hysteresis loops obtained for the $(Fe_{80}Nb_6B_{14})_{0.84}Tb_{0.16}$ alloys at temperature range from 10 K up to 300 K.

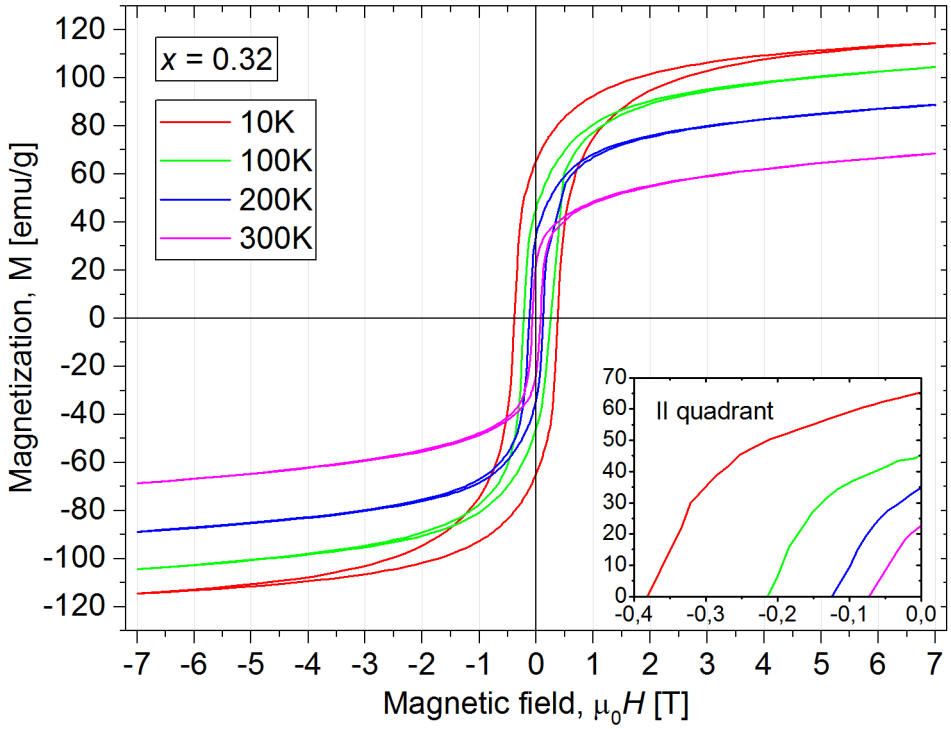


Figure 5.11. The magnetic hysteresis loops obtained for the $(Fe_{80}Nb_6B_{14})_{0.68}Tb_{0.32}$ alloys at temperature range from 10 K up to 300 K.

Table 5.3. Saturation magnetization $Ms^{7T}$ (at 7 T of external magnetic field), coercive field $H_C$, remanence $M_R$ and $|JH|_{max}$ as well as $|BH|_{max}$ parameters for the $(Fe_{80}Nb_6B_{14})_{1-x}Tb_x$ alloys. The measurement errors are in the level of the least significant digit.

| *x* | $M_S^{7T}$ [emu/g] *T* = 300K | $M_R$ [emu/g] *T* = 300K | $\mu_0 H_C$ [T] *T* = 300K | $\|BH\|_{max}$ [kJ/m$^3$] *T* = 300K | $\|JH\|_{max}$ [kJ/m$^3$] *T* = 300K | $\mu_0 H_C$ [T] *T* = 10K | $\|JH\|_{max}$ [kJ/m$^3$] *T* = 10K |
|---|---|---|---|---|---|---|---|
| **0.02** | 127 | 1.7 | 0.01 | - | - | 0.01 | - |
| **0.04** | 68 | 15.9 | 0.03 | 0.7 | 1.7 | 0.03 | 1.7 |
| **0.06** | 72 | 21.8 | 0.15 | 3.0 | 5.9 | 0.15 | 5.7 |
| **0.08** | 54 | 25.2 | 0.25 | 6.4 | 12.7 | 0.41 | 14.1 |
| **0.09** | 52 | 26.8 | 0.75 | 9.9 | 35.9 | 1.82 | 47.2 |
| **0.10** | 43 | 25.1 | 1.46 | 10.0 | 51.3 | 2.51 | 89.7 |
| **0.12** | 37 | 26.1 | 1.16 | 12.7 | 94.9 | 2.96 | 152.3 |
| **0.16** | 49 | 22.7 | 0.06 | 2.3 | 2.8 | 0.55 | 30.4 |
| **0.32** | 69 | 22.6 | 0.08 | 3.0 | 3.9 | 0.38 | 91.4 |

## 5.2. Influence of cooling rate on structural and magnetic properties of the $(Fe_{80}Nb_6B_{14})_{1-x}Tb_x$ alloys.

It is expected that in case of multiphase nanocrystalline alloys the magnetic properties dependent on i) chemical composition (for example, content and type of RE addition), ii) microstructure as well as iii) nature and intensity of magnetic exchange between magnetic phases. For bulk materials, in form of rods produced by vacuum suction casting technique, the process of solidification and microstructure formation corresponds to cooling rate during final step of preparation. In the case of vacuum suction the value of cooling rate is not so high (about $10^3$ K/s), therefore, controlling of microstructure requires a proper combination of chemical composition as well as varying sample diameter. High diameter corresponds to low cooling rate which usually results in nucleation and grain growth. Low mold diameter favors formation of nanocrystalline and amorphous structures.

The main goal of this part of investigations was to study the structural and magnetic properties of the $(Fe_{80}Nb_6B_{14})_{1-x}Tb_x$ bulk nanocrystalline alloys as a function of cooling rate controlled by mould diameter value. Base on the results of the previous researches the set of Terbium content values, $x$ = 0.1, 0.11 and 0.12 were chosen. Additionally, the alloys with $x$ = 0.08 and 0.06 were also taken into consideration in order to search new possibilities to reduce rate-earth content and simultaneously saving good hard magnetic properties.

Each selected compound were prepared using three kind of the melting mold with inner diameter equals to $d$ = 0.5 mm, 1 mm and 2 mm and about 3 cm in length. Moreover, it is important to note that all materials presented in this section were melted at temperature corresponding to 25 A of melting current.

### 5.2.1. Structural properties

The structural investigations were performed using different kind of measurements. Phase identification was performed based on $^{57}$Fe Mössbauer spectrometry supported by X-ray

patterns. Moreover, the microstructure of selected alloys was observed using Scanning Electron Microscope.

Figure 5.12 presents the X-ray patterns obtained for the $(Fe_{80}Nb_6B_{14})_{0.89}Tb_{0.11}$ alloys with diameters equal to 0.5, 1 and 2 mm. In a comparison to that, the theoretical Bragg's peaks corresponding to ternary hard magnetic phase $Tb_2Fe_{14}B$, soft magnetic phase $TbFe_2$ as well as $Fe_\alpha$ were also included.

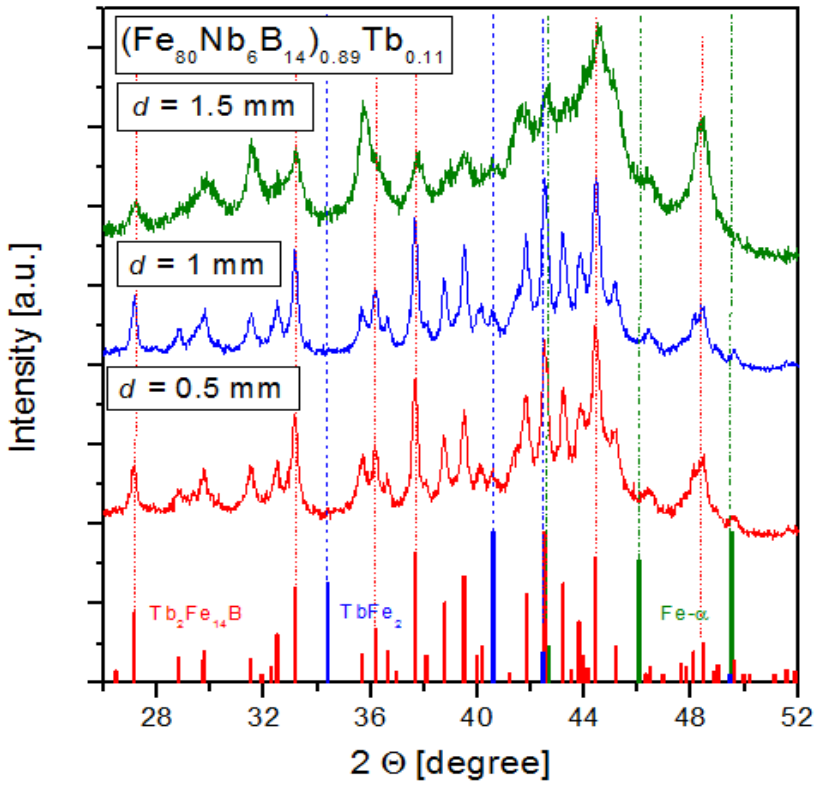


Figure 5.12. Part of the X-ray patterns measured for the alloys of the $(Fe_{80}Nb_6B_{14})_{0.89}Tb_{0.11}$ prepared using different cooling rate corresponding to $d$ = 0.5 mm, 1 mm and 2 mm.

The Mössbauer spectra were recorded for powders materials after grinding of as-cast rods. The measurements were carried out at room temperature without external magnetic field. For all investigated materials, the shapes of obtained spectra are complex and consist of a superposition of hyperfine structures corresponding to each iron sites in detected phases. Experimental spectra were deconvoluted by a fitting procedure to set of elementary Zeeman sextets. The final model consists of i) 6 components attributed to 6 iron sites of $Tb_2Fe_{14}B$ unit cell ($P4_2/mnm$), ii) 2 components corresponding to $TbFe_2$ phase, iii) one sextet of $Fe_\alpha$, iv) one paramagnetic component and, in some cases, FeB-like component.

The Mössbauer spectra measured and deconvoluted for the $(Fe_{80}Nb_6B_{14})_{0.9}Tb_{0.1}$ alloy prepared using the three different diameters of 0.5 mm, 1 mm and 2 mm are presented in Figure 5.13, Figure 5.14 and Figure 5.15, respectively. Moreover, Table 5.4 reports the content and the mean value of isomer shift, the quadrupole shifting / splitting as well as the hyperfine field for sets of components corresponding to each phases and each diameter of $(Fe_{80}Nb_6B_{14})_{0.9}Tb_{0.1}$ samples. On the other hand, the summation of phases composition of all compound for $x = 0.1$, 0.11 and 0.12 using $d = 0.5$ mm, 1 mm and 2 mm is presented in Table 5.5. The obtained results are in agreement with X-ray analyses. Around 65% up to 75% of the alloy content belongs to ternary hard magnetic phase. Most of the rest alloy composition is divided by the soft magnetic $TbFe_2$ (10-20%) phase and the paramagnetic component (around 15%) identified as $Tb_{1.1}Fe_4B_4$. In the case of $x = 0.11$ and diameter wider or equal to 1 mm, a small contribution of the $Fe_\alpha$ (5%) and FeB-like (less than 4%) phases were also detected. However based on both, X-ray diffraction as well as Mössbauer spectroscopy results, any clear and convincing changing tendency between different diameters of alloys were found. It can be noted that the Mössbauer parameters like Isomer shifts (IS), Quadripole shitfing (2ε) and Hyperfine field for most of the components are strongly deformed in comparison to its crystalline form which confirms a contribution of structural disorder inside the material.

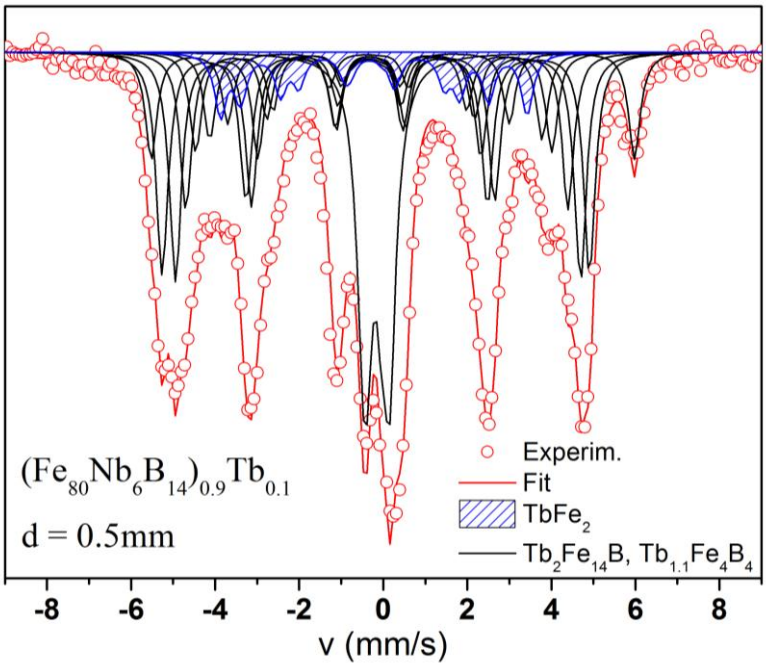


Figure 5.13. The Mössbauer spectrum deconvoluted to set of Zeeman sextets attributed to different phases for the $(Fe_{80}Nb_6B_{14})_{0.9}Tb_{0.1}$ alloy prepared using the mold with 0.5 mm in diameter [96].

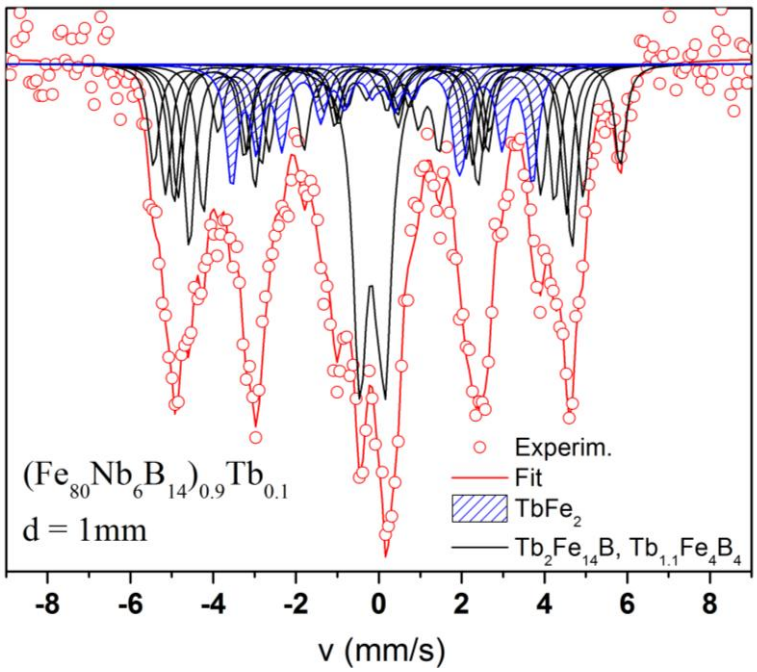


Figure 5.14. The Mössbauer spectrum deconvoluted to set of Zeeman sextets attributed to different phases for the $(Fe_{80}Nb_6B_{14})_{0.9}Tb_{0.1}$ alloy prepared using the mold with 1 mm in diameter [96].

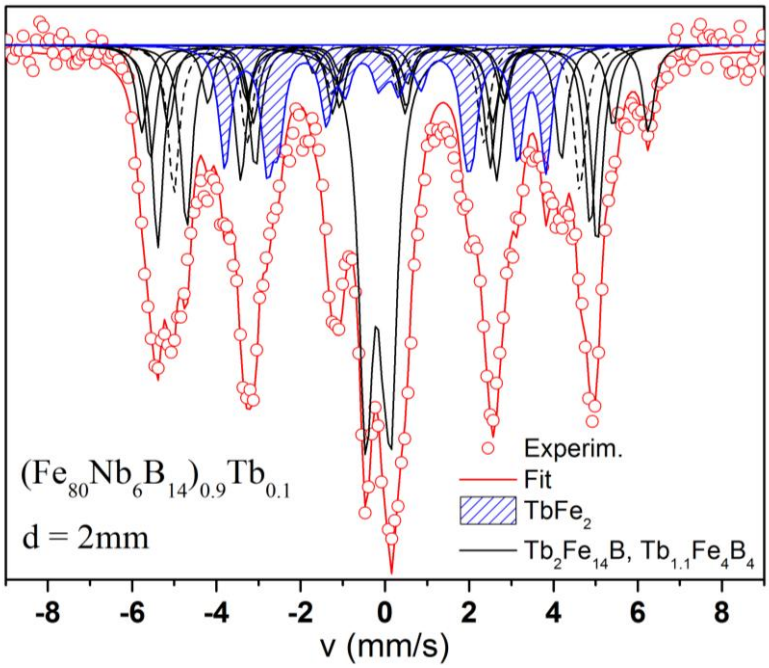


Figure 5.15. The Mössbauer spectrum deconvoluted to set of Zeeman sextets attributed to different phases for the $(Fe_{80}Nb_6B_{14})_{0.9}Tb_{0.1}$ alloy prepared using the mold with 2 mm in diameter [96].

Table 5.4. Mean values of Isomer shifts (IS), Quadripolar shifting / splitting (2ε / QS) and Hyperfine field ($B_{hf}$) as well as phase contents, for each phases based on the $^{57}Fe$ Mössbauer measurements for the $(Fe_{80}Nb_6B_{14})_{0.9}Tb_{0.1}$ alloy prepared using the mold with 0.5 mm, 1 mm and 2 mm in diameter.

| *d* [mm] | Phase | < IS > [mm/s] ± 0.01 | < 2ε/QS> [mm/s] ± 0.01 | < $B_{hf}$ > [T] ± 0.02 | Content [%] ± 2 |
|---|---|---|---|---|---|
| **0.5** | $Tb_2Fe_{14}B$ | -0.06 | 0.21 | 29.6 | 75± 2 |
| | $TbFe_2$ | -0.16 | -0.02 | 20.5 | 9± 2 |
| | $Tb_{1.1}Fe_4B_4$ | 0.01 | 0.49 | 0 | 16± 2 |
| **1** | $Tb_2Fe_{14}B$ | -0.06 | 0.27 | 29.3 | 65± 2 |
| | $TbFe_2$ | 0.2 | 0.12 | 20.0 | 15± 2 |
| | $Tb_{1.1}Fe_4B_4$ | 0.0 | 0.54 | 0 | 14± 2 |
| | FeB-like | 0.07 | -0.19 | 9.8 | 6± 2 |
| **2** | $Tb_2Fe_{14}B$ | -0.07 | 0.26 | 30.4 | 64± 2 |
| | $TbFe_2$ | 0.18 | 0.09 | 20.4 | 18± 2 |
| | $Tb_{1.1}Fe_4B_4$ | 0.01 | 0.49 | 0 | 18± 2 |

Table 5.5. The phase compositions based on $^{57}$Fe Mössbauer measurement for the family of the $(Fe_{80}Nb_6B_{14})_{1-x}Tb_x$ bulk nanocrystalline alloys prepared using three different mold with $d$ = 0.5 mm, 1 mm and 2 mm.

| Alloy | | Content [ % ] ± 2 | | | | |
|---|---|---|---|---|---|---|
| $x$ | $d$ [mm] | $Tb_2Fe_{14}B$ | $Fe_\alpha$ | $TbFe_2$ | $Tb_{1.1}Fe_4B_4$ | FeB-like |
| **0.10** | **0.5** | 75 | 0 | 9 | 16 | 0 |
| | **1** | 65 | 0 | 15 | 14 | 6 |
| | **2** | 64 | 0 | 18 | 18 | 0 |
| **0.11** | **0.5** | 67 | 0 | 19 | 14 | 0 |
| | **1** | 64 | 5 | 11 | 16 | 4 |
| | **2** | 67 | 5 | 9 | 17 | 2 |
| **0.12** | **0.5** | 66 | 0 | 21 | 13 | 0 |
| | **1** | 70 | 0 | 18 | 13 | 0 |
| | **2** | 68 | 0 | 18 | 14 | 0 |

Micrographs of the sample surfaces were performed using scanning electron microscopy SEM in SEI mode with magnification of 800 and 3300. Before this measurement the samples were cut and included into a resin. Next, flat surfaces by mechanical polishing were prepared. The images obtained for the alloys with 12 at.% of Tb content and the diameters equal to 2 mm, 1 mm and 0.5 mm are shown in Figure 5.16, Figure 5.17 and Figure 5.18, respectively. One may note that depending on cooling rate the specific microstructure is formed. In case of $d$ = 1 mm and 0.5 mm the micrographs reveal a formation of dendrite-like grains. The observed fragmentation increases with decreasing sample diameter. Figure 5.19 presents a picture of a surface structure for the $(Fe_{80}Nb_6B_{14})_{0.88}Tb_{0.12}$ alloy prepared with the smallest mold diameter (magnification of 3300). It is clear that the dendrite branches are micrometric or even sub-micrometric in size.

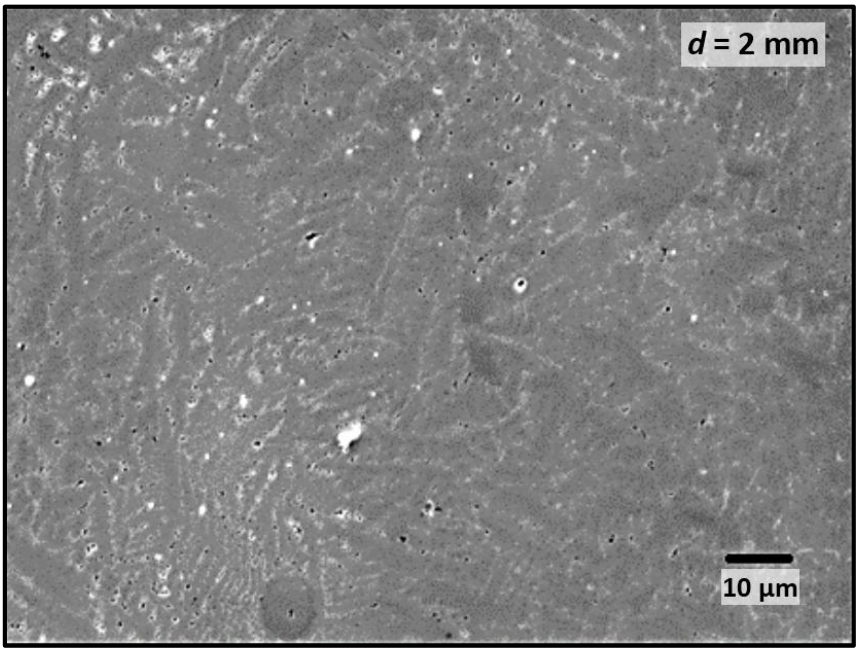


Figure 5.16. SEM image (SEI mode, magnification of 800) for the $(Fe_{80}Nb_6B_{14})_{0.88}Tb_{0.12}$ alloy with $d$ = 2 mm.

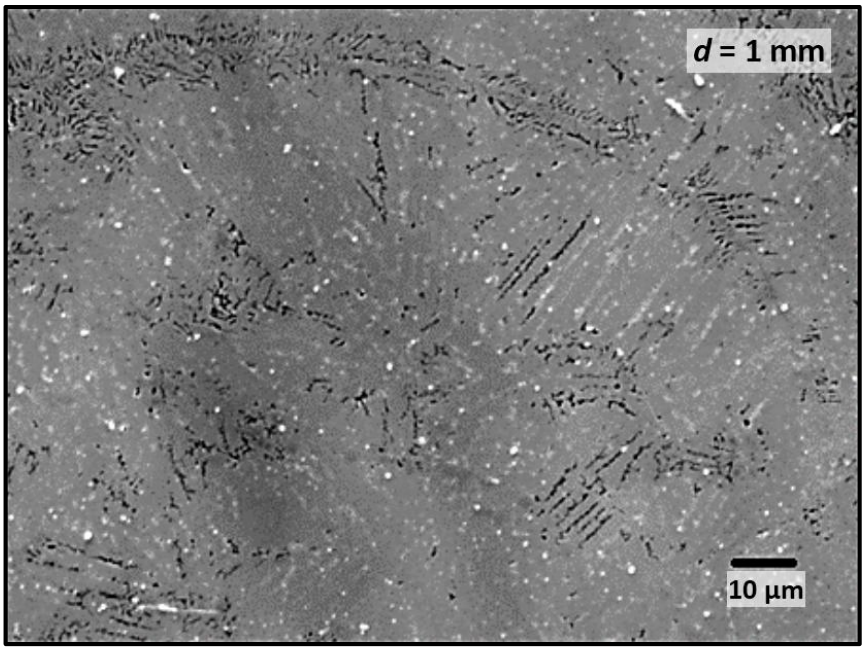


Figure 5.17. SEM image (SEI mode, magnification of 800) for the $(Fe_{80}Nb_6B_{14})_{0.88}Tb_{0.12}$ alloy with $d$ = 1 mm.

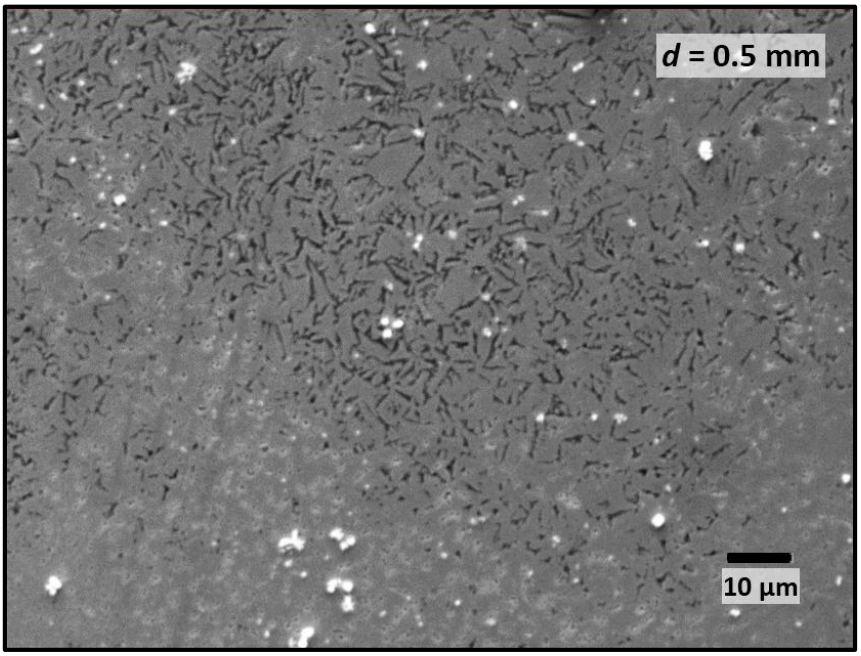


Figure 5.18. SEM image (SEI mode, magnification of 800) for the $(Fe_{80}Nb_6B_{14})_{0.88}Tb_{0.12}$ alloy with $d$ = 0.5 mm.

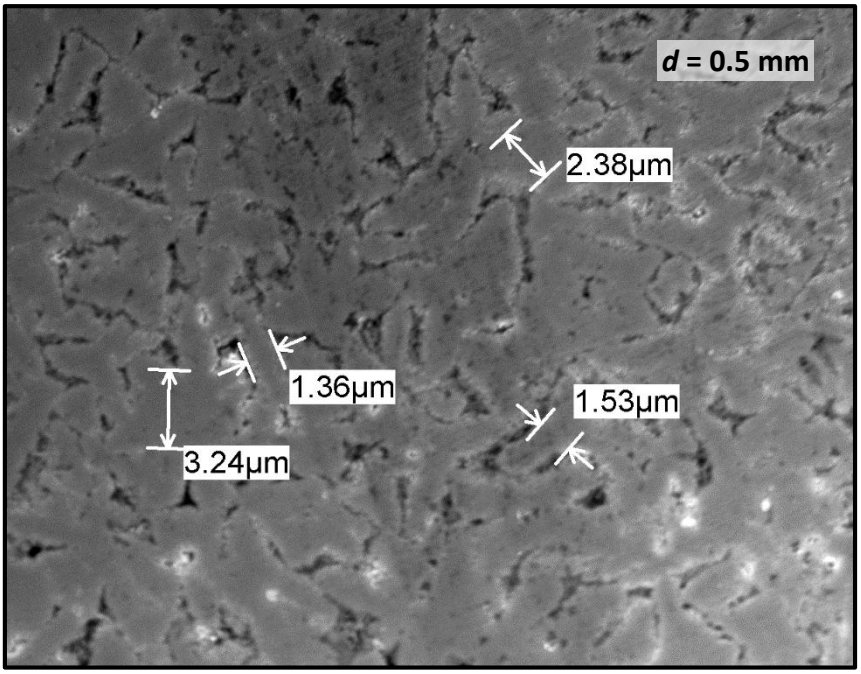


Figure 5.19. SEM image (SEI mode, magnification of 3300) for the $(Fe_{80}Nb_6B_{14})_{0.88}Tb_{0.12}$ alloy with $d$ = 0.5 mm.

## 5.2.2. Magnetic properties

The SQUID magnetometer measurements using a field up to 7 T were carried out for all prepared materials base on $(Fe_{80}Nb_6B_{14})_{1-x}Tb_x$ compound with $x$ = 0.06, 0.08, 0.1, 0.11, 0.12 as well as, the sample diameters equal to 2 mm, 1 mm and 0.5 mm. The experimental procedure consists sequential measurements starting from two runs at room temperature (300 K) and then one per each temperature step for $T$ = 250 K, 200 K, 150 K, 100 K, 50 K, 10 K and 2 K.

The magnetic hysteresis loops for alloy $x$ = 0.12 are presented in Figure 5.20Figure 5.21 andFigure 5.22 in case of $d$ = 2 mm, 1 mm and 0.5 mm, respectively. Figure 5.23 allows compering different diameters of this material measured at room temperature. The hysteresis loops associated with alloy $x$ = 0.11 are presented in Figure 5.24 and Figure 5.25. The last four Figures i.e. Figure 5.26, Figure 5.27, Figure 5.28 and Figure 5.29 consists of magnetic hysteresis loop related to $x$ = 0.12.

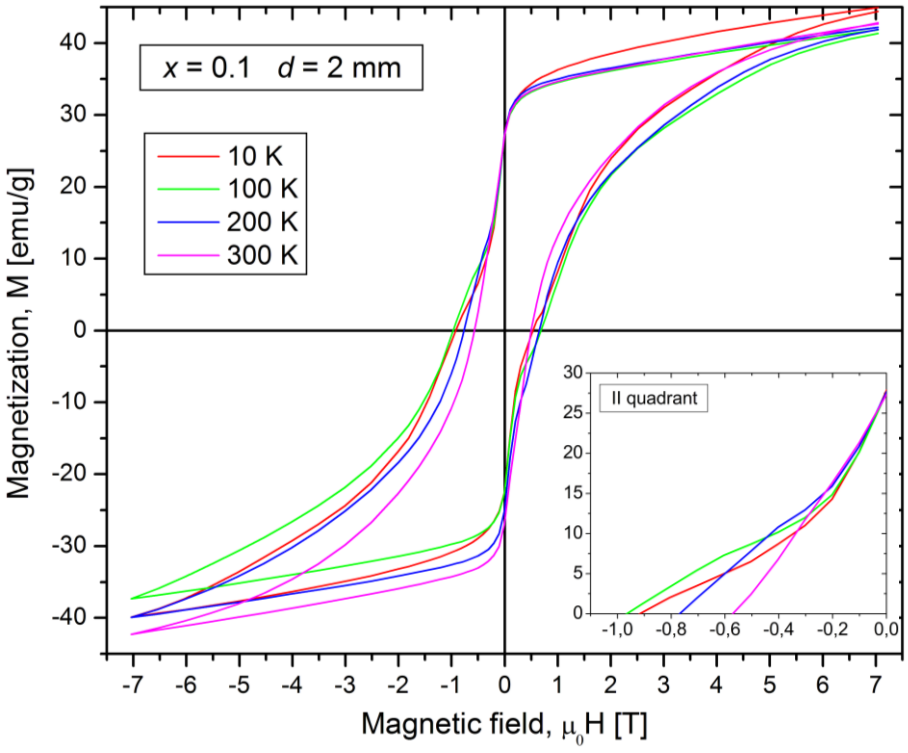


Figure 5.20. The magnetic hysteresis loops of the $(Fe_{80}Nb_6B_{14})_{0.9}Tb_{0.1}$ alloy prepared by using the mold with 2 mm in diameter, presented for different measurement temperature.

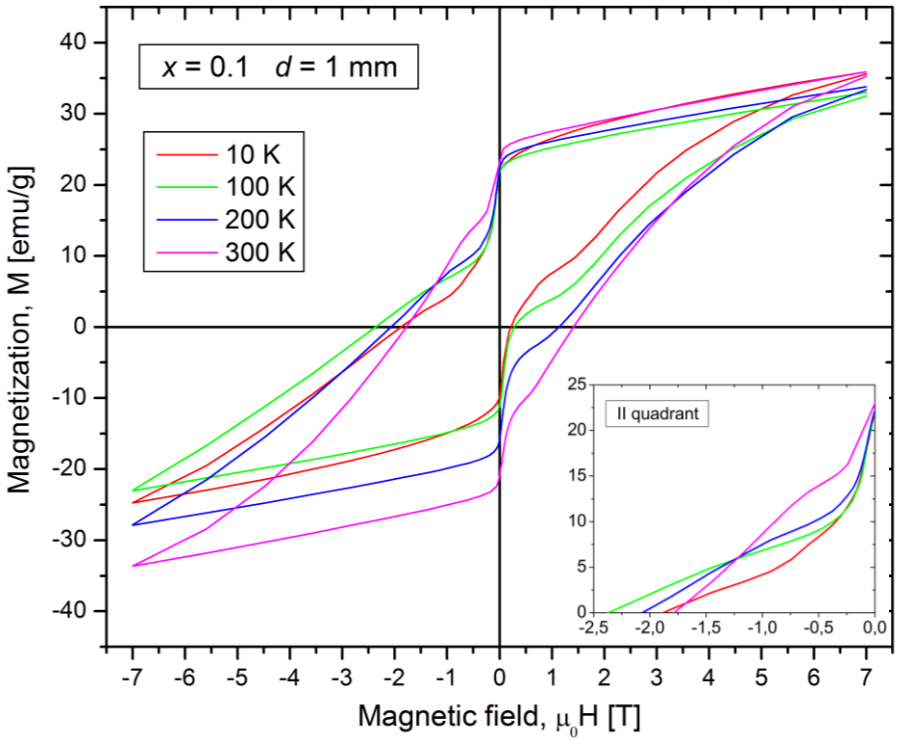


Figure 5.21. The magnetic hysteresis loops of the $(Fe_{80}Nb_6B_{14})_{0.9}Tb_{0.1}$ alloy prepared by using the mold with 1 mm in diameter, presented for different measurement temperature.

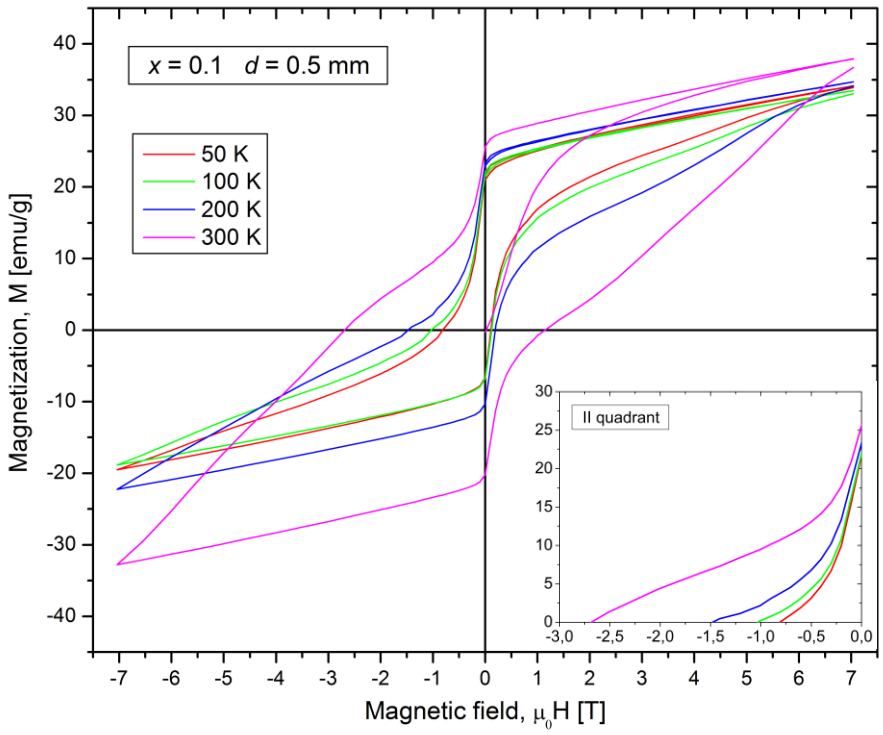


Figure 5.22. The magnetic hysteresis loops of the $(Fe_{80}Nb_6B_{14})_{0.9}Tb_{0.1}$ alloy prepared by using the mold with 0.5 mm in diameter, presented for different measurement temperature.

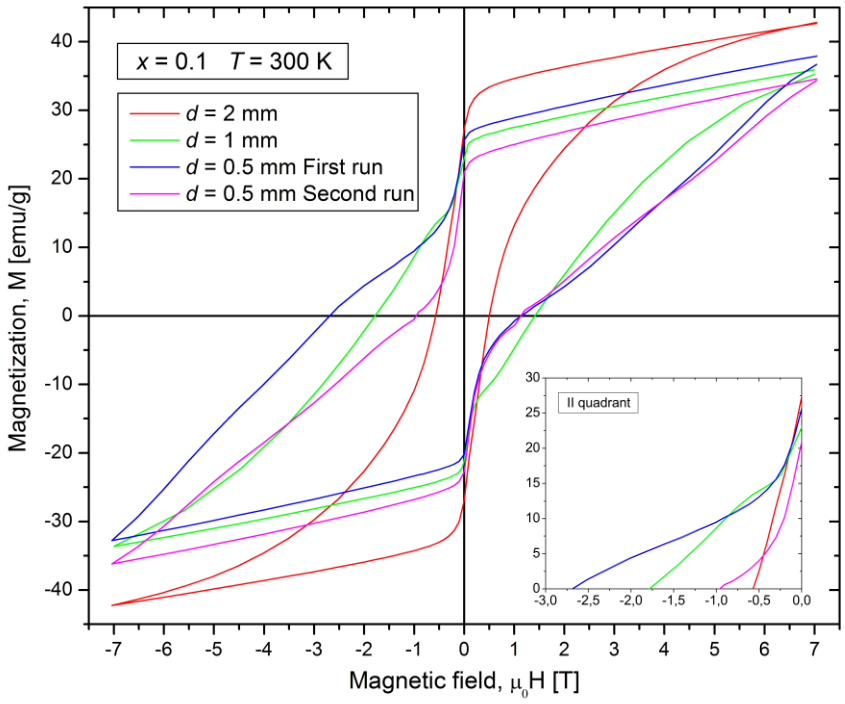


Figure 5.23. The comparison of magnetic hysteresis loops for the $(Fe_{80}Nb_6B_{14})_{0.9}Tb_{0.1}$ alloys with different diameter of sample measured at room temperature as well as first and second run for d = 0.5 mm.

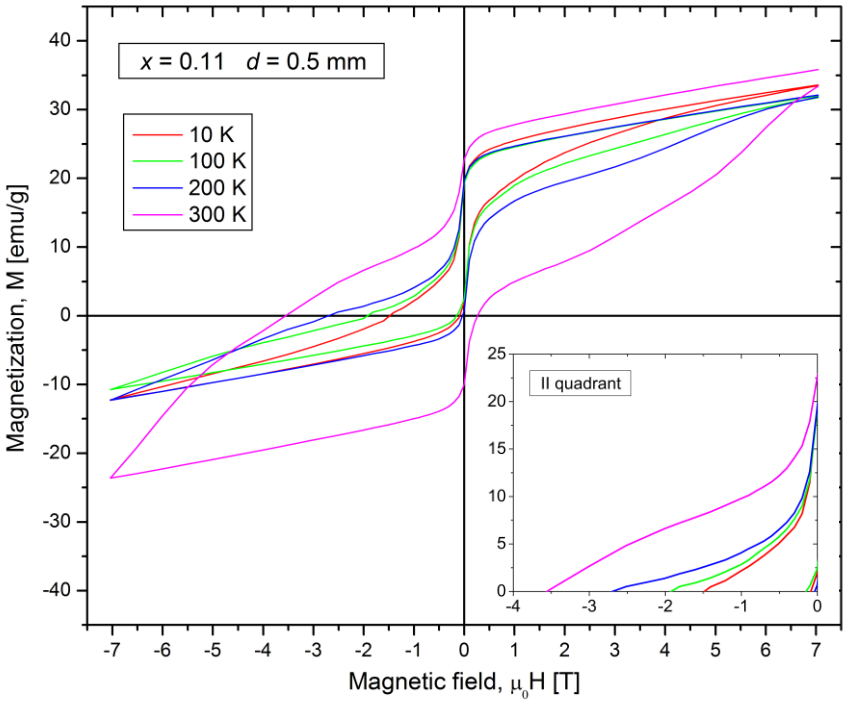


Figure 5.24. The magnetic hysteresis loops of the $(Fe_{80}Nb_6B_{14})_{0.89}Tb_{0.11}$ alloy prepared by using the mold with 0.5 mm in diameter, presented for different measurement temperature.

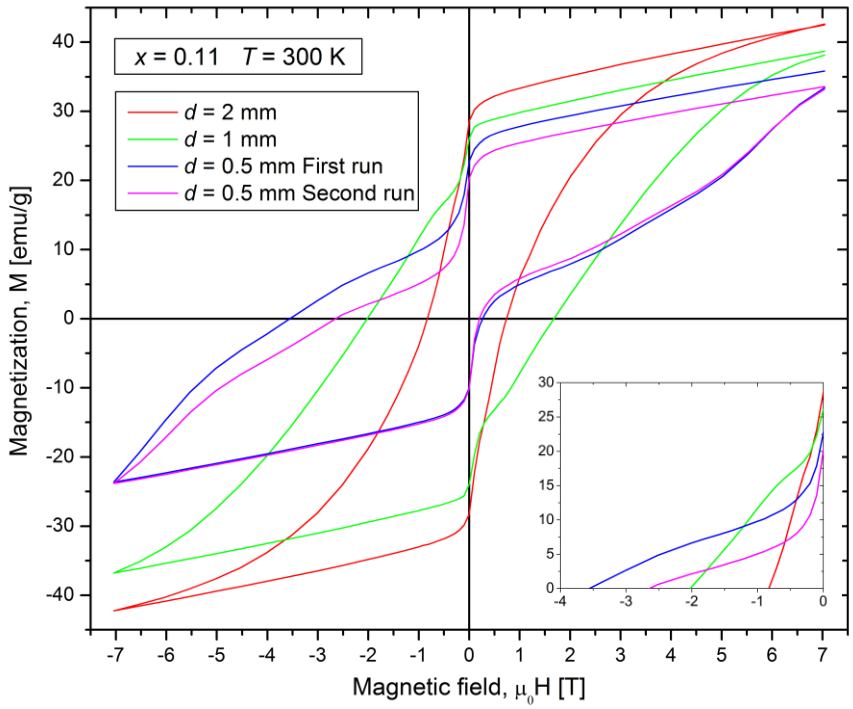


Figure 5.25. The comparison of magnetic hysteresis loops for the $(Fe_{80}Nb_6B_{14})_{0.89}Tb_{0.11}$ alloys with different diameter of sample measured at room temperature as well as first and second run for *d* = 0.5 mm.

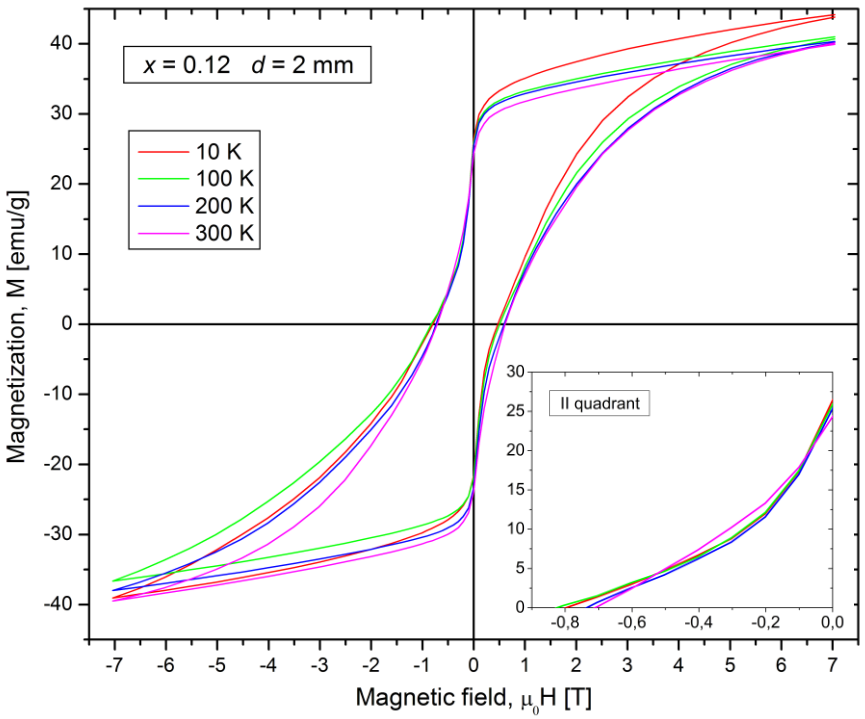


Figure 5.26. The magnetic hysteresis loops of the $(Fe_{80}Nb_6B_{14})_{0.88}Tb_{0.12}$ alloy prepared by using the mold with 2 mm in diameter, presented for different measurement temperature.

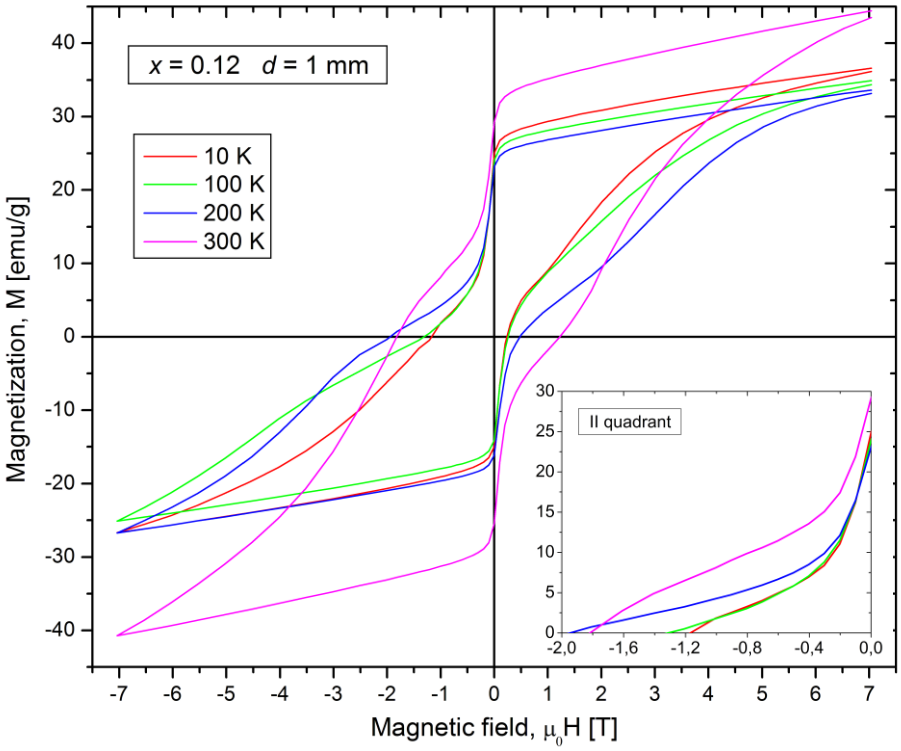


Figure 5.27. The magnetic hysteresis loops of the $(Fe_{80}Nb_6B_{14})_{0.88}Tb_{0.12}$ alloy prepared by using the mold with 1 mm in diameter, presented for different measurement temperature.

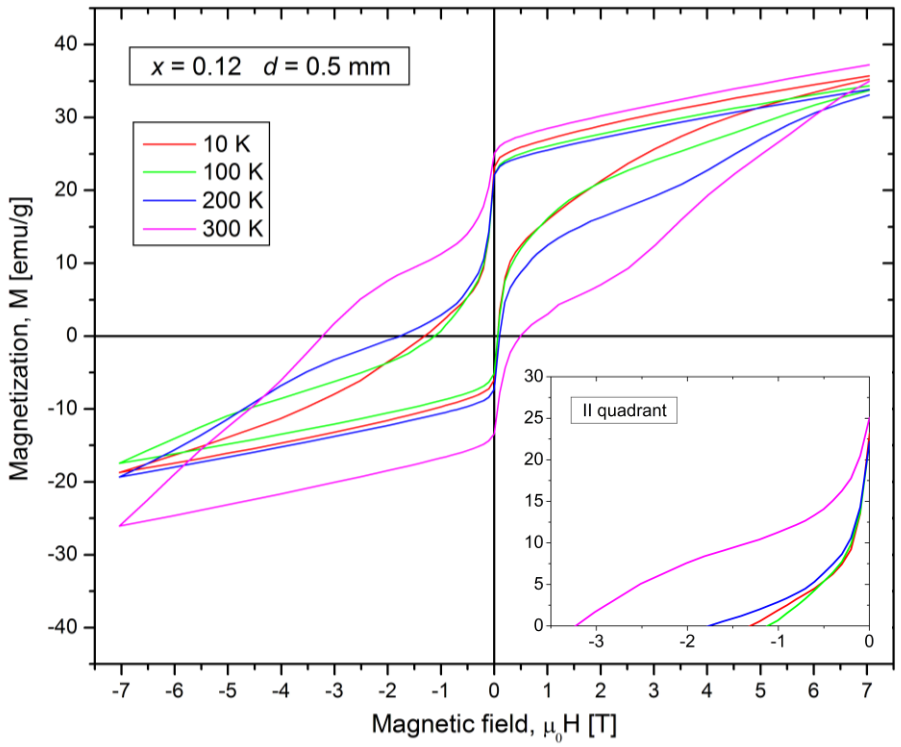


Figure 5.28. The magnetic hysteresis loops of the $(Fe_{80}Nb_6B_{14})_{0.88}Tb_{0.12}$ alloy prepared by using the mold with 0.5 mm in diameter, presented for different measurement temperature.

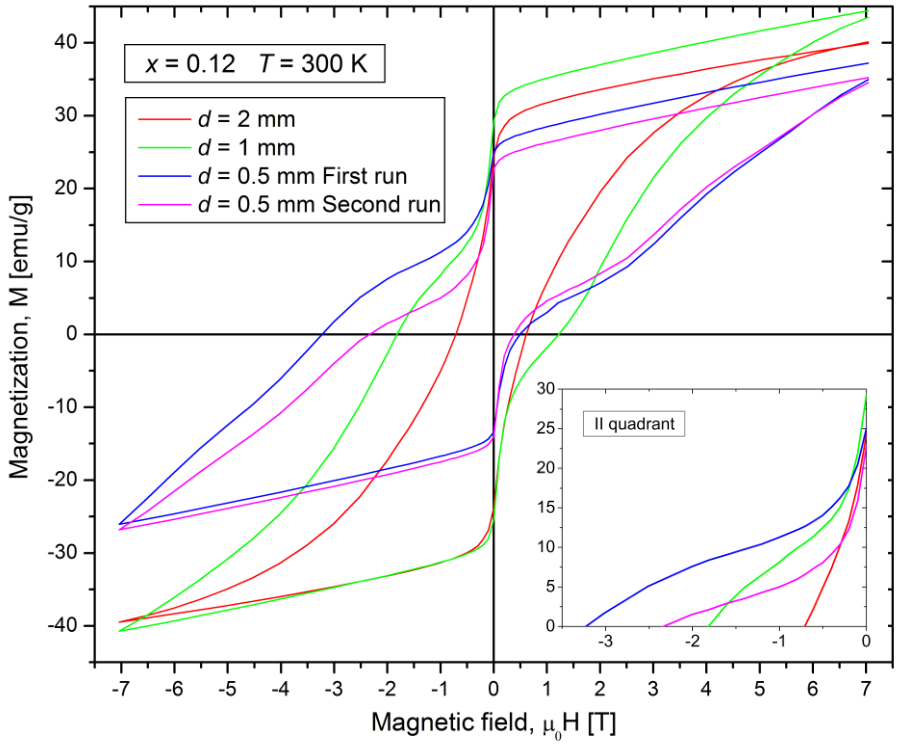


Figure 5.29. The comparison of magnetic hysteresis loops for the $(Fe_{80}Nb_6B_{14})_{0.88}Tb_{0.12}$ alloys with different diameter of sample measured at room temperature as well as first and second run for $d$ = 0.5 mm.

Based on the hysteresis loops the magnetic properties like coercivity field $H_C$, magnetic saturation determined at +7 T of magnetic field and $|JH|_{max}$ as well as $|BH|_{max}$ were estimated. One may note that for all exanimated cases (excluding the smallest Tb content, $x$ = 0.06) the hysteresis are asymmetric and shifted to the top of coordinate system which leads to non-equal coercivity $H_{C+}$ and $H_{C-}$ determined in I and II quadrant, respectively. Both of them, as well as other parameters were reported in Table 5.6.

Table 5.6. Room temperature values of saturation magnetization $M_S$, coercive field $H_C$ (determined in both quadrant), and maximal energy product $|BH|_{max}$ as well as $|JH|_{max}$ for the all studied alloys. The measurement errors are in the level of the least significant digit.

| **Alloy** | **Magnetic parameters at $T$ = 300 K** | | | | | |
|---|---|---|---|---|---|---|
| $x$ | $d$ [mm] | $M_S$ [emu/g] | $\mu_0 H_{C-}$ [T] | $\mu_0 H_{C+}$ [T] | $\|JH\|_{max}$ [kJ/m$^3$] | $\|BH\|_{max}$ [kJ/m$^3$] |
| **0.06** | 0.5 | 65.8 | 0.05 | 0.05 | - | - |
| | 1 | 82.4 | 0.07 | 0.07 | - | - |
| **0.08** | 0.5 | 44.2 | 2.46 | 1.21 | 77.2 | 7.5 |
| | 1 | 52.5 | 0.62 | 0.57 | 27.4 | 7.9 |
| **0.1** | 0.5 | 38.1 | 2.66 | 1.14 | 82.6 | 9 |
| | 1 | 36.0 | 1.79 | 1.42 | 71.2 | 9 |
| | 2 | 43.0 | 0.57 | 0.49 | 28.7 | 9.5 |
| **0.11** | 0.5 | 35.9 | 3.56 | 0.27 | 106 | 8.1 |
| | 1 | 38.7 | 2.02 | 1.68 | 91.5 | 10 |
| | 2 | 42.5 | 0.82 | 0.73 | 43 | 10.6 |
| **0.12** | 0.5 | 37.6 | 3.36 | 0.5 | 121 | 9 |
| | 1 | 40.2 | 1.82 | 1.20 | 65.3 | 10.2 |
| | 2 | 44.5 | 0.72 | 0.6 | 24.8 | 8 |

The highest coercivity corresponds to $x$ = 0.11, while for 6 at. % of Tb content any improvement of hard magnetic properties was not observed. Moreover, for all cases (excluding $x$ = 0.06) a significant magnetic hardening (an increase in coercive field) and a slight decrease in saturation magnetization (when $d$ decreases) were observed. In case of $x$ = 0.11, during changing diameter from 2 mm to 0.5 mm, the $H_C$ and $|JH|_{max}$ increases from 0.82 T to 3.56 T and 43 kJ/m$^3$ up to 106 kJ/m$^3$, respectively. It should be noted that for alloys with $d$ = 0.5 mm, the first and the second run at room temperature are not equal. It seems that it is caused by blocking effects of some extremely hard magnetic object that do not directly contribute to magnetization process but can influence the rest of volume of the alloy.

The magnetic domain observations were performed by MFM system. In this case, a value and direction of magnetic force between sample surface and microscope tip is measured. Obtained results are presented in a form of color map, where red and blue color corresponds to the attractive and repulsive force, respectively. Figure 5.30 and Figure 5.31 presents a surface observations of domain structure for the $(Fe_{80}Nb_6B_{14})_{0.88}Tb_{0.12}$ alloys prepared using the three different sample diameters $d$ = 2 mm, 1 mm and 0.5 mm. Similarly to the SEM observations, in all cases one may see non regular micro-metric domain structures. Moreover, the average size of the magnetic domain depends on applied cooling rates (i.e. sample diameters). Generally, the lowest sample diameter the smaller size of the magnetic domains. One may notice that in case of the alloy with $d$ = 0.5 mm some nano-metric domains (about 500 nm in size) were also observed, which is in a good agreement with the SEM images.

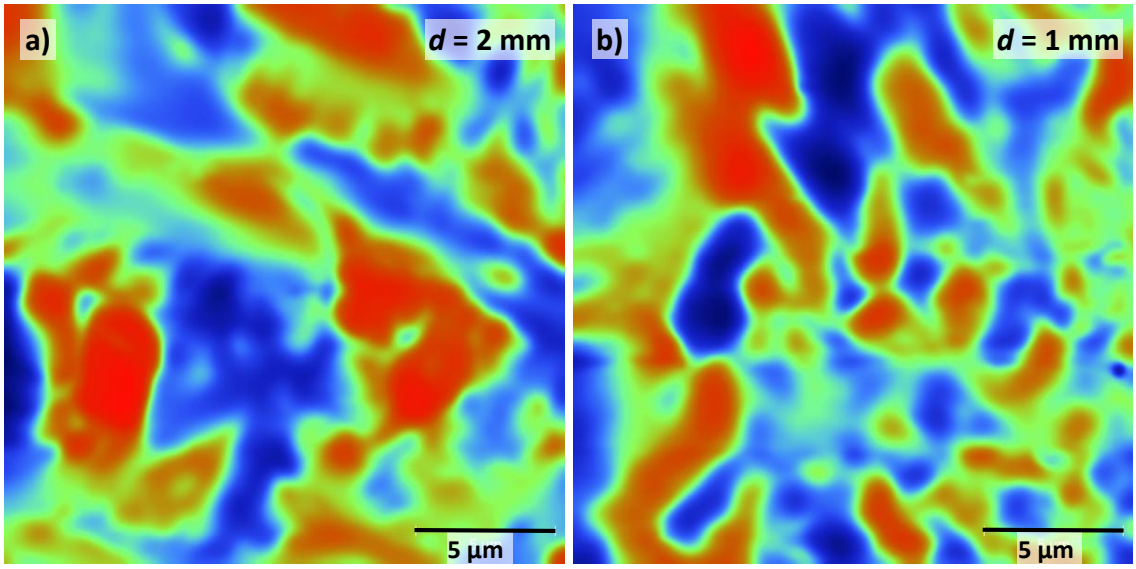


Figure 5.30. MFM magnetic domain observations for $(Fe_{80}Nb_6B_{14})_{0.88}Tb_{0.12}$ alloys with sample diameter equals 2 mm (a) and 1 mm (b). Color correspond to magnetization direction.

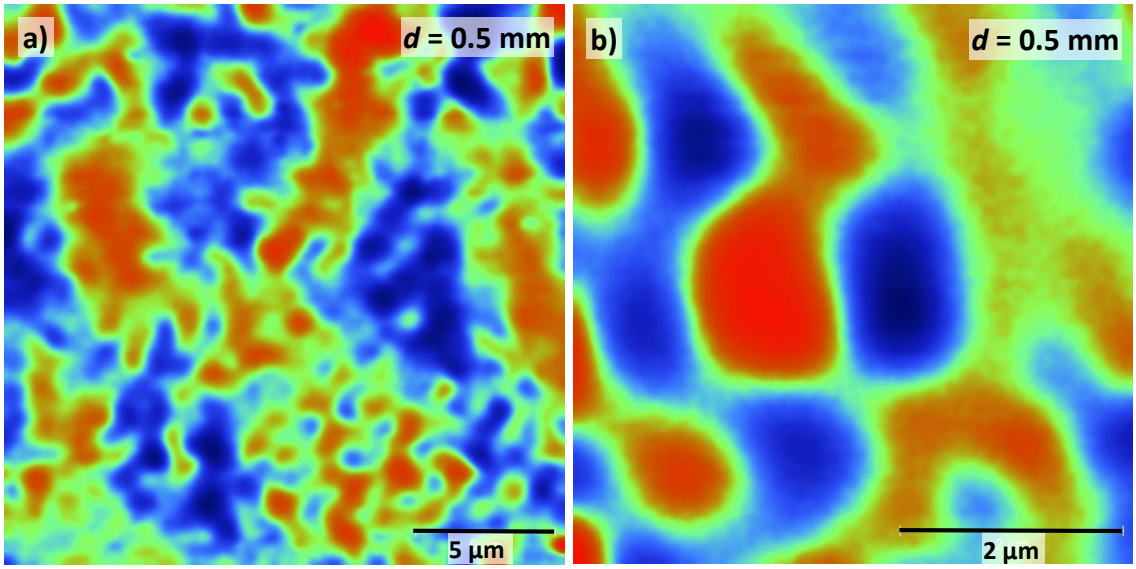


Figure 5.31. MFM magnetic domain observation for the $(Fe_{80}Nb_6B_{14})_{0.88}Tb_{0.12}$ alloys with 0.5 mm in diameter (a) and magnification of selected area in more fine-scale (b).

The magneto-optic Kerr microscopy allows observing magnetic domains and their magnetization processes in micro scale. Such investigations were carried out for all discussed alloys with 12 at.% of Tb content. However, this materials exhibit very hard magnetic properties and the applied magnetic field (approximately ± 1 T) is not high enough to saturate the sample. Therefore, only a part of sample volume are magnetically reversed during switching external magnetic field (from plus 1 T to minus 1 T) and optically, change its colour from black to white as presented in Figure 5.32 and Figure 5.33 (marked by the red circle) for two different areas. Moreover, some special software was created and differential computing analyses were performed in order to extract the parts of structure which reverse the magnetisation direction. The result of such test is shown in Figure 5.34.

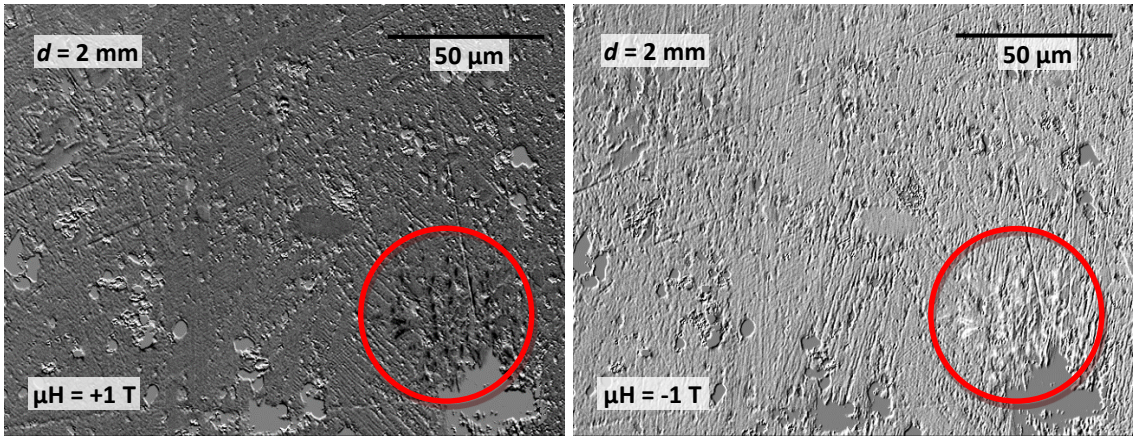


Figure 5.32. Kerr microscopy images obtained for selected area of $(Fe_{80}Nb_6B_{14})_{0.88}Tb_{0.12}$ alloy with 2 mm in diameter. Left and right pictures were captured in +1 T and -1 T of allayed magnetic field, respectively. In red circle one may see a switched domains.

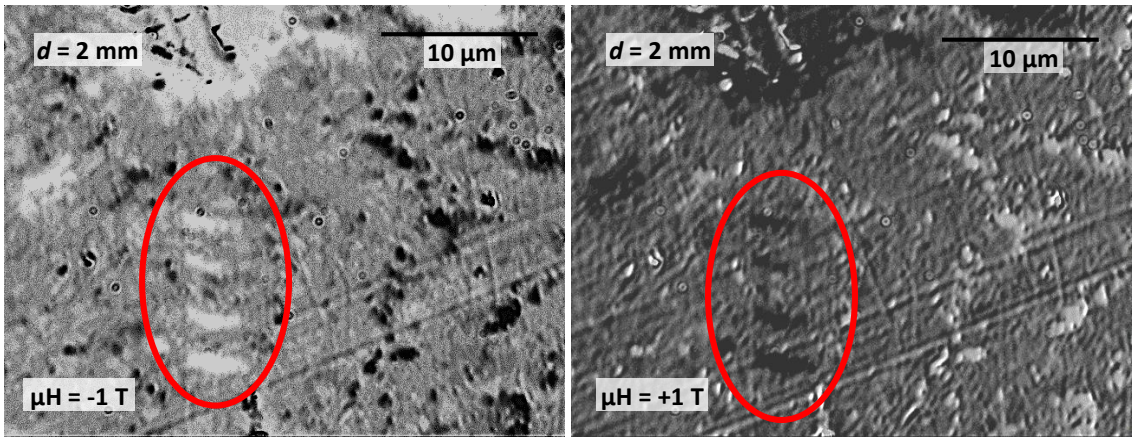


Figure 5.33. Another example of the magneto-optic Kerr microscopy images cared out for $(Fe_{80}Nb_6B_{14})_{0.88}Tb_{0.12}$ alloy with 2 mm in diameter.

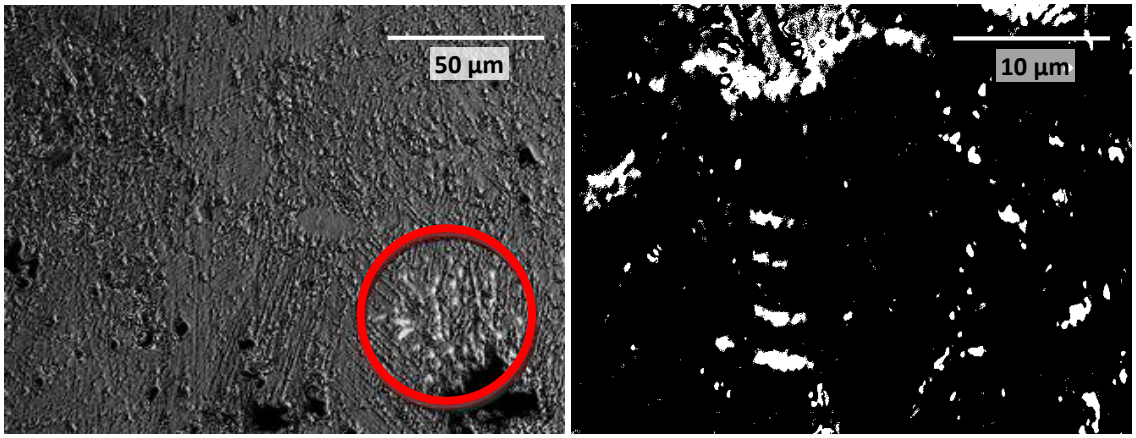


Figure 5.34. The parts of materials (white color) which changes magnetization direction during experiment, extracted by computer analysis. Left and right figure corresponds to the situations presented on Figure 5.32 and Figure 5.33, respectively.

## 5.3. Phase stability of $(Fe_{80}Nb_6B_{14})_{0.9}Tb_{0.1}$ alloys

It is a characteristic that nanocrystalline alloys are not thermodynamically stable and, during annealing, some phase transitions (or separations) are expected to be present [98]. Therefore, phase stability studies are important from scientific as well as application point of view. The chemical composition $(Fe_{80}Nb_6B_{14})_{0.9}Tb_{0.1}$ was chosen as a base for thermodynamic investigations and, for this purpose, series of samples using 4 different molds with $d$ = 2 mm, 1.5 mm, 1 mm and 0.5 mm were prepared. Phase stability was studied by means of the DSC technique (heating up to 900 K with a rate of 20 K/min). Changes in structural and magnetic properties, before and after heating in the DSC apparatus, were also determined.

Figure 5.35 presents the DSC results for four different diameters of sample. Generally, first part of the curves may be related to the structural relaxation, while after that some thermal effects corresponds to magnetic and structural transition are expected.

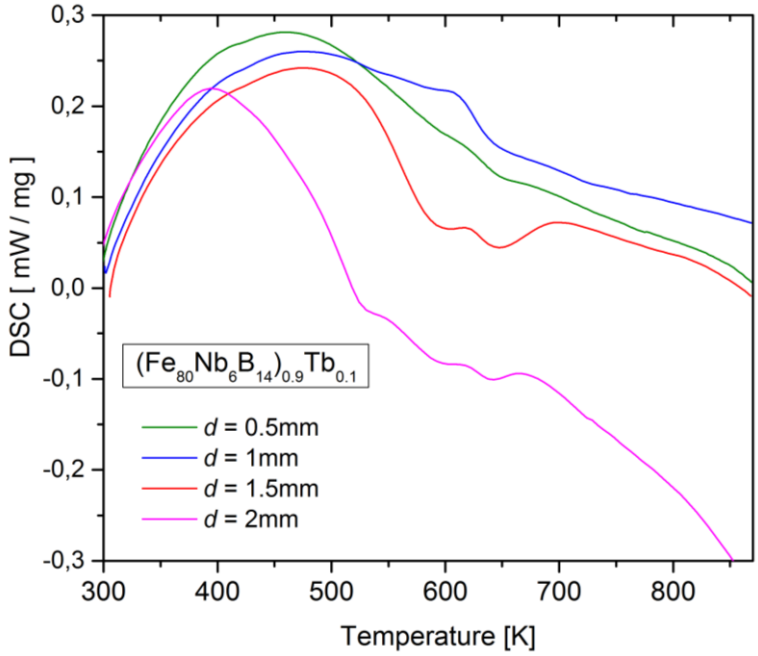


Figure 5.35. DSC curves obtained for different diameter of the $(Fe_{80}Nb_6B_{14})_{0.9}Tb_{0.1}$ alloys.

The comparison of $^{57}$Fe Mössbauer spectra before and after heating in case of alloys with $d$ = 1.5 mm is shown in Figure 5.36. Each spectrum were deconvoluted for series of Zeeman sextets by a least-square fit procedure and divided by identified phases. More

precision description including mean values of Mössbauer parameters attributed to individual phases as well as their contribution in materials in as-cast state and after heat treatment is summarized in Table 5.7 and Table 5.8, respectively. One may note that except the alloy with 1 mm in diameter, an increase of $Fe_{\alpha}$ and decrease of $Tb_2Fe_{14}B$ were detected.

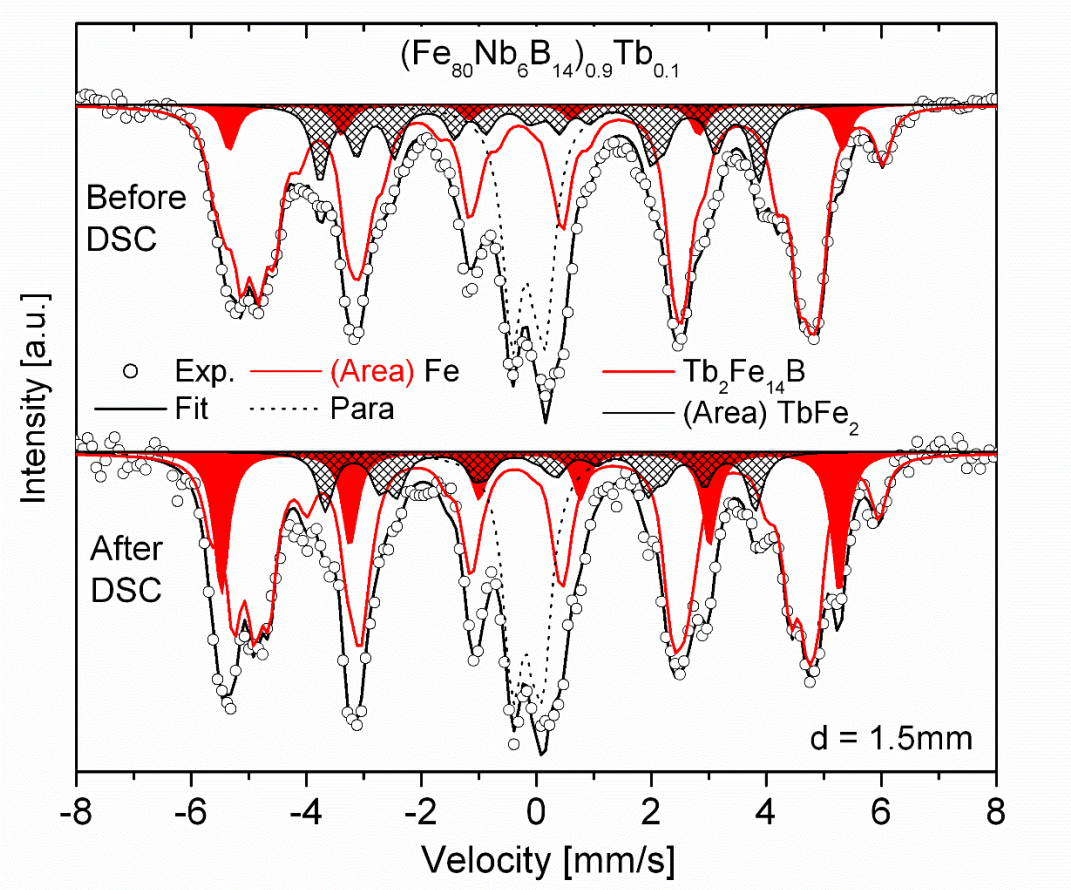


Figure 5.36. The $^{57}Fe$ Mössbauer spectra before (on the top) and after (on the bottom) heating up 900 K of the $(Fe_{80}Nb_6B_{14})_{0.9}Tb_{0.1}$ alloy with $d$ = 1.5 mm, with separation to identified pahses.

Table 5.7. Mean values of Isomer shifts (IS), Quadripole shifting (2ε) and Hyperfine field ($B_{hf}$) as well as phase contents, for each phases based on the $^{57}$Fe Mössbauer measurements for the $(Fe_{80}Nb_6B_{14})_{0.9}Tb_{0.1}$ alloy with $d$ = 0.5 - 2 mm in as-cast state.

| d | $Tb_2Fe_{14}B$ | | | | α-Fe | | | | $TbF_2$ | | | | $Tb_{1.1}Fe_4B_4$ | | | |
|---|---|---|---|---|---|---|---|---|---|---|---|---|---|---|---|---|
| | [%] ±2 | <$B_{hf}$> ±0.02 | <IS> ±0.01 | <2ε> ±0.01 | [%] ±2 | <$B_{hf}$> ±0.02 | <IS> ±0.01 | <2ε> ±0.01 | [%] ±2 | <$B_{hf}$> ±0.02 | <IS> ±0.01 | <2ε> ±0.01 | [%] ±2 | <$B_{hf}$> ±0.02 | <IS> ±0.01 | <QS> ±0.01 |
| 0.5 | **75** | 296 | -0.22 | 0.21 | | | | | **9** | 205 | -0.31 | -0.02 | **16** | 0 | -0.15 | 0.49 |
| 1 | **65** | 293 | -0.22 | 0.27 | | | | | **15** | 200 | 0.1 | 0.12 | **14** | 0 | -0.16 | 0.54 |
| 1.5 | **62** | 303 | -0.21 | 0.21 | **6** | 329 | -0.14 | 0.27 | **15** | 219 | 0.02 | 0.03 | **17** | 0 | -0.14 | 0.48 |
| 2 | **64** | 304 | -0.23 | 0.26 | | | | | **18** | 204 | 0.05 | 0.09 | **18** | 0 | -0.15 | 0.49 |

Table 5.8. The mean value of Mössbauer parameters (IS, 2ε, $B_{hf}$) and phase contributions in case of the $(Fe_{80}Nb_6B_{14})_{0.9}Tb_{0.1}$ alloy with $d$ = 0.5 - 2 mm, after heating up 900 K.

| d | $Tb_2Fe_{14}B$ | | | | α-Fe | | | | $TbFe_2$ | | | | $Tb_{1.1}Fe_4B_4$ | | | |
|---|---|---|---|---|---|---|---|---|---|---|---|---|---|---|---|---|
| | [%] ±2 | <$B_{hf}$> ±0.02 | <IS> ±0.01 | <2ε> ±0.01 | [%] ±2 | <$B_{hf}$> ±0.02 | <IS> ±0.01 | <2ε> ±0.01 | [%] ±2 | <$B_{hf}$> ±0.02 | <IS> ±0.01 | <2ε> ±0.01 | [%] ±2 | <$B_{hf}$> ±0.02 | <IS> ±0.01 | <QS> ±0.01 |
| 0.5 | **17** | 277 | -0.16 | -0.14 | **53** | 329 | -0.14 | 0.01 | **14** | 194 | -0.13 | -0.13 | **16** | 0 | -0.12 | 0.57 |
| 1 | **69** | 296 | -0.19 | 0.27 | | | | | **16** | 205 | 0.12 | 0.31 | **15** | 0 | -0.15 | 0.45 |
| 1.5 | **56** | 303 | -0.25 | 0.23 | **17** | 331 | -0.11 | 0.01 | **11** | 209 | 0.07 | 0.03 | **16** | 0 | -0.15 | 0.43 |
| 2 | **56** | 300 | -0.15 | 0.31 | **17** | 324 | -0.17 | -0.11 | **11** | 206 | 0.09 | 0.15 | **16** | 0 | -0.17 | 0.47 |

An example of the DSC curve in a comparison with thermomagnetic measurements for $d$ = 1.5 mm is presented in Figure 5.37. The $M(T)$ curve clearly indicates the Curie temperature $T_c$ is attributed to the $Tb_2Fe_{14}B$ phase. Moreover, the structural changes above 680 K (increase of M) related to a formation of a magnetic phase with higher $T_c$, is also detected. In an agreement to that, the DSC curve reveals two exothermal peaks which can be attributed to the magnetic transition and phase transition or changes. The alloys with other diameters exhibited similar behavior.

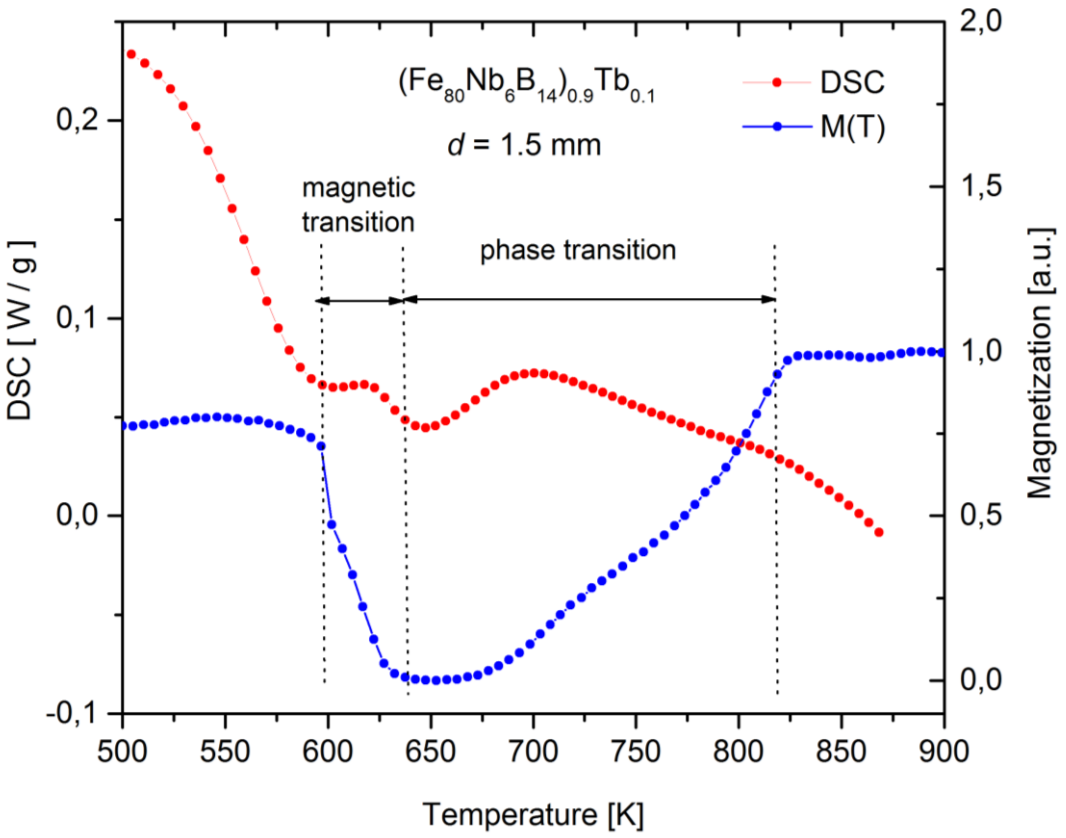


Figure 5.37. Comparison of differential scanning calorimetric and magnetic balance curves for the $(Fe_{80}Nb_6B_{14})_{0.9}Tb_{0.1}$ alloy with d = 1.5 mm [99].

The changes, occurring during heating in the DSC experiment, have an influence on magnetic properties. For each tested samples magnetic characterization was performed on their two states: as-cast and after heating up to 900 K. The magnetic hysteresis loops for alloys with $d$ = 0.5, 1, 1.5 and 2 mm in diameter are presented in Figure 5.38, Figure 5.39, Figure 5.40 and Figure 5.41, respectively. As may expect a great hardening effect with the increase of cooling rate was observed. The coersivity increases form 0.57 T in case of $d$ = 2 mm up to 2.66 T when $d$ = 0.5 mm. Moreover, all examined samples changes magnetic properties according to the applied heating. A significant transformation of $H_C$ from 2.66 T to 0.005 T and $M_S$ from 38 emu/g to 100 emu/g, due to conversion of hard magnetic phase to $Fe_\alpha$, one can note for the sample with $d$ = 0.5 mm.

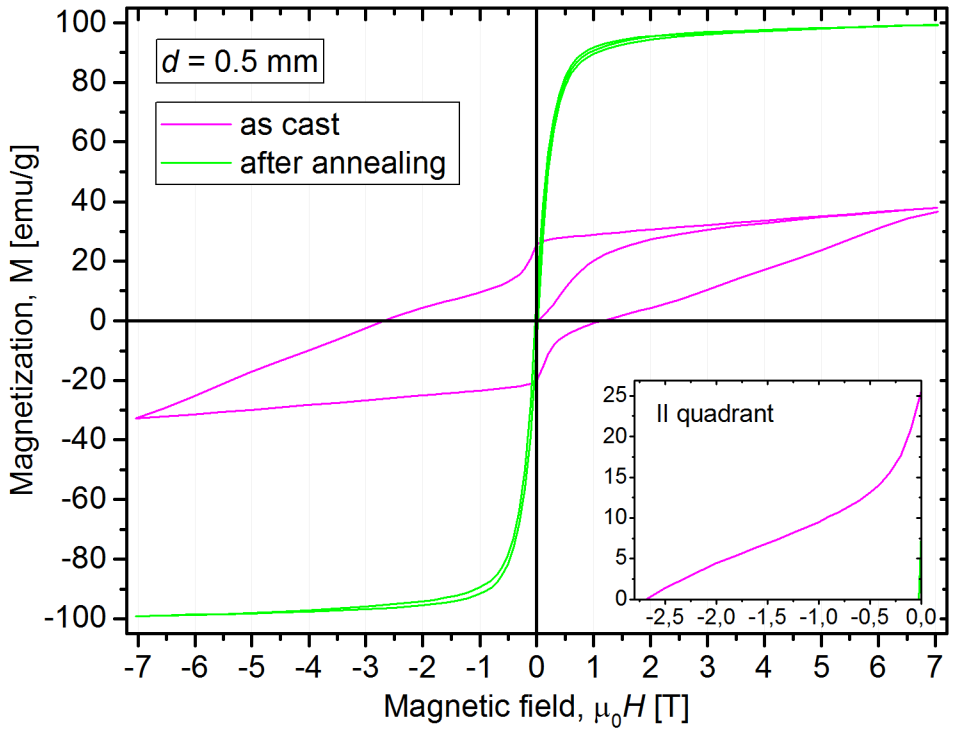


Figure 5.38. The magnetic hysteresis loops of the $(Fe_{80}Nb_6B_{14})_{0.9}Tb_{0.1}$ alloy prepared by using the mold with 0.5 mm in diameter, before and after heating up 900 K.

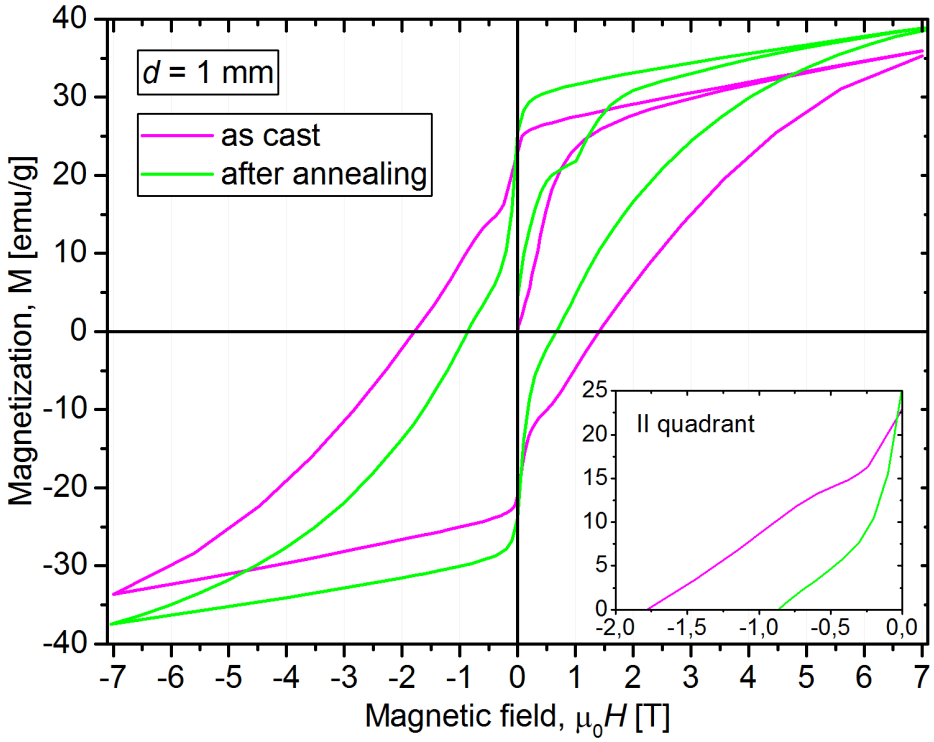


Figure 5.39. The magnetic hysteresis loops of the $(Fe_{80}Nb_6B_{14})_{0.88}Tb_{0.12}$ alloy prepared by using the mold with 1 mm in diameter, before and after heating up 900 K.

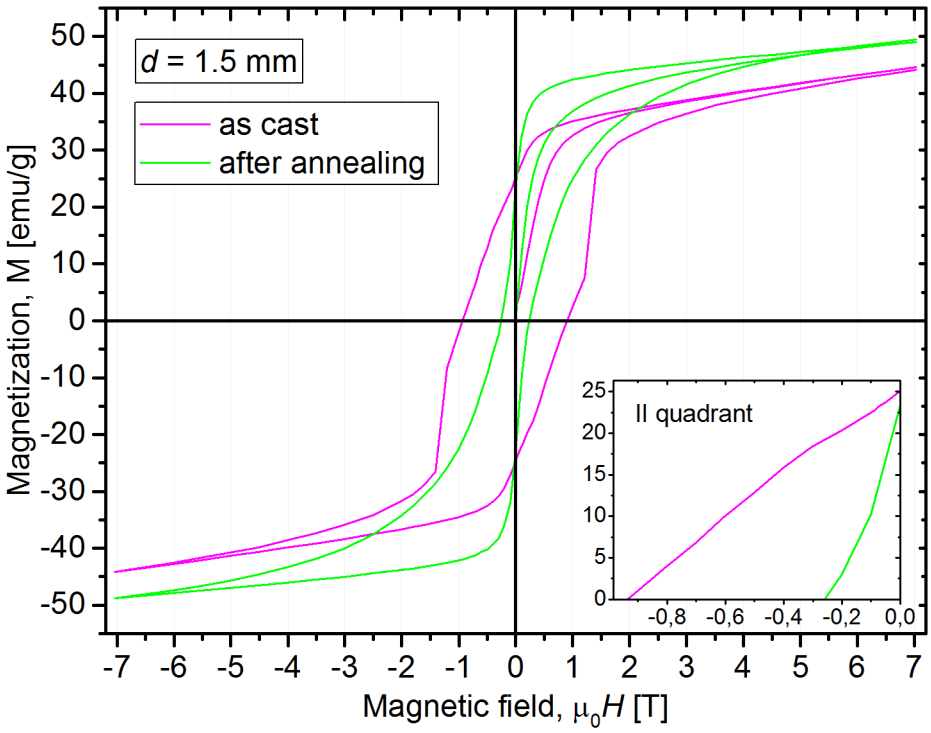


Figure 5.40. The magnetic hysteresis loops of the $(Fe_{80}Nb_6B_{14})_{0.88}Tb_{0.12}$ alloy prepared by using the mold with 1.5 mm in diameter, before and after heating up 900 K.

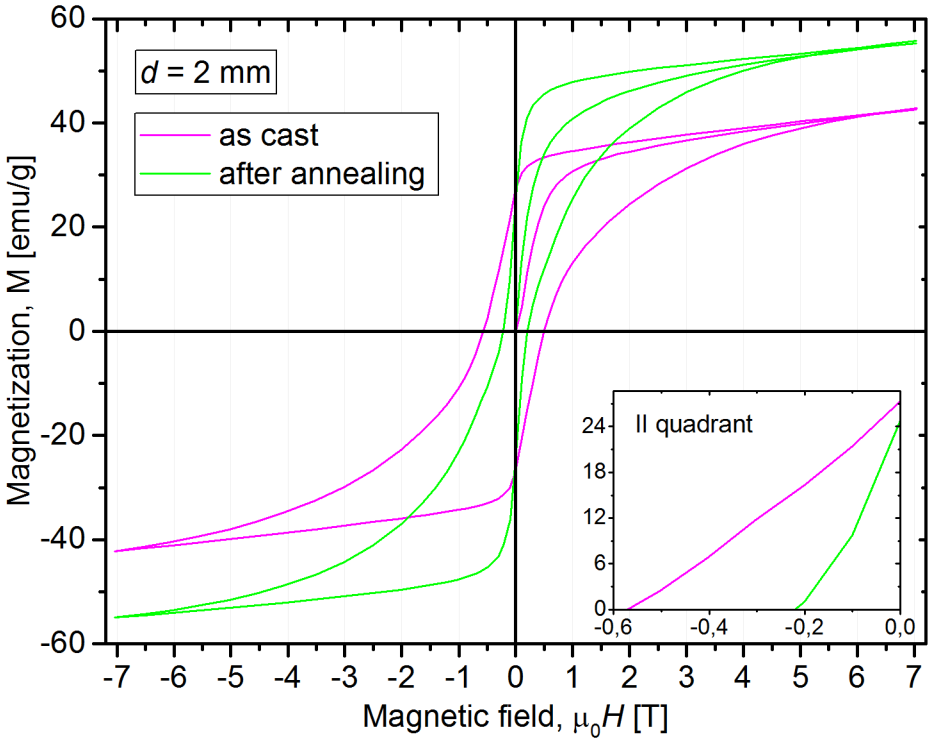


Figure 5.41. The magnetic hysteresis loops of the $(Fe_{80}Nb_6B_{14})_{0.88}Tb_{0.12}$ alloy prepared by using the mold with 2 mm in diameter, before and after heating up 900 K.

## 5.4. Effect of milling on structural and magnetic properties of $(Fe_{80}Nb_6B_{14})_{1-x}Tb_x$ alloys

Despite the fact that bulk materials have some advantages, for many application a powder or nano-powder form is preferred. However, pulverization of bulks can cause different effects due to structure deformation, decrease of crystallite size, breaking direct magnetic interaction or even phase changes. Therefore, investigations of influence of milling on the magnetic properties are important from application as well as scientific pint of view.

In this section the magnetic and structural changes under the milling process are presented. For this purpose, the $(Fe_{80}Nb_6B_{14})_{0.88}Tb_{0.12}$ and $(Fe_{80}Nb_6B_{14})_{0.92}Tb_{0.08}$ alloys with 1.5 mm in diameter were taken into account. The first one was chosen due to its optimal magnetic properties, while the second one contains lower amount of Tb which has an economical meaning. The bulk alloys were pulverized by means of the low energy grinder (one agate ball with diameter equal to 3cm). The milling process was carried out for 24h in liquid DMF (Dimetyloformamid) to prevent the oxidation.

The structural studies were carried out by X-ray diffraction technique and the results are shown in Figure 5.42 and Figure 5.43 for $x = 0.08$ and $x = 0.12$, respectively. One may see the significant broadening of the Bragg's peaks in both cases which confirms a decrease of crystallite mean diameter $d$. The changes were from 28 nm to 13 nm in case of $(Fe_{80}Nb_6B_{14})_{0.92}Tb_{0.08}$ alloy and from 32 nm to 12 nm for the alloy with higher Tb concentration. Moreover, for the $(Fe_{80}Nb_6B_{14})_{0.92}Tb_{0.08}$ alloy, the phase composition is not so sensitive to the pulverization, while in the second case, a remarkable increase of $TbFe_2$ content was observed.

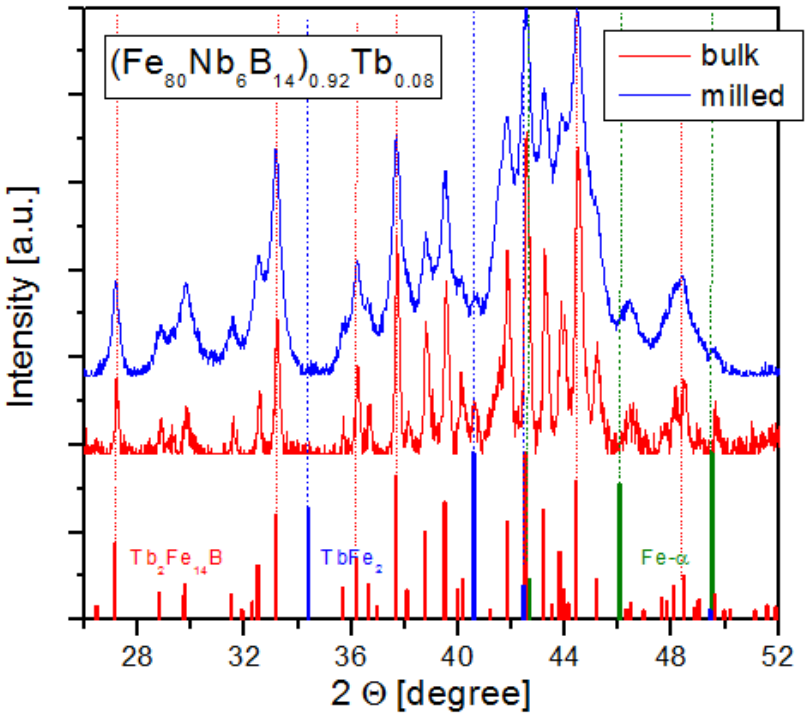


Figure 5.42. X-ray diffraction patterns measured for the $(Fe_{80}Nb_6B_{14})_{0.92}Tb_{0.08}$ alloy before and after milling.

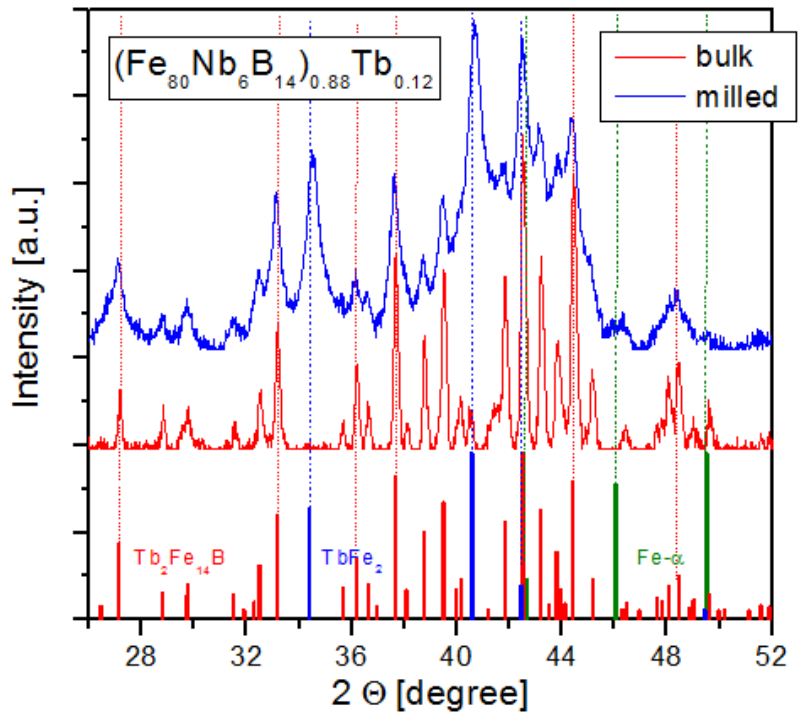


Figure 5.43. X-ray diffraction patterns measured for the $(Fe_{80}Nb_6B_{14})_{0.88}Tb_{0.12}$ alloy before and after milling.

Figure 5.44 and Figure 5.45 presents magnetic hysteresis loops of discussed materials for $x$ = 0.08 and $x$ = 0.12, respectively. In both cases magnetic properties were measured before and after milling as well as at high and low temperature. A significant decrease of coercive field during milling can be seen for $x$ = 0.12. In this case, $H_C$ is equal to 1.16 T and 0.36 T before and after pulverization (at room temperature). Such effect especially distinct at low temperature can be attributed to the observed decrease of $Tb_2Fe_{14}B$ content as well as to a breaking of direct inter-grains magnetic coupling (occurring in the bulks) that is a feature of non-sintered powder. In the case of the alloy with $x = 0.08$ at $T = 300$ K the shape of hysteresis loop is similar but in the case of milled sample remanent magnetization increases from 24 emu/g up to 40 emu/g. At low temperature a significant difference between hysteresis loops of bulk and milled alloys is observed. For the pulverized sample remanent magnetization is also high but coercive field $H_C$ and the area of the loops decreases.

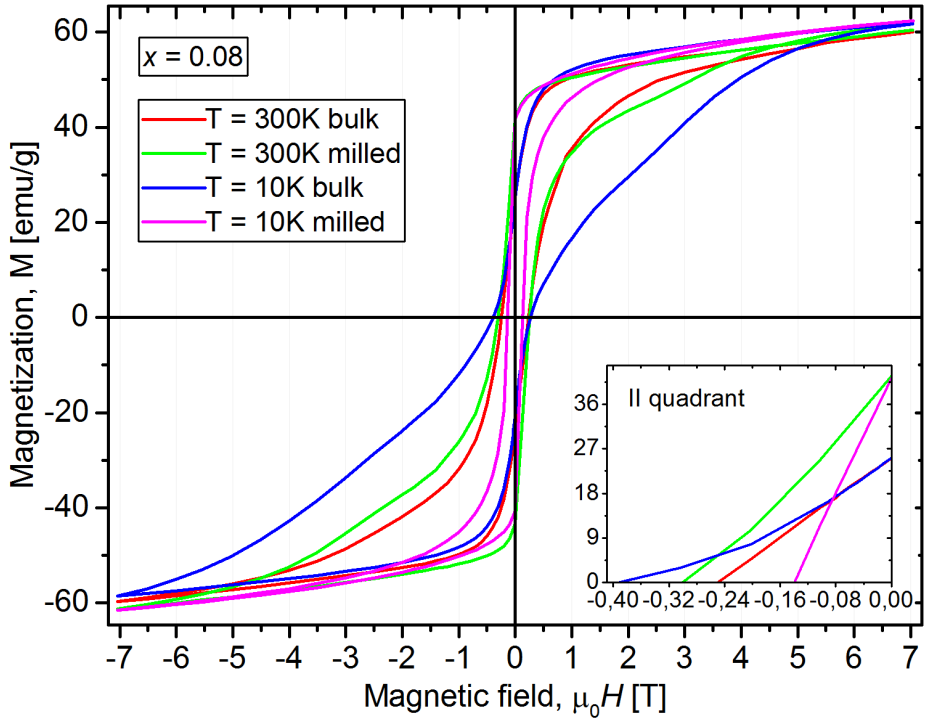


Figure 5.44. The magnetic hysteresis loops of the $(Fe_{80}Nb_6B_{14})_{0.92}Tb_{0.08}$ alloy prepared by using the mold with 1.5 mm in diameter, before and after milling.

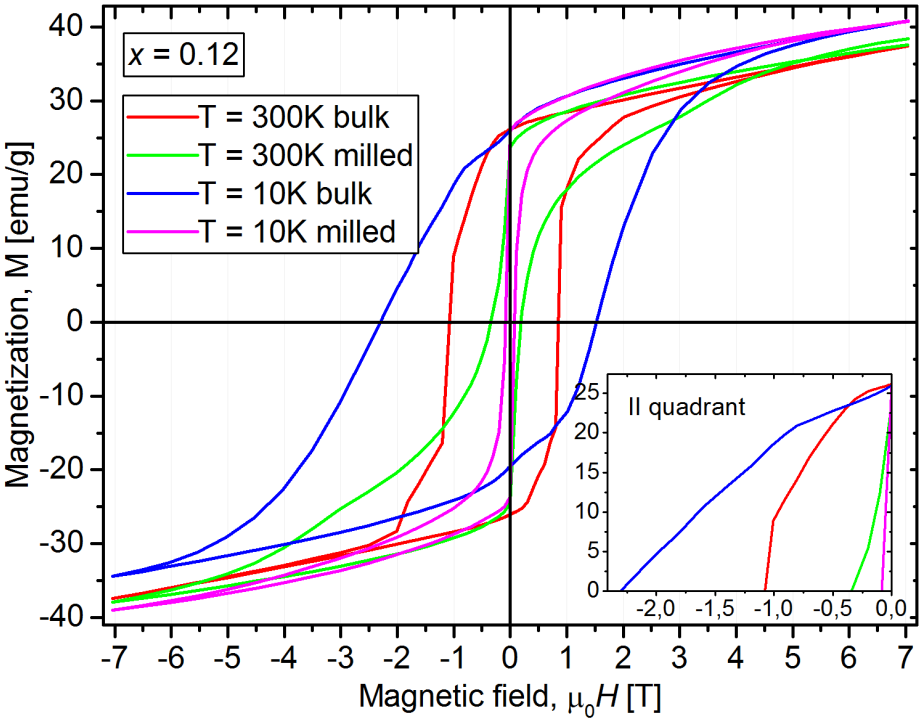


Figure 5.45. The magnetic hysteresis loops of the $(Fe_{80}Nb_6B_{14})_{0.88}Tb_{0.12}$ alloy prepared by using the mold with 1.5 mm in diameter, before and after milling.

## 5.5. Influence of alloying additions on selected properties of the Fe-Nb-B-X alloys.

Based on the preliminary studies, described in previous sections, the Terbium element was chosen as optimal rare earths addition, which provides extremely high coercivity. However, antiferromagnetic coupling between Tb and Fe leads to relatively low value of magnetic remanence and consequently low value of maximum energy product. In addition to that, due to high price of Terbium, any chipper replacement without degeneration of hard magnetic properties is desired. Therefore, a series of samples base on Fe-Nb-B-RE with different alloying addition like Er, Pr, Nd as well as Pt were prepared and investigated. Additionally, an influence of Boron and Niobium content on magnetic properties was also studied.

### 5.5.1. Influence of Er

Figure 5.46 presents magnetic hysteresis loops measured at room temperature for four alloys based on $(Fe_{80}Nb_6B_{14})_{1-x}Er_x$ with $x$ = 0.04, 0.08, 0.12 and 0.16. The materials were prepared using the form with 1.5mm in diameter. For all exanimated cases the coercivity is relatively low and rises up to 0.1 T for 16 at.% of Erbium addition. On the other hand, the magnetic saturation decreases from 100 emu/g to 20 emu/g for $x$ equal to 0.04 and 0.16, respectively.

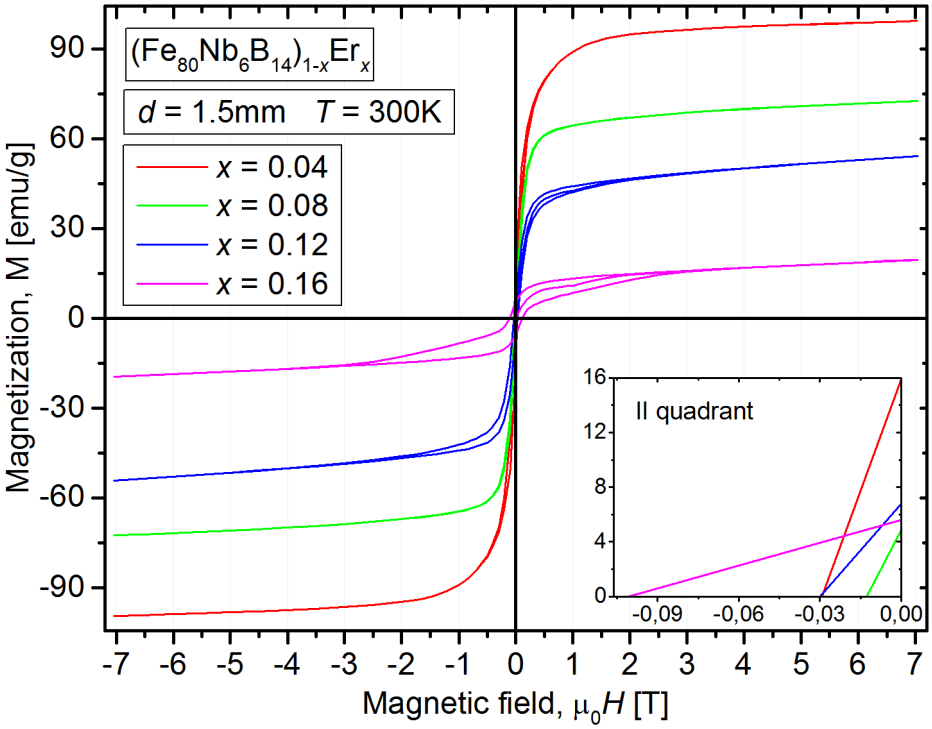


Figure 5.46. The magnetic hysteresis loops of the $(Fe_{80}Nb_6B_{14})_{1-x}Er_x$ alloys prepared by using the mold with 1.5 mm in diameter, measured at room temperature.

## 5.5.2. Influence of Pr

Magnetic properties of $(Fe_{80}Nb_6B_{14})_{0.88}Pr_{0.12}$ alloy, measured by the SQUID magnetometer, are presented in Figure 5.47. The measurements were carried out at different temperatures ranged from 10 K to 300 K. Moreover, the same chemical composition was used to obtain samples with two diameters: 1.5mm and 0.5mm. Magnetic hysteresis loops for these samples are compared in Figure 5.48. In both cases, the coercivity, remanence and magnetic saturation are equal to 0.1 T, about 30 emu/g and about 100 emu/g, respectively. Generally, any significant changes of magnetic properties in a function of sample diameter were not observed.

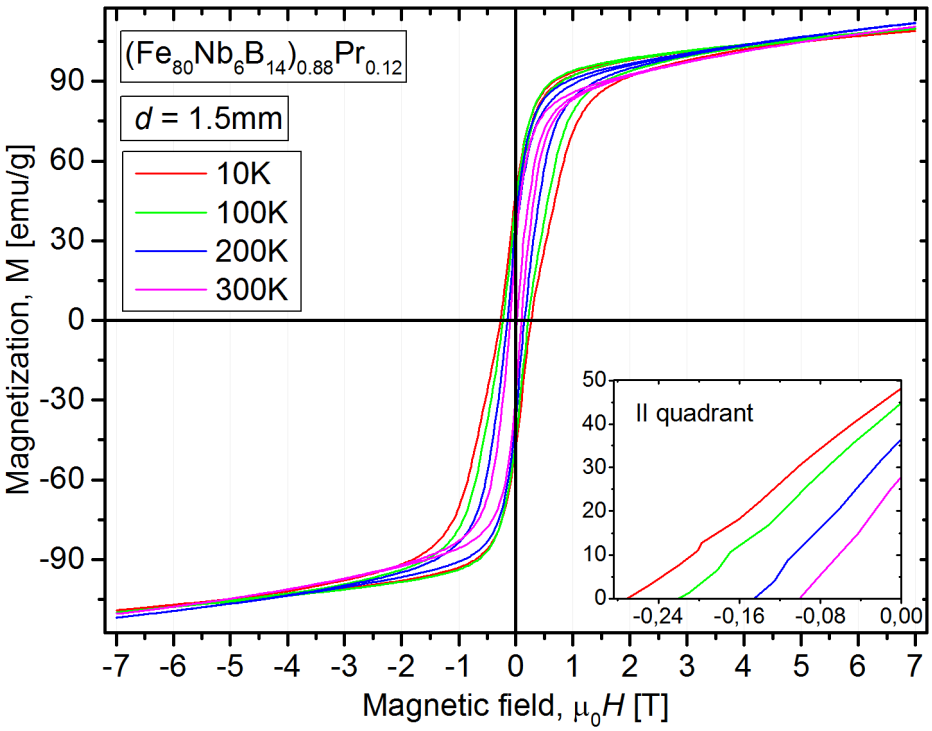


Figure 5.47. The magnetic hysteresis loops of the $(Fe_{80}Nb_6B_{14})_{0.88}Pr_{0.12}$ alloys prepared by using the mold with 1.5 mm in diameter.

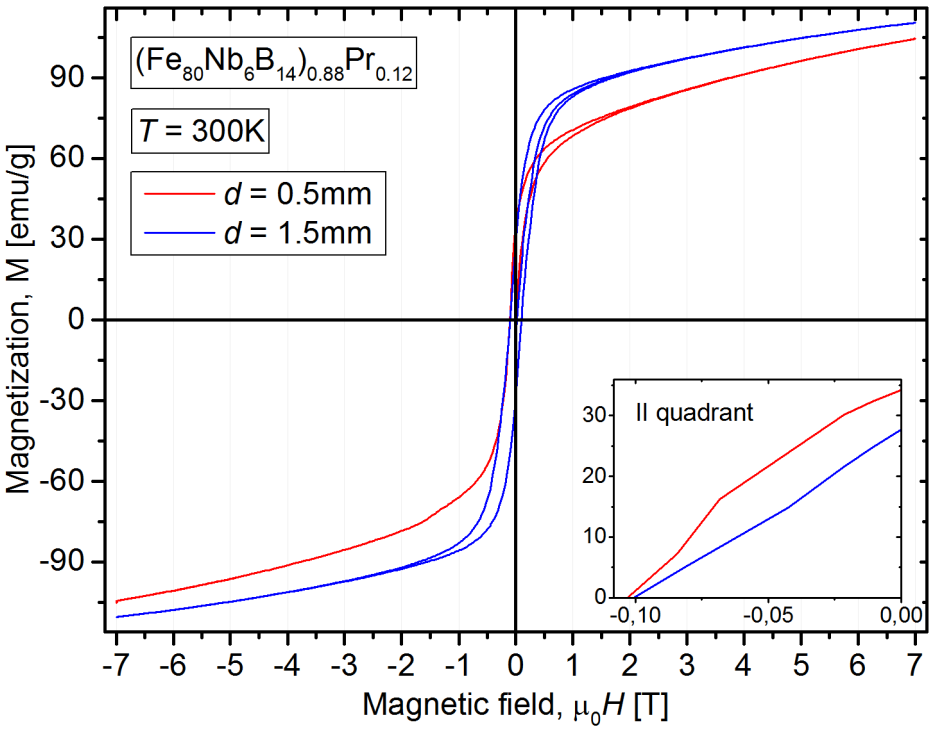


Figure 5.48. The magnetic hysteresis loops of the $(Fe_{80}Nb_6B_{14})_{0.88}Pr_{0.12}$ alloys prepared by using the mold with 0.5mm as well as 1.5 mm in diameter, measured at room temperature.

### 5.5.3. Influence of Nd

One of the most common chemical compositions for permanent magnet is based on Fe-B-Nd compounds. In a contrast to the antiferromagnetic coupling between Fe and Tb, a mixture of Fe and the so-called light rare earths (like Nd) leads to ferromagnetic interactions and simultaneously an increase of $M_S$. Therefore, phase structure and magnetic properties of the $(Fe_{80}Nb_6B_{14})_{1-x}Nd_x$ ($x$=0.08, 0.12, 0.16) bulk nanocrystalline alloys prepared by making use of mold casting technique with 1.5 mm of form diameter were studied.

Figure 5.49 presents X-ray patterns, including sets of Bragg's peaks attributed to different crystal phases, obtained for the discussed materials. The performed phase analysis (see Table 5.9) reveals that the contribution of $Nd_2Fe_{14}B$ increases from 45 % for $x$ = 0.08 to 85 % for $x$ = 0.16. Simultaneously, Fe content decreases with increasing Nd content i.e. from 30 % for $x$ = 0.08 to 25 % for $x$ = 0.12. For the alloy with 16 % of Nd the Fe phase was not detected. In the case of the samples with $x$ = 0.08 and $x$ = 0.16 a formation of Nd and B oxides were observed.

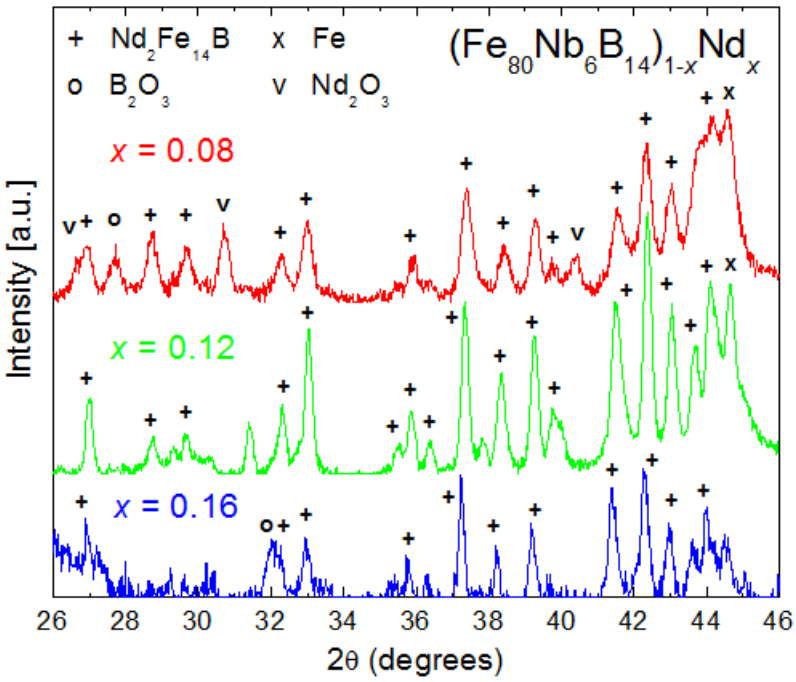


Figure 5.49. The X-ray patterns of the $(Fe_{80}Nb_6B_{14})_{1-x}Nd_x$ alloys prepared by using the mold with 1.5 mm in diameter; the identification of Bragg's peaks are also presented [100].

Table 5.9. Crystal phases, unit cell parameters and size of nanograins obtained from XRD patterns for the $(Fe_{80}Nb_6B_{14})_{1-x}Nd_x$ alloys.

| Alloy | Phases [%] ±2 | Unit cell parameters of $Nd_2Fe_{14}B$ [Å] | Size of nano-grains [nm] ±10 |
|---|---|---|---|
| **$(Fe_{80}Nb_6B_{14})_{0.92}Nd_{0.08}$** | $Nd_2Fe_{14}B$ (45%), Fe (30%), $B_2O_3$ (10%), $Nd_2O_3$ (15%) | a=b=8.806 ±0.003, c=12.147 ±0.002 | 17 |
| **$(Fe_{80}Nb_6B_{14})_{0.88}Nd_{0.12}$** | $Nd_2Fe_{14}B$ (75%), Fe (25%) | a=b=8.793 ±0.001, c=12.172 ±0.001 | 22 |
| **$(Fe_{80}Nb_6B_{14})_{0.84}Nd_{0.16}$** | $Nd_2Fe_{14}B$ (85%), $B_2O_3$ (15%) | a=b=8.806 ±0.002, c=12.207 ±0.004 | 20 |

Figure 5.50 presents thermomagnetic curves M(*T*) in the temperature range from 300 K to 1100 K. In all studied compounds the first magnetic transition corresponding to Curie point of $Nd_2Fe_{14}B$ was determined at temperature about 600 K. The second magnetic transition at temperature about 1043K is attributed to the Curie point of iron. The observed increase of magnetization with increasing temperature, between these magnetic transitions, is surely related to crystallization of the residual amorphous phase and/or iron separation.

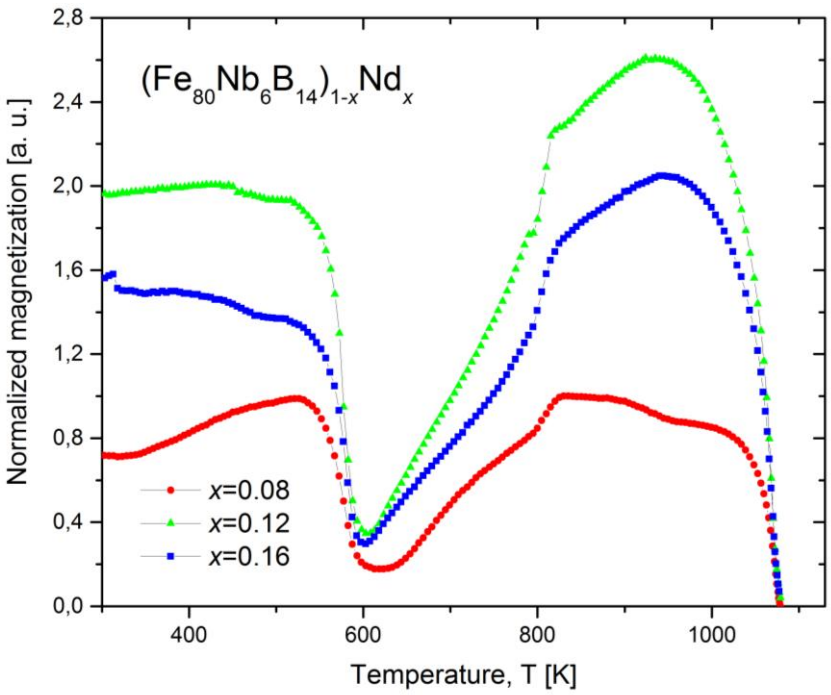


Figure 5.50. The thermomagnetic curves M(*T*) of the $(Fe_{80}Nb_6B_{14})_{1-x}Nd_x$ alloys measured by Faraday magnetic balance in temperature range from 300 K to 1100 K [100].

Magnetic hysteresis loops for all investigated samples are presented in Figure 5.51. In addition, Figure 5.52 presents an example of temperature comparison for one selected alloy ($x = 0.08$). In agreement with the phase composition (the ternary $Nd_2Fe_{14}B$ phase is dominant) one can see that all of the tested alloys reveal hard magnetic properties. The coercive field at 300 K is equal to 0.2 T, 0.11 T and 0.13 T for $x = 0.08$, 0.12 and 0.16, respectively. Moreover, the saturation magnetization $M_s$ is about 120 emu/g for 8 at. % of Nd alloying addition and decreases to less than 90 for $x = 0.16$.

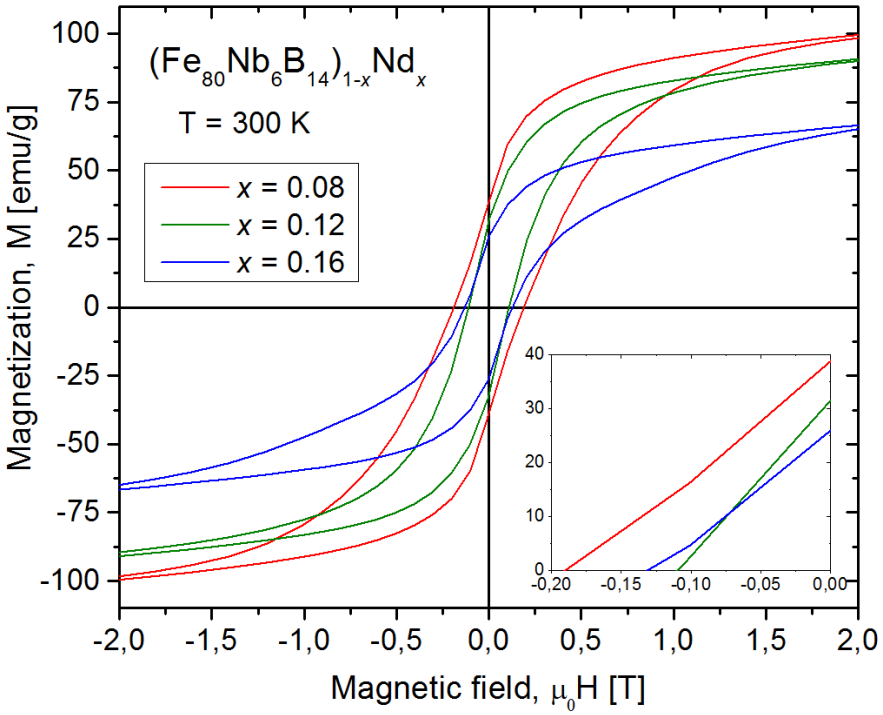


Figure 5.51. The magnetic hysteresis loops of the $(Fe_{80}Nb_6B_{14})_{1-x}Nd_x$ alloys prepared by using the mold with 1.5 mm in diameter, measured at room temperature.

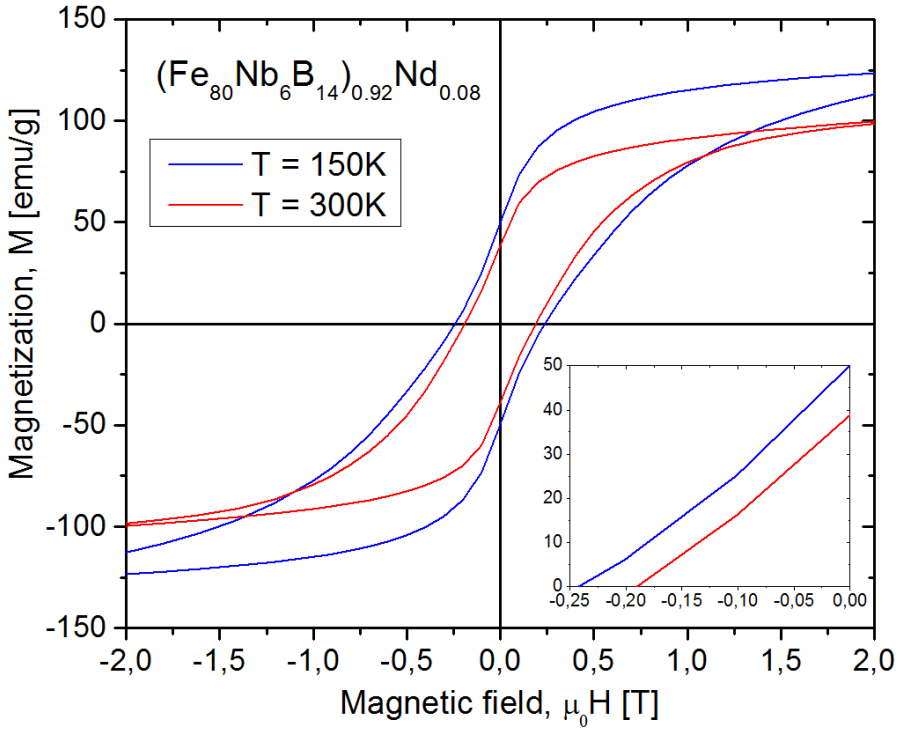


Figure 5.52. The magnetic hysteresis loops of the $(Fe_{80}Nb_6B_{14})_{0.92}Nd_{0.08}$ alloys prepared by using the mold with 1.5 mm in diameter, measured at 150 K and 300 K.

## 5.5.4. Influence of Pt

One of the promising directions of permanents magnets production are the compounds of Fe and Pt. In this case the hard magnetic properties are provided by tetragonal FePt phase (L10), usually obtained using heat treatment after material production. However, interesting idea is an examination of the vacuum suction technique in the context of a formation of the L10 phase in one step during the suction casting action. Therefore, the series of samples based on $(Fe_{80}Nb_6B_{14})_{1-x}Pt_x$ compound for $x$ = 0.15, 0.3, 0.4 and 0.6 were prepared. The influence of cooling rate, controlled by sample diameter from 0.5 mm to 1.5 mm, were also investigated.

Figure 5.53 presents the X-ray diffraction patterns for prepared alloys. Moreover, the structural and magnetic analyses were summarized in Table 5.10. The main phase FePt (A1) is the face centered cubic structure with relatively soft magnetic properties. In the case of alloys with $x$ = 0.15, 0.3 and 0.6 one can observe a mixture of soft magnetic phases such as fcc-FePt, $Fe_\alpha$ and $Fe_2B$. Note that the phase composition does not depend on the

sample diameter which suggests that the obtained cooling rate for applied molds is not sufficient to change the microstructure of such compounds.

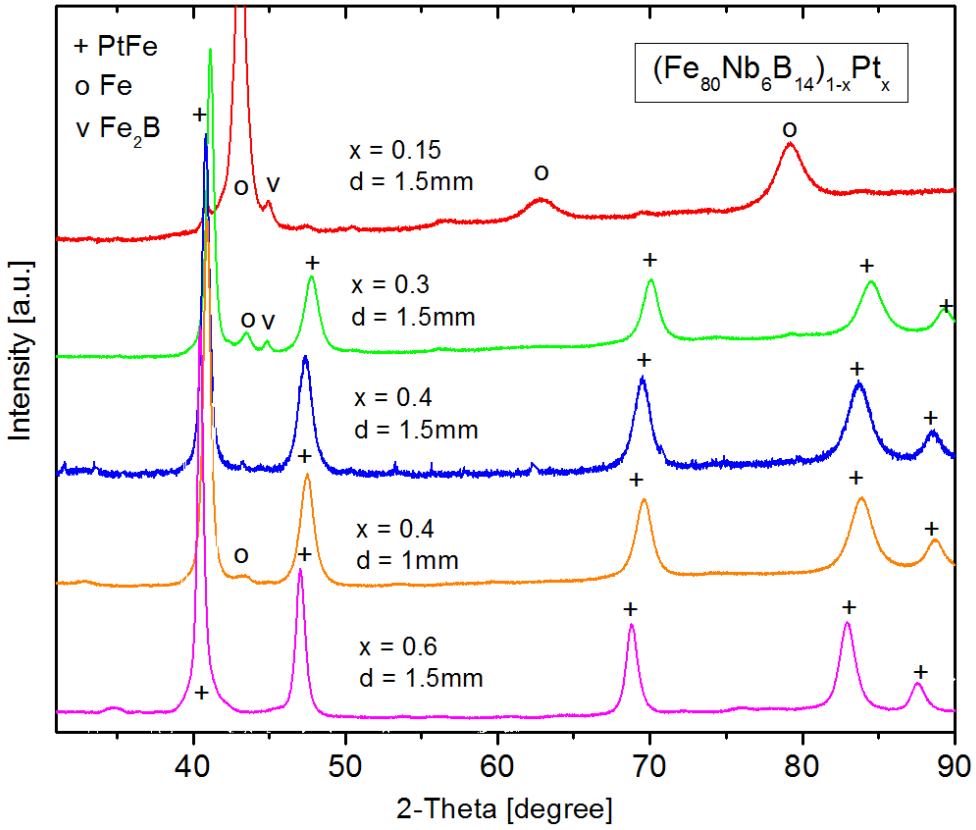


Figure 5.53. The X-ray patterns of the $(Fe_{80}Nb_6B_{14})_{1-x}Pt_x$ alloys prepared by using the mold with 1 mm and 1.5 mm in diameter.

Table 5.10. Some magnetic parameters determined from the hysteresis loops of the $(Fe_{80}Nb_6B_{14})_{1-x}Pt_x$ alloys and phase structure detected by X-ray diffraction. The measurement errors for magnetic parameters are in the level of the least significant digit.

| Alloy *x* | *d* [mm] | $H_c$ [T] | $M_s$ [emu/g] | $M_r$ [emu/g] | Phases [%] ±2 |
|---|---|---|---|---|---|
| **0.15** | **1.5** | 0.026 | 63 | 7.5 | $Fe_\alpha$ 73%, $Fe_2B$ 24%, fcc-FePt 3% |
| **0.3** | **1.5** | 0.019 | 73 | 7.9 | fcc-FePt 80%, Fe 9%, $Fe_2B$ 11% |
| **0.4** | **1.5** | 0.2 | 59 | 25.2 | fcc-FePt |
| **0.4** | **1** | 0.182 | 58 | 20.7 | fcc-FePt, Fe 3% |
| **0.4** | **0.5** | 0.195 | 54 | 21 | - |
| **0.6** | **1.5** | 0.032 | 27 | 5.5 | fcc-FePt, $Fe_2B$ |

Hysteresis loops measured at room temperature for the examined alloys with 1.5 mm in diameter are presented in Figure 5.54, while Figure 5.55 shows a comparison for the samples with different diameters (0.5 mm, 1 mm and 1.5 mm) and the same Pt content ($x$ = 0.4). One can see that the change of the solidification rate (or the sample diameter) does not affect the magnetic hysteresis, which means that the crystallization is too fast for the used suction casting method. Figure 5.56 presents several magnetic measurements at different temperatures ranged from 10 K to 300 K. As shown, the coercive field increases with decreasing temperature, which is expected and can be explained by a contribution of the so-called thermal energy to the pinning mechanism of magnetization.

Concluding this part, the material with 40 at. % of Pt exhibits the best hard magnetic properties. In this case the coercive field $H_C$ and saturation magnetization $M_S$ are equal to 0.2 T and 67 emu/g (at 7 T of external magnetic field), respectively. In the case of the alloys with lower or higher Pt content ($x$ = 0.15, 0.3, 0.6) the higher values of $M_S$ (up to 75 emu/g for $x$ = 0.3) were observed, however, with low coercive field about 0.02 T.

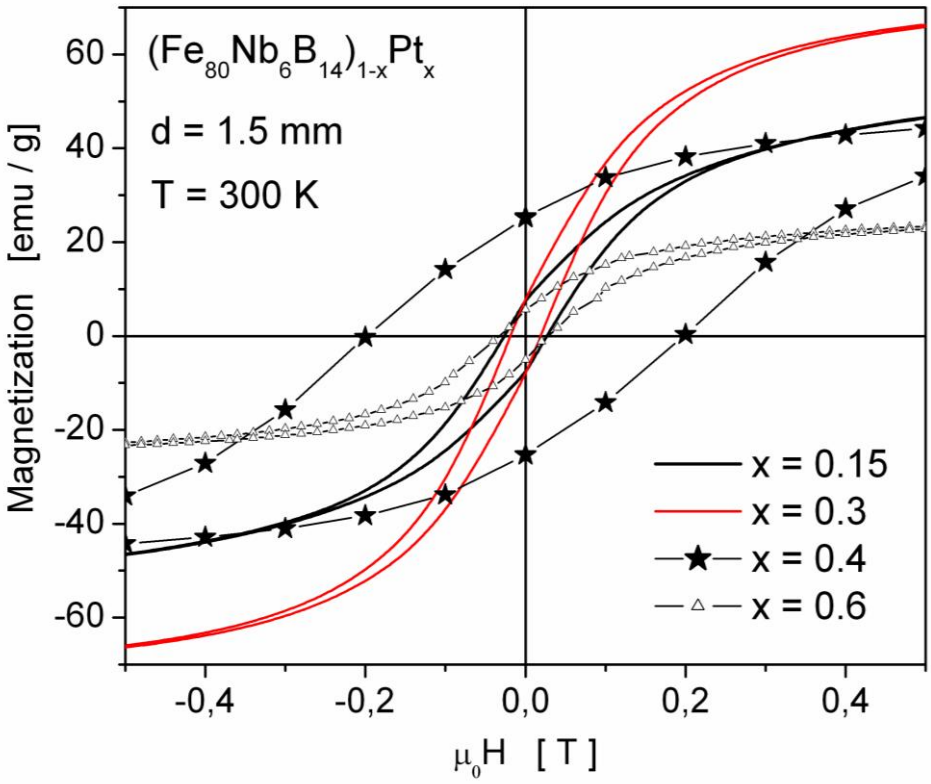


Figure 5.54. The magnetic hysteresis loops of the $(Fe_{80}Nb_6B_{14})_{1-x}Pt_x$ alloys prepared by using the mold with 1.5 mm in diameter, measured at room temperature [101].

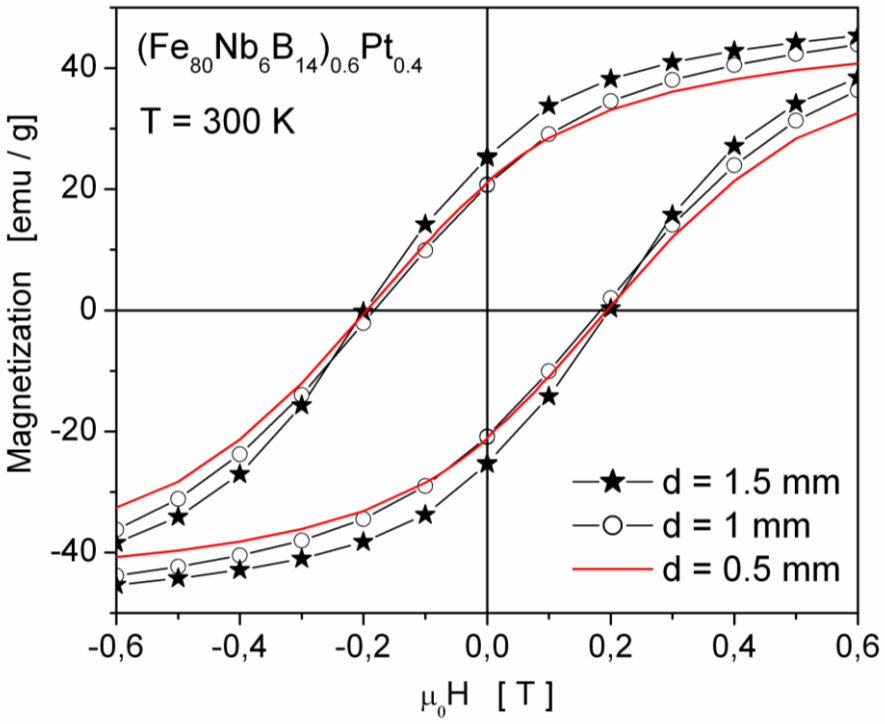


Figure 5.55. The magnetic hysteresis loops of the $(Fe_{80}Nb_6B_{14})_{0.6}Pt_{0.4}$ alloys prepared by using the mold with 0.5 mm, 1 mm and 1.5 mm in diameter, measured at room temperature [101].

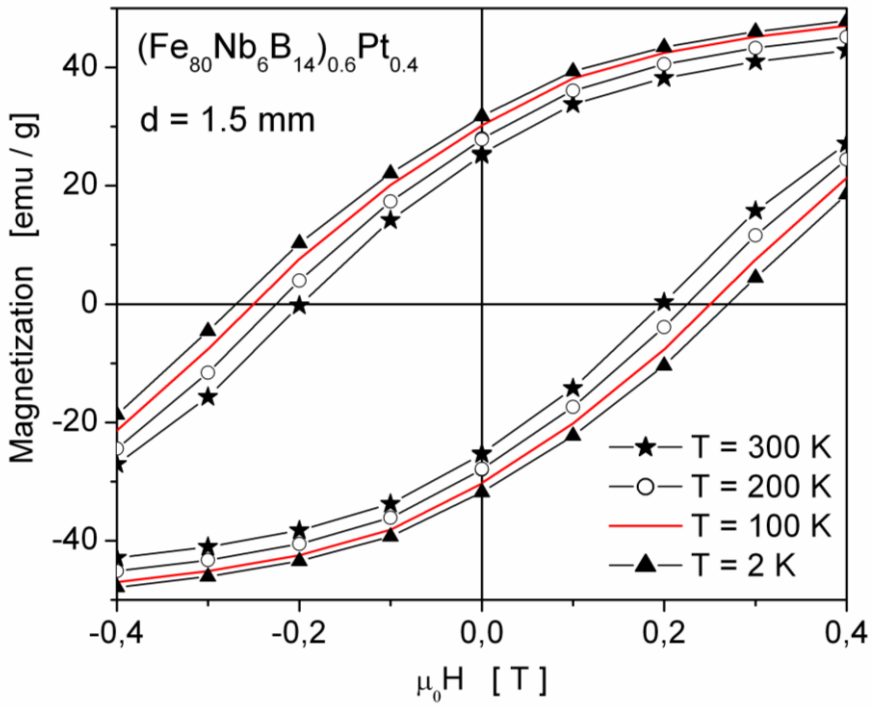


Figure 5.56. The magnetic hysteresis loops of the $(Fe_{80}Nb_6B_{14})_{0.6}Pt_{0.4}$ alloy prepared by using the mold with 1.5 mm in diameter, measured at different temperature from 2K up to 300K [101].

### 5.5.5. Influence of B

In order to study the influence of Boron content on magnetic properties, the two series of samples were prepared: $(Fe_{86}B_{14})_{1-x}Tb_x$ and $(Fe_{78}B_{22})_{1-x}Tb_x$. Each series include the tree different contents of Tb, i.e. $x = 0.04$, 0.08 and 0.12 (optimal). All materials were obtained using the form with 1.5mm in diameter. Magnetic properties of investigated samples were measured by SQUID magnetometer in various temperatures from 10 K to 300 K.

Figure 5.57, Figure 5.58 and Figure 5.59 presents hysteresis loops for the first series of $(Fe_{86}B_{14})_{1-x}Tb_x$, for $x = 0.04$, 0.08 and 0.12. The alloy series with higher content of Boron were presented in Figure 5.60, Figure 5.61 and Figure 5.62. Moreover, Figure 5.63 include a comparison of all hysteresis determined at room temperature. As one may expected, the magnetic saturation depends on iron as well as alloying addition content. It decreases from 140 emu/g to 55 emu/g for 4 at.% and 12 at.% of Tb, respectively. Higher content of Boron leads to similar tendency. Full comparison of magnetic properties was shown in Table 5.11.

All studded alloys exhibit soft magnetic properties with coercivity lower than 0.05 T for $x$ = 0.04 - 0.08 and about 0.25 T in case of 12 at.% of Terbium addition. Strong deterioration of hard magnetic properties for alloys prepared without Niobium suggests very important role of this element in crystallization process and formation of favorable for magnetic hardening microstructure.

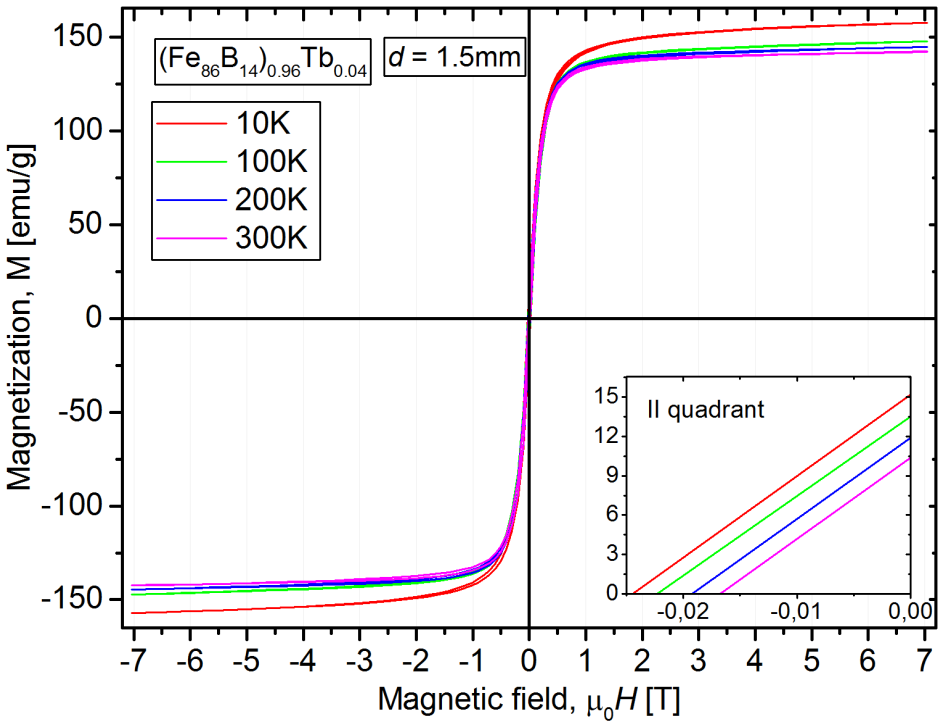


Figure 5.57. The magnetic hysteresis loops of the $(Fe_{86}B_{14})_{0.96}Tb_{0.04}$ alloys prepared by using the mold with 1.5 mm in diameter, measured at different temperature.

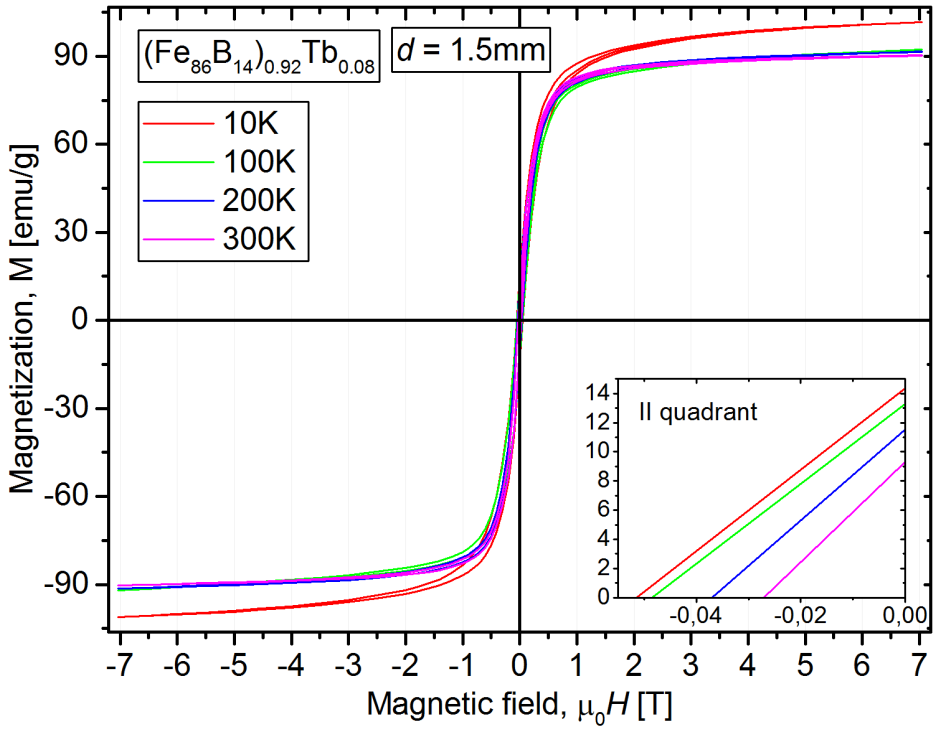


Figure 5.58. The magnetic hysteresis loops of the $(Fe_{86}B_{14})_{0.92}Tb_{0.08}$ alloys prepared by using the mold with 1.5 mm in diameter, measured at different temperature.

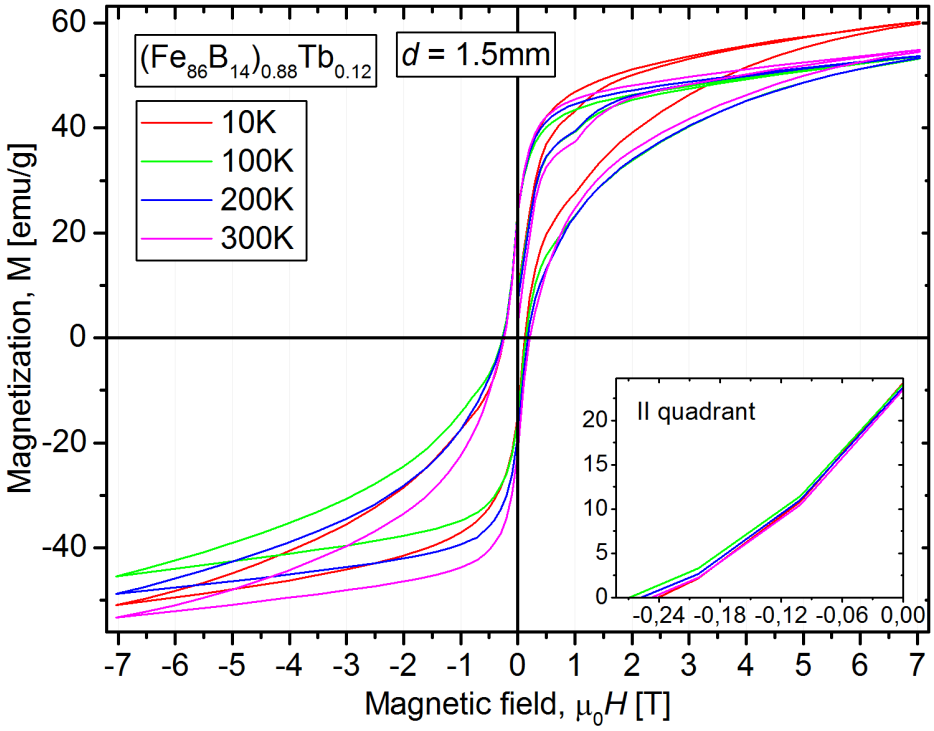


Figure 5.59. The magnetic hysteresis loops of the $(Fe_{86}B_{14})_{0.88}Tb_{0.12}$ alloys prepared by using the mold with 1.5 mm in diameter, measured at different temperature.

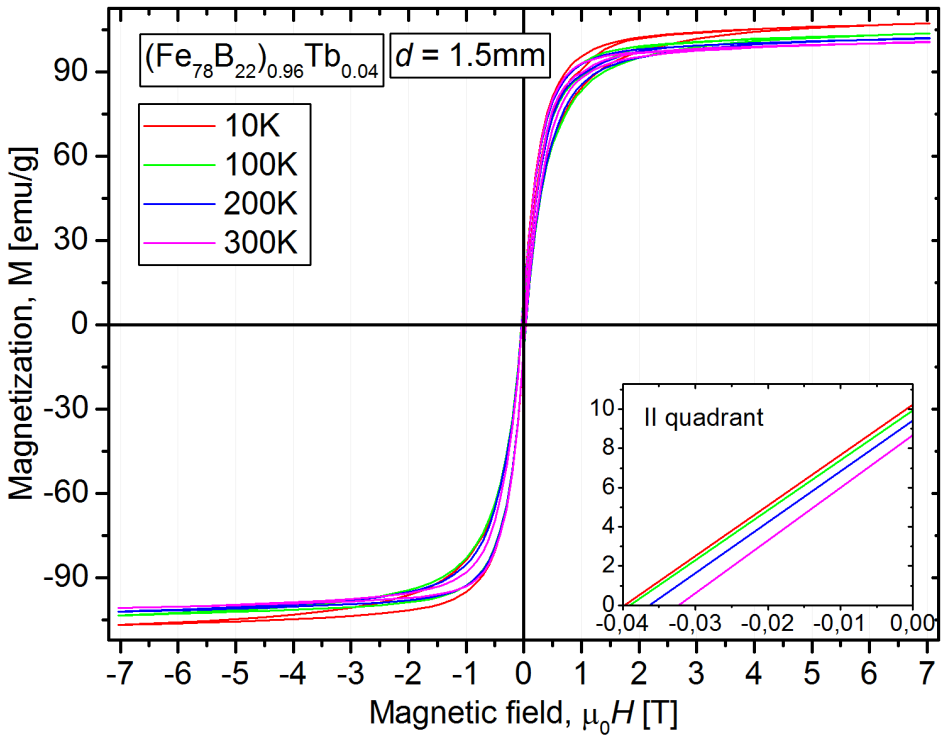


Figure 5.60. The magnetic hysteresis loops of the $(Fe_{78}B_{22})_{0.96}Tb_{0.04}$ alloys prepared by using the mold with 1.5 mm in diameter, measured at different temperature.

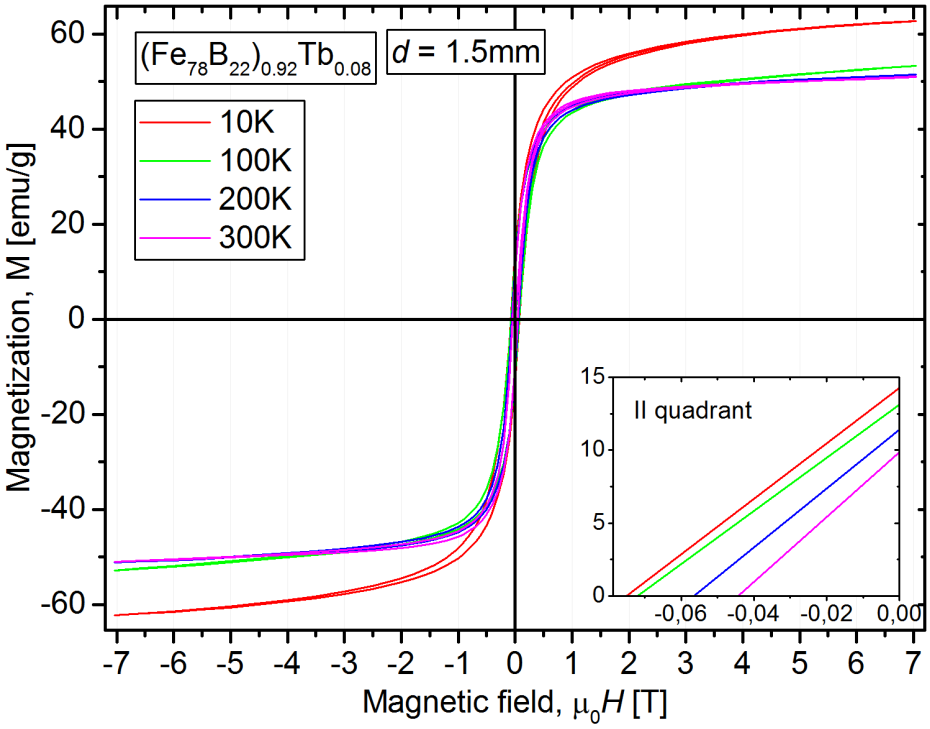


Figure 5.61. The magnetic hysteresis loops of the $(Fe_{78}B_{22})_{0.92}Tb_{0.08}$ alloys prepared by using the mold with 1.5 mm in diameter, measured at different temperature.

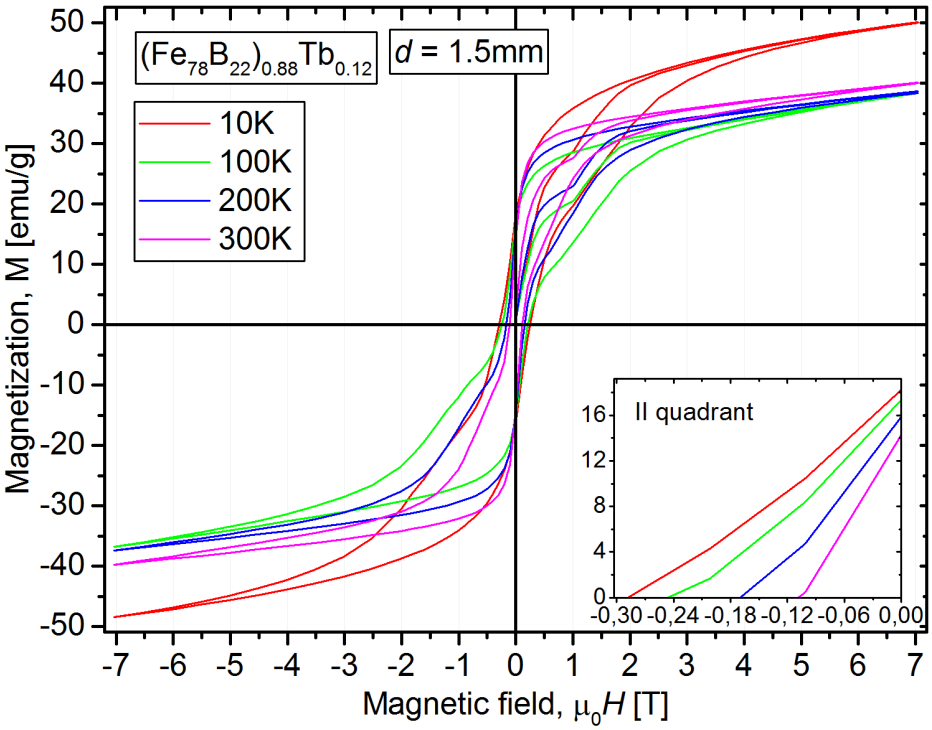


Figure 5.62. The magnetic hysteresis loops of the $(Fe_{78}B_{22})_{0.88}Tb_{0.12}$ alloys prepared by using the mold with 1.5 mm in diameter, measured at different temperature.

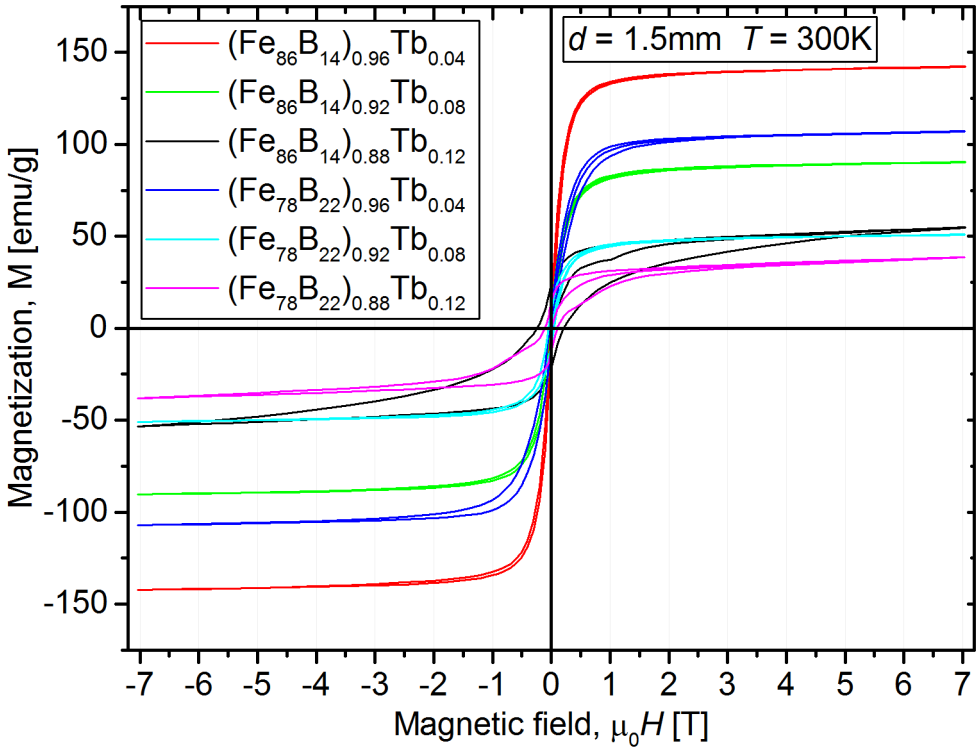


Figure 5.63. The comparison of magnetic hysteresis loops all studied alloys prepared by using the mold with 1.5 mm in diameter, measured at room temperature.

Table 5.11. Magnetic properties of the Fe-B-Tb alloys measured at room temperature. The measurement errors are in the level of the least significant digit.

| Alloy | $H_C$ [T] | $M_S$ [emu/g] | $M_R$ [emu/g] |
|---|---|---|---|
| $(Fe_{86}B_{14})_{0.96}Tb_{0.04}$ | 0.017 | 145 | 10.5 |
| $(Fe_{86}B_{14})_{0.92}Tb_{0.08}$ | 0.028 | 90 | 9 |
| $(Fe_{86}B_{14})_{0.88}Tb_{0.12}$ | 0.24 | 53 | 24 |
| $(Fe_{78}B_{22})_{0.96}Tb_{0.04}$ | 0.032 | 100 | 8.5 |
| $(Fe_{78}B_{22})_{0.92}Tb_{0.08}$ | 0.043 | 50 | 10 |
| $(Fe_{78}B_{22})_{0.88}Tb_{0.12}$ | 0.11 | 40 | 14 |

## 5.6. Concluding remarks of the preliminary researches

As it was shown, the varying Tb content is responsible for the observed changes in the phase structure of the Fe-Nb-B-Tb group of bulk alloys. The carried out XRD and Mössbauer measurements reveal the maximum of the $Tb_2Fe_{14}B$ hard magnetic phase (76 %) correlated with the minimum of the $TbFe_2$ and the lack of α-Fe soft phases, as shown in Figure 5.64. This means that the balance between the hard and soft phases can be controlled by proper terbium content.

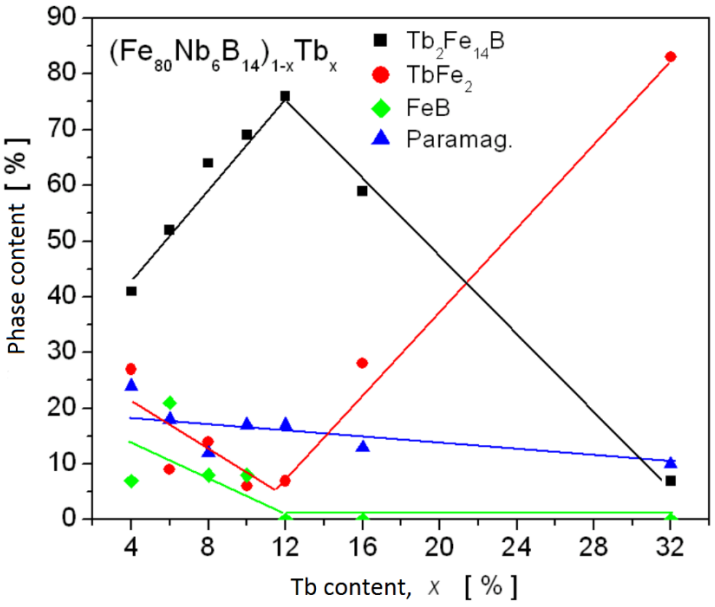


Figure 5.64. The phase structure of the $(Fe_{80}Nb_6B_{14})_{1-x}Tb_x$ alloys.

Magnetic properties of the investigated alloys are correlated with the changes of the phase structure. The measured magnetic characteristics also show the extrema of the magnetic parameters. Figure 5.65 presents the dependence of the *x* parameter on the magnetic saturation, magnetic remanence, coercive field and the $|JH|_{max}$ parameter. One can see that the minima of $M_S$ and $M_R$ as well as maxima of $H_c$ and $|JH|_{max}$ are attributed to the maximum of the $Tb_2Fe_{14}B$ phase (about 10 – 12 at. % of Tb). It is clear that higher content of the magnetically hard component causes the observed effects, mainly due to antiferromagnetic Tb-Fe coupling and its high magnetocrystalline anisotropy. Note, the samples were prepared using the mold diameter of 1.5 mm and the melting current 25 A.

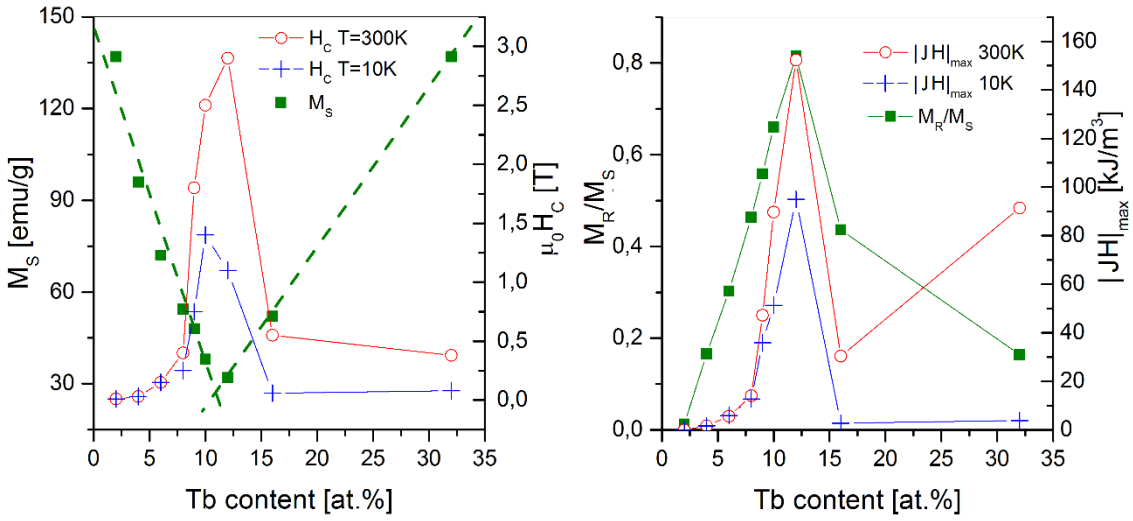


Figure 5.65. Selected magnetic parameters as a function of Tb content for the $(Fe_{80}Nb_6B_{14})_{1-x}Tb_x$ alloys [97].

Interesting effects were obtained studying the influence of cooling rate (or sample diameter) on structural and magnetic properties of the examined alloys. The samples were prepared using the molds with diameters $d$ = 0.5, 1, and 2 mm. As the XRD and Mössbauer measurements show, the phase structure is not so sensitive to the sample diameter. However, for $d$ = 0.5 mm one can see a tendency of the increasing $Tb_2Fe_{14}B$ content. In contrary to this, the SEM and MFM observations reveal the important differences in microstructure. In fact, for the lower diameters (0.5 and 1 mm) the formation of dendrite-like grains was observed. The grains are rather micrometric but their branches are of submicrometric size which can be a source of additional magnetic anisotropies. This conclusion is fully confirmed by the MFM pictures, when, on average, magnetic domains are smaller with the decreasing sample diameter.

The changes in microstructure have strong influence on magnetic properties of the alloys in question. Figure 5.66 shows the influence of sample diameter on selected magnetic parameters for the $(Fe_{80}Nb_6B_{14})_{0.9}Tb_{0.1}$ and $(Fe_{80}Nb_6B_{14})_{0.88}Tb_{0.12}$ alloys. The presented curves also indicate that the observed magnetic hardening effect is attributed to the change of the cooling rate and, as its consequence, the formation of the dendritic grains.

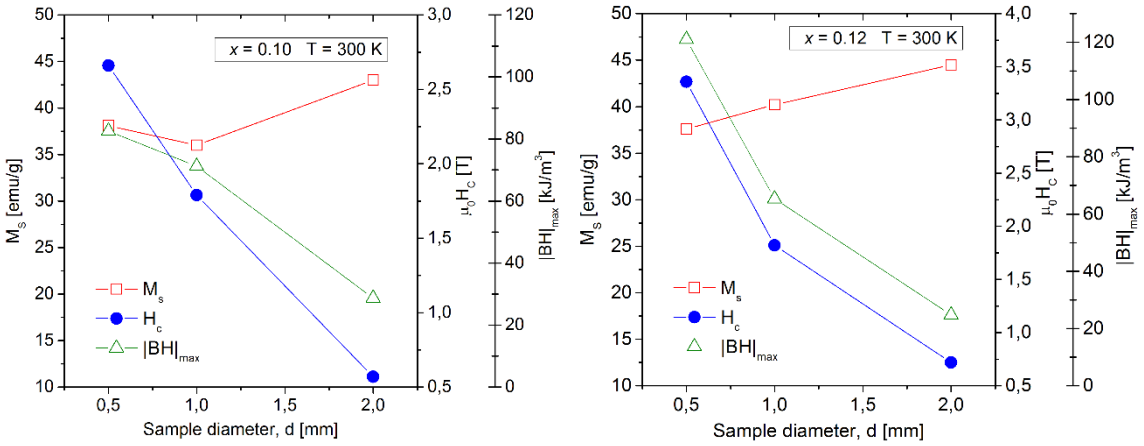


Figure 5.66. Selected magnetic parameters as a function of the sample diameter *d* for the $(Fe_{80}Nb_6B_{14})_{0.9}Tb_{0.1}$ and $(Fe_{80}Nb_6B_{14})_{0.88}Tb_{0.12}$ alloys [96].

For possible applications the phase stability has an important meaning. This aspect was studied by means of the DSC, Mössbauer spectroscopy and magnetic techniques. The measurements were carried out before and after the heating during the DSC experiment. Generally, the tested alloys are not stable and some changes of the phase structure and magnetic properties were observed. In all cases the deterioration of hard magnetic properties occurred that is caused by the formation of α-Fe soft magnetic phase during heating. This effect is especially strong for the sample with $d$ = 0.5 mm.

In the frame of the preliminary researches, the influence of the pulverization degree was also studied that has a practical and scientific meaning. After grinding of the bulk material the three effects were observed: i) increase of the $TbFe_2$ phase content, ii) broadening of the XRD reflexes, indicating the decrease of the crystallite sizes and iii) deterioration of hard magnetic properties, suggesting an important role of the dendritic microstructure as well as direct magnetic interactions.

Apart from the main direction of these investigations, the substitution of Tb by the other RE metals or Pt does not toward to satisfactory results, however, they were useful for further main researches. Summarizing the above, the most interesting are the alloys with about 12 at. % of Tb prepared using the mold with inner diameter of 0.5 mm. Moreover, the preliminary results reveal the strong correlation between microstructure and the desired hard magnetic properties.

# 6. Main researches

## 6.1. Influence of melting current on structural and magnetic properties of Fe-Nb-B-Tb alloys

Based on preliminary investigations, it is well established that the magnetic properties of Fe-Nb-B-RE nanocomposites strongly depend on their chemical composition and cooling rate, controlled by sample diameter. Accounting hard magnetic properties, Terbium was determined as the most promising alloying addition with optimal content around 12 at. %. Moreover, decrease in sample diameter (increase of cooling rate) leads to a significant magnetic hardening. It should be underlined that, in the preliminary researches, all the examined samples were prepared with the value of melting current equals 25 A. It is expected that this parameter may affect the phase content, microstructure and consequently magnetic properties of the examined alloys. Therefore, the studies referring to the influence of melting current, applied during vacuum suction casting, are of great importance. Examination procedure bases on series of the $(Fe_{80}Nb_6B_{14})_{0.88}Tb_{0.12}$ alloys prepared using the form with 1.5 mm in diameter and four different values of melting current $I$ = 15 A, 25 A, 35 A and 45 A. Phase identification were performed by X-ray diffraction and $^{57}Fe$ Mössbauer spectroscopy in the transmission geometry. Structural observation were carried out by scanning electron microscopy SEM, energy-dispersive X-ray spectroscopy EDS as well as magnetic force microscopy MFM. For these measurements the samples were included into a resin and then mechanically polished. Magnetic studies base on SQUID magnetometer in the temperature range 300 K – 750 K and magnetic field up to 7 T.

### 6.1.1. Structural properties

As was shown in Figure 6.1 the phase identification indicates significant content of hard magnetic $Tb_2Fe_{14}B$ phase (around 90%), small amount of $TbFe_2$ as well as a few percent of other phases like $Fe_2TbB_2$ and FeO. Chemical composition of all exanimated samples

is similar and any remarkable changes in a function of melting current were not observed. The all estimated structural parameters were summarized in Table 6.1.

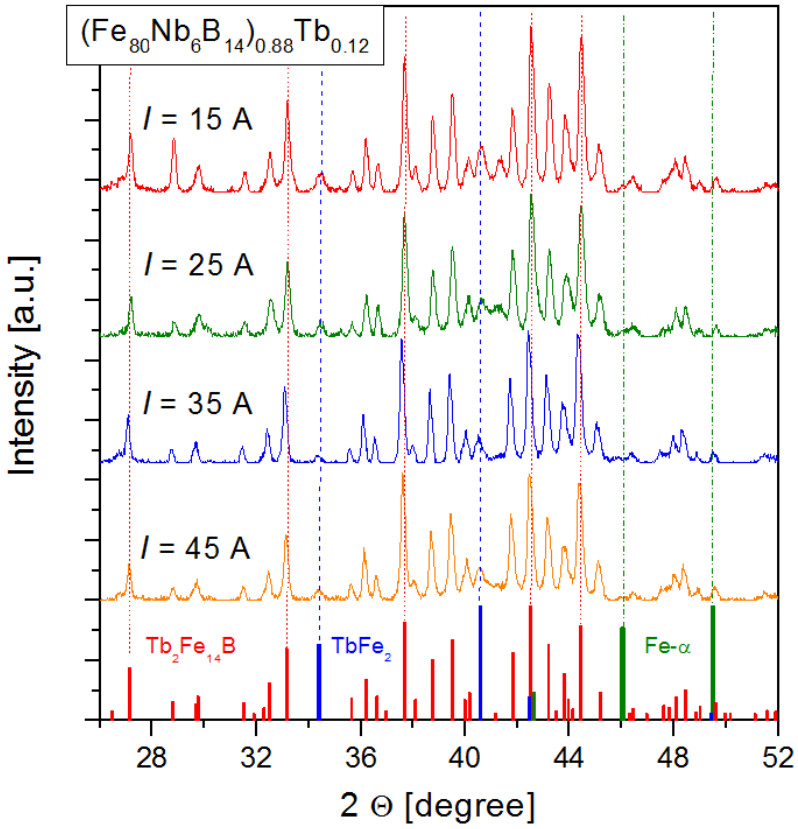


Figure 6.1. The part of X-ray diffraction patterns of the $(Fe_{80}Nb_6B_{14})_{0.88}Tb_{0.12}$ alloys prepared using different value of melting current.

Table 6.1. The phase composition and structural parameters estimated base on the X-ray diffraction patterns of the $(Fe_{80}Nb_6B_{14})_{0.88}Tb_{0.12}$ alloys prepared using different value of melting current.

| *I* [A] | $Tb_2Fe_{14}B$ [%] ±2 | $TbFe_2$ [%] ±2 | $Fe_2TbB_2$, FeO [%] ±2 | Unit cell [Å] | grain size [nm] ±10 |
|---|---|---|---|---|---|
| **15** | 87 | 4 | 9 | a= 8.758 ±0.001<br>c= 12.043 ±0.002 | 30 |
| **25** | 87 | 4 | 9 | a= 8.757 ±0.001<br>c= 12.042 ±0.002 | 27 |
| **35** | 94 | 3 | 3 | a= 8.779 ±0.001<br>c= 12.073 ±0.002 | 31 |
| **45** | 92 | 4 | 4 | a= 8.771 ±0.001<br>c= 12.059 ±0.001 | 30 |

Very important are the performed SEM observations, indicating microstructure of the tested alloys prepared using different melting current *I*. Generally, the two kinds of micrographs were obtained for the samples of *I* = 15, 25 A and *I* = 35, 45 A. Figure 6.2 presents the SEM picture for the representative value of *I* = 15 A and *I* = 35 A. In the case of higher melting current, one may observe a formation of dendrite-like grains with micro and even sub-micrometric sizes. The grains are smaller in the outer part of the rod which is probably related to higher cooling rate near the copper mold. Different situation were detected for the material prepared using *I* = 15 A. In this case a relatively week contrast, suggesting only some chemical separations, is observed. More detailed analyses were performed using EDS technique.

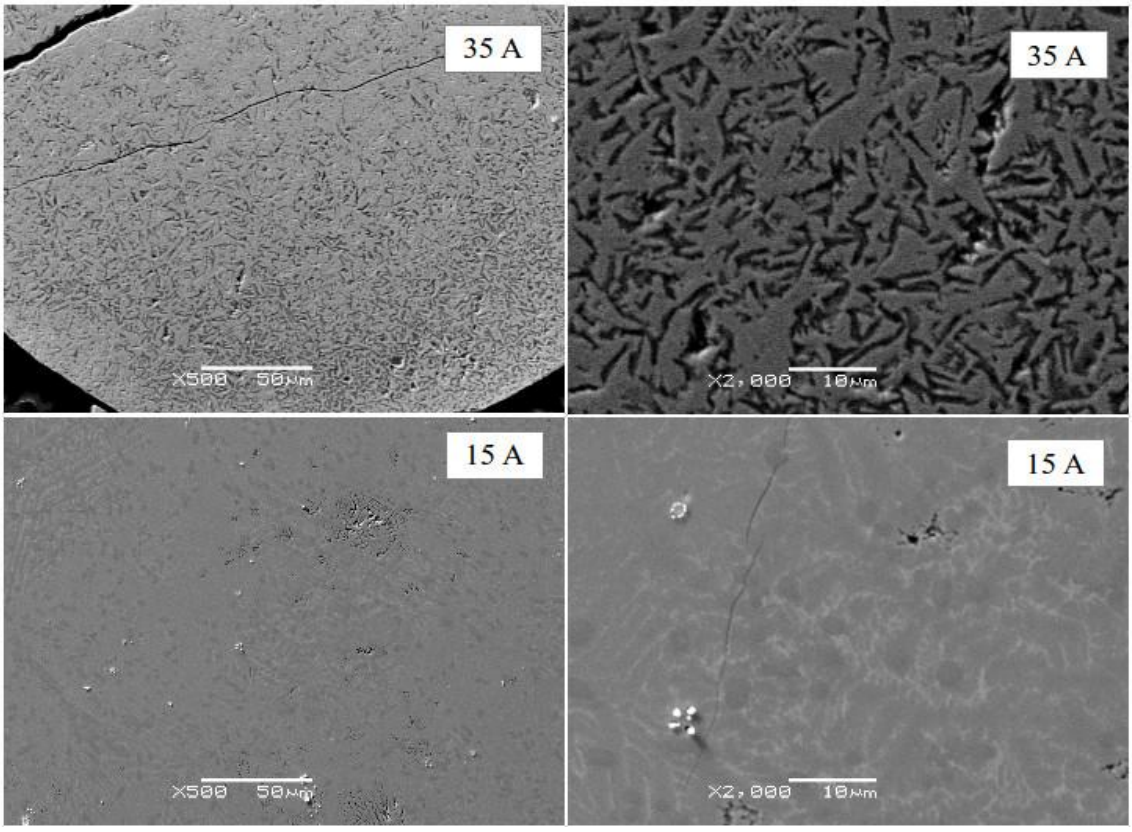


Figure 6.2. SEM (SEI mode, magnification of 500 and 2000) pictures registered for the $(Fe_{80}Nb_6B_{14})_{0.88}Tb_{0.12}$ alloys prepared with melting current *I* = 15 A and *I* = 35 A [102].

A SEM BSE image including element maps of Nb, Fe and Tb performed for $(Fe_{80}Nb_6B_{14})_{0.88}Tb_{0.12}$ alloy obtained with melting current equals 35 A is presented in Figure 6.3. Moreover, the red contours, indicating some areas for better clarity, are plotted

in the same places in each figure. It may be noted that the dendritic grains, presented by bright area in the SEM image, are composed of Fe and Tb, surely forming the $Tb_2Fe_{14}B$ phase, while the area between dendrite branches are reached of Nb. The similar kind of microstructure in case of sample prepared with $I$ = 45 A were also recorded.

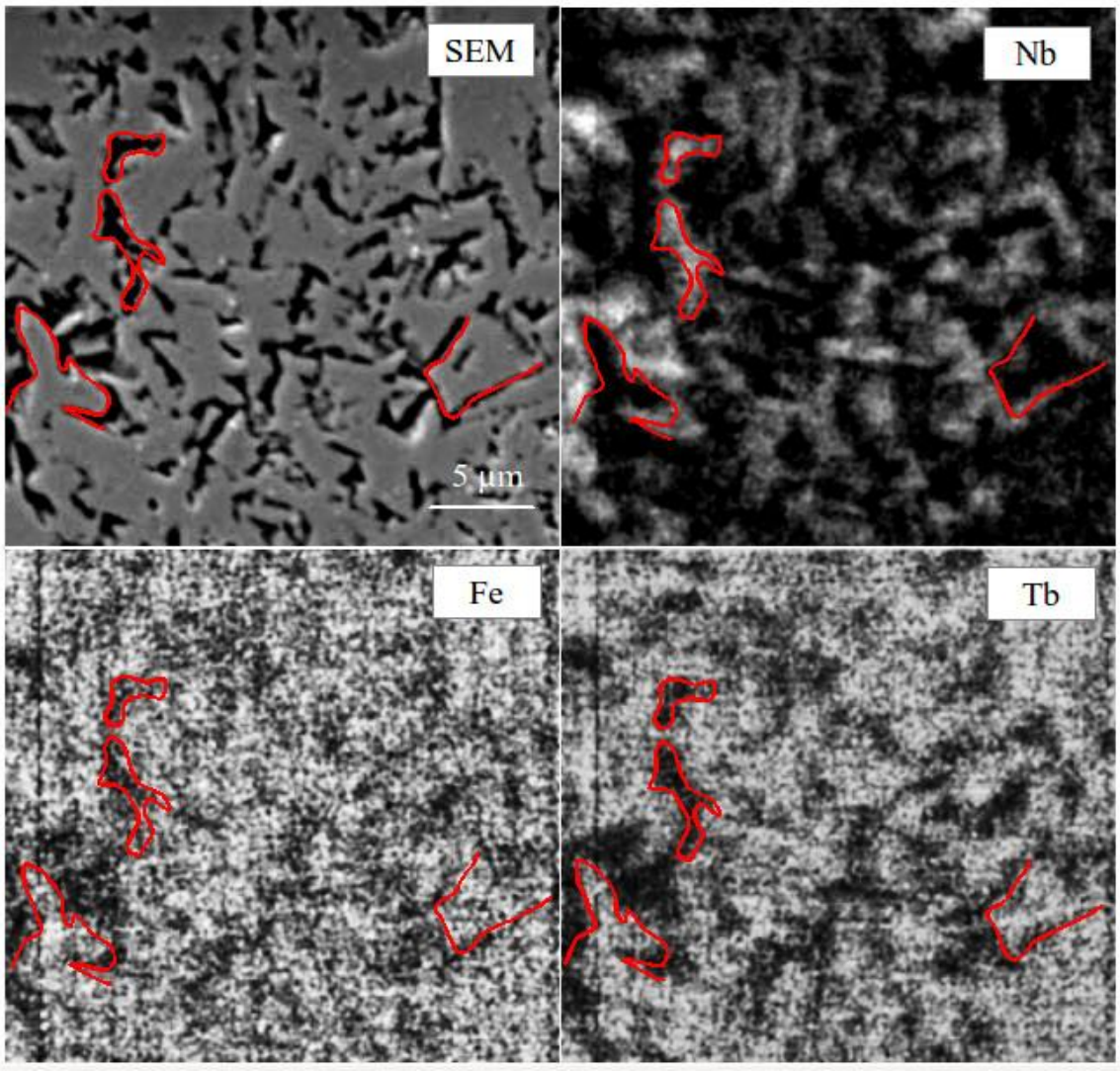


Figure 6.3. Element maps (EDS) for the $(Fe_{80}Nb_6B_{14})_{0.88}Tb_{0.12}$ alloy prepared with melting current $I$ = 35 A. The red contours, indicating some areas reach and poor of Nb, are plotted in the same places in each figures [102].

In opposite to the situation described above, the microstructure of the materials prepared with low (15 A and 25 A) melting current is completely different. In this cases only some Nb and Tb separations are detected as can by noted in Figure 6.4 by dark and white marks, respectively.

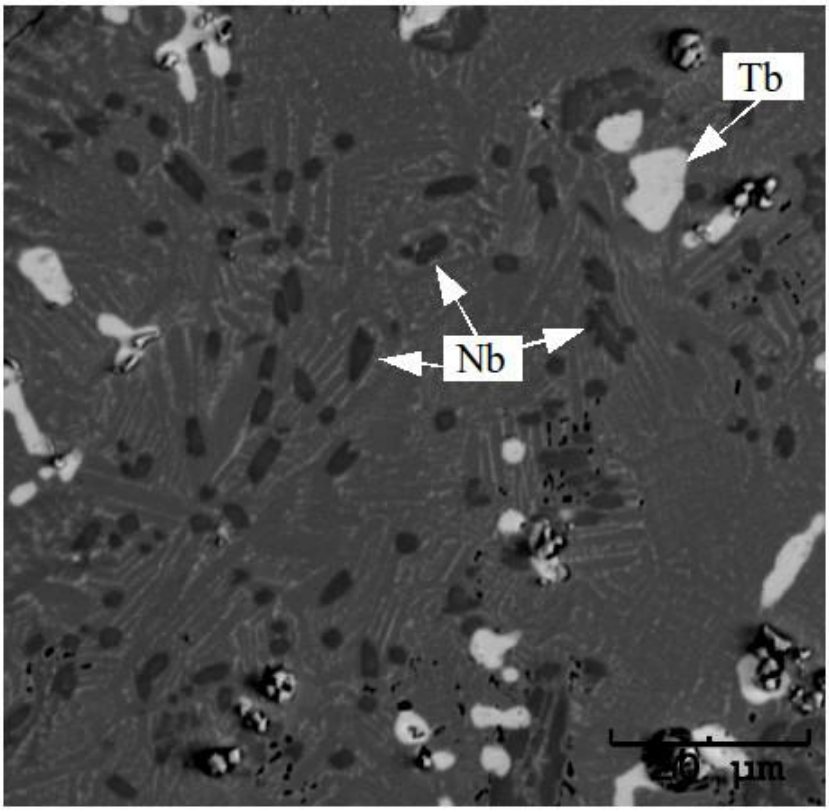


Figure 6.4. SEM (BSE mode) picture for the $(Fe_{80}Nb_6B_{14})_{0.88}Tb_{0.12}$ alloys prepared with melting current $I$ = 15 A [102].

## 6.1.2. Magnetic properties

Figure 6.5 presents the magnetic hysteresis loops measured using SQUID Magnetometer at room temperature for all exanimated materials prepared using the melting current $I$ = 15 A, 25 A, 35 A and 45 A. One may note that magnetic properties are strongly different and depend on the $I$ parameter, which is in fully agreement with the structural observations. The magnetic saturation slightly decreases while coercive field $H_c$ significantly rises with increasing melting current. The highest $H_c$ equals 5.7 T was observed for $I$ = 35 A, while in case of $I$ = 15 A and 25 A, the $H_c$ is equal to around 1.3 T. Table 6.2 summarizes the most important magnetic parameters of discussed materials.

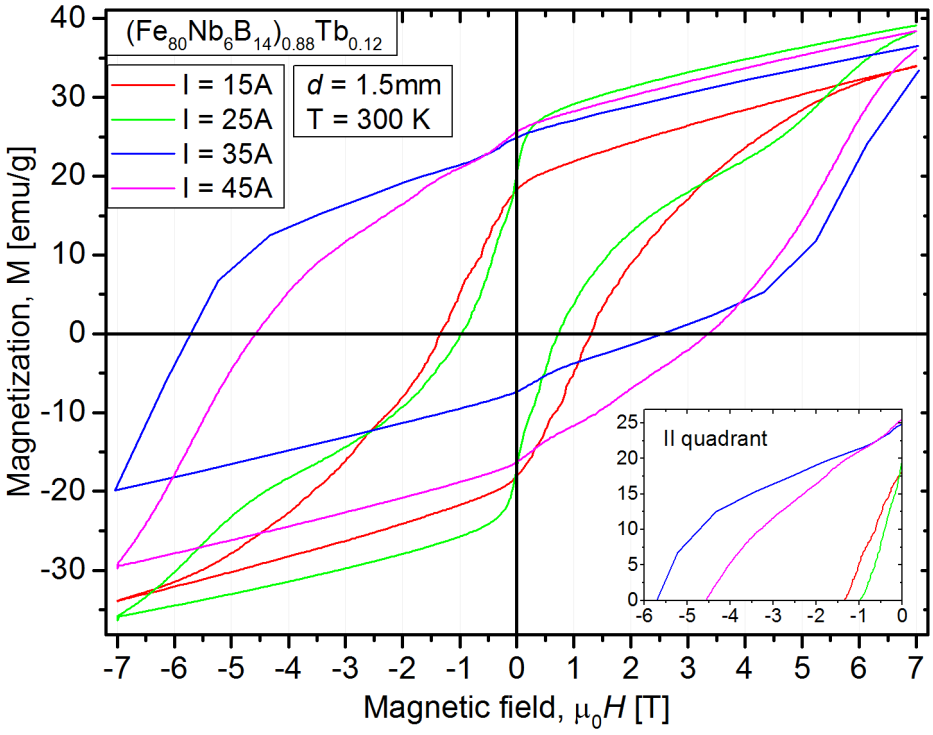


Figure 6.5. Magnetic hysteresis loops for the $(Fe_{80}Nb_6B_{14})_{0.88}Tb_{0.12}$ alloys with diameter equal to 1.5mm, prepared with melting current $I$ = 15 A, 25 A, 35 A and 45 A.

Table 6.2. Selected magnetic parameters of the $(Fe_{80}Nb_6B_{14})_{0.88}Tb_{0.12}$ alloys prepared using melting current $I$ = 15, 25, 35 and 45 A, measured in as-cast state at room temperature ($H_c$ – coercive field, $M_{7T}$ – magnetization in 7 T, $M_r$ – remanence magnetization, $B_r$ – remanence induction, $|JH|_{max}$, $|BH|_{max}$ – energetic parameters). The measurement errors are in the level of the least significant digit.

| $I$ [A] | $\mu_0 H_c$ [T] | $M_{7T}$ [emu/g] | $M_r$ [emu/g] | $B_r$ [T] | $\|JH\|_{max}$ [kJ/m$^3$] | $\|BH\|_{max}$ [kJ/m$^3$] |
|---|---|---|---|---|---|---|
| **15** | 1.35 | 34 | 18.2 | 0.18 | 51 | 6.1 |
| **25** | 0.96 | 39 | 19.8 | 0.2 | 33 | 5.9 |
| **35** | 5.7 | 36.5 | 24.9 | 0.25 | 412 | 12.2 |
| **45** | 4.57 | 38.5 | 25.4 | 0.25 | 284 | 12.5 |

## 6.2. Influence of Nb on Fe-Nb-B-Tb alloys

It is good determined that magnetic properties of discussed materials are related to specific microstructure formed during melting and suction process preformed using vacuum suction technique. Moreover, one may expect that cooling rate obtaining by this method is in order to $10^3$ K / s. Generally, that rate is not sufficient to prevent crystallization of alloys base on pure Fe-B-Tb chemical composition without additional elements. This situation was confirmed during preliminary investigations (described in section 5.5.5). In the other hand, it is known fact that in amorphous alloys the Nb addition slows down diffusion of iron [17] which, in a combination with a specific cooling rate during the casting procedure, may affect the phase content and microstructure. Therefore, one can expect that Niobium content for Fe-Nb-B-Tb alloys plays important role in formation of magnetic properties of final materials.

The aim of this section is to study an influence of Nb content on the phase structure and magnetic properties of the $(Fe_{86-x}Nb_xB_{14})_{0.88}Tb_{0.12}$ ($x$ = 2, 4, 6 and 8) bulk nanocrystalline alloys prepared using 1.5 mm mold and the optimal melting current of 35 A.

### 6.2.1. Structural properties

The X-ray diffraction patterns of all exanimated alloys are presented on Figure 6.6. In addition, the theoretical pattern of the expected $Tb_2Fe_{14}B$ phase is also included. Contents of this phase were estimated in the level higher than 90 % independently on the $x$ parameter. The results from the qualitative and quantitative phase analysis as well as the cell parameters are listed in Table 6.3.

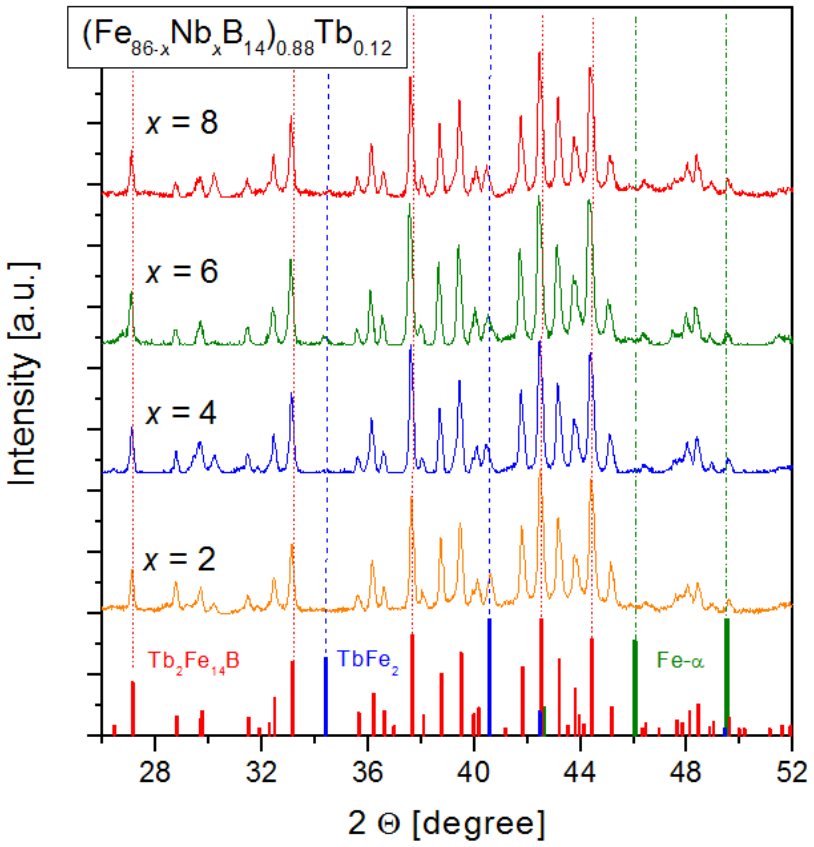


Figure 6.6. XRD patterns for the $(Fe_{86-x}Nb_xB_{14})_{0.88}Tb_{0.12}$ alloys prepared using $I$ = 35 A and the reference pattern of $Tb_2Fe_{14}B$ phase.

Table 6.3. Phase content, the cell parameters determined from XRD patterns of the $(Fe_{86-x}Nb_xB_{14})_{0.88}Tb_{0.12}$ alloys (the melting current $I$ = 35 A).

| Nb content $x$ | $Tb_2Fe_{14}B$ [%] ± 2 | $Fe_2TbB_2$ [%] ± 2 | $TbFe_2$ [%] ± 2 | $a$ [Å] | $c$ [Å] |
|---|---|---|---|---|---|
| **2** | 93 | 4 | - | 8.801 ±0.01 | 12.073 ±0.01 |
| **4** | 90 | - | 5 | 8.775 ±0.01 | 12.055 ±0.02 |
| **6** | 94 | 3 | 3 | 8.779 ±0.02 | 12.073 ±0.02 |
| **8** | 92 | - | 4 | 8.775 ±0.01 | 12.057 ±0.02 |

Figure 6.7 shows the Nb maps comparison (EDS) registered for the alloys with varying Nb_content. One may note that in the case of $x$ = 2 and 4 the Nb distribution is rather smooth. On the other hand, for material with $x$ = 6, there are clearly visible regions with

high Nb concentration spread all over the sample. In case of $x$ = 8 the situation is similar, however also some agglomerations of Nb element can be observed.

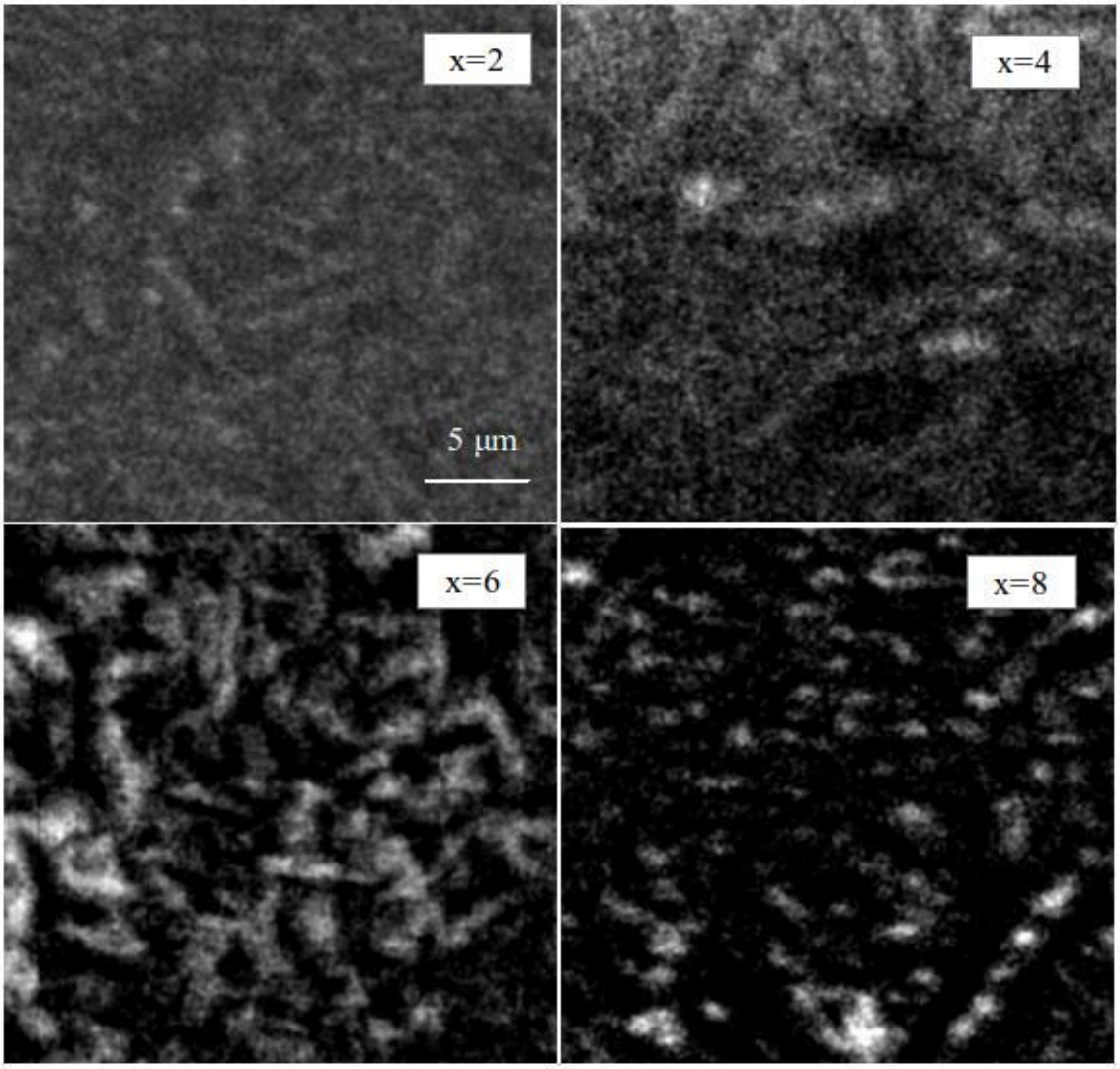


Figure 6.7. Nb maps (EDS) registered for the $(Fe_{86-x}Nb_xB_{14})_{0.88}Tb_{0.12}$ alloys prepared with melting current $I$ = 35 A. (a) $x$ = 2, (b) $x$ = 4, (c) $x$ = 6, (d) $x$ = 8 [102].

## 6.2.2. Magnetic properties

The magnetic hysteresis loops measured using SQUID magnetometer at room temperature in field up to 7 T for all studied material ($x$ = 2, 4, 6, 8) are presented on Figure 6.8. Moreover, the magnetic parameters (indicating in second quarter) are collected in Table 6.4. As can be seen, the coercivity as well as $|JH|_{max}$ increase with increasing Nb content, reaching a maximum for $x$ = 6 ($H_c$ = 5.7 T, $|JH|_{max}$ = 412 kJ/m$^3$.

Note that in case of 6 and 8 at. % of Nb content the magnetic hysteresis loops are unclosed and asymmetric.

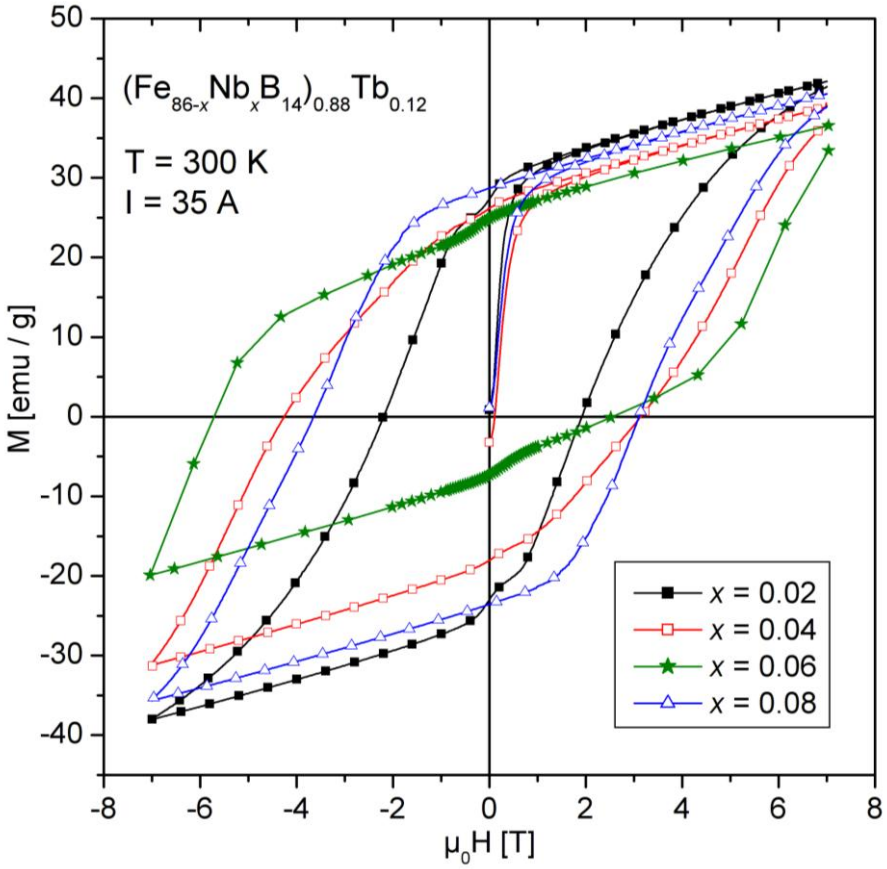


Figure 6.8. Hysteresis loops (measured at room temperature) for the $(Fe_{86-x}Nb_xB_{14})_{0.88}Tb_{0.12}$ alloys prepared using melting current equal to 35 A [102].

Table 6.4. Selected magnetic parameters of the $(Fe_{86-x}Nb_xB_{14})_{0.88}Tb_{0.12}$ alloys prepared using melting current $I$ = 35 A and measured in as-cast state at room temperature ($H_c$ – coercive field, $M_{7T}$ – magnetization in 7 T, $M_r$ – remanence magnetization, $B_r$ – remanence induction, $|JH|_{max}$, $|BH|_{max}$ – energetic parameters described in text). The measurement errors are in the level of the least significant digit.

| $x$ | $\mu_0 H_c$ [T] | $M_{7T}$ [emu/g] | $M_r$ [emu/g] | $B_r$ [T] | $\|JH\|_{max}$ [kJ/m$^3$] | $\|BH\|_{max}$ [kJ/m$^3$] |
|---|---|---|---|---|---|---|
| **2** | 2.16 | 42.12 | 27.34 | 0.27 | 150 | 13.7 |
| **4** | 4.23 | 38.93 | 26.15 | 0.26 | 275 | 13.3 |
| **6** | 5.70 | 36.53 | 24.88 | 0.25 | 412 | 12.2 |
| **8** | 3.68 | 40.54 | 28.71 | 0.29 | 345 | 16.2 |

The magnetic force microscopy pictures recorded for the alloys with different Nb content are presented in Figure 6.9. The red and blue areas can be attributed to attractive and repulsive force acting on the MFM tip, respectively. As may expect based on the SEM observations, the magnetic domain structure is related to Nb-reach regions which are nonmagnetic (or magnetically week). In all exanimated cases the domain structure is irregular with typical size of domain in order of tens micrometers. However, for the material with $x = 6$ the domains are clearly smaller and even some areas below 1 μm were also observed.

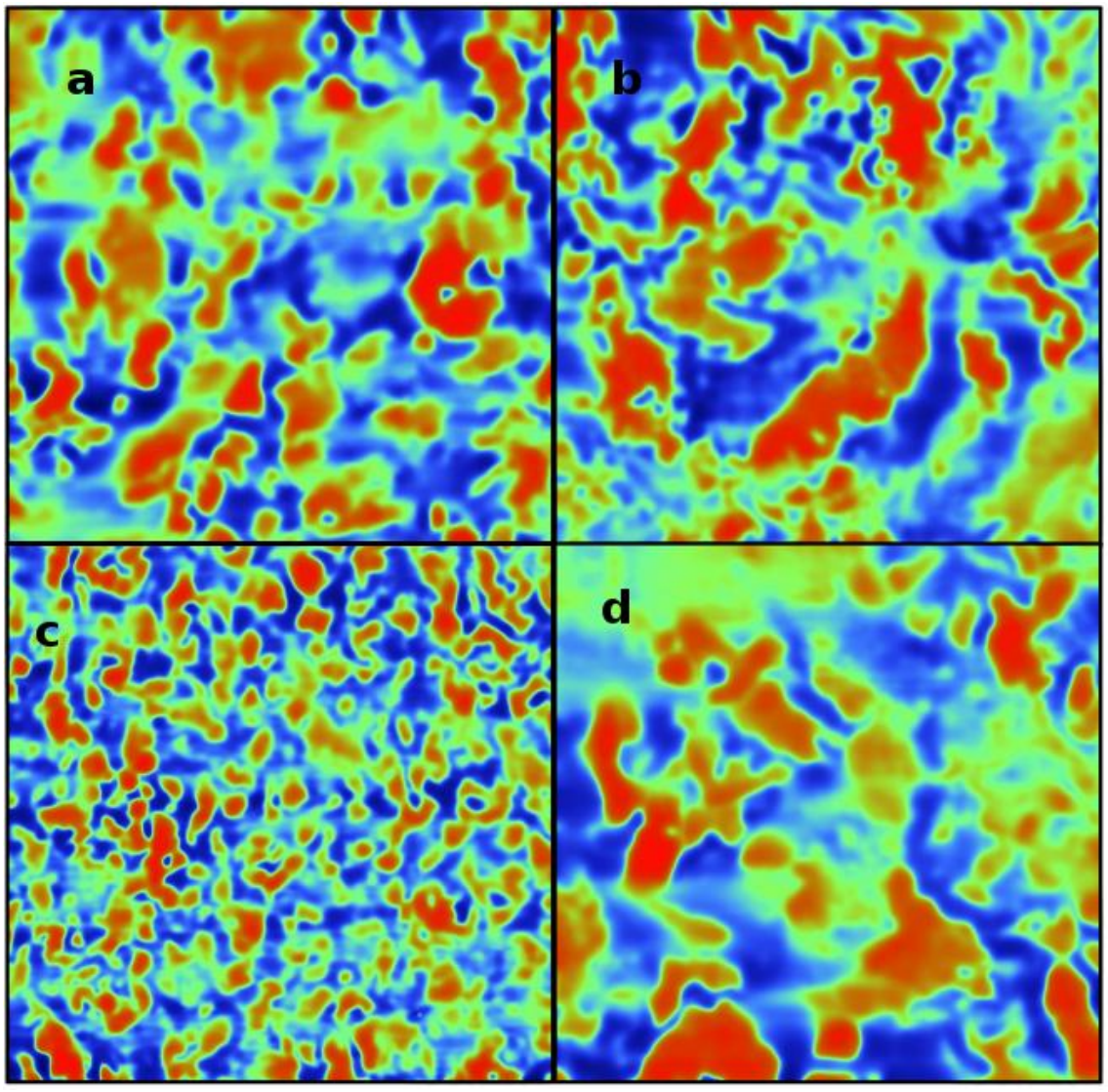


Figure 6.9. MFM pictures (scan 40 x 40 μm) for the $(Fe_{86-x}Nb_xB_{14})_{0.88}Tb_{0.12}$ alloys prepared with melting current $I = 35$ A. (a) $x = 2$, (b) $x = 4$, (c) $x = 6$, (d) $x = 8$ [102].

## 6.3. Effect of field annealing on hard magnetic properties of the $(Fe_{80}Nb_6B_{14})_{0.88}Tb_{0.12}$ alloy

From application point of view, very important information is a temperature dependence on magnetic properties, especially for temperatures higher than 300 K. Therefore, a material with the highest value of coercivity i.e. $(Fe_{80}Nb_6B_{14})_{0.88}Tb_{0.12}$, prepared using the form with 1.5 mm in diameter and melting current equal to 35 A was chosen to perform temperature investigations.

Figure 6.10 presents the magnetic hysteresis loops obtained for the as-cast material measured in wider range of temperature up to 700 K. As may expect, the magnetic properties decrease with increasing temperature. However, it should be noted that at $T$ = 550 K, the coercivity is still higher than 1 T with a decrease of magnetic remanence by only about 25 %.

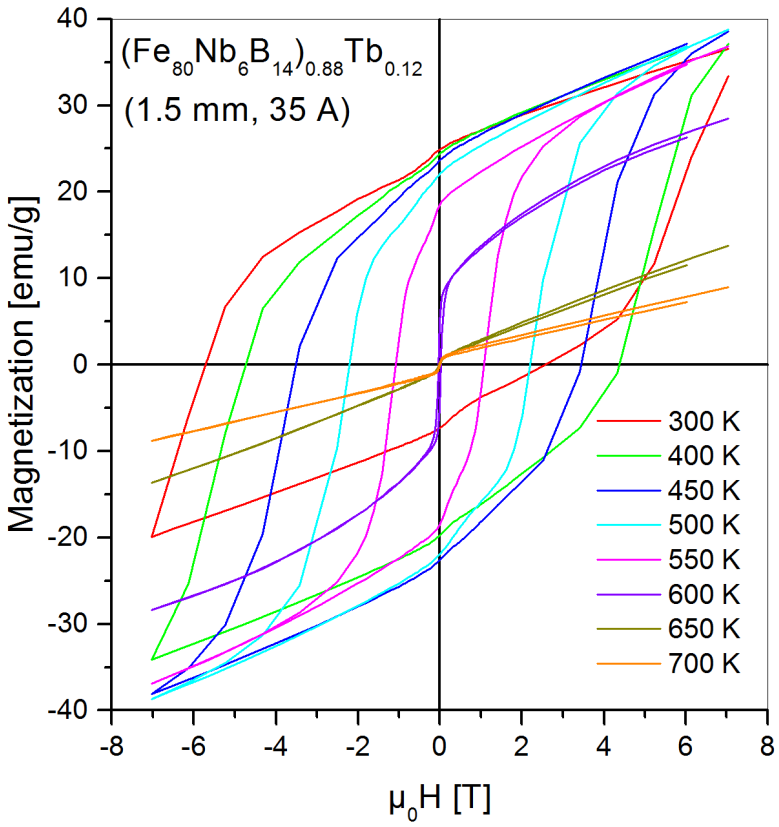


Figure 6.10. Hysteresis loops for the $(Fe_{80}Nb_6B_{14})_{0.88}Tb_{0.12}$ alloy measured at different temperatures [102].

As one can see, the hysteresis loop at room temperature is unclosed and asymmetric which suggests a presents of some ultra-hard magnetic objects with very high magnetic anisotropy. In order to change of magnetic direction for these objects, the high temperature and high magnetic field should be applied. Such procedure, consisting of heating up to 700 K and cooling down to room temperature in the vicinity of 7 T magnetic field was performed and the measurements of magnetic hysteresis loops at different temperatures were repeated. The results are plotted on Figure 6.11. It should be underlined that after field annealing the coercivity at room temperature is higher than 7 T which is the best result obtaining for all discussed in this thesis materials, prepared using the form with 1.5 mm in diameter.

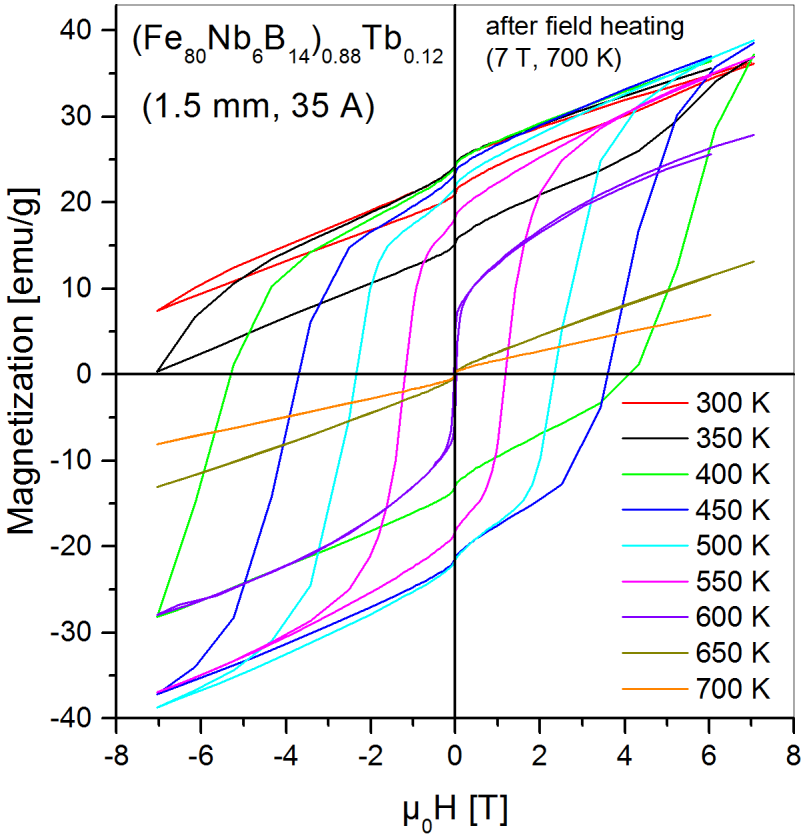


Figure 6.11. Hysteresis loops for the $(Fe_{80}Nb_6B_{14})_{0.88}Tb_{0.12}$ alloy measured at different temperatures after field cooling from 700 K in 7 T.

Figure 6.12 shows the comparison of three different states for the same sample: as-cast, after heating up to 700 K without external magnetic field and similar heating in the vicinity of 7 T magnetic field. It can be noted that the heating without field leads to little increasing of soft magnetic phase (small decreasing of magnetization near to Y axis), while after the second heating in presents of magnetic field the contribution of soft phase decreasing. Such behavior suggests a partial spring-exchange coupling between the soft and hard phases due to the fact that all structural changes should be seen after firs heating. In order to better demonstration of this phenomena, the a d*M*/d*H* curves calculated for the discussed hysteresis loops were plotted in Figure 6.13.

Finally, the temperature dependences of coercivity and remanence for the $(Fe_{80}Nb_6B_{14})_{0.88}Tb_{0.12}$ alloy in the as-cast state and after the described annealing are presented in Figure 6.14.

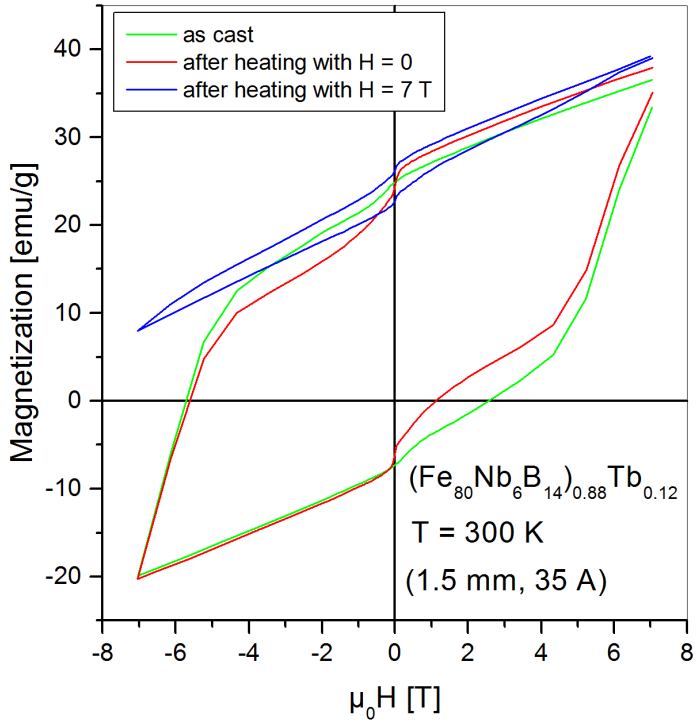


Figure 6.12. Hysteresis loops for the $(Fe_{80}Nb_6B_{14})_{0.88}Tb_{0.12}$ alloy measured at different state of sample: as-cast , after heating up to 700 K with and without applied external magnetic field [102].

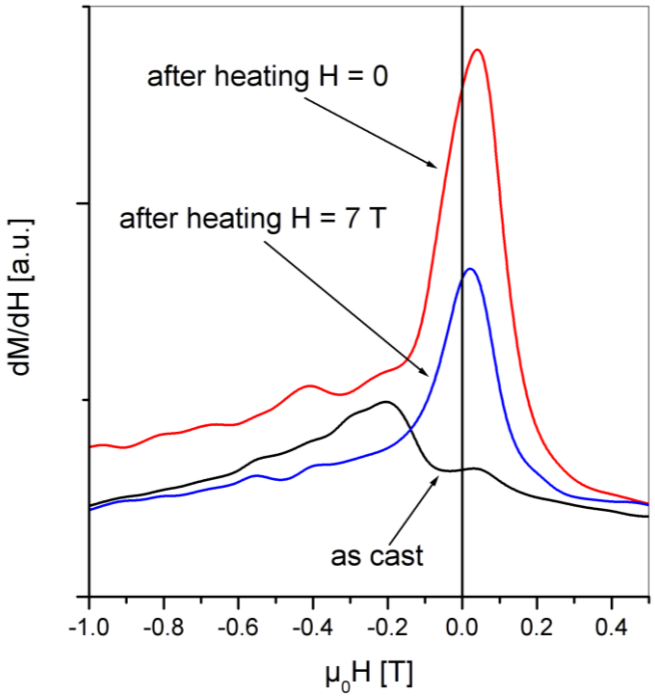


Figure 6.13. Derivatives of magnetization for the $(Fe_{80}Nb_6B_{14})_{0.88}Tb_{0.12}$ alloy measured at different sate of sample: as-cast , after heating up to 700 K with and without applied external magnetic field [102].

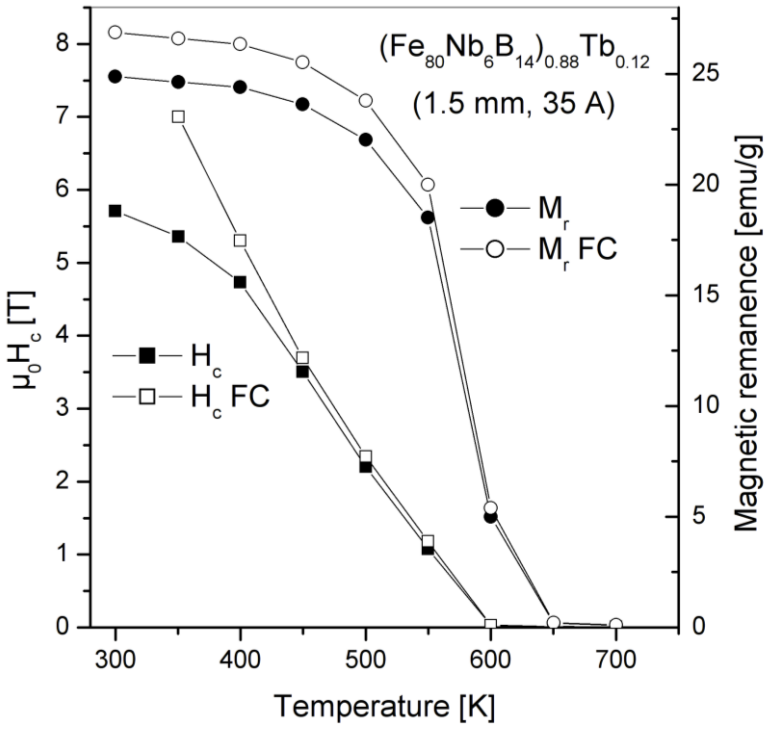


Figure 6.14. Temperature dependence of coercivity and remanence for the $(Fe_{80}Nb_6B_{14})_{0.88}Tb_{0.12}$ alloy without and with field cooling (FC) from 700 K in 7 T [102].

# 6.4. Influence of Y addition on magnetic properties of the Fe-Nb-B-Tb/Y alloys

For a practical meaning, permanent magnets should characterize simultaneously – high coercivity as well as high magnetic remanence. In the case of our studied alloys ultra-high coercive field is reached i.e., more than 7 T at room temperature for the $(Fe_{80}Nb_6B_{14})_{0.88}Tb_{0.12}$ alloy after field annealing. Unfortunately, Tb and Fe are antiferromagnetically coupled that results in relatively low values of magnetic saturation and, in a consequence, low magnetic remanence. Therefore, a partial substitution of Tb by Y, as a non-magnetic element, is particularly interesting. Such replacement may cause two desired effects: i) an increase of magnetic saturation by withdrawing a part on Tb from the opposite to Fe magnetic sublattice and ii) formation of $Y_2Fe_{14}B$ phase. Moreover, as was shown by Tan et al [77], which investigated a $Fe_{67-x}Co_{10}Nd_3Y_xB_{20}$ ($x$ = 0, 2, 6, 10) alloys prepared by suction casting technique, a small addition of Y (6 at.%) can improve the glass-forming ability (GFA) of such materials. The expected occurrence of the Yttrium and Terbium ternary phases (high saturation and ultra-high coercivity, respectively) may leads to the so-called spring-exchange coupling preferred for improving the $|BH|_{max}$ parameter as well as decreasing the content of rare earths in permanent magnets. Therefore, the studies of $(Fe_{80}Nb_6B_{14})_{0.88}Tb_{0.12-x}Y_x$ compounds may be important from scientific as well as application point of view.

## 6.4.1. Structural properties

In this section a series of alloys base on $(Fe_{80}Nb_6B_{14})_{0.88}Tb_{0.12-x}Y_x$ chemical composition will be considered. The $x$ parameter corresponds to Yttrium content and it is equal to 0.0, 0.02, 0.04, 0.06, 0.08, 0.1 and 0.12. All samples were prepared using optimal technology conditions i.e. the form with 1 mm in diameter and melting current equals 35 A. Selected part of X-ray patterns is presented in Figure 6.15. Moreover the phases analysis is summarized in Table 6.5. For the all investigated alloys a significant content (about 94%) of ternary phase $(Tb / Y)_2Fe_{14}B$ supplemented by little addition of $(Tb/Y)Fe_2$ phase was detected. Note, that due to a strong resemblance of X-ray patterns, a separation between $Y_2Fe_{14}B$ and $Tb_2Fe_{14}B$ phases was impossible.

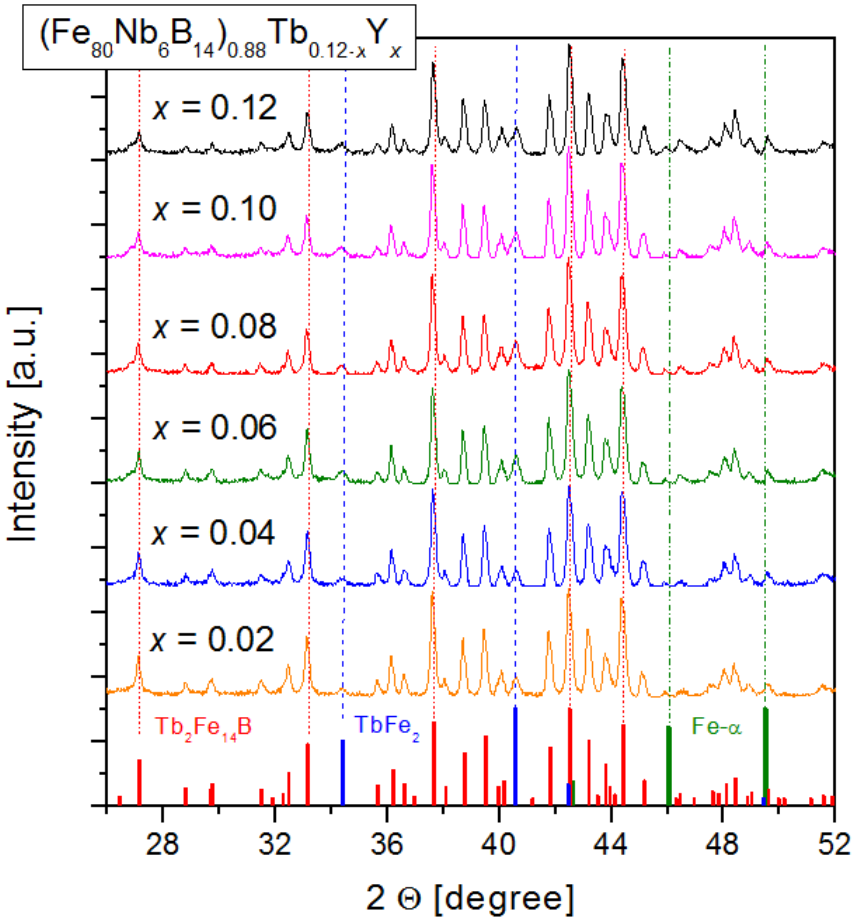


Figure 6.15. The part of X-ray patterns for the $(Fe_{80}Nb_6B_{14})_{0.88}Tb_{0.12-x}Y_x$ alloys with $d$ = 1 mm and $I$ = 35 A.

Table 6.5. The phase composition estimated base on the X-ray diffraction patterns of the $(Fe_{80}Nb_6B_{14})_{0.88}Tb_{0.12-x}Y_x$ alloys.

| Phase | Phase content vs. $x$ (Y content) [%] ±2 | | | | | |
|---|---|---|---|---|---|---|
| | 0.12 | 0.10 | 0.08 | 0.06 | 0.04 | 0.02 |
| **$(Tb / Y)_2Fe_{14}B$** | 95 | 93 | 94 | 93 | 94 | 95 |
| **$(Tb / Y)Fe_2$** | 5 | 7 | 6 | 7 | 6 | 5 |

## 6.4.2. Magnetic properties

Figures from Figure 6.16 to Figure 6.22 present magnetic hysteresis loops measured at four different temperatures for all discussed samples starting from $x$ = 0.0 (without Yttrium) to $x$ = 0.12 (without Terbium), respectively. As may be noted, in case of materials with high content of Tb (more than 6 at. %), the hysteresis are asymmetrical and opened. This situation was also observed in previous sections and suggests that some of the magnetic objects are blocked and 7 T of external magnetic field is not sufficient to change its direction, especially at low temperatures.

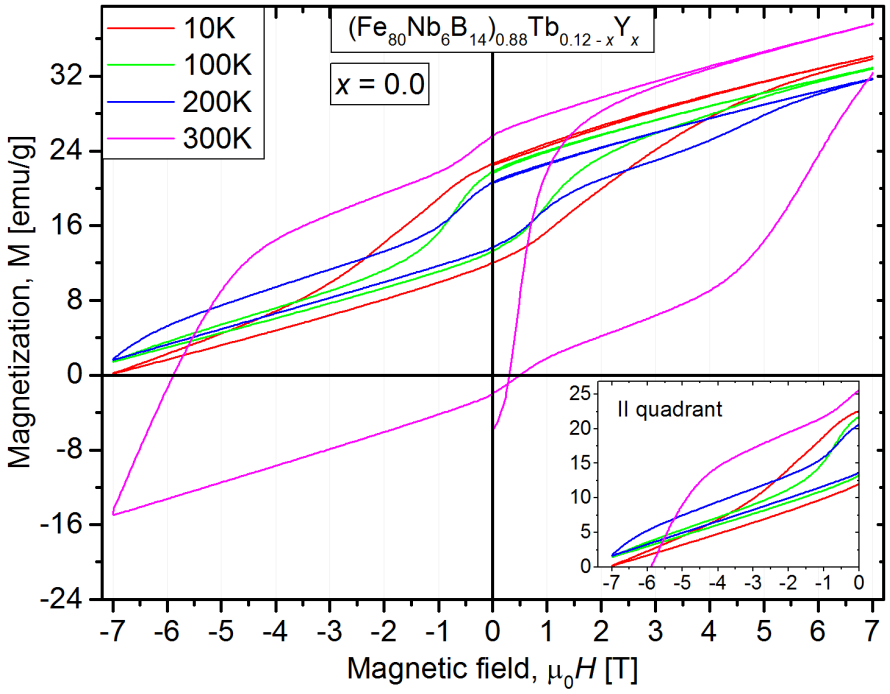


Figure 6.16. The magnetic hysteresis loops measured at different temperatures for the $(Fe_{80}Nb_6B_{14})_{0.88}Tb_{0.12}$ alloy; melting current and diameter are equal to 35 A and 1 mm.

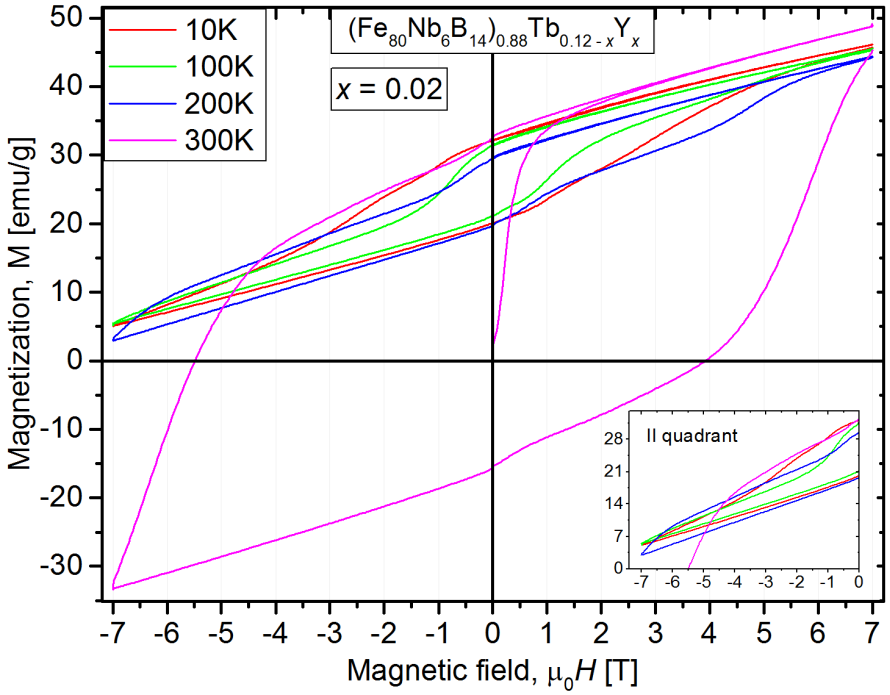


Figure 6.17. The magnetic hysteresis loops measured at four different temperatures for the $(Fe_{80}Nb_6B_{14})_{0.88}Tb_{0.10}Y_{0.02}$ alloy prepared using melting current equal to 35 A and form with 1 mm in diameter.

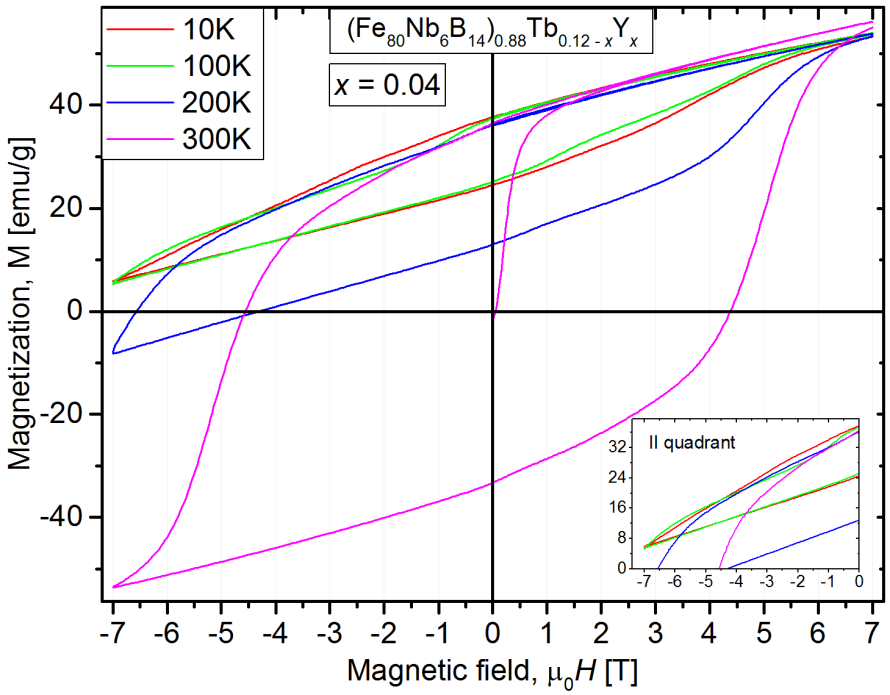


Figure 6.18. The magnetic hysteresis loops measured at four different temperatures for the $(Fe_{80}Nb_6B_{14})_{0.88}Tb_{0.08}Y_{0.04}$ alloy; melting current and diameter equals 35 A and 1 mm.

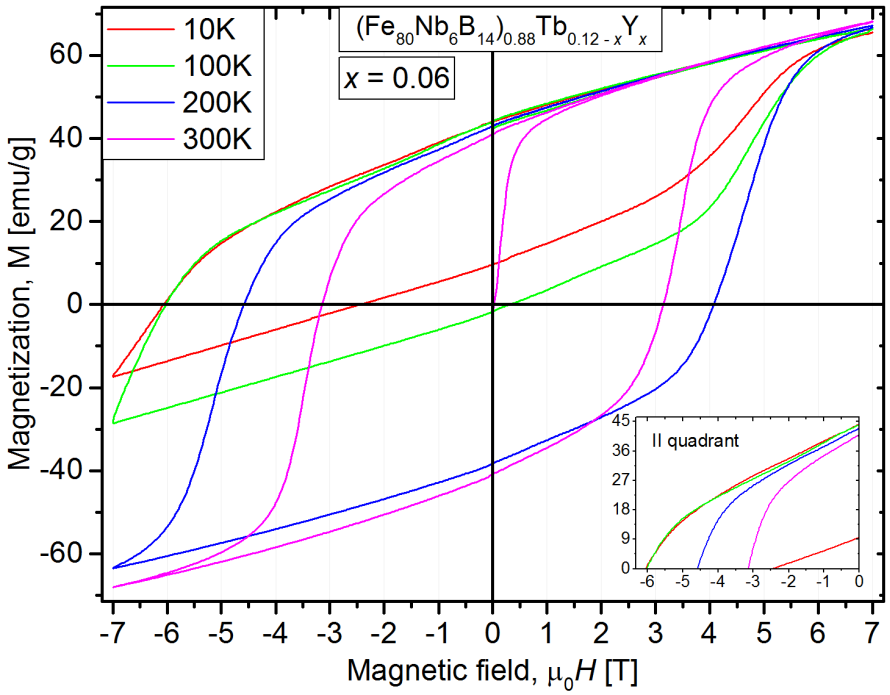


Figure 6.19. The magnetic hysteresis loops measured at four different temperatures for the $(Fe_{80}Nb_6B_{14})_{0.88}Tb_{0.06}Y_{0.06}$ alloy; melting current and diameter equals 35 A and 1 mm.

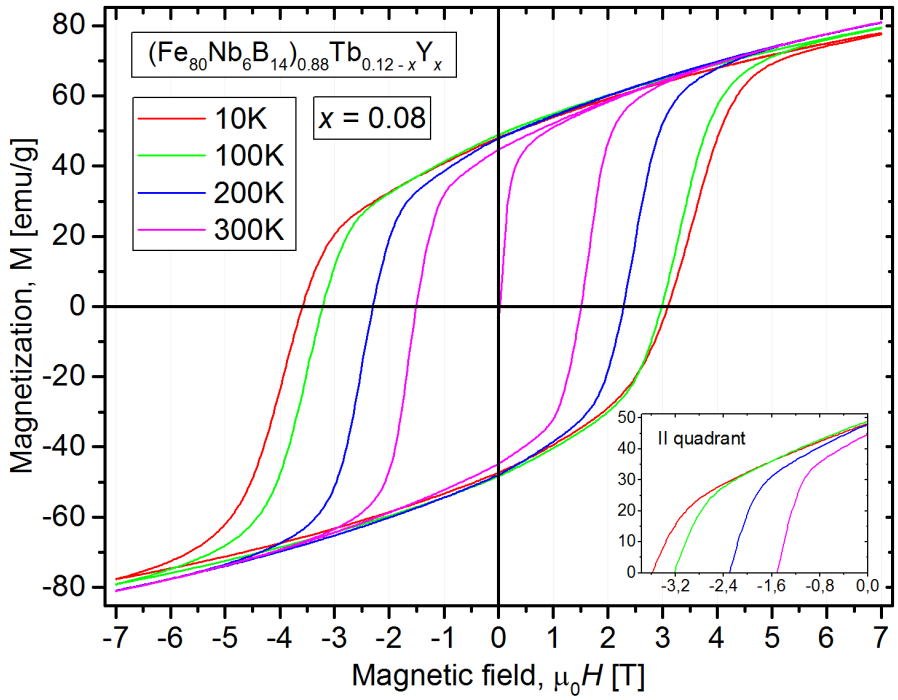


Figure 6.20. The magnetic hysteresis loops measured at four different temperatures for the $(Fe_{80}Nb_6B_{14})_{0.88}Tb_{0.04}Y_{0.08}$ alloy; melting current and diameter equals 35 A and 1 mm.

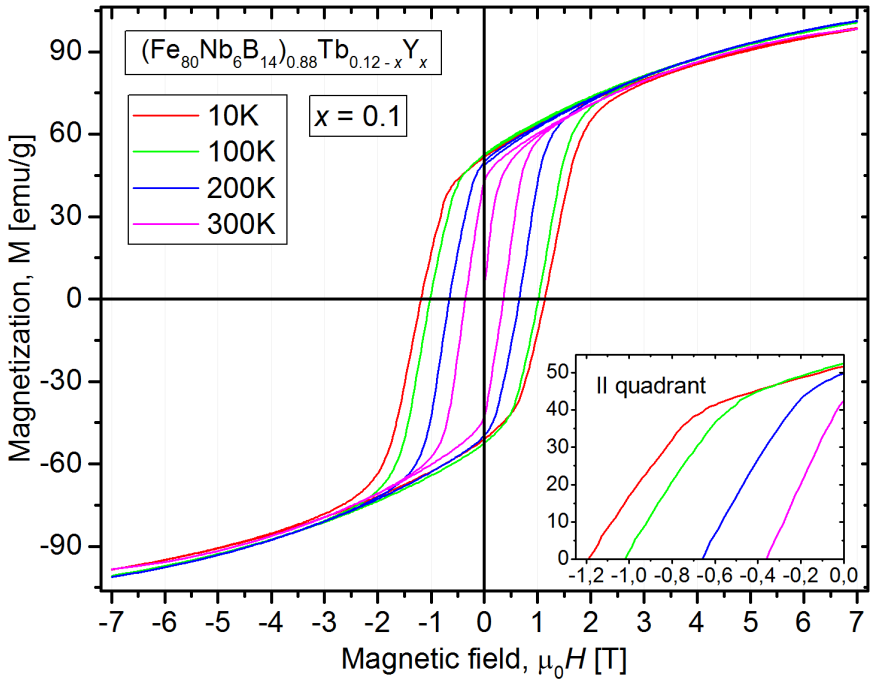


Figure 6.21. The magnetic hysteresis loops measured at four different temperatures for the $(Fe_{80}Nb_6B_{14})_{0.88}Tb_{0.02}Y_{0.1}$ alloy prepared using melting current equal to 35 A and form with 1 mm in diameter.

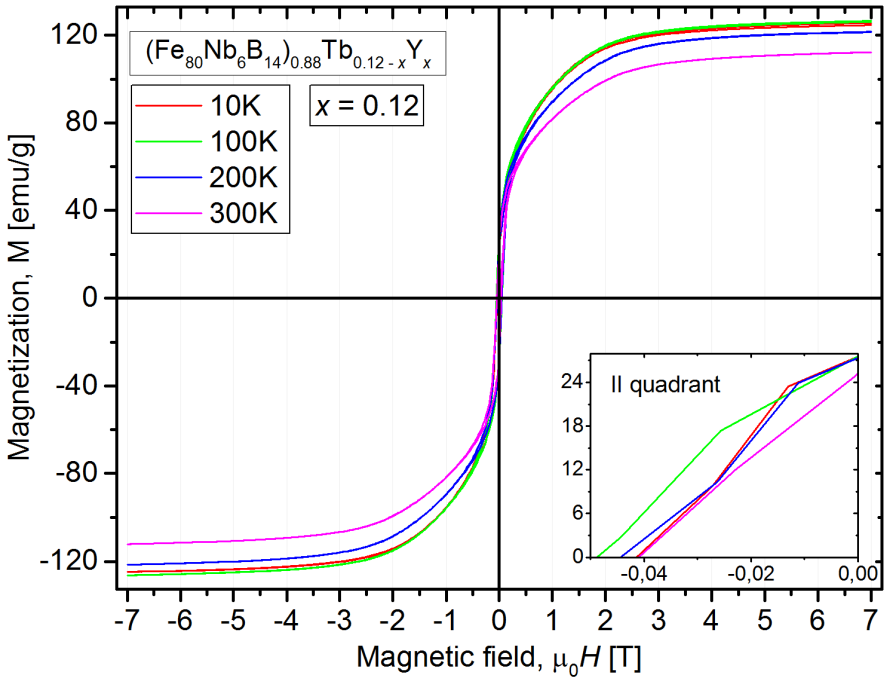


Figure 6.22. The magnetic hysteresis loops measured at four different temperatures for the $(Fe_{80}Nb_6B_{14})_{0.88}Y_{0.12}$ alloy prepared using melting current equal to 35 A and form with 1 mm in diameter.

The comparison of all hysteresis loops measured at room temperature was plotted in Figure 6.23. Moreover, Table 6.6 summarizes the magnetic properties of discussed materials including remanence, coercivity measured in negative and positive external magnetic field, magnetic saturation at 7 T and the energy parameters: $|BH|_{MAX}$ as well as $|JH|_{MAX}$. It can be noted that the magnetic saturation increases with Y content, which indicates that hard magnetic phase $Tb_2Fe_{14}B$ is replaced by $Y_2Fe_{14}B$ phase with higher saturation. As may be expected the coercivity decreases with decreasing Tb content, however, it is also important to note that in case of material with 8 at. % of Y (only 4 at. % of Tb) the coercivity is still relatively high and equals 1.5 T. On the other hand, the magnetic saturation as well as remanence increases with increasing Y content and in the case of $x = 0.08$ there are equal to 81 emu / g and 44.7 emu / g, respectively. Moreover, maximum energy product $|BH|_{MAX}$ reaches 33.8 KJ/m$^3$ (for $x = 0.08$) which is three times higher than in case of material without Yttrium. The values of selected magnetic parameter were plotted as a function of $x$ in Figure 6.24 and Figure 6.25.

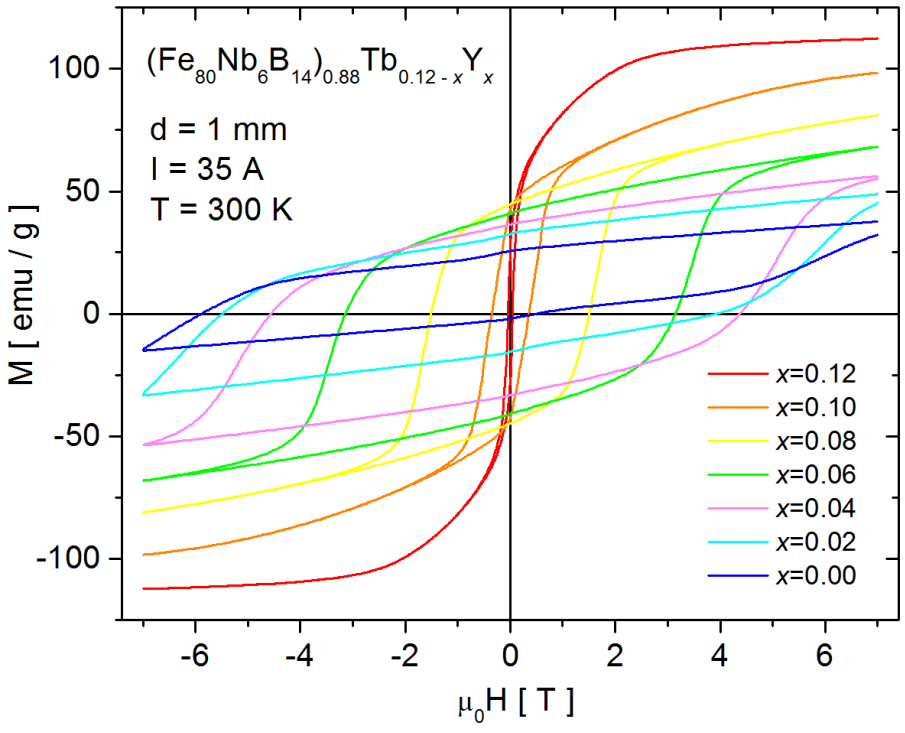


Figure 6.23. The comparison of magnetic hysteresis loops at room temperature for the $(Fe_{80}Nb_6B_{14})_{0.88}Tb_{0.12-x}Y_x$ alloys with different Y and Tb content, prepared using melting current equals 35 A and form with 1 mm in diameter.

Table 6.6. The magnetic properties of $(Fe_{80}Nb_6B_{14})_{0.88}Tb_{0.12-x}Y_x$ alloys i.e. saturation at 7 T, coercivity measured in negative and positive external magnetic field, remanence as well as reduced remanence and the energy parameters. The measurement errors are in the level of the least significant digit.

| *x* | $M_S$ [ emu /g ] | $-\mu_0H_C$ [ T ] | $+\mu_0H_C$ [ T ] | $M_R$ [ emu / g ] | $M_R/M_S$ [ a. u. ] | $\|JH\|_{MAX}$ [ kJ/m3 ] | $\|BH\|_{MAX}$ [ kJ/m3 ] |
|---|---|---|---|---|---|---|---|
| **0.12** | 112 | 0.05 | 0.05 | 25 | 0.22 | 2.21 | 1.8 |
| **0.1** | 99 | 0.35 | 0.35 | 42.5 | 0.43 | 32.6 | 17.6 |
| **0.08** | 81 | 1.5 | 1.5 | 44.7 | 0.55 | 256 | 33.8 |
| **0.06** | 68 | 3.15 | 3.15 | 41 | 0.6 | 432 | 27 |
| **0.04** | 56 | 4.57 | 4.4 | 36.6 | 0.65 | 489.7 | 22.1 |
| **0.02** | 49 | 5.43 | 4 | 32.5 | 0.66 | 531.5 | 16.2 |
| **0** | 38 | 5.88 | 0.5 | 25.5 | 0.67 | 463.8 | 11.6 |

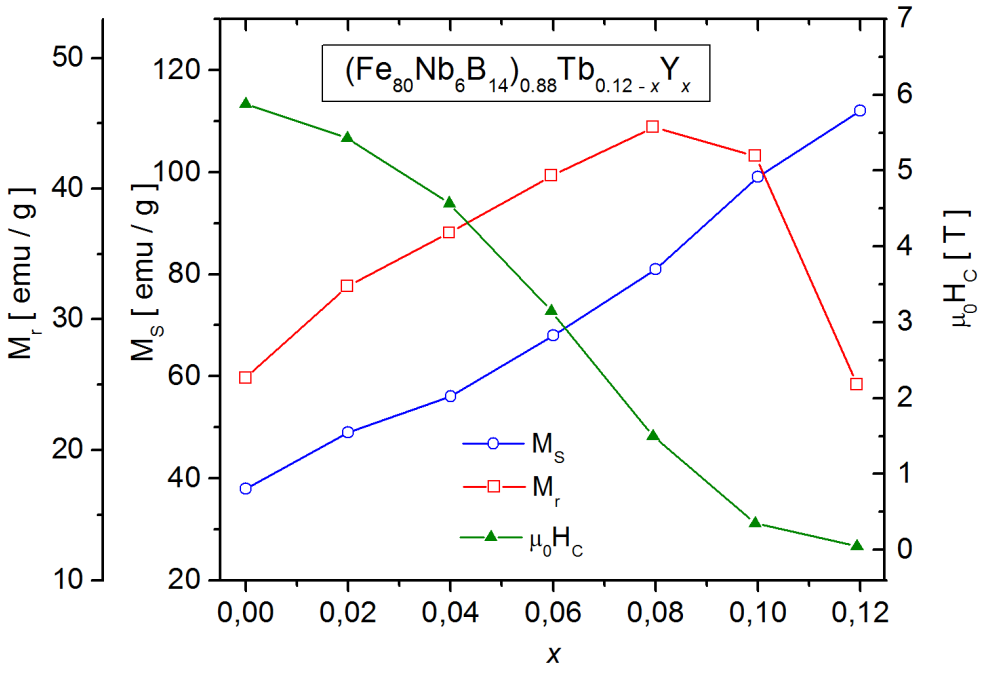


Figure 6.24. The magnetic remanence, saturation (at 7 T) and coercivity measured in negative external magnetic field measured at room temperature and plotted as a function of *x* parameter for the $(Fe_{80}Nb_6B_{14})_{0.88}Tb_{0.12-x}Y_x$ type alloys.

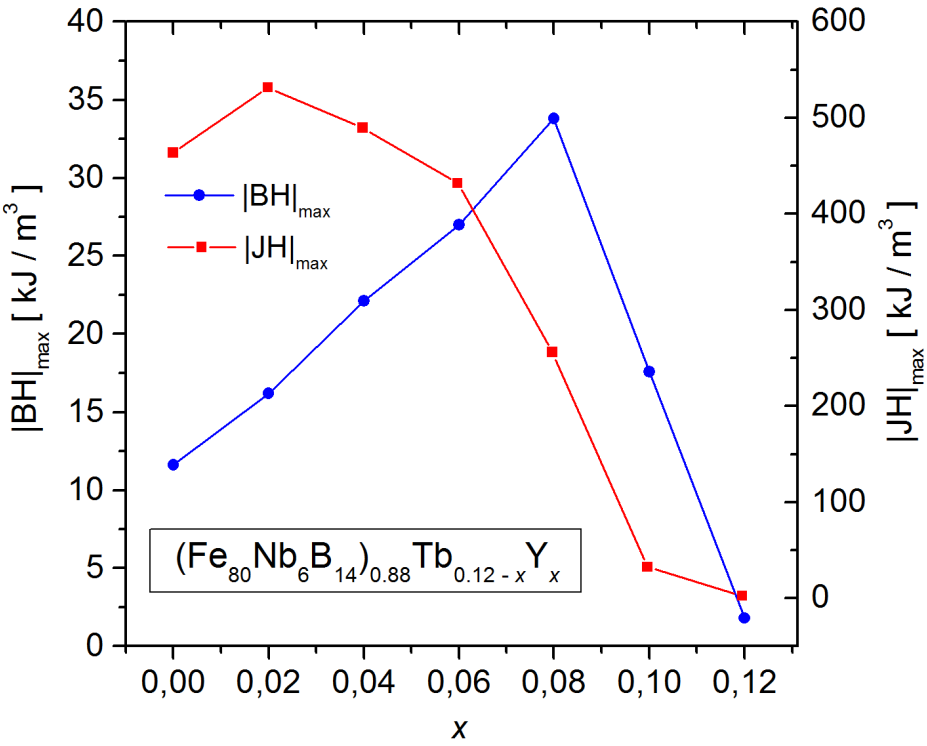


Figure 6.25. The maximal energy product properties: $|BH|_{MAX}$ and $|JH|_{MAX}$ plotted as a function of $x$ parameter for the $(Fe_{80}Nb_6B_{14})_{0.88}Tb_{0.12-x}Y_x$ type alloys.

## 6.5. Influence of cooling rate on structural and magnetic properties of $(Fe_{78}Nb_8B_{14})_{1-x}Tb_x$ alloys

The structural and magnetic properties of alloys produced by the vacuum suction technique can be controlled by two important parameters – melting current using during preparation procedure and sample diameter corresponding to cooling rate of melted material. Generally, decreasing of sample diameter (for example to 0.5 mm) leads to strong magnetic hardening effect as were presented in section 5.2 referring to the $(Fe_{80}Nb_6B_{14})_{1-x}Tb_x$ ($x$ = 0.06, 0.08, 0.1, 0.11 and 0.12) compounds. In this section, selected properties of series of alloys $(Fe_{78}Nb_8B_{14})_{1-x}Tb_x$ ($x$ = 0.08, 0.1, 0.12), prepared using the optimal melting current of 35 A is presented. Each chemical composition were prepared using three different diameter, $d$ = 0.5 mm, 1 mm and 1.5 mm. The optimal chemical composition is expected for $x$ = 0.12, however, lower Tb content is important form economical point of view. Structural observation were carried out using X-ray diffraction and Scanning Electron Microscope. Magnetic investigations were performed using Magnetic Force Microscope as well as SQUID Magnetometer in temperature range from 10 K to 300 K and external magnetic fields up to 7 T.

The selected part of X-ray patterns for material with optimal chemical composition prepared with three different diameters is presented in Figure 6.26. Moreover, Figure 6.27 shows comparison of results obtained for smaller Tb content. The phase analysis corresponding to this figures is summarized in Table 6.7 and Table 6.8, respectively. The alloys consists mainly hard magnetic phase $Tb_2Fe_{14}B$ and some soft magnetic additions like $TbFe_2$, Fe-O and Nb-Fe-B compounds. The contribution of obtained phases varies slightly depending on the Tb content as well as sample diameter, however any clear tendency was not noted.

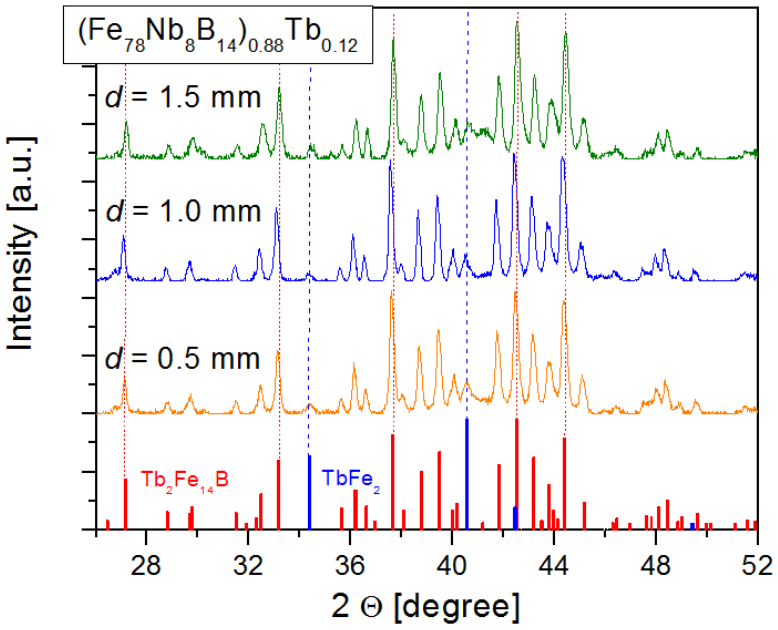


Figure 6.26. Part of X-ray patterns for the $(Fe_{78}Nb_8B_{14})_{0.88}Tb_{0.12}$ alloys prepared with different value of sample diameter.

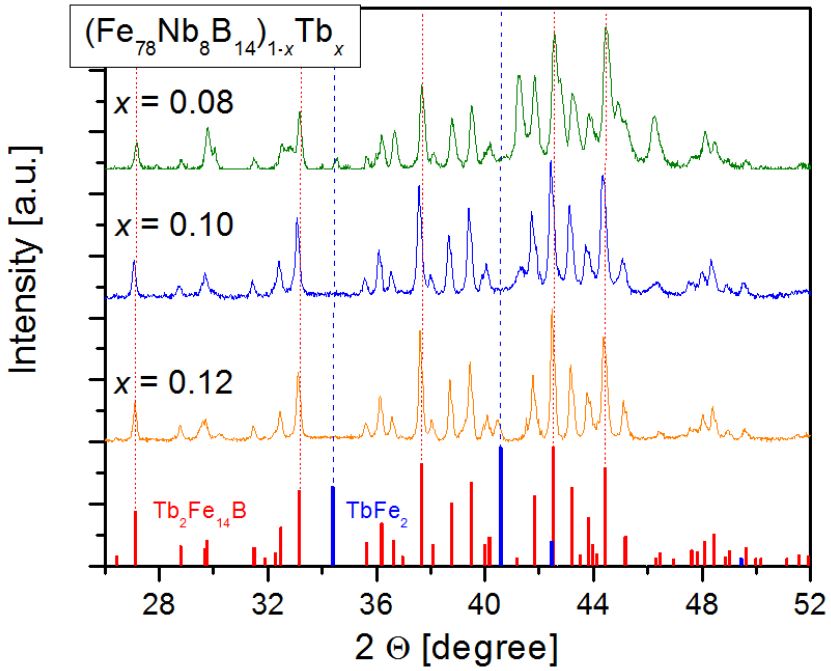


Figure 6.27. Part of the X-ray patterns for the $(Fe_{78}Nb_8B_{14})_{1-x}Tb_x$ alloys prepared with different content of Tb addition.

Table 6.7. The phase composition estimated base on the X-ray diffraction patterns of the $(Fe_{78}Nb_8B_{14})_{0.88}Tb_{0.12}$ alloys prepared with different value of sample diameter.

| *d* [mm] | $Tb_2Fe_{14}B$ [%] ±2 | $TbFe_2$ [%] ±2 | $Fe_2O_3$ [%] ±2 |
|---|---|---|---|
| **1.5** | 77 | 5 | 18 |
| **1** | 95 | 5 | - |
| **0.5** | 82 | 3 | 15 |

Table 6.8. The phase composition and structural parameters estimated base on the X-ray diffraction patterns of the $(Fe_{78}Nb_8B_{14})_{1-x}Tb_x$ alloys.

| *x* [A] | $Tb_2Fe_{14}B$ [%] ±2 | $TbFe_2$ [%] ±2 | B-Fe-Tb, Fe-O, Nb-Fe-B [%] ±2 | Unit cell [Å] | grain size [nm] ±10 |
|---|---|---|---|---|---|
| **0.08** | 63 | 5 | 32 | a= 8.757 ±0.001<br>c=12.034 ±0.002 | 26 |
| **0.1** | 89 | - | 11 | a= 8.779 ±0.001<br>c=12.068 ±0.001 | 30 |
| **0.12** | 85 | 3 | 12 | a=8.771 ±0.001<br>c=12.054 ±0.002 | 37 |

Figure 6.28, Figure 6.29 and Figure 6.30 present an example of sample surface obtained for three different diameter $d$ = 0.5 mm, 1 mm and 1.5 mm for the alloys with 12 at.% of Tb addition. One may note that depending on cooling rate the specific microstructure is formed. A formation of dendrite-like grains with micrometric (or even smaller) dimensions is clearly visible. Moreover, in case of material prepared with lower cooling rate, a flat spaces also appear, while for alloy with $d$ = 0.5 mm and 1 mm the grains are spread out for whole surface.

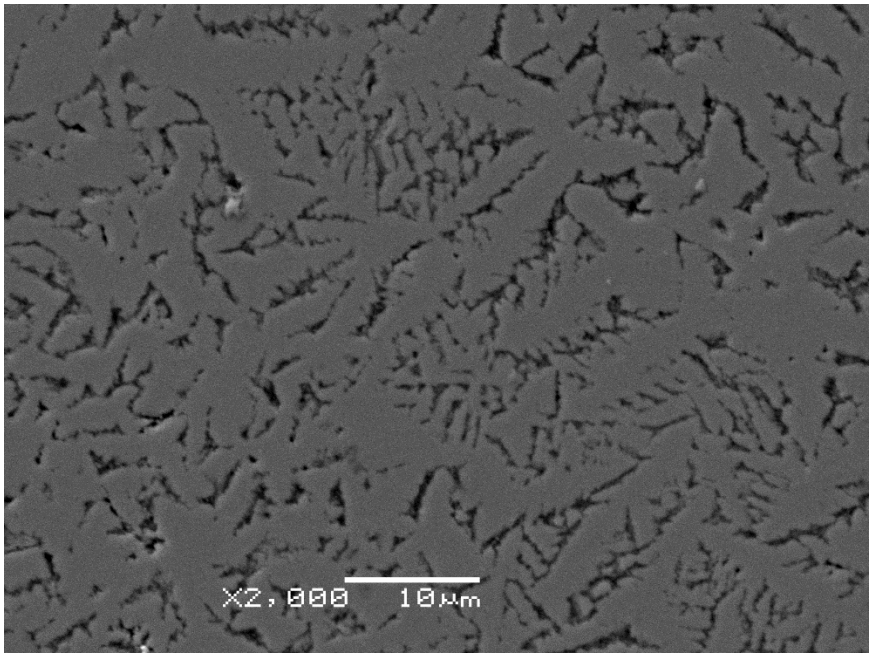


Figure 6.28. SEM image (SEI mode) for the $(Fe_{78}Nb_8B_{14})_{0.88}Tb_{0.12}$ alloy with $d$ = 0.5 mm.

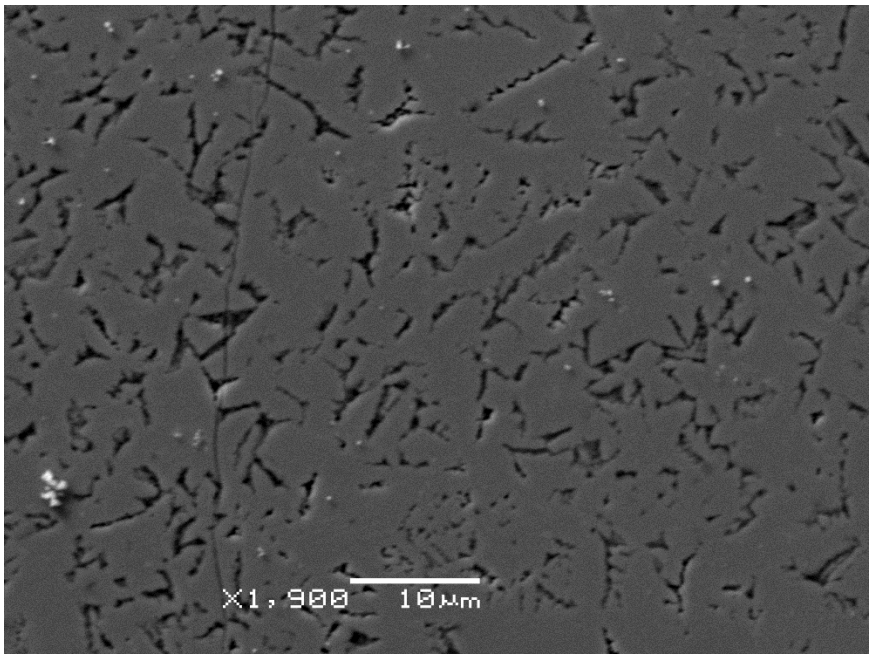


Figure 6.29. SEM image (SEI mode) for the $(Fe_{78}Nb_8B_{14})_{0.88}Tb_{0.12}$ alloy with $d$ = 1 mm.

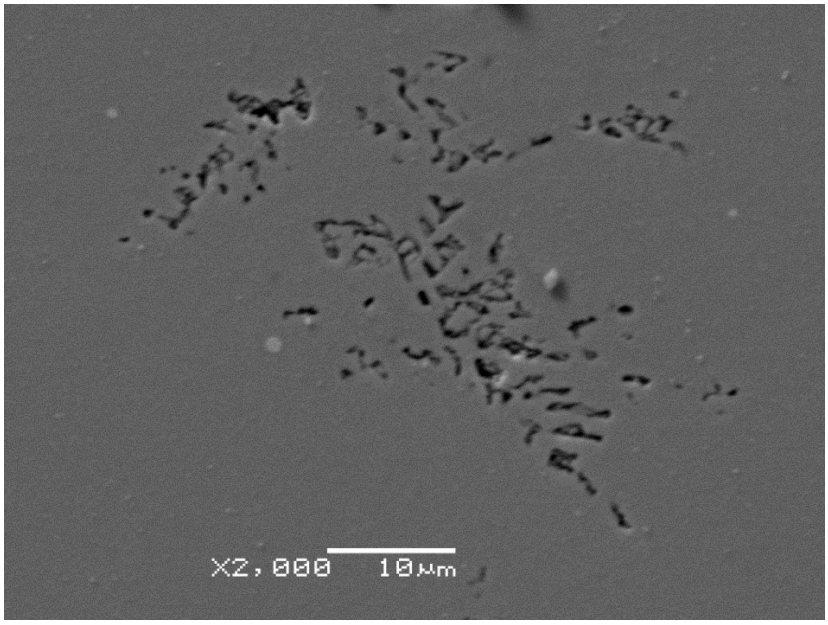


Figure 6.30. SEM image (SEI mode) for the $(Fe_{78}Nb_8B_{14})_{0.88}Tb_{0.12}$ alloy with $d$ = 1.5 mm.

The magnetic hysteresis loops for the series of samples with $x$ = 0.08, 0.1 and 0.12 were presented in sets of Figure 6.31 - Figure 6.33, Figure 6.34 - Figure 6.36 and Figure 6.37 - Figure 6.39, respectively. Each set consists of three Figures with different diameters: $d$ = 0.5 mm, 1 mm and 1.5 mm. Moreover, selected materials measured at room temperature were also compared in Figure 6.40. Generally, presented results are in agreement with studies performed during preliminary investigations. The coercivity strongly increases with decreasing sample diameter as well as increasing of Tb content. It is important to note that in the case of material with 8 at. % of Terbium addition, the coercivity is still relatively high and equals 1.23 T for $d$ = 1 mm. The strongest magnetic hardening effect was observed for the alloys with $x$ = 0.1 i.e., coercive field increases from 1.16 T to 5.6 T for diameter $d$ = 1.5 mm and 0.5 mm, respectively. Similar tendency can be seen in the case of material with optimal chemical composition ($x$ = 0.12), however the hysteresis loop is strongly asymmetrical and opened. Such situation suggests that real coercivity may be much higher after magnetic saturation in higher (> 7 T) external magnetic field. Indeed, the $(Fe_{78}Nb_8B_{14})_{0.88}Tb_{0.12}$ alloy with $d$ = 0.5 mm was chosen for further investigation in external magnetic field range up to 14 T as presented in Figure 6.41. In this case the hysteresis loop is almost symmetrical and the measured **coercivity is equal to 8.6 T after saturation in 14 T** of external magnetic field. The magnetic parameters for all discussed materials are summarized in Table 6.9.

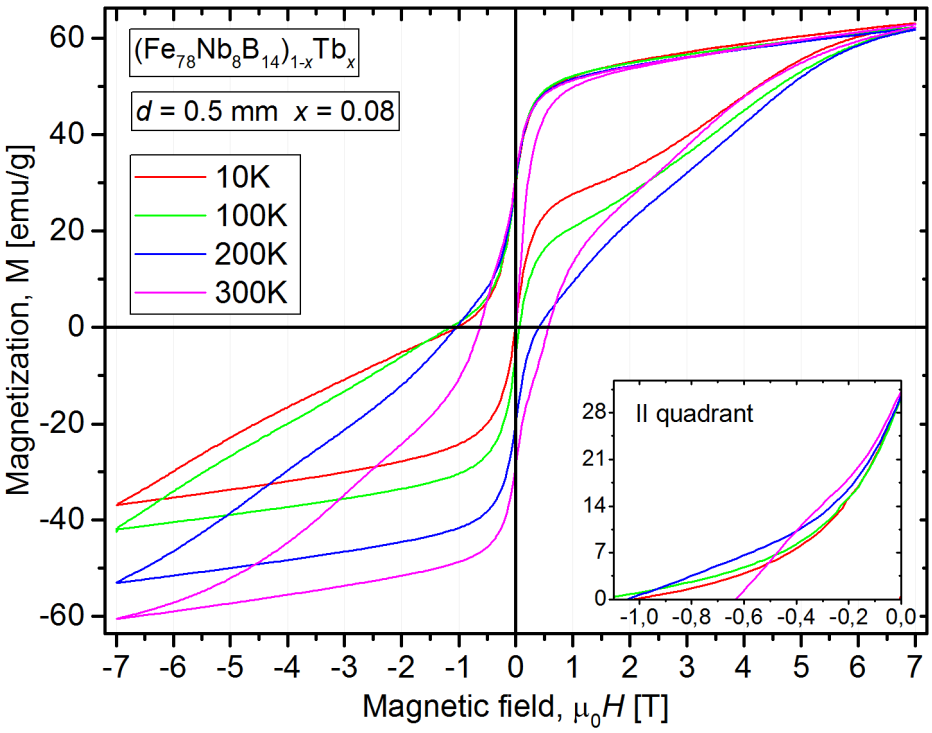


Figure 6.31. The magnetic hysteresis loops (T = 10 – 300 K) of the $(Fe_{78}Nb_8B_{14})_{0.92}Tb_{0.08}$ alloy prepared using melting current equal to 35 A and form with 0.5 mm in diameter.

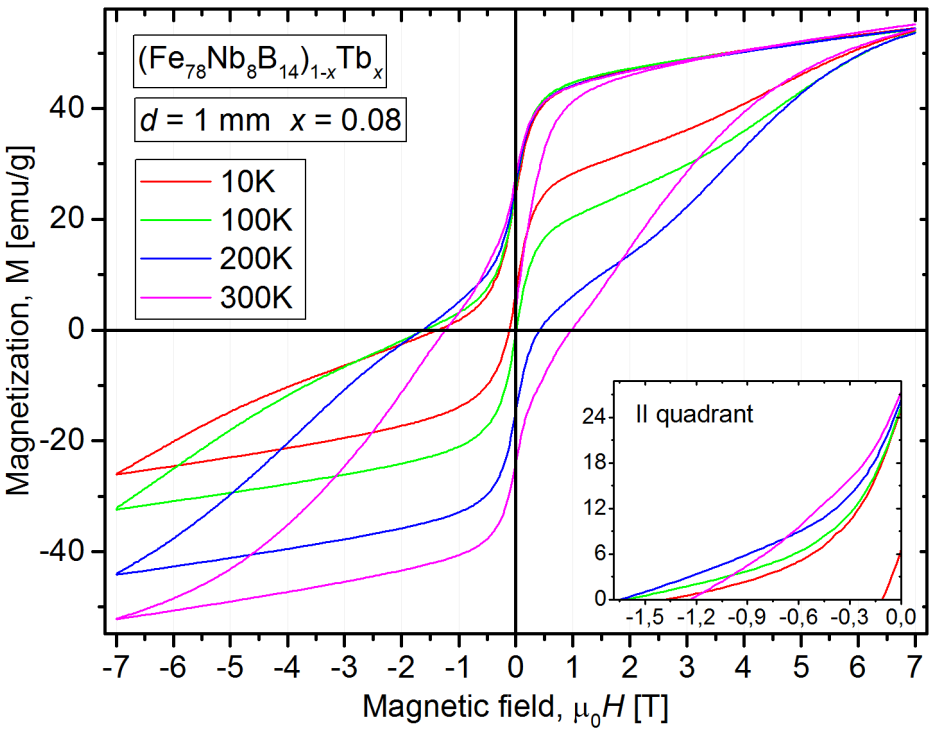


Figure 6.32. The magnetic hysteresis loops (T = 10 – 300 K) of the $(Fe_{78}Nb_8B_{14})_{0.92}Tb_{0.08}$ alloy prepared using melting current equal to 35 A and form with 1 mm in diameter.

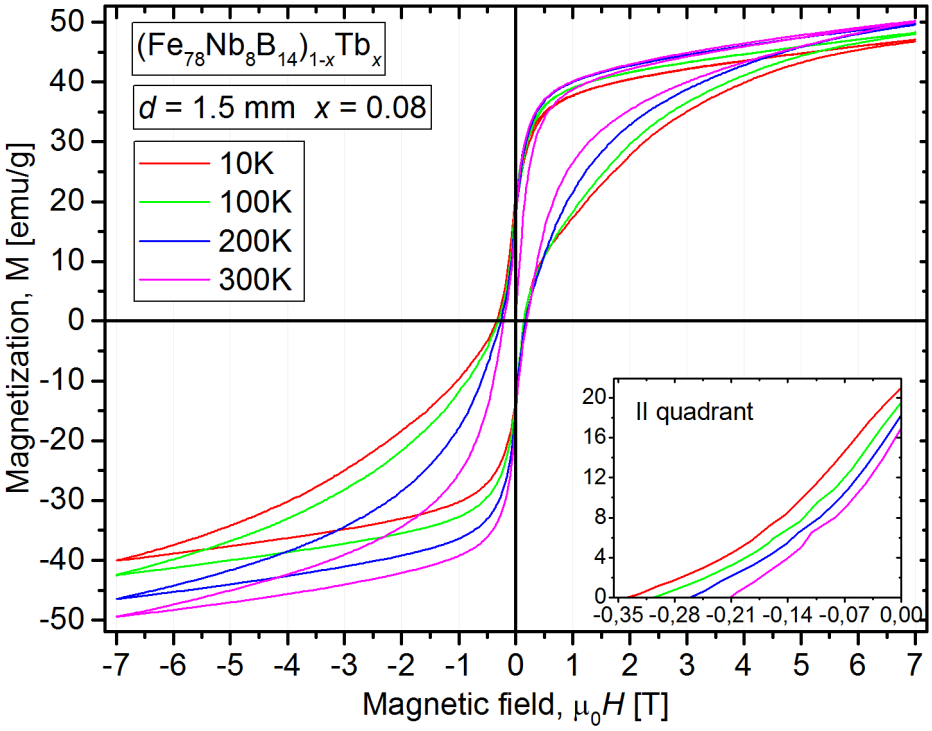


Figure 6.33. The magnetic hysteresis loops (T = 10 – 300 K) of the $(Fe_{78}Nb_8B_{14})_{0.92}Tb_{0.08}$ alloy prepared using melting current equal to 35 A and form with 1.5 mm in diameter.

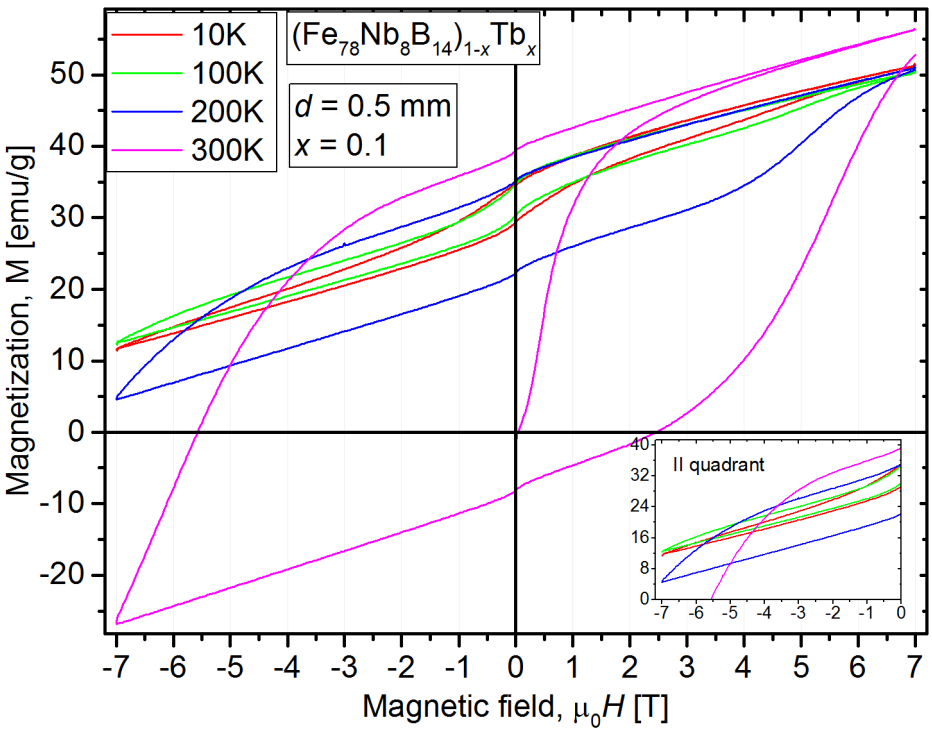


Figure 6.34. The magnetic hysteresis loops (T = 10 – 300 K) of the $(Fe_{78}Nb_8B_{14})_{0.9}Tb_{0.1}$ alloy prepared using melting current equal to 35 A and form with 0.5 mm in diameter.

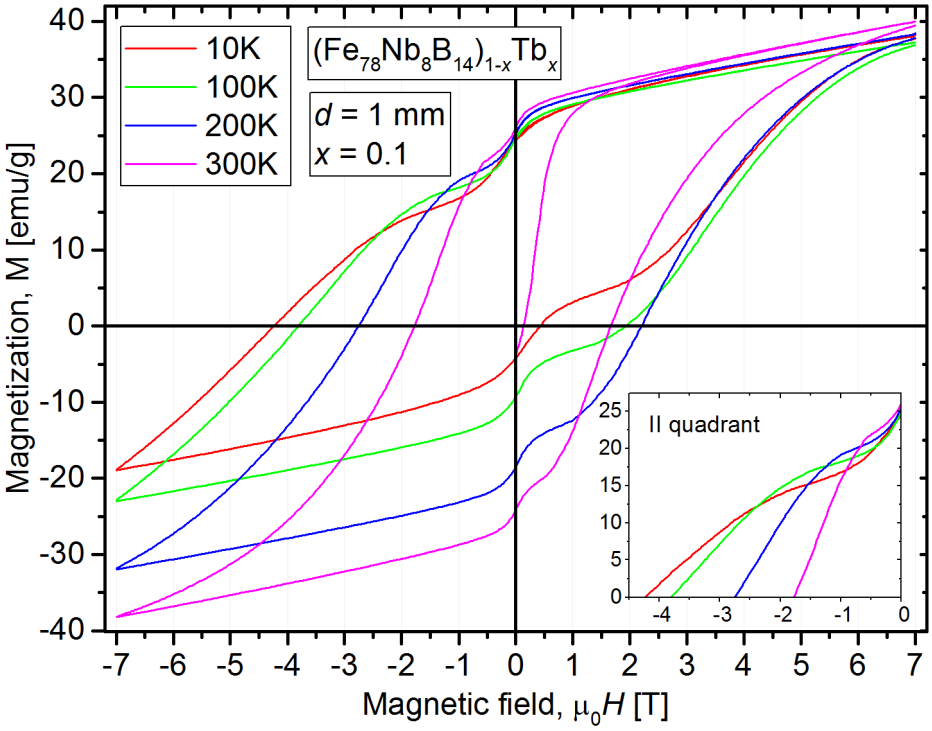


Figure 6.35. The magnetic hysteresis loops (T = 10 – 300 K) of the $(Fe_{78}Nb_8B_{14})_{0.9}Tb_{0.1}$ alloy prepared using melting current equal to 35 A and form with 1 mm in diameter.

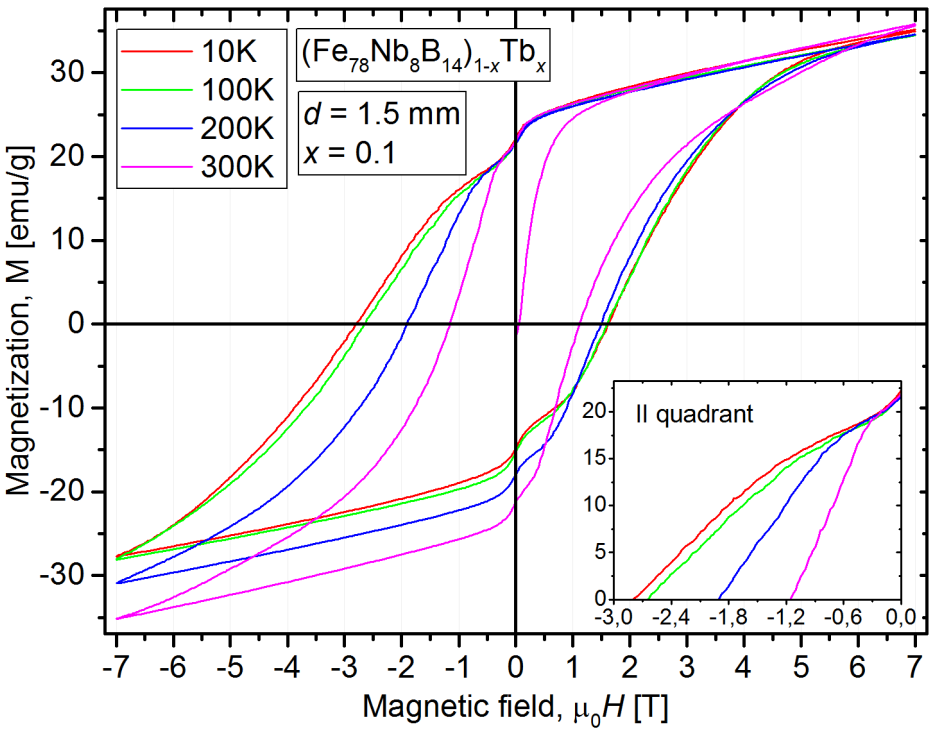


Figure 6.36. The magnetic hysteresis loops (T = 10 – 300 K) of the $(Fe_{78}Nb_8B_{14})_{0.9}Tb_{0.1}$ alloy prepared using melting current equal to 35 A and form with 1.5 mm in diameter.

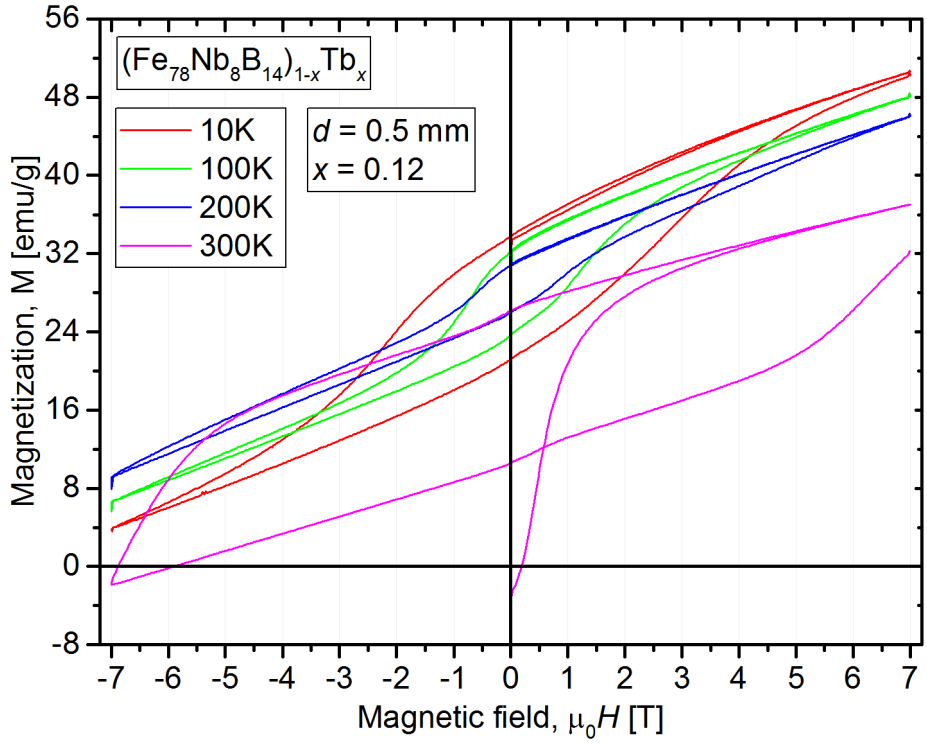


Figure 6.37. The magnetic hysteresis loops (T = 10 – 300 K) of the $(Fe_{78}Nb_8B_{14})_{0.88}Tb_{0.12}$ alloy prepared using melting current equal to 35 A and form with 0.5 mm in diameter.

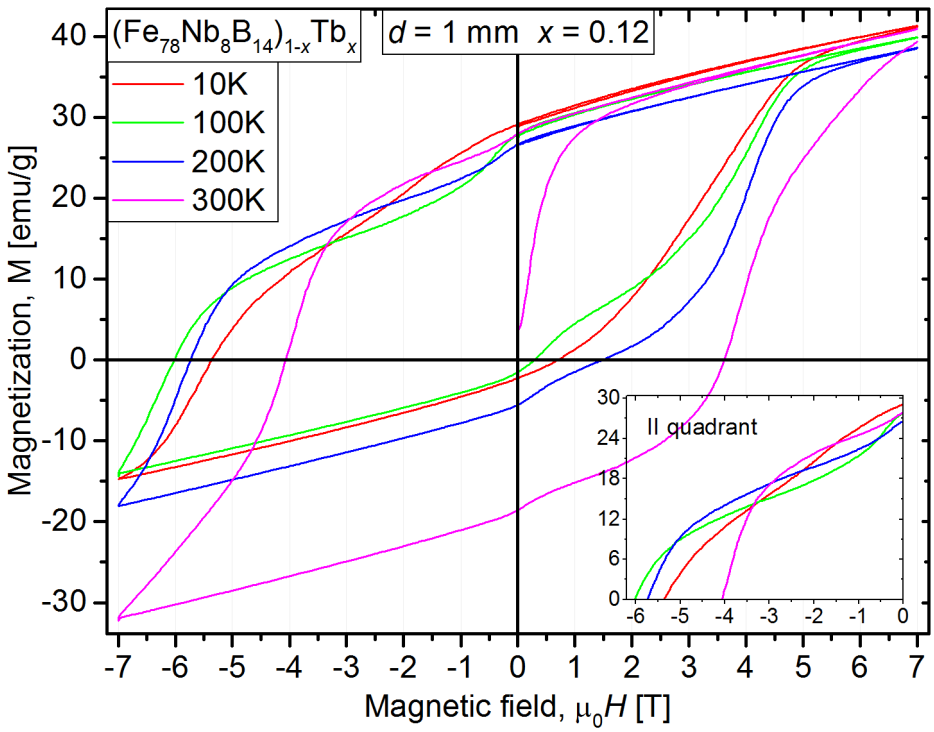


Figure 6.38. The magnetic hysteresis loops (T = 10 – 300 K) of the $(Fe_{78}Nb_8B_{14})_{0.88}Tb_{0.12}$ alloy prepared using melting current equal to 35 A and form with 1 mm in diameter.

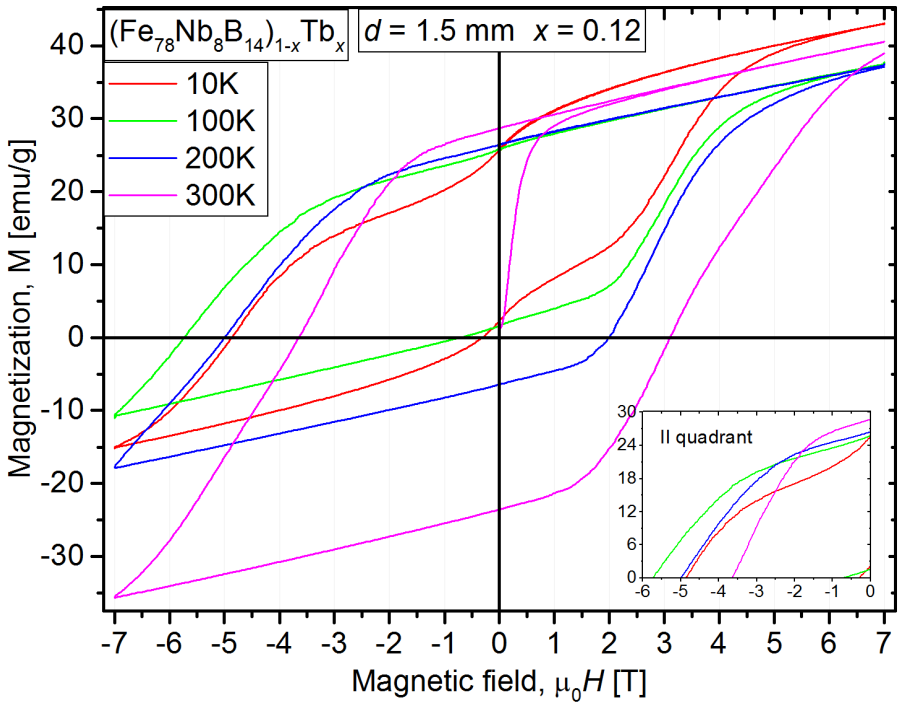


Figure 6.39. The magnetic hysteresis loops (T = 10 – 300 K) of the $(Fe_{78}Nb_8B_{14})_{0.88}Tb_{0.12}$ alloy prepared using melting current equal to 35 A and form with 1.5 mm in diameter.

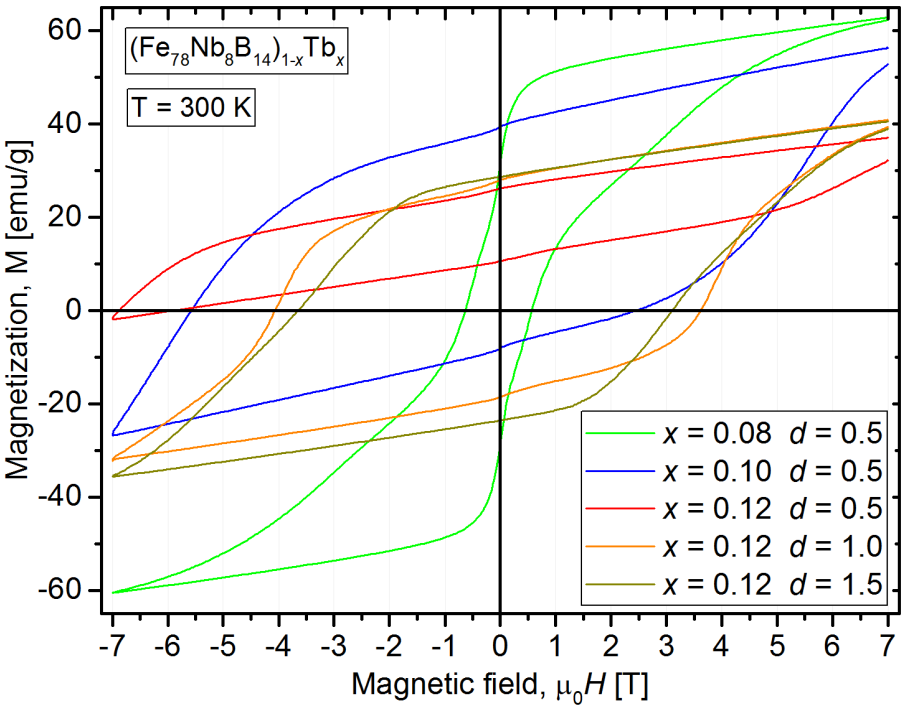


Figure 6.40. The magnetic hysteresis loops measured at room temperature obtaining for the $(Fe_{78}Nb_8B_{14})_{0.88}Tb_{0.12}$ ($d$ = 0.5 mm) alloy (red line) in comparison to the materials with higher diameters as well as lower Tb content.

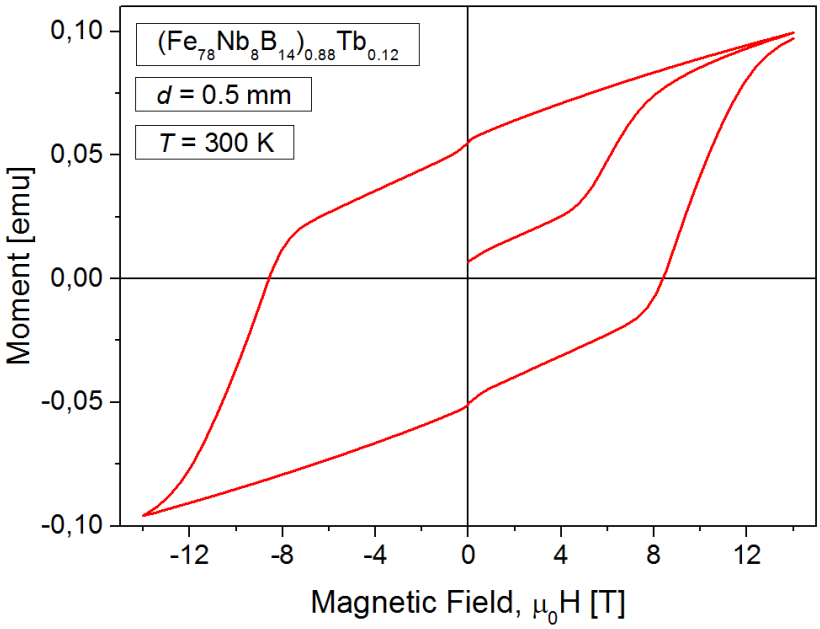


Figure 6.41. The magnetic hysteresis loops measured at room temperature for the $(Fe_{78}Nb_8B_{14})_{0.88}Tb_{0.12}$ ($d$ = 0.5 mm) alloy measured in external magnetic field range ±14 T.

Table 6.9. Summarize of magnetic parameters for the $(Fe_{78}Nb_8B_{14})_{1-x}Tb_x$ alloys prepared using the form with diameter $d$, including magnetic saturation at 7 T, remanence and coercivity measured at positive $\mu_0H_{c+}$ and negative $\mu_0H_{c-}$ external magnetic field as well as maximum energy parameters $|JH|_{max}$ and $|BH|_{max}$. The measurement errors are in the level of the least significant digit.

| $x$ | $d$ [mm] | $M_S$ [emu/g] | $M_R$ [emu/g] | $\mu_0H_{c-}$ [T] | $\mu_0H_{c+}$ [T] | $\|JH\|_{max}$ [kJ/m$^3$] | $\|BH\|_{max}$ [kJ/m$^3$] |
|---|---|---|---|---|---|---|---|
| **0.08** | **0.5** | 62.5 | 30 | 0.63 | 0.55 | 35 | 11 |
| **0.08** | **1** | 55 | 27.5 | 1.23 | 0.99 | 47 | 9.8 |
| **0.08** | **1.5** | 50 | 17 | 0.21 | 0.19 | 5 | 2.5 |
| **0.1** | **0.5** | 56.2 | 39 | 5.6 | 2.51 | 700 | 29.5 |
| **0.1** | **1** | 40 | 25 | 1.8 | 1.65 | 127 | 12 |
| **0.1** | **1.5** | 35.5 | 21.5 | 1.16 | 1.13 | 62 | 8.7 |
| **0.12** | **0.5** | 37 | 25.8 | 6.9 | - | 590 | 13.3 |
| **0.12** | **1** | 41 | 28 | 4.1 | 3.61 | 408 | 15 |
| **0.12** | **1.5** | 40.6 | 28.7 | 3.66 | 3.1 | 340 | 16.1 |

Figure 6.42, Figure 6.43 and Figure 6.44 present a surface observations of domain structure for the $(Fe_{78}Nb_8B_{14})_{0.88}Tb_{0.12}$ alloys prepared with diameter $d$ = 0.5 mm, 1 mm

and 1.5 mm, respectively. Similarly to the SEM observations, in all cases one may see non regular micro-metric domain structures. Similar as in case of alloys with 6 at. % of Nb content (described in section 5.2.2) the average size of the magnetic domain depends on applied cooling rates i.e. decreases with decreasing of sample diameter.

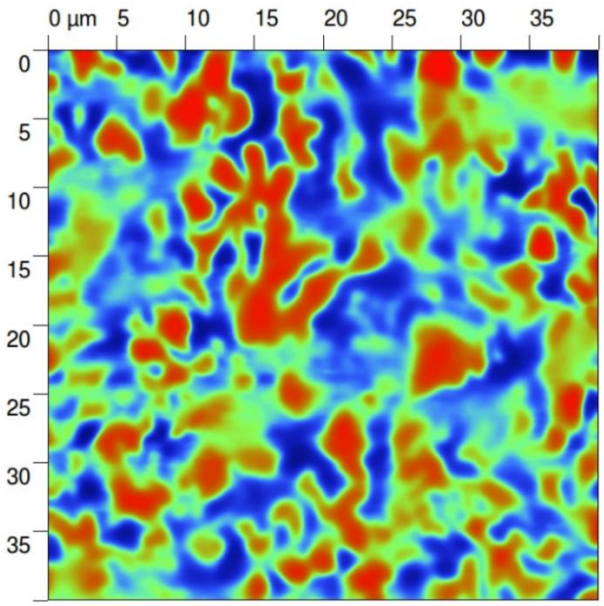


Figure 6.42. MFM pictures (scan 40 x 40 µm) for the $(Fe_{78}Nb_8B_{14})_{0.88}Tb_{0.12}$ alloy prepared with melting current $I$ = 35 A and diameter $d$ = 0.5 mm.

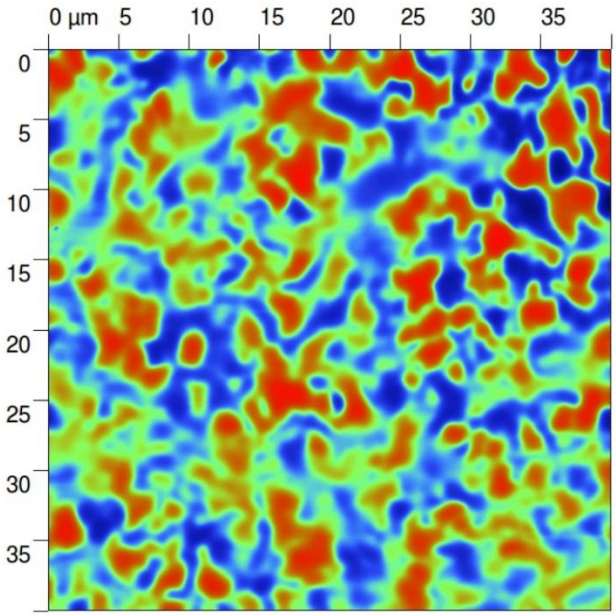


Figure 6.43. MFM pictures (scan 40 x 40 µm) for the $(Fe_{78}Nb_8B_{14})_{0.88}Tb_{0.12}$ alloy prepared with melting current $I$ = 35 A and diameter $d$ = 1 mm.

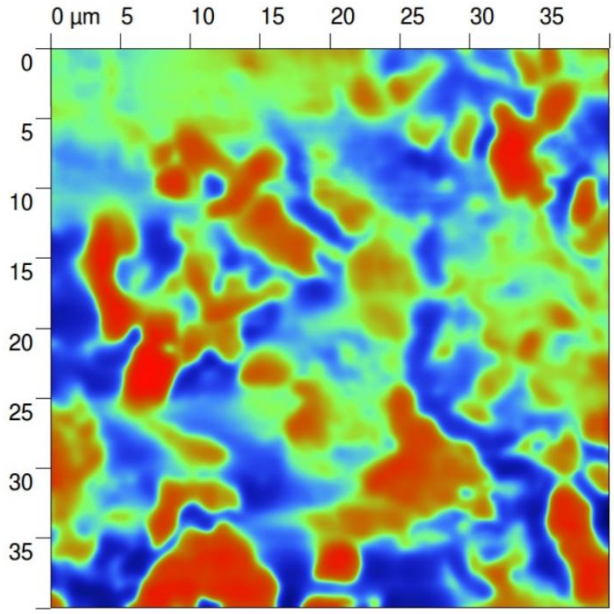


Figure 6.44. MFM pictures (scan 40 x 40 µm) for the $(Fe_{78}Nb_8B_{14})_{0.88}Tb_{0.12}$ alloy prepared with melting current $I$ = 35 A and diameter $d$ = 1.5 mm.

## 6.6. Structural and magnetic properties of the $(Fe_{80}Nb_6B_{14})_{1-x}Dy_x$ ($x$ = 0.08, 0.10, 0.12, 0.16) bulk nanocrystalline alloys.

In this chapter, structural and magnetic properties of the $(Fe_{80}Nb_6B_{14})_{1-x}Dy_x$ ($x$=0.08, 0.10, 0.12, 0.16) bulk nanocrystalline alloys are presented. The alloys were prepared using the vacuum suction casting technique using the melting current 35 A. The samples were in the form of rods with different diameters $d$ = 1.5, 1 and 0.5 mm. Phase identification was performed with the use of X-ray diffraction. Magnetic measurements were carried out by applying of the SQUID magnetometer in the external magnetic field up to 7 T. Magnetic domain observations were performed by the means of MFM. For this measurements the crushed samples were included into a resin and then mechanically polished. MFM images were collected with the silicon probe coated by 40 nm thick cobalt alloy film. The cantilever resonant frequency and its force constant were about 75 kHz, and 2.8 N $m^{-1}$, respectively.

### 6.6.1. Structural properties

Figure 6.45 shows the obtained XRD patterns for the $(Fe_{80}Nb_6B_{14})_{1-x}Dy_x$ ($x$ = 0.08, 0.1, 0.12 and 0.16) bulk nanocrystalline alloys with diameter $d$ = 1.5 mm. From these patterns one may determine a contribution of different phases (see Table 6.10). Using the the Sherrer equation the mean crystallites sizes of the $Dy_2Fe_{14}B$ phase were estimated about 30 – 40 nm independently on the $x$ parameter.

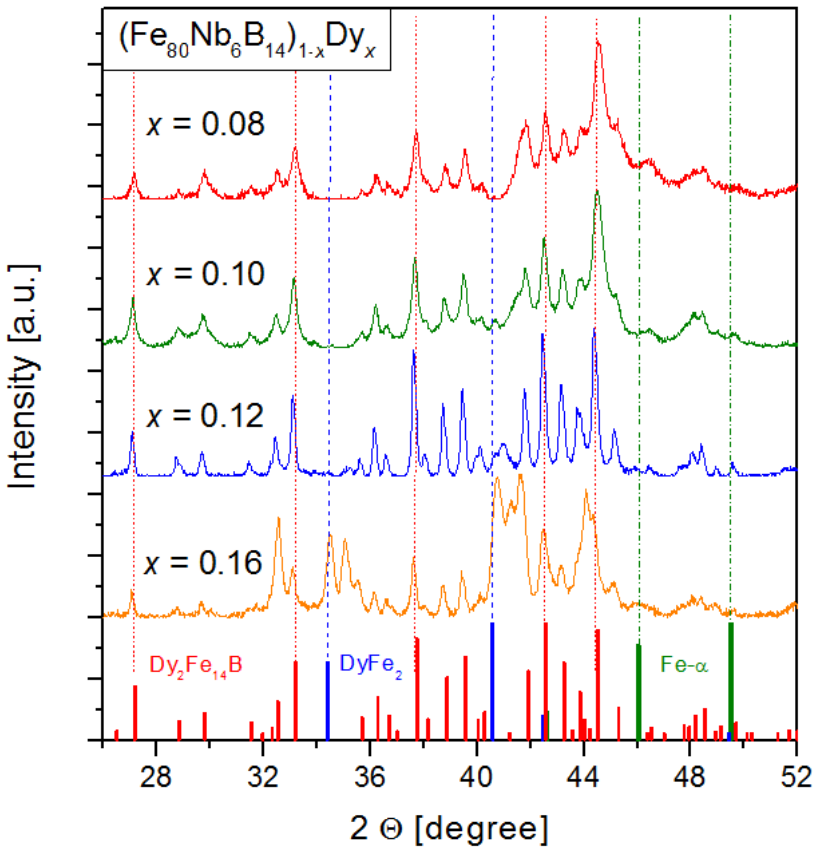


Figure 6.45. XRD patterns for the $(Fe_{80}Nb_6B_{14})_{1-x}Dy_x$ ($x$ = 0.08, 0.1, 0.12 and 0.16) bulk nanocrystalline alloys with diameter $d$ = 1.5 mm.

As shown, the obtained alloys consist of different phases i.e., magnetically hard $Dy_2Fe_{14}B$ as well as other relatively soft Dy-Fe, Fe-B and Fe phases. The highest contribution of $Dy_2Fe_{14}B$ was observed for the alloy with $x$ = 0.12.

The alloys with 12 at.% of Dy were prepared by the use of molds with different inner diameters $d$ = 1.5, 1 and 0.5 mm. This means that the samples were cooled with different rates. The obtained XRD patterns (not shown here) do not reveal any significant differences which indicate that in our case the phase structure is independent on the applied cooling rates.

Table 6.10. Phase contribution for the $(Fe_{80}Nb_6B_{14})_{1-x}Dy_x$ ($x$=0.08, 0.1, 0.12 and 0.16) bulk nanocrystalline alloys with diameter $d$ = 1.5 mm.

| $x$ | $Dy_2Fe_{14}B$ [%] ±2 | $DyFe_2$, $DyFe_3$ [%] ±2 | Fe [%] ±2 | $Fe_2B$, $Fe_3B$ [%] ±2 | Other [%] ±2 |
|---|---|---|---|---|---|
| **0.08** | 72% | 10% | 10% | 8% | - |
| **0.1** | 75% | 10% | 8% | 7% | - |
| **0.12** | 90% | 4% | - | - | FeNbB (6%) |
| **0.16** | 38% | 32% | - | - | $NbFe_2$ (15%), $Nb_2FeB_2$ (15%) |

The observations of microstructure were carried out by means of the SEM (in BEC mode) and EDS techniques. Figure 6.46 shows the SEM picture of the $(Fe_{80}Nb_6B_{14})_{0.88}Dy_{12}$ alloy with diameter $d$ = 0.5 mm as well as the EDS spectra related to the dark and bright areas. In this case, one may see the micrometric or even submicrometric grains enriched with niobium (see the dark areas). For the alloys with higher diameters, i.e. lower cooling rate, the observed grains are larger, as presented in Figure 6.47.

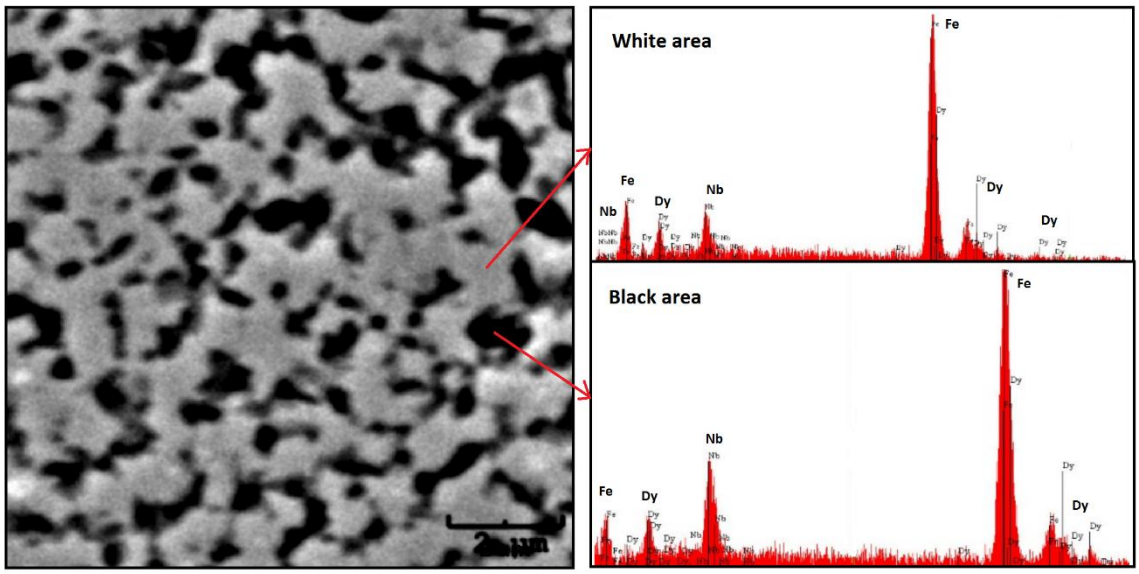


Figure 6.46. The SEM picture (on the left) and the EDS spectra (on the right) for the $(Fe_{80}Nb_6B_{14})_{0.88}Dy_{12}$ alloy with diameter $d$ = 0.5 mm.

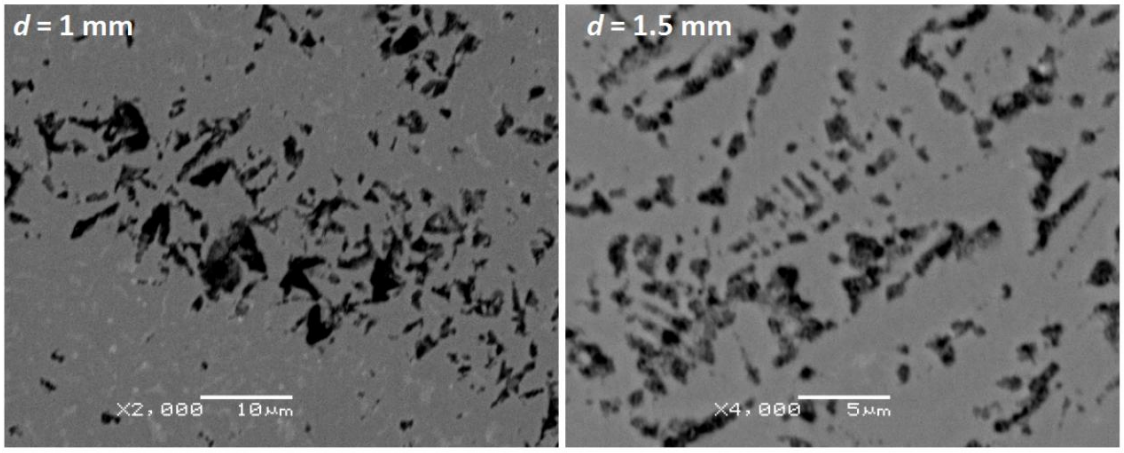


Figure 6.47. The SEM pictures for the $(Fe_{80}Nb_6B_{14})_{0.88}Dy_{12}$ alloy with diameterr $d$ = 1 mm (on the left) and $d$ = 1.5 mm (on the right).

## 6.6.2. Magnetic properties

The phase contents as well as the changes in microstructure exert an influence on magnetic properties of the tested alloys. Figure 6.48 depicts magnetic hysteresis loops (magnetization $M$ vs. magnetic field $H$) measured at room temperature and up to ±7 T for the the $(Fe_{80}Nb_6B_{14})_{1-x}Dy_x$ ($x$=0.08, 0.1, 0.12 and 0.16) bulk nanocrystalline alloys with diameter $d$ = 1.5 mm. Generally, the basic magnetic parameters such as coercive field $H_c$, magnetic remanence $M_r$ and magnetic saturation $M_s$ strongly depend on the Dy content. The highest coercivity ($\mu_0 H_c$ = 1.2 T) was observed for the alloy with $x$ = 0.12.

The highest $H_c$ associated with the highest contribution of $Dy_2Fe_{14}B$ phase was the reason we chose the $(Fe_{80}Nb_6B_{14})_{0.88}Dy_{0.12}$ alloy for further studies referring to an influence of cooling rate on magnetic properties. As it was mentioned this aim was achieved by casting the same alloy compositions but using different mold inner diameters. The change in magnetic characteristics is presented in Figure 6.49. One may see the increase of magnetic remanence and significant increase of coercive field ($\mu_0 H_c$ = 5.5 T for $d$ = 0.5 mm). Table 6.11 shows selected magnetic parameters for the alloys examined. From application point of view especially important are $H_c$, energy products $|BH|_{max}$ and $|JH|_{max}$ (determined in the second quadrant). The $|BH|_{max}$ parameter describes maximum energy of the stray field produced by the sample while $|JH|_{max}$ ($J = \mu_0 M$) is related to energy of external magnetic

field that may demagnetize the sample and can be a measure of materials resistance from external magnetic fields.

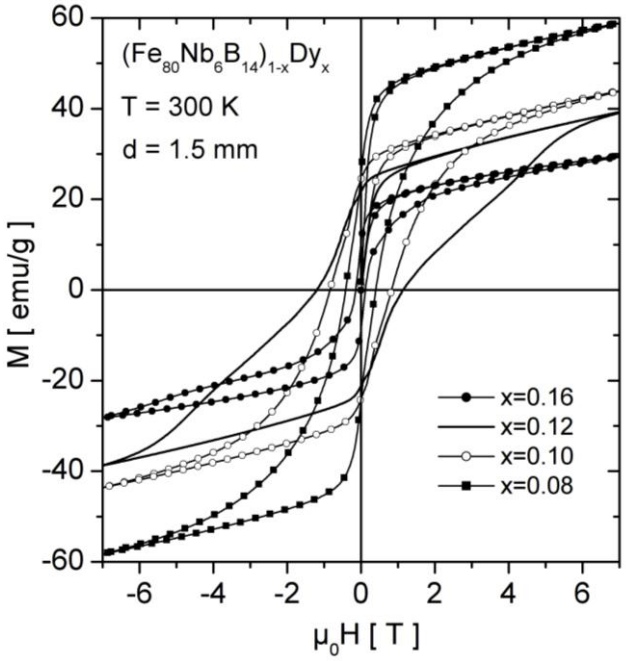


Figure 6.48. Magnetic hysteresis loops measured at room temperature for the the $(Fe_{80}Nb_6B_{14})_{1-x}Dy_x$ ($x$=0.08, 0.1, 0.12 and 0.16) alloys with diameter d = 1.5 mm.

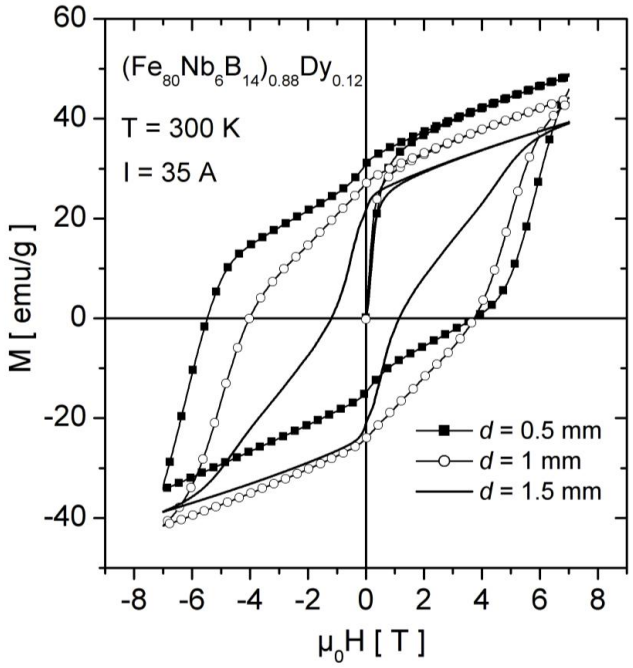


Figure 6.49. Magnetic hysteresis loops measured at room temperature for the $(Fe_{80}Nb_6B_{14})_{0.88}Dy_{0.12}$ alloys with different diameter $d$.

Table 6.11. Selected magnetic parameters determined from hysteresis loops for the $(Fe_{80}Nb_6B_{14})_{1-x}Dy_x$ alloys. The measurement errors are in the level of the least significant digit.

| $x$ | $d$ [mm] | $\mu_0 H_c$ [T] | $M_r$ [emu/g] | $M_s$ (7T) [emu/g] | $\|BH\|_{max}$ [kJ/m$^3$] | $\|JH\|_{max}$ [kJ/m$^3$] |
|---|---|---|---|---|---|---|
| **0.08** | **1.5** | 0.42 | 24.9 | 58.6 | 6.8 | 18.2 |
| **0.1** | **1.5** | 0.85 | 24.1 | 43.7 | 9.8 | 38.5 |
| **0.12** | **1.5** | 1.2 | 21.6 | 39.1 | 7.6 | 48.8 |
| **0.16** | **1.5** | 0.15 | 10.1 | 29.7 | 1.9 | 3.1 |
| **0.12** | **1** | 4.1 | 27.2 | 44.1 | 10.5 | 207 |
| **0.12** | **0.5** | 5.5 | 31.4 | 48.7 | 12.4 | 386 |

The highest values of $H_c$, $|BH|_{max}$ and $|JH|_{max}$ were found for $(Fe_{80}Nb_6B_{14})_{0.88}Dy_{0.12}$ alloy with $d$ = 0.5 mm.

Let us notice that hysteresis loop for this alloy is asymmetric and is not closed even in 7 T external magnetic field. It may be caused by some blocking and irreversibility effects. In this context, it is worth to present the first and second run of $M(H)$ loops for the same sample (see Figure 6.50).

The "volume" magnetic measurements can be supplemented by surface observations of the domain structure, as shown in Figure 6.51 and Figure 6.52 for the $(Fe_{80}Nb_6B_{14})_{0.88}Dy_{0.12}$ alloy with $d$ = 0.5 mm and $d$ = 1.5 mm, respectively. In the both cases one may see non regular micro-metric domain structure. Moreover, for the alloy with $d$ = 0.5 mm some nano-metric domains (about 500 nm in size) were also observed.

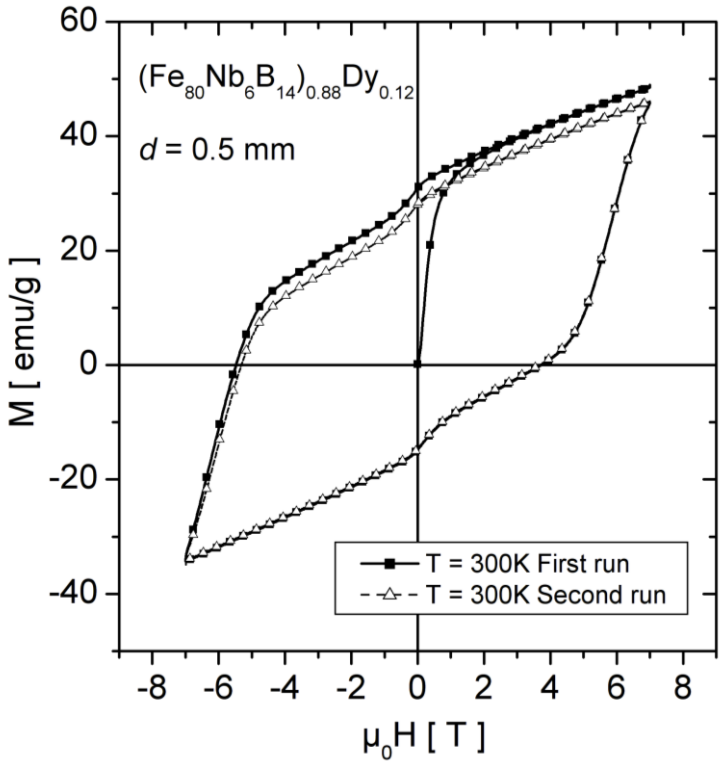


Figure 6.50. The first and second run of hysteresis loops for the $(Fe_{80}Nb_6B_{14})_{0.88}Dy_{0.12}$ alloys with diameter $d$ = 0.5 mm.

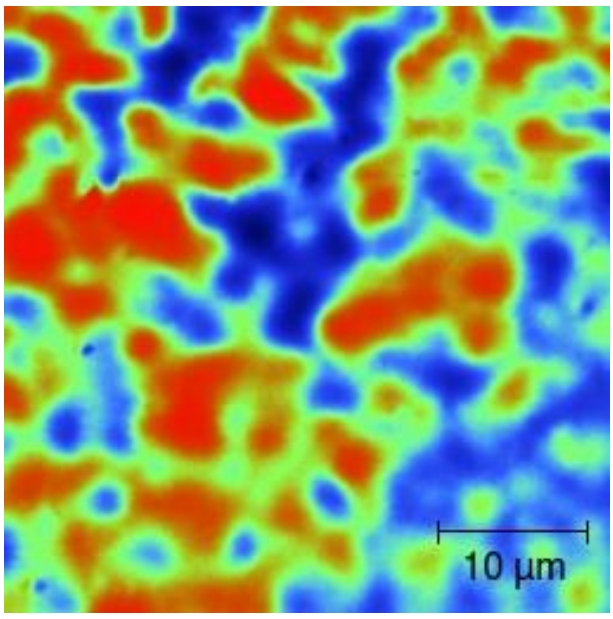


Figure 6.51. MFM image for the $(Fe_{80}Nb_6B_{14})_{0.88}Dy_{0.12}$ alloy with $d$ = 0.5 mm.

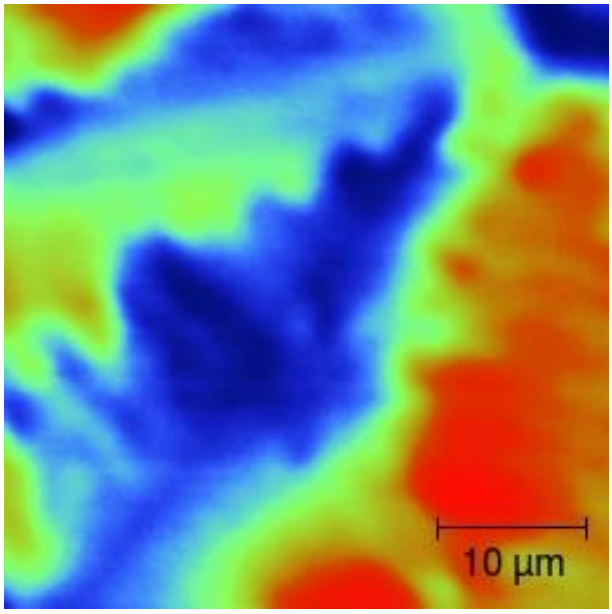


Figure 6.52. MFM image for the $(Fe_{80}Nb_6B_{14})_{0.88}Dy_{0.12}$ alloy with $d$ = 1.5 mm.

Results presented in this section indicate that it is possible to obtain bulk alloys of Fe-Nb-B-Dy type characterized by very high coercivity (in our case 5.5 T). The main question is: what is responsible for the observed magnetic hardening effect. First of all the obtained alloys can be considered as a kind of nano-composites with dominated hard magnetic $Dy_2Fe_{14}B$ and other relatively soft Dy-Fe, Fe-B and Fe phases. The average crystallites size of the main phase is in order of tens nm. The highest value of $H_c$ for the alloy containing 12 at.% of Dy can be explained by the highest $Dy_2Fe_{14}B$ content. Interesting is the fact that the applied different cooling rates (different sample diameters) significantly changes magnetic properties but do not influence phase structure of the alloys tested. This means that the observed magnetic hardening should be attributed to microstructure and/or internal stresses. The MFM observations strongly support the conclusion. In fact, for the sample with $d$ = 1.5 mm (Figure 6.52) the magnetic domains are rather smooth and regular in shape, while for the sample with $d$ = 0.5 mm (Figure 6.51) they are smallest and ragged. The mentioned factors, as an additional source of magnetic anisotropy, are responsible for the "disordered" magnetic domain structure. Let's analyze the $M(H)$ curves. The open and asymmetric hysteresis loop for the $(Fe_{80}Nb_6B_{14})_{0.88}Dy_{0.12}$ alloy with $d$ = 0.5 mm (see Figure 6.49) indicates an appearing of some ultra-hard magnetic objects that do not change magnetization direction even in 7 T magnetic field. Interactions between these

objects and the rest volume can cause the observed shift of $M(H)$ dependence in the same mechanism as classical exchange-bias effect.

# 7. Numerical analysis

## 7.1. Numerical analysis of time-depended effects in the Fe-Nb-B-Tb alloys

In a group of hard magnets based on bulk nanocrystalline alloys of Fe, RE and other alloying additions one can observe some favorable to magnetic hardening phenomena like interaction between nanograins as well as pinning and blocking of domain wall motion. Such phenomena lead to appearance of the so-called time dependent magnetization effects, which were described in section 2.3.3. Analysis of empirical $M(t)$ curves can give some important information about activation energy, relaxation time $\tau$ etc. connected with the magnetic domain blocking effects. However, such analysis is complex due to the fact that magnetic relaxation can be attributed to different components with different $\tau$.

In order to analysis of empirical $M(t)$ curves for studied materials the developed numerical method were tested. Next, the algorithm was used to analyze two alloys of $(Fe_{80}Nb_6B_{14})_{0.92}Tb_{0.08}$ and $(Fe_{78}Nb_8B_{14})_{0.84}Tb_{0.16}$. Both of them were prepared using 25 A of melting current and the mold with 1.5 mm in diameter.

### 7.1.1. Numerical method

As was noted, the magnetic relaxation process can be attributed to different magnetic components in prepared material. Such components can be related to soft and hard magnetic phases, interaction between nanograins and structures with different anisotropy. Each of them may be characterized by different relaxation time $\tau$ or even some distribution of $\tau$. However, the number of expected components as well as shape of its distributions is not obvious, therefore a typical methods based on fixed number of continuous functions (e.g. Gaussian or log-normal) performing optimization only selected parameters (like average value $\mu$ and standard deviation $\sigma$) may leads to wrong results.

In presented approach, the wider range of relaxation times were divided into $n$ number of channels. Each $j$-th channel is connected with a number of objects $N_j$ with relaxation time $\tau_j$. By the providing of this approach to the model of M($t$) described in section 2.3.3 (formula (2.75)) as well as the $\chi^2$ test described in section 2.3.4, the final optimization problem can be express as:

$$\chi^2 = \frac{1}{m}\sum_{i=1}^{m}\frac{\left(M_i - M_s\sum_{j=1}^{n}\frac{N_j}{\sum_{k=1}^{n}N_k}\left(1-\exp\left(\frac{-t_i}{\tau_j}\right)\right)\right)^2}{\sigma_i^2} \tag{7.1}$$

where $m$ is the number of experimental magnetization points $M_i$ measured in the time $t_i$ with error $\sigma_i$ and $M_S$ is the magnetic saturation at $t=\infty$. As a result of optimization method one can obtain values of $N_j$ (as a distribution of $\tau$) that correspond to minimum of $\chi^2$. It should to be underlined that this method gives results without any assumptions about a shape of the distribution and number of components.

Due to very high number of possible solutions, for example in case of 100 channels $N_j$ with 1 ‰ resolution there is $1000^{100}$ possibilities to test, one of the non-deterministic, evolution algorithm - Simulated annealing (SA, see section 2.3.4) were chosen for testing. In order to improve the reality of final solutions the additions optimization condition i.e. the minimum of local entropy were also provided to the standard SA procedure:

$$S_j^{loc} = -\sum_{i=j-p}^{j+p} N_i'' \times \log(N'') \tag{7.2}$$

where $p$ is the parameter related to range of local entropy and $N_i$'' is equal to:

$$N_i'' = \frac{N_i}{\sum_{k=j-p}^{j+p} N_k} \tag{7.3}$$

Moreover, in order to verify and improve the results provided by SA algorithm with channels division approach, the alternative method with the use of continuous functions and other evolution algorithm, so-called Particle swarm optimization (PSO) were also developed and tested.

### 7.1.2. Tests and parameters of algorithm

In order to test the efficiency of developed numerical method, a set of M($t$) curves were generated based on well-known distribution of relaxation time. An example of such curves was presented in Figure 2.25 in section 2.3.3. The tests include several different type of Gaussian distribution and their combination like: one narrow and broad component, two symmetrical and no-symmetrical components with well or bed separation between them as well as combinations of three components. Next, based on the generated M($t$) curves and trial and error method, the optimal parameters of SA algorithm were estimated. In this case the number of channels $n$ = 100, range of local entropy $p$ = 5, annealing temperature $T_a$ = 0.01, cooling rate $c$ = 0.999 ($T_a := c * T_a$ after each 100 steps) and channel resolution $\Delta N$ = 0.1%.

Figure 7.1 presents the final results for selected testing data. The red color corresponds to obtained fitting, while the black line indicates the original distributions which were used to generate the input data with their average value $\mu$ and standard deviation $\sigma$. One can see that the narrow components are fitted very well, while the shape and/or intensity of wider component is not perfect, however, fully enough to estimate the value μ and σ parameters. It is important to note that in each exanimated case the obtained results allow to estimate the number of components without any preliminary assumptions.

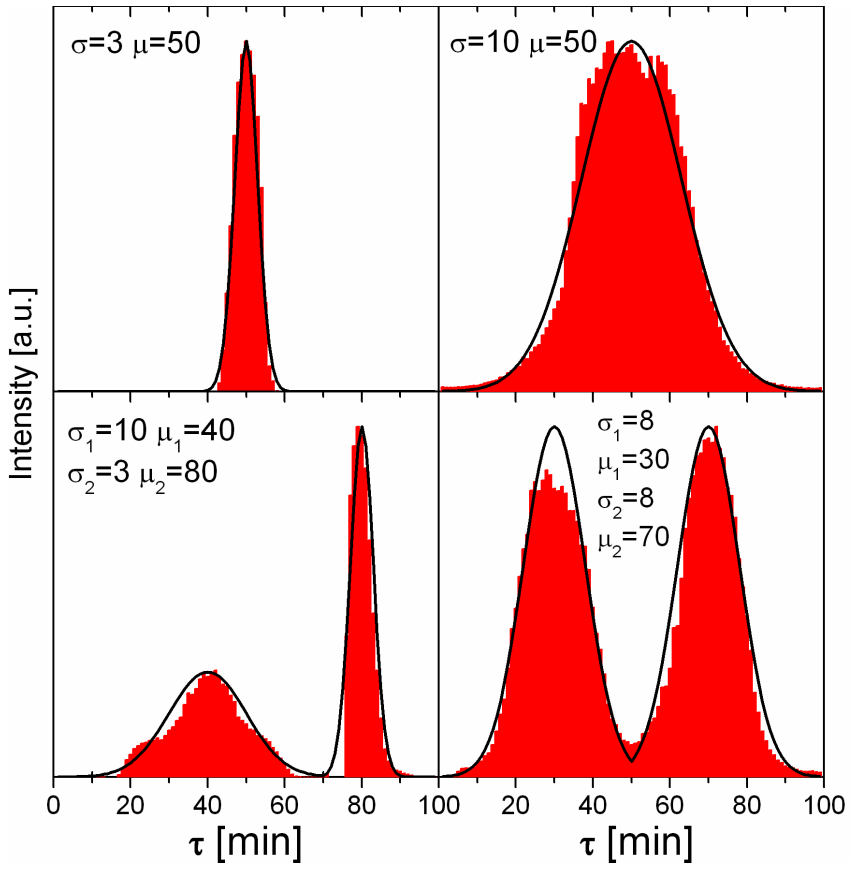


Figure 7.1. The selected results (red color) obtained by SA procedure in comparison to original distribution (black line) used to prepare the initial testing data [39].

In the case of real experimental data, two kinds of imperfection of M(t) curves are expected – measuring error and finite time of measurement. Both of them may influence quality of calculations and should be taken into account. Therefore, during the next test the generated M(t) curve have been cut after short measuring time ($t_m$ = 100 min) as well as the 5% of statistical error (with uniform distribution) were introduces. The results of such tests for three components input data were presented in Figure 7.2.

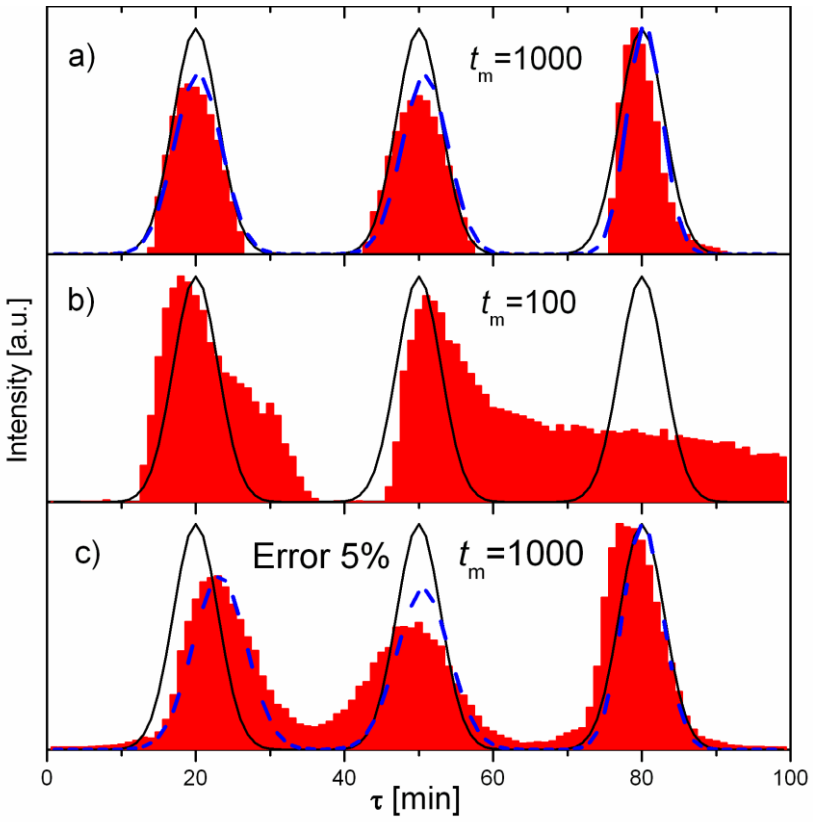


Figure 7.2. The results provided by SA procedure (red color) and after additions PSO corrections (blue line) in comparison to the original distribution (black line), from the initial data: a) without any imperfections, b) with very short measurement time, c) with statistical error [39].

As may note short measuring time leads to strong distortion of the distribution shape, especially for higher value of $\tau$. Therefore, during real analysis the measuring time should be much longer than expected relaxation time of the components. In perfect situation, the measurement is carried out until the M($t$) curve is fully saturated. On the other hand, a few present of statistical error leads to a slight deterioration of results, however, obtained fitting allows pre-estimating the number of components, their shape and position.

Alternative approach to the solution of time relaxation problem consists in using the fixing number of continues functions and fitting their parameters like average value and standard deviation of Gaussian distributions. Such method is much easier to solve from numerical point of view, however needs some assumptions difficult to predict. On the other hand, based on preliminary analysis e.g. using the SA method described in previous paragraph, obtained result may be improved by additional calculations with continuous functions. Moreover, in order to verify the reliability of SA algorithm as well as

comparing the performance, an another numerical method so-called Particle Swarm Optimization (PSO) [45] were implemented and tested.

The blue line on the Figure 7.2 corresponding to fitting obtaining by PSO analysis using SA results as an initial data. Other examples of such tests were summarized in Table 7.1. It can be noted that for the easiest tests using only one component, both methods produces perfect results in collaboration as well as independent. In case of more complicated combinations of components, the SA algorithm with channel division approach provides slightly better approximation, however, the best results one can obtain after additional PSO fitting. For the most difficult tests, including three components, short time of measurement and statistical error, typical approach using continuous functions is definitely not enough to solve the time dependent magnetization problem, while the SA with channel division method provides quite good estimation of components without any preliminary assumptions.

Table 7.1. The comparison of average value and standard deviation for each components which were used to generate testing data to the results obtained using SA procedure, PSO procedure (with continuous functions) as well as both of this methods [39].

| **Gaussian function** | | | **SA** | | **PSO** | | **SA+PSO** | |
|---|---|---|---|---|---|---|---|---|
| **Shape** | $\mu$ | $\sigma$ | $\mu$ | $\sigma$ | $\mu$ | $\sigma$ | $\mu$ | $\sigma$ |
| **narrow** | 50 | 3 | 50 | 3 | 50 | 3 | 50 | 3 |
| **broad** | 50 | 10 | 50 | 10 | 50 | 10 | 50 | 10 |
| **combinations** | 40 | 10 | 41 | 10 | 39.5 | 9.1 | 40 | 9.4 |
| | 80 | 3 | 79 | 3 | 79.6 | 3.5 | 80 | 3.3 |
| **two equal** | 30 | 8 | 30 | 8 | 30.3 | 9.1 | 30 | 7.2 |
| | 70 | 8 | 70 | 8 | 70.2 | 7.9 | 70 | 8 |
| **three equal** | 20 | 3 | 19 | 3 | unstable results | | 20 | 3 |
| | 50 | 3 | 50 | 3 | | | 51 | 3 |
| | 80 | 3 | 79 | 2 | | | 80 | 2.5 |
| **three equal + error** | 20 | 3 | 22 | 3 | - | | 23 | 3 |
| | 50 | 3 | 49 | 4 | | | 51 | 3 |
| | 80 | 3 | 78 | 3 | | | 80 | 3 |
| **three equal, $t_m$=100** | 20 | 3 | 18 | see Figure 7.2 | - | | - | |
| | 50 | 3 | 52 | | | | | |
| | 80 | 3 | - | | | | | |

## 7.1.3. Analysis of experimental results

For analysis of time relaxation of magnetization effects two alloys described in previous chapter were chosen: $(Fe_{80}Nb_6B_{14})_{0.92}Tb_{0.08}$ and $(Fe_{78}Nb_8B_{14})_{0.84}Tb_{0.16}$ prepared using 25 A of melting current and the mold with 1.5 mm in diameter. It may be recalled that the coercivity at room temperature for this materials equals 0.25 T and 0.06 T, respectively. The measurements were carried out by high sensitive SQUID magnetometer in two steps. First, the external magnetic field $H$ = -7 T was used in order to saturate of the materials. Next, the field was switching off or alternating to the $H$ value ($H$=0 T, 0.1 T, 0.5 T, 1 T), and the M($t$) curves were recorded for about 130 minutes. Moreover, the measurements were carried out at two different temperatures equals 250 K and 300 K. The recorded curves M($t$) in relation to magnetic saturation of material are presented in Figure 7.3.

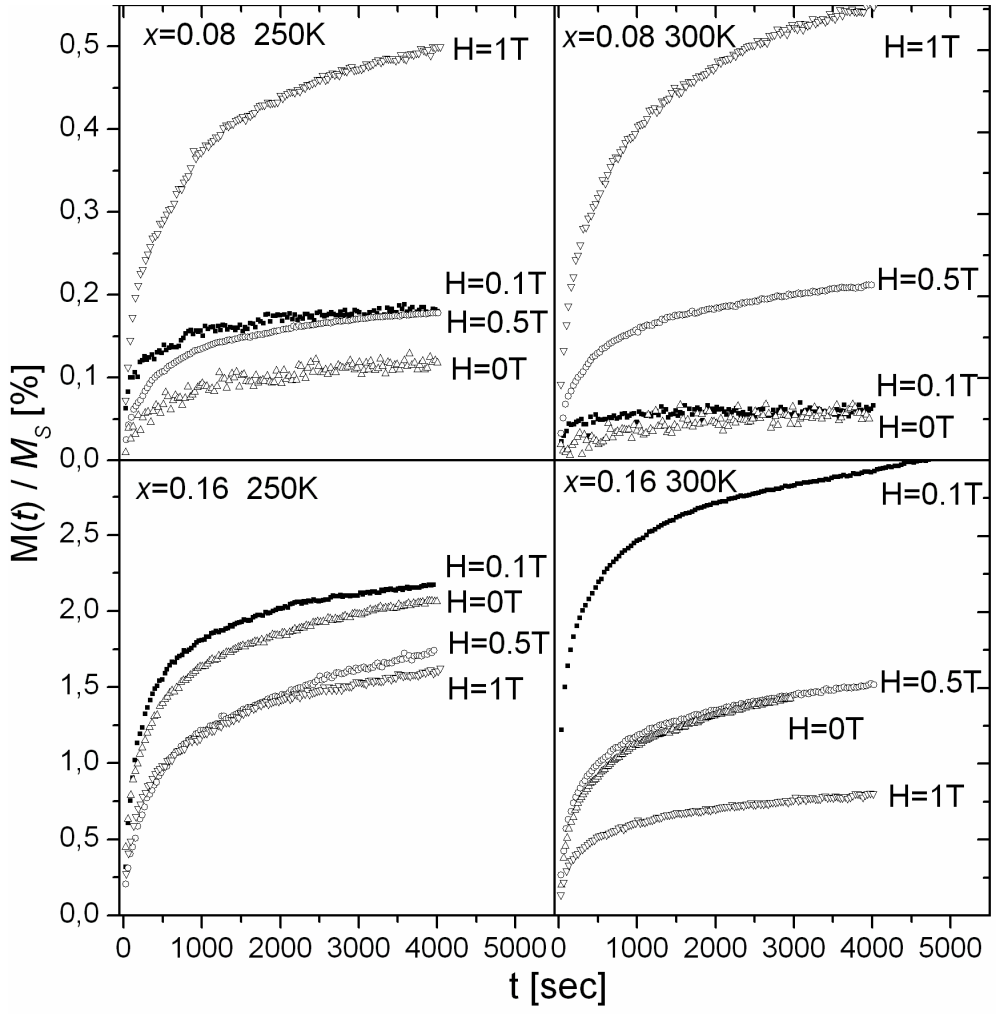


Figure 7.3. The normalized M($t$) curves measured for the $(Fe_{80}Nb_6B_{14})_{1-x}Tb_x$ alloys at two different temperatures and several values of $H$ (external magnetic field during measurement) [39].

The obtained results reveal a strong dependence on the relaxation of $H$, $T$ as well as Tb content. In the case of alloy with 8 at. % of Tb, the intensity of remanence relaxation is close to 0.5% of $M_S$ and lower than 0.1 % of $M_S$ for $H$ = 1 T and $H$ = 0 T, respectively. Such effect is expected due to the hard magnetic properties of this material which leads to "trapped" the magnetic moments in energetic caves, so, higher energy (provided by external field) is required to change of their direction. On the other hand, for material with 16 at.% of Tb, the relaxation intensity is much higher (2% at 250K, 1.5% at 300K for $H$ = 0 T). Moreover, close to the coercivity ($H$ = 0.1 T) the maximum of relaxation intensity (2.2% at 250 K and 3% at 300 K) one can observed.

Figure 7.4 presents the results of analysis carried out by SA method described in previous paragraphs. Due to the fact that the applied model requires the value of magnetic saturation $M_S$ the non-saturated component of M($t$) curves (if exist) were subtracted before calculations. The M($t$) curves measured in $H$ = 0 and $H \approx H_C$ were selected for analysis in two different temperatures, however in case the material with 8 at.% of Tb and $H$ = 0, the relaxation intensity was too low to obtain stable results.

For the alloy with $x$ = 0.08 one can see three well separated components with Gaussian-like shapes. The components are similar for both temperatures, however, the last one ($\tau \approx 800$) has higher intensity at 250 K. In case of material with 16 at.% Tb content, a shift of the positions of the components into lower $\tau$ with increase of magnetic field or temperature can be noted. First component is related to quick change of magnetization after switching the magnetic field, while the next one are correlated with magnetic domains characterized by higher activation energy. Therefore, higher temperature or magnetic field is required to change their magnetization direction which is related to shift of the $\tau$ distribution.

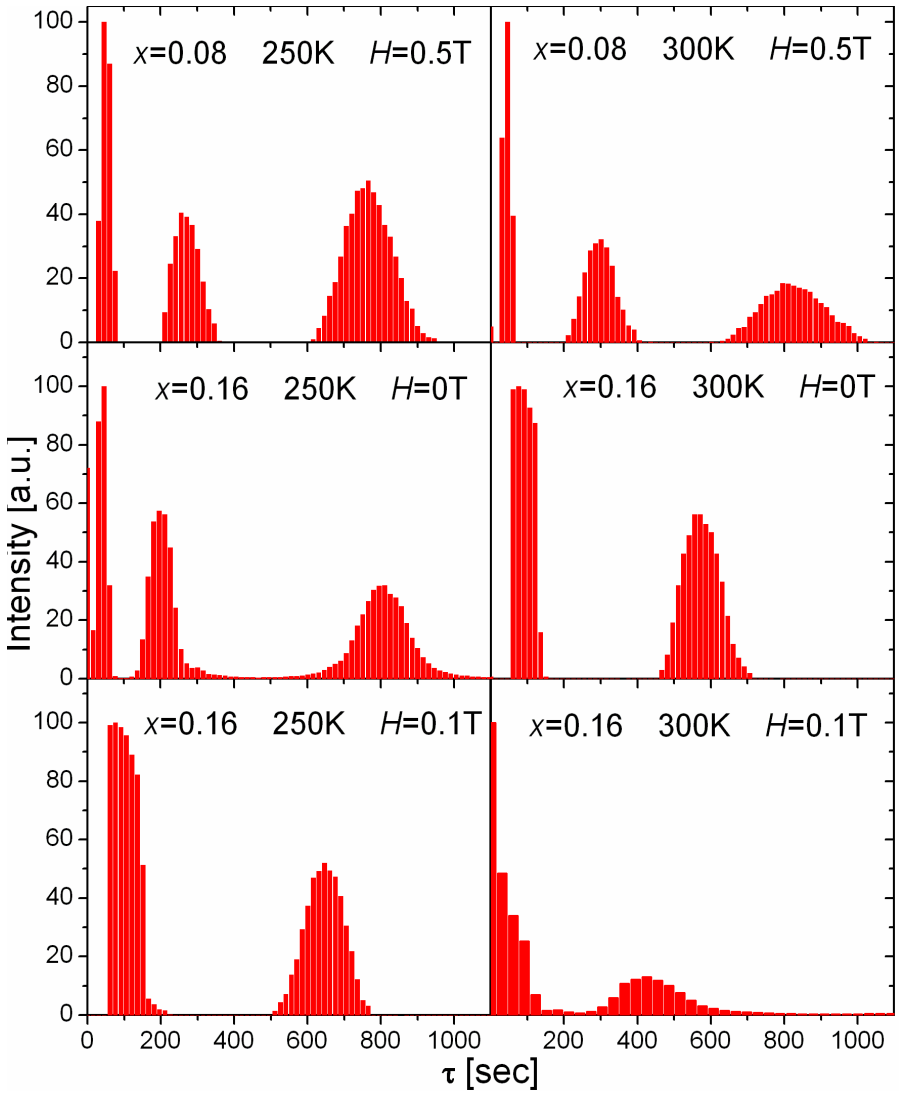


Figure 7.4. Analysis of relaxation time of magnetization performed at 250 K and 300 K for the $(Fe_{80}Nb_6B_{14})_{1-x}Tb_x$ alloys with and without presents of external magnetic field $H$ during measurement [39].

## 7.2. Magnetization processes of nanoparticles embedded into ferromagnetic matrix

Based on preliminary investigations, it is well known that in the group of Fe-Nb-B-RE alloys mostly two phases are expected - magnetically hard $Tb_2Fe_{14}B$ and relatively soft $TbFe_2$. In addition, the shift and shape of hysteresis loops suggests an occurrence of hard and ultra-hard magnetic objects which are "frozen" after first magnetization and can be consider as additional source of exchange anisotropy. Therefore, the simulations of magnetization process of such systems may be interesting from technical as well as scientific point of view. A role of interactions between magnetically hard and ultra-hard particles was studied based on Simulated Annealing (SA) and Monte Carlo simulations in a frame of the 3-D Heisenberg model.

### 7.2.1. Simulation procedure and test

Performed simulations are related to system of $N$ = 125000 spins in cubic box with dimensions 10 x 10 x 10 nm. The spins are regularly placed with a distance of 0.2 nm and randomly orientated. The boundary conditions correspond to infinite number of system copies in each directions. The energy of such system was calculated in the frame of the 3-D Heisenberg model expressed by the equation:

$$E = -\sum_{i,j} J_{ij}\overrightarrow{S_i}\overrightarrow{S_j} - \sum_i K_i(\overrightarrow{S_i}\cdot\overrightarrow{n_i})^2 - g\mu_B\mu_0\sum_i \overrightarrow{H_i}\cdot\overrightarrow{S_i} \qquad (7.4)$$

where $\overrightarrow{S_i}$ is the spin vector on site $i$, $J_{ij}$ is the exchange parameter, $K_i$ is the anisotropy constant (per site), $\overrightarrow{n_i}$ is the easy magnetization axis, $\overrightarrow{H_i}$ is the magnetic field on site $i$ and $g$, $\mu_B$, $\mu_0$ are the Lande factor, the Bohr magneton and the vacuum permeability, respectively.

Generally, the main idea of simulation procedure can be described as follows:

1. Init the annealing temperature $T_{SA}$ as well as random direction of each spin.
2. Change the orientation (by defined angle) of one side of selected spin, also at random.

3. Calculate the energy difference $\Delta E$ between the energy of the system before and after step 2, using the formula (7.4).
4. Check the following conditions:
    a. if $\Delta E < 0$ accept changes i.e. go to step 5, else
    b. make a test with the probability $\exp(\frac{\Delta E}{T_{SA}})$ and go to step 5 if pass, else
    c. make the same change (as in step 2) performing to hole cluster (determined using the Wang approach [103]) and go to step 5 if $\Delta E < 0$ or $\exp\left(\frac{\Delta E}{T_{SA}}\right)$ test passed, else
    d. make the changes back if all conditions are not satisfied and go to step 2.
5. After 10x$N$ iterations decrease $T_{SA}$, go to step 2 if $T_{SA}$ is bigger than final temperature.
6. Perform 4000x$N$ iterations keeping constant temperature and calculate the average magnetization.

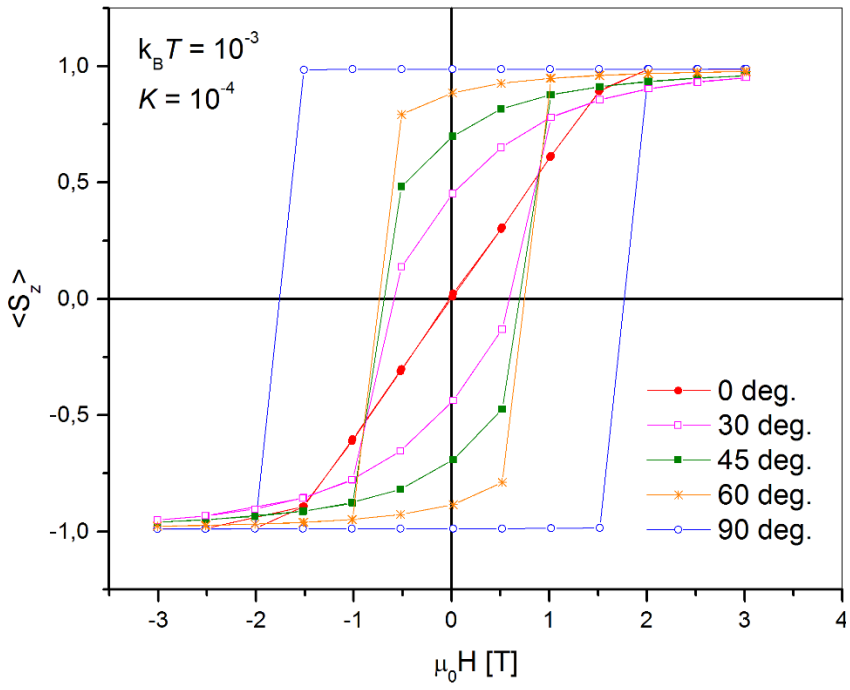


Figure 7.5. Simulation of spherical particle magnetization with different angle between $\overrightarrow{n_i}$ and $\overrightarrow{H_i}$.

The hysteresis loops obtained during the first test of spherical particle ($K_i^P$ = $10^{-4}$ eV) were presented in Figure 7.5. In this case different angles (0º, 30º, 45º, 60º, 90º) between easy magnetization axis and direction of external magnetic field were compared. As may

expected, for angle equal to 0º, a straight line typical for paramagnetic behavior was observed, while rectangular hysteresis with the highest coercivity corresponds to angle 90º. All of the hysteresis are symmetrical and closed. This case relates to the Stoner-Wohlfarth model of magnetization of superparamagnetic particles.

### 7.2.2. Simulation of nanoparticle in ultra-hard magnetic matrix

For the main simulations the system of spins described above was divided for three regions (see Figure 7.6):

1. Spherical particle in the center of system with the exchange parameter $J_{ij}^{P} = 10^{-2}$ eV and anisotropy constant $K_i^{P} = 10^{-4}$ eV. The radius of particle is equal to 3.5nm. This part corresponds to relatively hard, ferromagnetic object. Boundary of particle i.e. space between particle and matrix with 0.5nm in thickness and anisotropy constant $K_i^{B} = 0$. Generally, this part corresponds to disorder and not perfect coupling on the surface of particle (that take place in real nanocomposite materials) and "transfers" the interactions between hard and ultra-hard phases. The impact of exchange parameter ($J_{ij}^{B} = 10^{-5}$ - $5x10^{-4}$ eV), which is directly responsible for the particle-matrix (P-M) coupling, were studied during simulations.
2. Matrix with ultra-high anisotropy constant $K_i^{M} = 10^{-3}$ eV and exchange parameter $J_{ij}^{M} = 10^{-2}$ eV (the same as particle), which fills the rest of free space of the system. The easy magnetization axis of matrix was directed to the top, according to direction of external magnetic field.

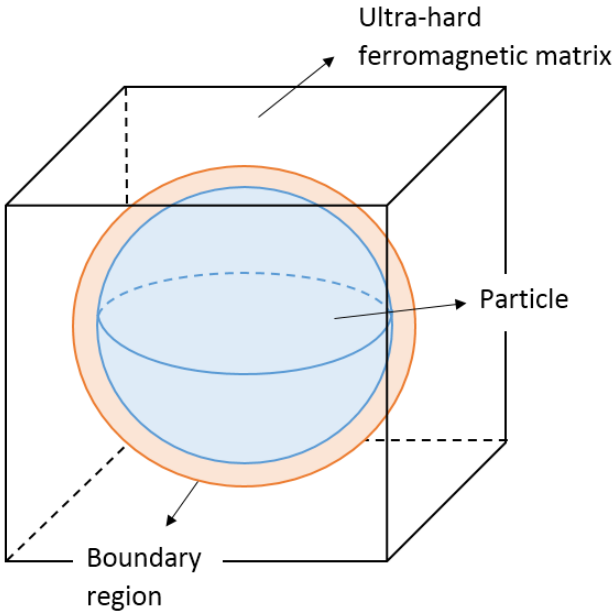


Figure 7.6. Schema of the simulated particles embedded in to ultra-hard ferromagnetic matrix.

The simulations where performed for three cases of angles between particle and matrix easy magnetization axis directions: parallel, with the angle 45º and perpendicular.

Moreover, it is important to note that all spins in the system were equal to 1. The external magnetic field up to ±5 T as well as $K_i^M$ parameter were chosen taking into account that the directions of spins inside the matrix should not change during simulation.

Figure 7.7, Figure 7.9 and Figure 7.11 presents the magnetic hysteresis loops of particle obtained for three different values of angle between easy magnetization axis of particle and matrix equal to 0º, 45º and 90º, respectively. Each figure contains three series for $J_{ij}^B$ = $5x10^{-5}$ eV, $1x10^{-4}$ and $5x10^{-4}$ eV. Magnetization of the particle was determined as average projection of spins to the z-axis (of the whole system and after subtraction of the matrix contribution). As may note all hysteresis are shifted and appearing of their asymmetry is observed. Especially interesting is the case with perpendicular P-M configuration, where the stronger P-M coupling causes coercivity and exchange-bias effect (significant shift along field axis).

Configuration of spins (a quarter of central section) during simulations in selected points on the hysteresis were presented on Figure 7.8, Figure 7.10 and Figure 7.12, similar as before – according to parallel, 45º and perpendicular P-M configuration, respectively.

Each figure shows a) the first magnetic saturation at +4 T of external magnetic field, b) opposite magnetic saturation at – 4 T and c) – d) bottom remanence i.e. determined in the third and fourth quadrant. Last case i.e. d) is related to simulations with exchange parameter of boundary equal to $5x10^{-4}$ eV, while a) – c) cases corresponds to lower $J_{ij}^{B}$ equals $5x10^{-5}$ eV.

One can note, that in all exanimated cases at temperature $k_B T = 10^{-4}$ eV the spins belongs to particle section are coupled and creates cluster. The same situation for matrix section can be also observed. In addition, as may expect due to the established simulation conditions, the direction of spins in matrix is similar to its easy magnetization axis independently form direction of external magnetic field. Especially interesting is the comparison of particle and boundary behavior for higher and lower boundary exchange parameter (e.i. cases c) and d) in Figure 7.8, Figure 7.10 and Figure 7.12). It is clearly visible that higher exchange leads to stronger particle-matrix coupling and consequently, the direction of particle magnetization is a competition between anisotropy, field and the matrix, while without coupling the direction of easy magnetization axis is preferred. This situation directly corresponds to the shift of hysteresis loops.

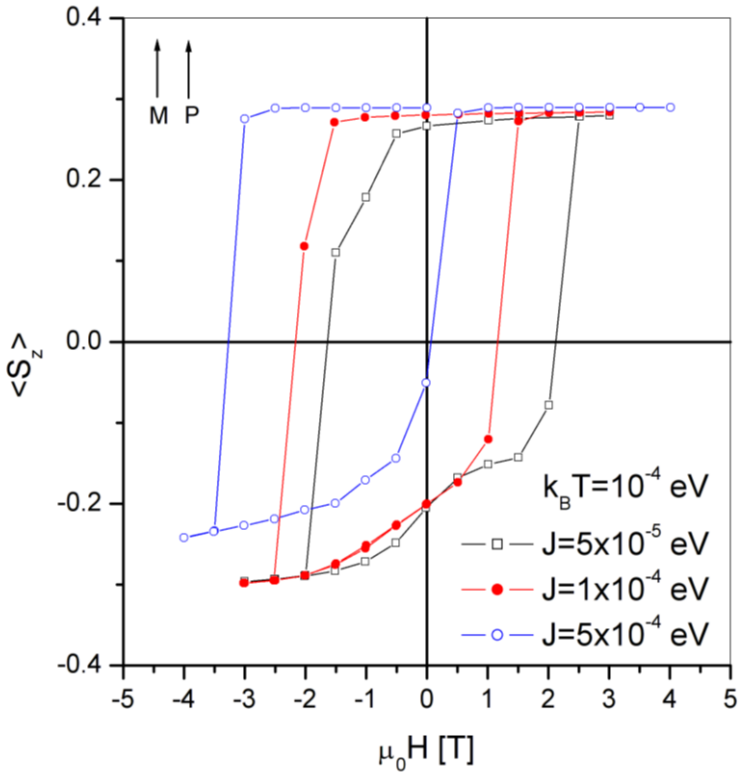


Figure 7.7. Magnetic hysteresis loops simulated for $J_{ij}^{B}$ = $10^{-5}$ - $5x10^{-4}$ eV and parallel configuration of the P-M easy magnetization axis [104].

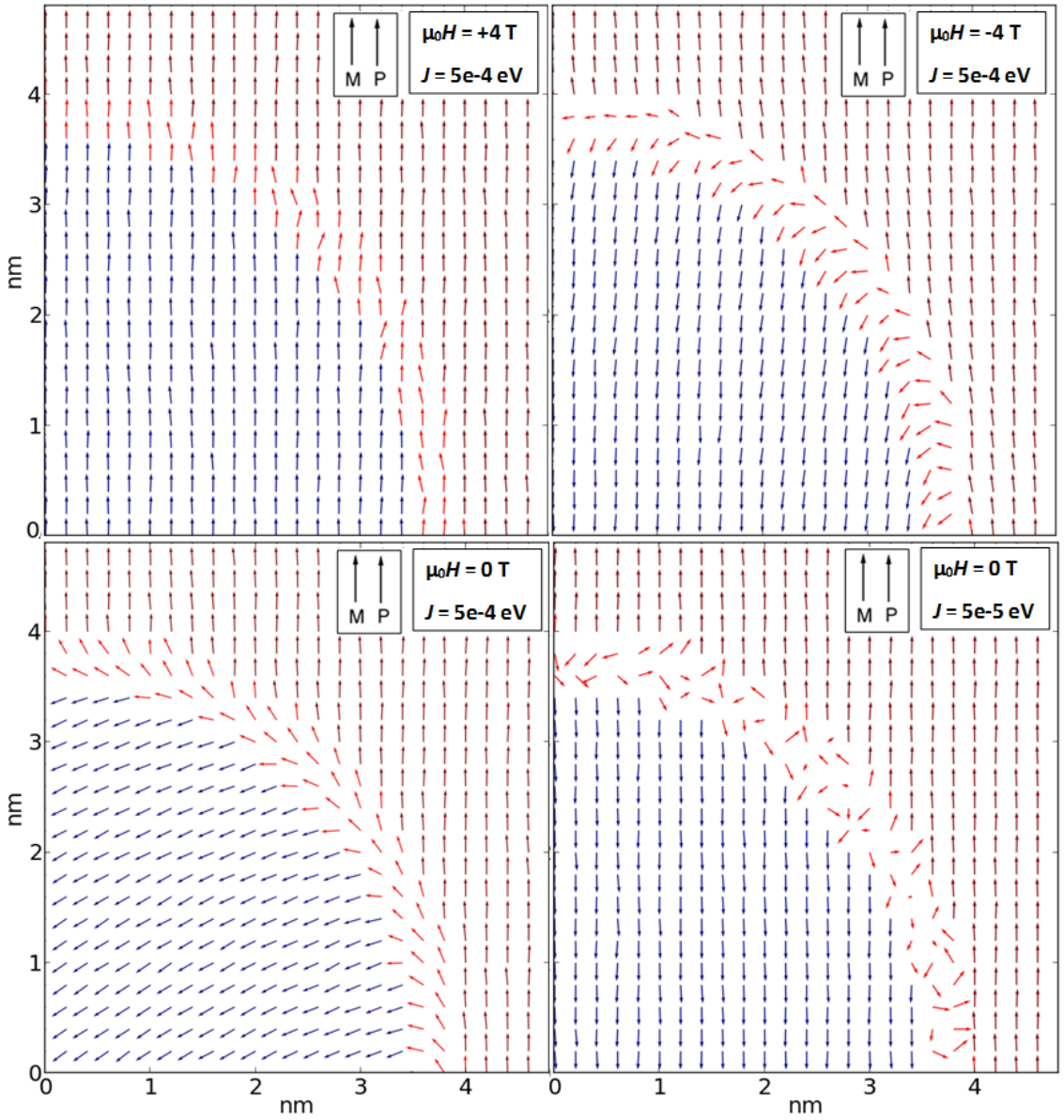


Figure 7.8. Spin configurations for the selected points of magnetic hysteresis loops presented on Figure 7.7 with parallel P-M configuration. a) saturation in positive field, b) saturation in negative field, c) bottom remanence ($M < 0$), d) bottom remanence for case with $J_{ij}^{B} = 5\text{x}10^{-5}$ eV.

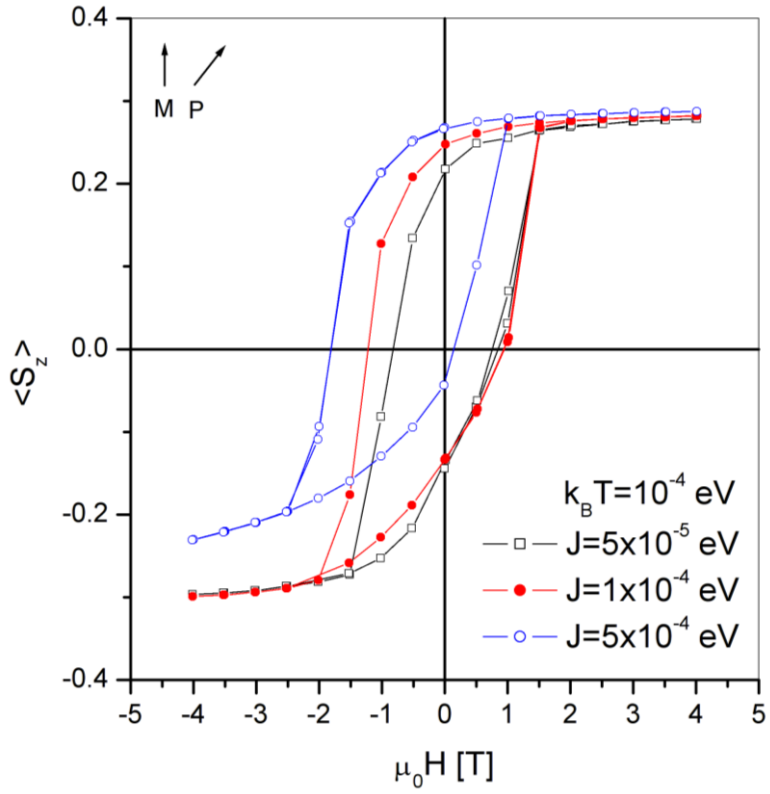


Figure 7.9. Magnetic hysteresis loops simulated for $J_{ij}^{B}$ = $10^{-5}$ - 5x$10^{-4}$ eV and 45º configuration of the P-M easy magnetization axis [104].

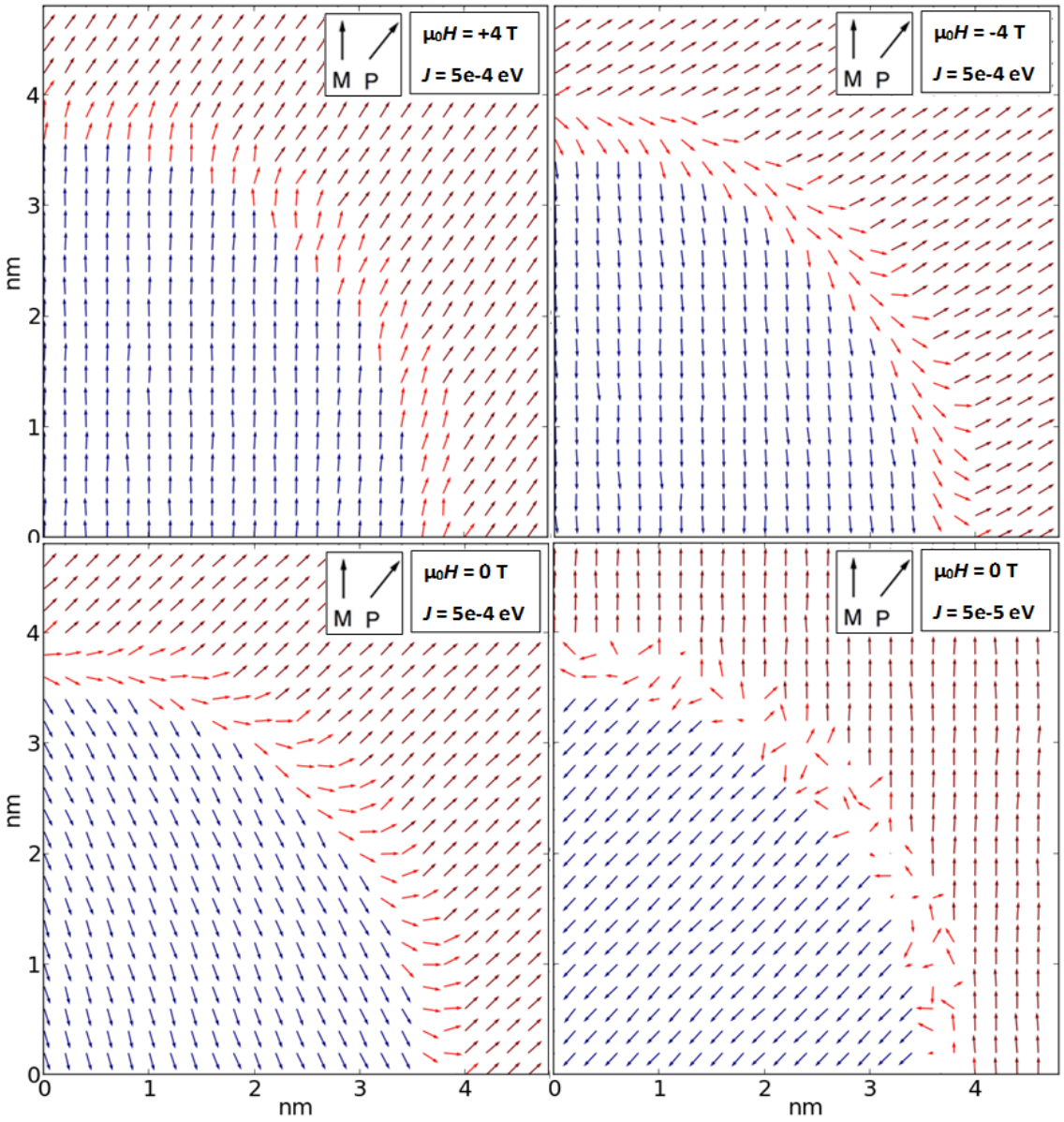


Figure 7.10. Spin configurations for the selected points of magnetic hysteresis loops presented on Figure 7.9 with 45º P-M configuration. a) saturation in positive field, b) saturation in negative field, c) bottom remanence ($M < 0$), d) bottom remanence for case with $J_{ij}^{B} = 5\text{x}10^{-5}$ eV.

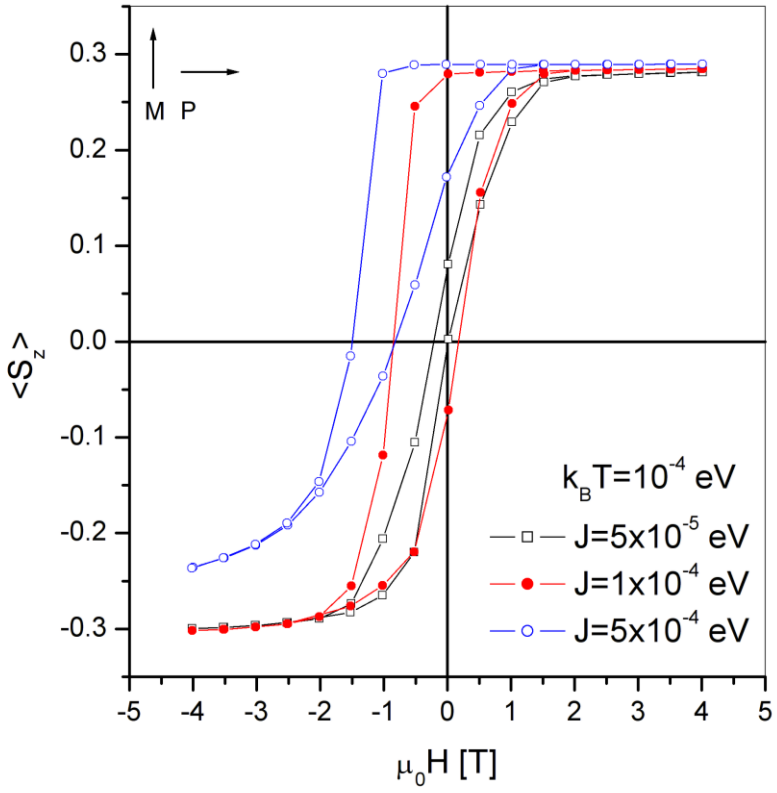


Figure 7.11. Magnetic hysteresis loops simulated for $J_{ij}^{B}$ = $10^{-5}$ - $5x10^{-4}$ eV and perpendicular configuration of the P-M easy magnetization axis [104].

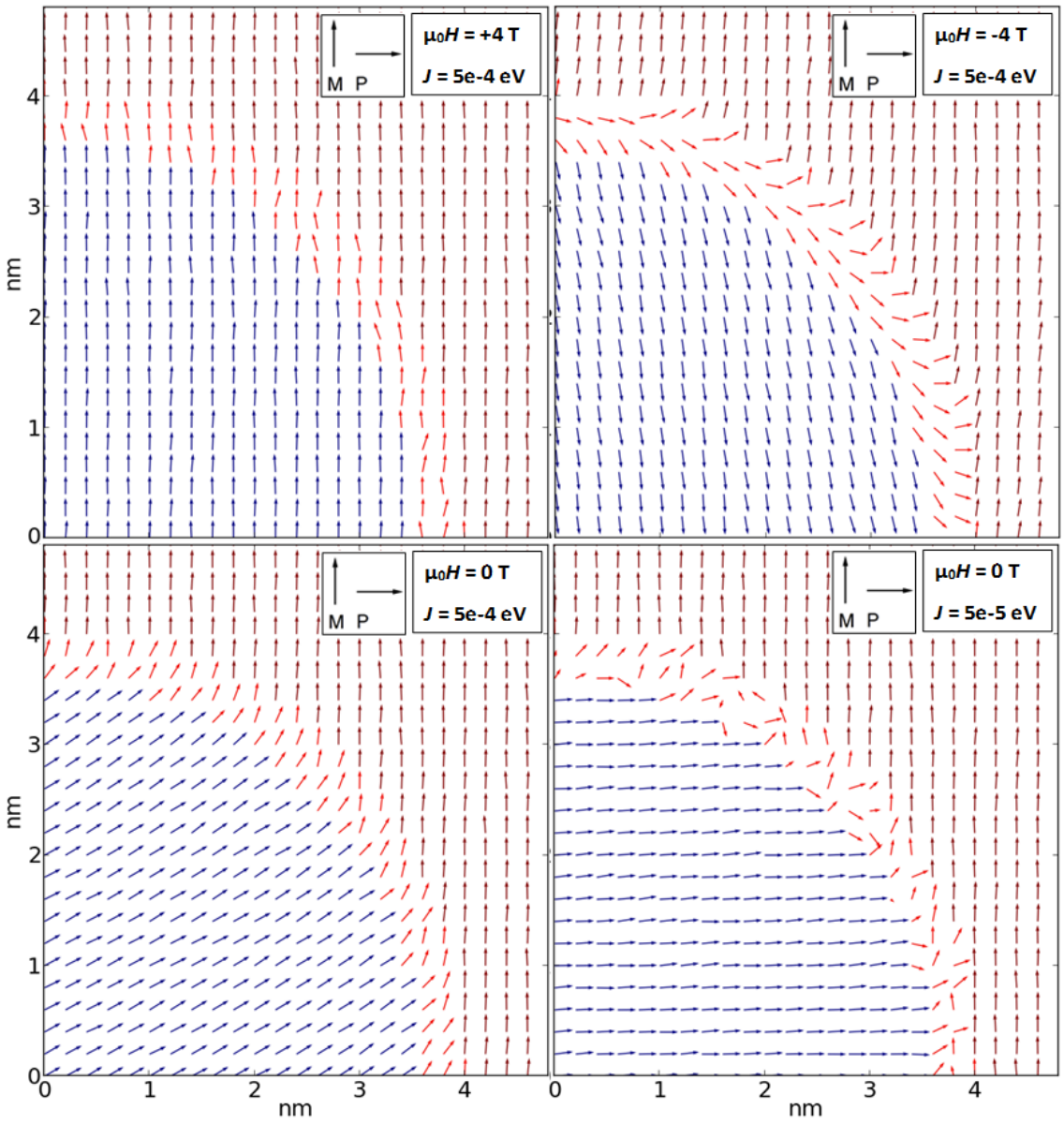


Figure 7.12. Spin configurations for the selected points of magnetic hysteresis loops presented on Figure 7.11 with perpendicular P-M configuration. a) saturation in positive field, b) saturation in negative field, c) bottom remanence ($M < 0$), d) bottom remanence for case with $J_{ij}^{B} = 5\text{x}10^{-5}$ eV.

Figure 7.13 presents comparison of hysteresis loops simulated for different temperatures form $5\text{x}10^{-4}$ eV to $5\text{x}10^{-3}$ eV with $J_{ij}^{B} = 5\text{x}10^{-4}$ eV and 45º P-M configuration. Moreover, an example of spin configuration in remanence point at $k_B T = 5\text{x}10^{-3}$ eV were shown on Figure 7.14. As one may note, increase of temperature leads to decreasing of magnetic saturation as well as symmetrical hysteresis. Such phenomenon is expected due to the fact

that the temperature causes a spin disorder in the boundary region and therefore, the additional exchange anisotropy is not related to the direction of easy axis of the matrix.

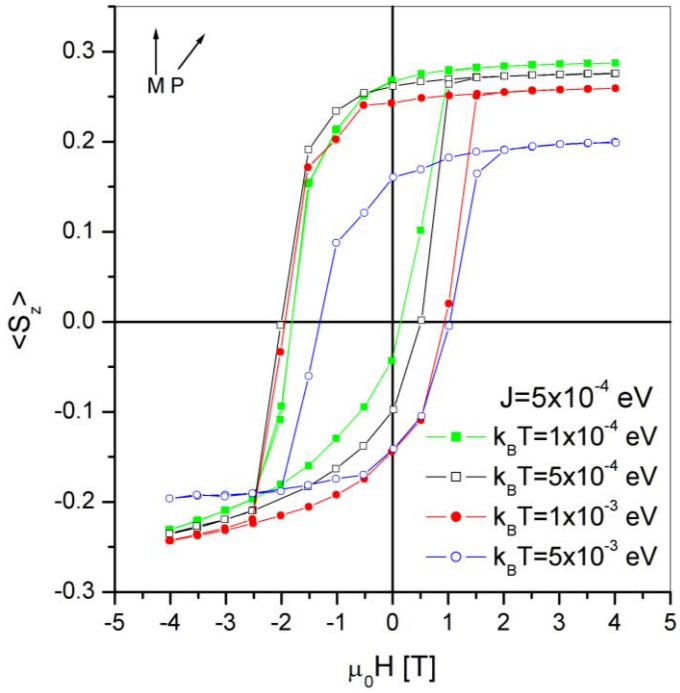


Figure 7.13. Comparison of magnetic hysteresis loops at different temperature for $J_{ij}^{B}$ = 5x10$^{-4}$ eV and 45º P-M configuration [104].

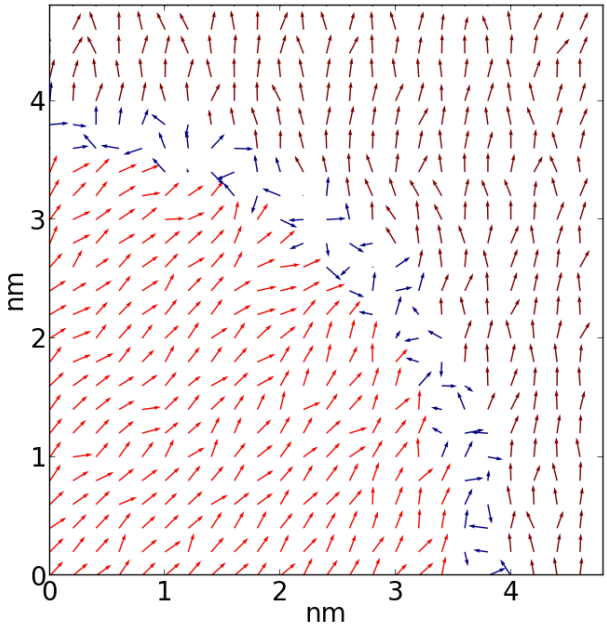


Figure 7.14. Spins configuration at bottom remanence hysteresis point in case of $k_BT$ = 5 x10$^{-3}$ eV [104].

In real magnetic nanocomposites it is expected that the spins are "frozen" parallel or anti-parallel to external magnetic field due to random distribution of easy magnetization axes for the phase with ultra-hard magnetic properties. Figure 7.15 shows the magnetic hysteresis loops related to 0º, 45º and 90º P-M configuration however, including parallel and anti-parallel matrix spins alignment. It should be underlined that obtained results suggests typical double phase system, while the different anisotropy is attributed to different direction of "frozen" matrix spins and originated from the same particle.

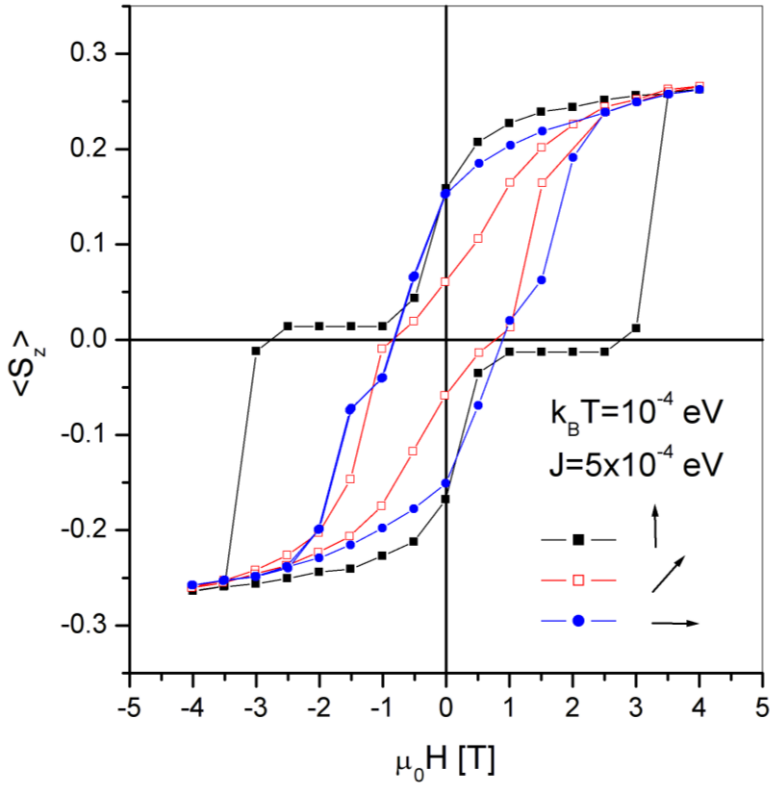


Figure 7.15. Hysteresis loops for the 0º, 45º and 90º P-M configuration with parallel and anti-parallel orientation of spins inside the matrix [104].

## 7.3. Modeling of high-coercive magnetic nanocomposities by the random field model

In section 5.2.2 a high coercivity of (about 3.6 T) in Fe-Nb-B-Tb type of bulk nanocrystalline alloys was reported. Especially important is the example of the first and the second run of magnetic hysteresis loops presented in Figure 5.29 related to the $(Fe_{80}Nb_6B_{14})_{0.88}Tb_{0.12}$ alloy with diameter $d = 0.5$ mm. In this case the loops are complex, asymmetric, unclosed and reveal a difference between the runs. The obtained results allow modelling such materials in the following way. The hysteresis shape suggests a presence of soft, hard and ultra-hard magnetic components as was schematically shown in Figure 7.16a. For the as-cast material, the objects with extremely high anisotropy are randomly dispersed and their total magnetization is equal to zero. These objects do not directly contribute to the change of magnetization, however, they can influence their surroundings by direct or indirect interactions. The possible interactions can be considered as an additional internal random magnetic field (with the mean value equal to zero) acting on the less-hard and soft magnetic phases. After the first magnetic saturation, the distribution of the random field can shift, due to some blocking effects, giving non-zero expected value.

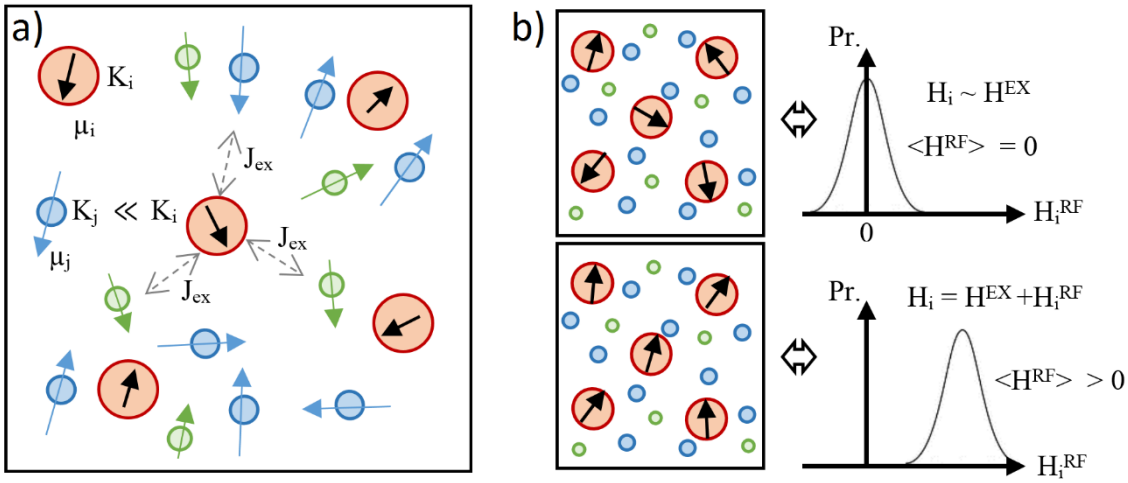


Figure 7.16 a) The schematic presentation of soft (green), hard (blue) and ultra-hard (red) magnetic objects with their magnetic moment μ and anisotropy coefficient K in discussed material; b) the correlation between state of ultra-hard magnetic object and random field distribution as well as field $H_i$ "feeling" by i-th simulated object.

As were described in section 2.2.3 the magnetic properties of the non-interacting, single domain nanoparticles (at temperature T = 0 K) can be described by *the Stoner-Wohlfarth (S-W) model*. Moreover, the dynamic of the system in high temperature can be analyzed in a frame of the so-called *Two-level energetic model* described in section 2.3.2. Finally, magnetization of the system can be determined in the following two steps. Firstly, form the S-W model the energy minima and energy barrier between them is given. Secondly, in a population of the magnetic objects, one may calculate how many objects are in the energy minima at a defined temperature.

In order to carry out the simulations of magnetization processes, the designed system consists of one or two type of sets of spherical magnetic object corresponding to soft and hard magnetic phases. Both of them are characterized by anisotropy coefficient $K_1$ and $K_2$ as well as magnetic moment $\mu_1$ and $\mu_2$ for the first and second phases, respectively. The magnetic objects of ultra-hard phase were not directly included in the simulation, however their impact on surroundings was modeled by additional random field $H^{RF}$ introduced into the system. Finally, the energy of *i*-th magnetic object can be calculated by the formula based on the S-W model:

$$E_i = K_i \sin(\theta_0 - \theta)^2 - \mu_i \mu_0 (H^{EX} + H_i^{RF}) \cos\theta \qquad (7.5)$$

where $\theta$ is the angle between magnetization and field, $\theta_0$ is the angle between easy magnetization axis and field. The model consists of uniform distribution of $\theta_0$ from 0 to $\pi$ for each type of magnetic object. Moreover, $H^{EX}$ is external magnetic field and $H_i^{RF}$ is additional field randomized (during each step) for *i*-th magnetic object based on normal distribution described by average value $< H^{RF} >$ as well as standard deviation $\sigma_{RF}$. It is important to note that $< H^{RF} >$ is 0 at the beginning of hysteresis loop simulation and increases up to the fixed value (due to some blocking effects) for the last point on virgin magnetization curve. Such situation (schematically shown in Figure 7.16b) corresponds to impact of ultra-hard magnetic object, which are partially ordering during the first magnetization and "frozen" after that. Let note, that the introducing of random field to the system supplements the S-W model for interactions between objects, which is not supported by the standard S-W approach.

Finally, the simulation procedure can be summarized as follows:

**Step 1**. Initialize object in random state and set random field with $< H^{RF} > = 0$.

**Step 2**. Calculate energy of each object using formula (7.5) and random value of $H_i^{RF}$ based on normal distribution.

**Step 3**. Find minima of $E_i(\theta)$ and calculate amount of magnetic object in the first (let say X) and second (let say Y) minimum i.e. $N_X$ and $N_Y$ based on the equations (2.70), and (2.71) (for details see section 2.3.2).

**Step 4**. Calculate magnetization $M_i$ for each object:

$$M_i = \mu_i(N_Y cos\theta_Y + N_X cos\theta_X) \tag{7.6}$$

where $\theta_Y$ and $\theta_X$ are the value of $\theta$ for Y and X state energy minima, respectively.

**Step 5**. Calculate the total magnetization of the system and update average value of random field $< H^{RF} >$ as well as $H^{EX}$.

**Step 6**. Repeat the procedure starting from step 2 for full simulation of hysteresis loop double run at room temperature in $H^{EX}$ range from -1T to +1T including 100 points and 5000 magnetic objects.

### 7.3.1. Results of simulations

Figure 7.17 shows simulated hysteresis loops obtained for one magnetic component and four different combinations of random field parameters. In this case all magnetic objects are characterized by anisotropy coefficient $K_1$ and magnetic moment $\mu_1$ equal to 1 eV and $10^4$ $\mu_B$, respectively. As may expect, simulations without additional random field leads to classical – symmetrical, one-component hysteresis loop. On the other hand, positive average vale of random filed $<H^{RF}>$ = 0.3 T shifts hysteresis loops to the left direction as well as provides asymmetries in the X axis. Such behaviour can be easy explained taking into account the total magnetic field $H_i = H^{EX} + H_i^{RF}$ "feeling" by $i$-th object. Additional value of $H_i^{RF}$ increases the total magnetic field in the I and IV quadrants of coordinate system and consequently, accelerates the ordering of magnetic object according to field direction. In the II and III quadrants the situation is opposite. It is important to note, that the highest absolute value of $H_i$ in the III quadrant is equal to 0.7 T, therefore some of the magnetic object are not fully saturated. This situation is manifested by asymmetrical values of positive and negative magnetic saturation. Moreover, the increase of standard deviation for random field distribution $\sigma_{RF}$ leads to larger dispersion of total magnetic

field “feeling” by each object and consequently, decreases the slope of the obtained hysteresis loop.

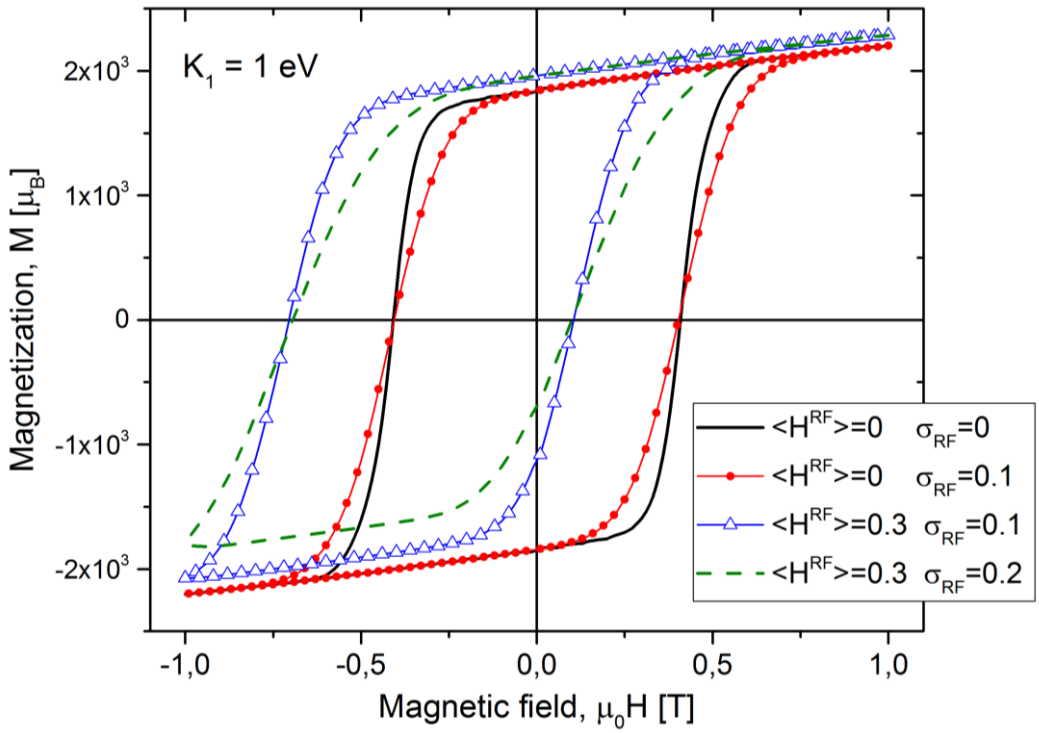


Figure 7.17. The simulated hysteresis loops obtained for one component system with different parameter of additional random field $H^{RF}$.

In order to perform the quantitative analysis of experimental measurements the more complicated, multi-component systems were also studied. Figure 7.18 presents the example of hysteresis loops obtained for sets of two kind of magnetic object corresponds to soft and hard magnetic phases. For all disused cases, the anisotropy coefficient of soft component $K_1 = 0.7$ eV were chosen, while the hard one is represented by $K_2 = 1$ eV, also with the linear distribution from 1 to 1.6 eV. In order to improve the clarity of multi-component impact, the additional random field was turn off. The simulated hysteresis loops show classical shape characteristic for double-phases materials with non-interacting magnetic objects. The proportion between amount of soft and hard objects was defined as 1:1 and 1:4 (denoted as 4x in the figures). The most interesting example includes the distribution of anisotropy for the hard component. The applied external magnetic field (+/- 1 T) is not sufficient to reach fully saturation of magnetic object with anisotropy

coefficient up to 1.6 eV. Such situation was chosen for further analysis due to the good correlation with the experimental data.

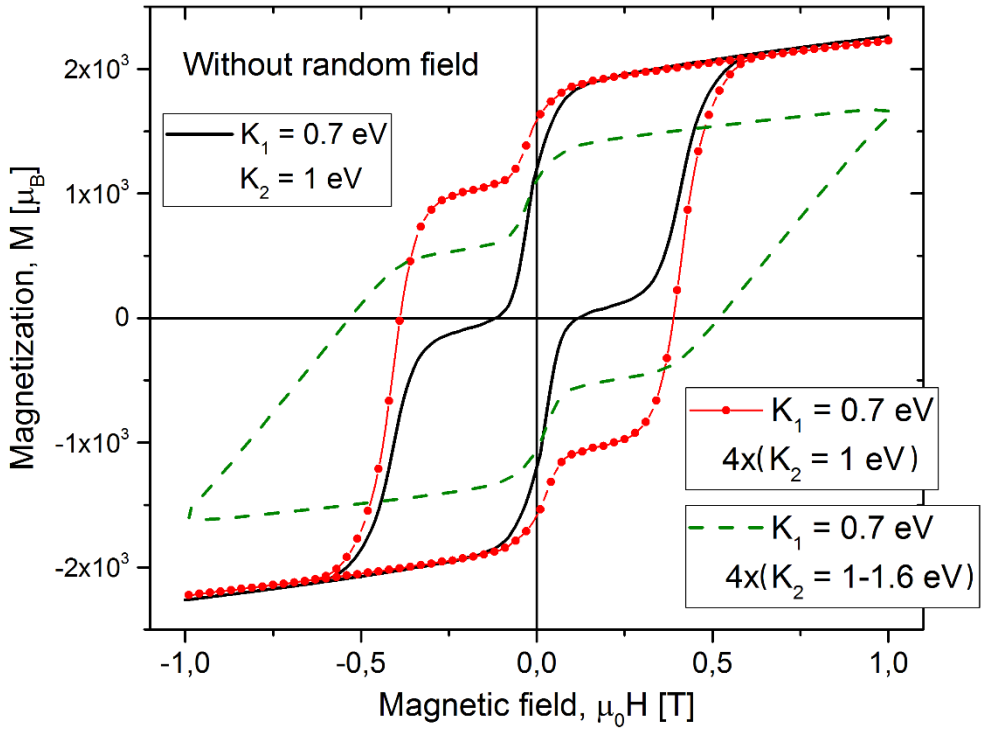


Figure 7.18. The simulated hysteresis loops for the system including two type of magnetic component with different proportion of anisotropy coefficient and amount of objects.

Figure 7.19 shows comparison of measured and simulated magnetic hysteresis loop. Performed simulation based on the system consists of the two kind of magnetic component - as previous, soft phase ($K_1$ = 0.7 eV) and hard phase ($K_2$ = 1 - 1.6 eV) with proportion of amount 1:4, respectively. The average value of additional random field $\langle H^{RF} \rangle$ = 0.1 T as well as standard deviation of Gaussian distribution $\sigma_{RF}$ = 0.3 were chosen by the trial and error steps. The obtained hysteresis corresponds to all characteristic features of the measured $M(H)$ curves for $(Fe_{80}Nb_6B_{14})_{0.88}Tb_{0.12}$ bulk alloy ($d$ = 0.5 mm, $I$ = 25 A). Especially important is a comparison of the first and second run of the simulation for the same system - similar to the measurement procedure performed for the real material. In both cases the second run is not identical with the previous one, which indicates that some of the magnetic object are "frozen" after the first magnetization and do not take direct part in the further magnetization process.

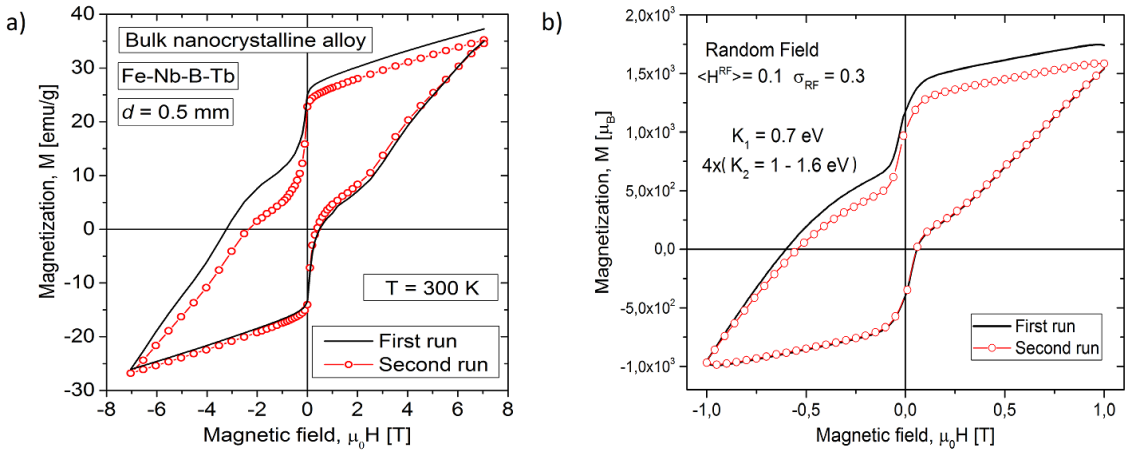


Figure 7.19. The firs and the second run of magnetic hysteresis loops obtained by a) measurement of $(Fe_{80}Nb_6B_{14})_{0.88}Tb_{0.12}$ bulk alloy as well as b) simulation based on S-W model with additional random field and two type of magnetic components.

The carried out simulations prove that the proposed approach, including the additional random field, can be applied for modelling magnetization processes in hard magnetic materials. In fact, in relation to magnetic systems with ultra-hard interacting magnetic object, the random field allow for quantitative analysis of asymmetric, not fully saturated and opened, multi-phases hysteresis loops.

# 8. Discussion

The subject of hard magnetic materials is important from the both practical as well as scientific point of view. The researches in this field are focused on new materials with strong enough hard magnetic properties but with lower rare earth content than for the classical Nd rich alloys. In the literature, one can find the following main directions: i) improvement of coercivity of RE-free permanent magnets, ii) decrease of Re content making a profit of innovative preparation technology and iii) improvement of magnetic remanence by interactions with magnetically soft Fe-based phases – also leading to the desired decrease of RE content. Moreover, a form of the alloys has an important meaning (i.e., thin melt spun ribbon, powders, sintered powders, thin layers or bulks). In many cases the bulk form is required that can broaden possible application of permanent magnets in electronics, sensors or MEMS devices.

This thesis relates to the two last goals listed above. The starting point is the used vacuum suction casting as the preparation method of the bulk materials, allowing formation of nano/microstructure in one step – just after casting. In fact, it is possible taking into account relatively high cooling rate (in order of 1000 K/s) and the so-called glass forming ability of the examined alloys. Important is the fact that these two factors can be controlled by the diameter of the mold and a proper alloying additions, respectively.

The idea of this work is based on the following facts:

- In the Fe-Nb-B type of amorphous alloys, Nb as an alloying addition causes a slowing down of diffusion processes of Fe and in a consequence, makes its crystallization more difficult. This allows controlling the formation of microstructure of the alloys prepared using a technology with fixed cooling rate.
- The best known hard magnetic phase is the $RE_2Fe_{14}B$ compound. If the RE is the so-called light rare earth (below Gd in the periodic table) the compound has high remanence while for the heavy RE the compound it has high coercivity with relatively low remanence due to antiferromagnetic coupling between the Fe and RE magnetic moments.

- Addition of RE to the Fe-Nb-B alloys should lead to the formation of a composite containing the $RE_2Fe_{14}B$ phase and other soft magnetic phases like α-Fe, Fe-B, Fe-RE. A balance between the phases should be controlled by a proper chemical composition of the examined materials.
- The vacuum suction casting is a good method of bulks preparation. Cooling rate can be controlled by the mold diameters, but in a short range, therefore, a proper Nb content should allow slowing down of crystallization that can result in a formation of a preferred for hard magnetic properties microstructure.

The above and the results of the preliminary researches prompted us to choice Tb as the RE addition (10 – 12 at.%) and 6 – 8 at.% of Nb. Additionally, the influence of the Tb/Y substitution as well as replacement of Tb by Dy were studied. For the selected cases, the impact of the cooling rate (controlled by the sample diameter) was also tested.

Similarly to the results presented in the preliminary researches, the phase structure depends on the RE content. The XRD and Mössbauer experiments indicate the formation of mainly $Tb_2Fe_{14}B$, $Tb_2Fe$ and some paramagnetic phases. For all studied cases, the maximum of the $Tb_2Fe_{14}B$ phase is observed for 12 at.% of the Tb addition. Moreover, the minimum of the $Tb_2Fe$ content is correlated with this maximum. For lower Tb concentration one may observed the increase contribution of the α-Fe phase.

Negative, but interesting, results were obtained testing the phase structure as a function of the sample diameter. As it was shown any significant changes were observed that, in a comparison with the changes in magnetic properties, suggests an important role of microstructure. In fact, the carried out SEM observations reveal the formation of the dendrite-like grains of different phases dependently on the sample diameter and the Tb concentration. The EDS maps clearly show the main two areas i.e., roughly say, with and without Nb. The grains without Nb contain Fe and Tb that surely form the hard magnetic $Tb_2Fe_{14}B$ phase. Interesting is that these grains are micrometric but with nanometric dendrite branches which can be a source of additional magnetic anisotropies.

The changes in mictrostructure are correlated with the observed changes in the magnetic properties. As it was shown, the coercivity, remanence and the $|JH|_{max}$ parameter strongly

depends on the RE content as well as the sample diameter. In Table 8.1 the parameters measures for the all investigates alloys are collected.

The highest coercivity, higher than 7 T, was obtained for the $(Fe_{80}Nb_6B_{14})_{0.88}Tb_{0.12}$ alloys (d= 1.5 mm, I = 35 A) after the field-annealing. This composition also has the highest $H_c$ = 5.7 T in the as-cast state. The highest $|JH|_{max}$ = 700 kJ/m$^3$ was observed for the $(Fe_{78}Nb_8B_{14})_{0.88}Tb_{0.12}$ alloys (d= 0.5 mm, I = 35 A) and the highest $|BH|_{max}$ = 33.8 kJ/m$^3$ was observed for the $(Fe_{80}Nb_6B_{14})_{0.88}Tb_{0.04}Y_{0.08}$ alloys (d= 1.5 mm, I = 35 A). It should be also mentioned that for one sample of $(Fe_{78}Nb_8B_{14})_{0.88}Tb_{0.12}$ alloys (d= 0.5 mm, I = 35 A) the hysteresis loop was measured in the field of ±14 T. In this case the coercive field riches the value of 8.6 T.

The correlation between the structural and magnetic properties reveal the important role of the chosen preparation technology for the bulk materials. As shown, the rapidly quenched alloys can contain dendrite microstructure when crystallization is slowed down and/or the cooling rate is increased. It seems that Nb, as an atom with large radius, is the key point for controlling the formation of the preferred for hard magnetic properties microstructure. This conclusion is strongly supported by the dependence of the crystallization enthalpy of iron crystallization in the Fe-Nb-B amorphous alloys [105]. Figure 8.1 presents the influence of Nb content on coercovity $H_C$, the $|JH|_{max}$ parameter and the crystallization enthalpy (data taken from [105]) for the $(Fe_{86-x}Nb_xB_{14})_{0.88}Tb_{0.12}$ alloys. One may see that the parameters have the maxima for the Nb content equal to 6 at. % which proves that the slowing down of crystallization, in the combination of the proper cooling rate, is responsible for the observed magnetic hardening effect.

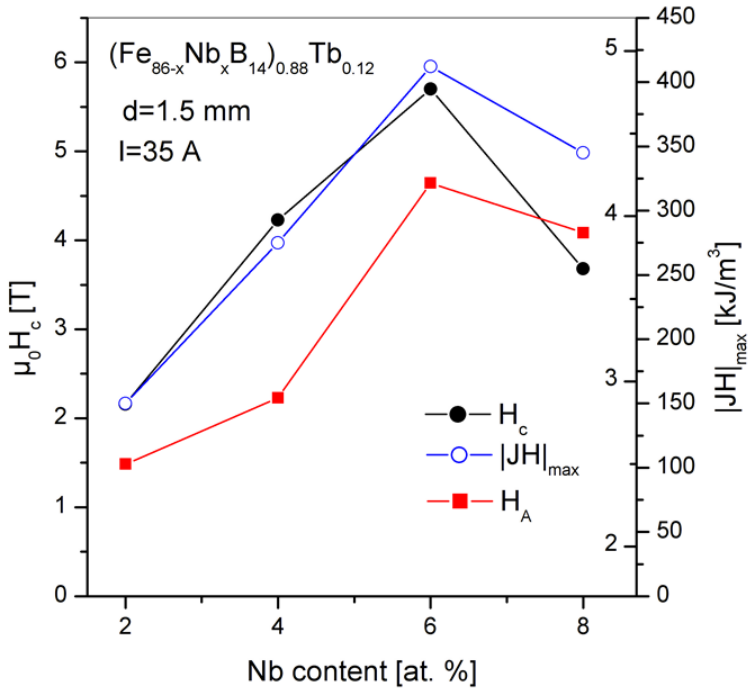


Figure 8.1. Coercivity and |JH|max parameter determined from the hysteresis loops for the $(Fe_{86-x}Nb_xB_{14})_{0.88}Tb_{0.12}$ alloys. Based on the data from [105], activation enthalpy ($H_A$) of iron crystallization for the $Fe_{86-x}Nb_xB_{14}$ amorphous alloys is plotted.

The obtained results allow us to describe the magnetization processes of the examined alloys in the context of the specific microstructure. First of all, the unclosed and shifted hysteresis loops suggests an existence of some ultra-hard magnetic objects that do not directly contribute to the change of magnetization but they are a source of the exchange anisotropy (like in the exchange-bias effect) and in this way exert an influence of the less hard magnetic surroundings. Accounting the SEM images, one can state that the nanometric dendrite branches can plays the role of the ultra-hard magnetic objects – they have high magnetic anisotropy (magnetocrystalline and surface of type) and low magnetic moment (low size). Therefore, the change of magnetization of these objects is, in our case, impossible up to 7 T magnetic field. This hypothesis is confirmed by the carried out thermal treatment when the change of magnetization of these objects is forced by the annealing in high temperature (700 K) and simultaneously high external magnetic field (7 T). After such annealing the coercivity significantly increases which is a result of the induced anisotropy caused by a partial ordering of the object magnetic moments.

Some kind of micro-magnetic characterization can be carried out by means of the numerical analysis of magnetic moment and energy barrier distributions, described in the section 2.3.2. In the case of the interacting system and with the assumption that the pinning mechanism is responsible for the magnetization processes, this method can reveal the distributions related to the pinning centers. Now, the energy barrier is an apparent value including magnetic anisotropy as well as possible interactions. Despite the difficulty in interpretation of the later, the determination of the distributions give important information about magnetic microstructure of the material. Figure 8.2a shows the derivatives of magnetization curves measured at 300 K for the $(Fe_{86-x}Nb_xB_{14})_{0.88}Tb_{0.12}$ alloys. Temperature shift of the maximum of d$M$/d$H$, determined at 200 K and 300 K, for the $(Fe_{84}Nb_2B_{14})_{0.88}Tb_{0.12}$ alloy is depicted in the inset of Figure 8.2a. In some cases, more than one maximum is observed that means that the distribution has more than one component. Figure 8.2b shows results of the described above analysis based on the temperature shift of the d$M$/d$H$ maxima. Assuming that the magnetic moment per unit cell of $Tb_2Fe_{14}B$ equals to 8 $\mu_B$, one can estimate the mean diameter $D$ of the pinning centers. In the case of alloy with $x = 2$ (the lowest coercivity), the pinning centers have, on average, magnetic moment equal to 3400 $\mu_B$ ($D \approx 7.4$ nm) and they are blocked by the energy barrier of 0.93 eV. In the optimal point, i.e. for $x = 6$, the mean magnetic moment decreases to 1000 $\mu_B$ ($D \approx 5$ nm), and the energy barrier increases to more than 1.2 eV. The performed analysis indicates a significant dependence of the Nb content on the pinning center parameters. One may observe a characteristic optimum at 6 at. %, i.e. a high energetic barrier and simultaneously a low magnetic moment – both expected for hard magnetic materials.

The hypothesis of the ultra-hard magnetic objects and they influence on magnetization processes is confirmed by the carried out simulations. The simulations refer to the magnetic behavior of hard magnetic particles embedded into ultra-hard magnetic matrix. The obtained results confirm that the ultra-hard magnetic objects (simulated by the matrix) can significantly influence the magnetization processes of the whole material and can be an origin of the high coercivity as well as multiphase shape of the hysteresis loops.

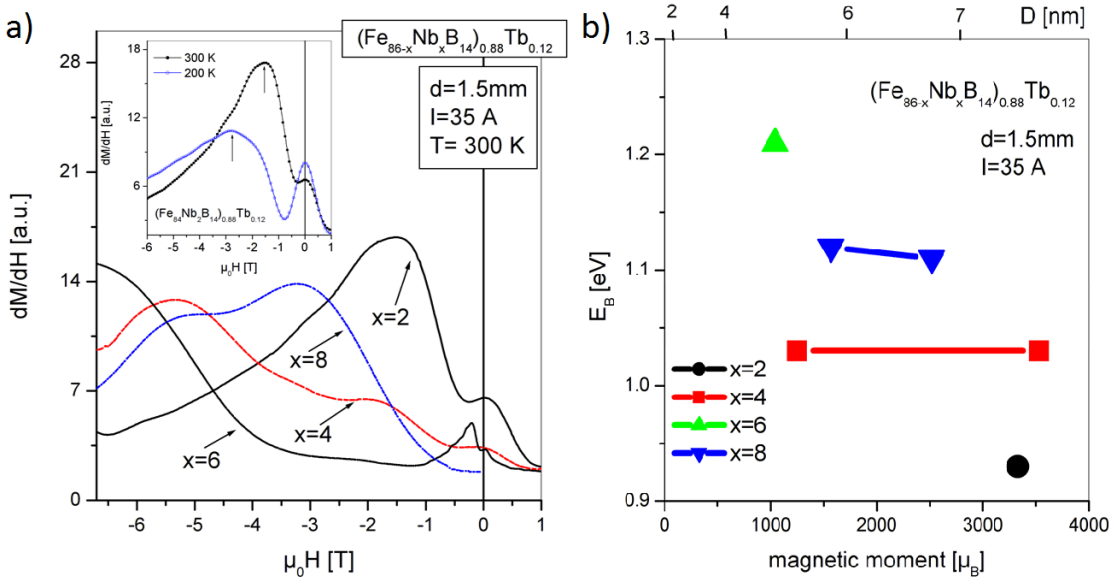


Figure 8.2. a) Derivatives of magnetization curves measured at 300 K for the $(Fe_{86-x}Nb_xB_{14})_{0.88}Tb_{0.12}$ alloys. The inset shows derivatives of magnetization curves measured at 200 K and 300 K for the $(Fe_{84}Nb_2B_{14})_{0.88}Tb_{0.12}$ alloy; b) Main components of the pinning centers as a function of the energy barrier $E_B$ and the mean magnetic moment $\mu_B$. The magnetic moment is converted into the mean diameter $D$ of the pinning centers [102].

In other approach, the objects can be a source of the so-called internal random (or quenched) magnetic field that, similarly to the Weiss field in ferromagnetism, describes direct interactions between the ultra-hard and the rest magnetic objects. In the frame of this model, the obtained hysteresis loops are in a good agreement with the experimental curves that is consistent with the micro-magnetic picture of the studied alloys.

Summarizing this discussion, one may conclude that the main achievement of this work if the fabrication of the alloys characterized by ultra-high magnetic coercivity (more than 7 T at room temperature) which in the case of the bulk materials is a unique feature and is presented (published in [102]) for the first time. Such materials can be a starting point for designing of new hard magnetic composites (sintered powders, spring magnets or bulk alloys) based on the knowledge collected in this thesis.

Table 8.1. The all investigated samples type of $(Fe_{1-a-b}Nb_aB_b)_{1-x}RE_x$ prepared by vacuum suction technique using the mold with inner diameter *d* and power of melting *I*, selected magnetic parameters and page number of section with details were also included.

| L.p. | *a* | *b* | *RE* | *x* [at.%] | *d* [mm] | *I* [A] | $M_S^{7T}$ [emu/g] | $M_R$ [emu/g] | $\mu_0 H_C$ [T] | $\|BH\|_{max}$ [kJ/m$^3$] | $\|JH\|_{max}$ [kJ/m$^3$] | Page |
|---|---|---|---|---|---|---|---|---|---|---|---|---|
| 1 | 6 | 14 | Tb | 2 | 1.5 | 25 | 127 | 1.7 | 0.01 | - | - | 98 |
| 2 | 6 | 14 | Tb | 4 | 1.5 | 25 | 68 | 15.9 | 0.03 | 0.7 | 1.7 | 98 |
| 3 | 6 | 14 | Tb | 6 | 1.5 | 25 | 72 | 21.8 | 0.15 | 3 | 5.9 | 98 |
| 4 | 6 | 14 | Tb | 8 | 1.5 | 25 | 54 | 25.2 | 0.25 | 6.4 | 12.7 | 98 |
| 5 | 6 | 14 | Tb | 9 | 1.5 | 25 | 52 | 26.8 | 0.75 | 9.9 | 35.9 | 98 |
| 6 | 6 | 14 | Tb | 10 | 1.5 | 25 | 43 | 25.1 | 1.46 | 10 | 51.3 | 98 |
| 7 | 6 | 14 | Tb | 12 | 1.5 | 25 | 37 | 26.1 | 1.16 | 12.7 | 94.9 | 98 |
| 8 | 6 | 14 | Tb | 16 | 1.5 | 25 | 49 | 22.7 | 0.06 | 2.3 | 2.8 | 98 |
| 9 | 6 | 14 | Tb | 32 | 1.5 | 25 | 69 | 22.6 | 0.08 | 3 | 3.9 | 98 |
| 10 | 6 | 14 | Tb | 6 | 1 | 25 | 82.4 | 14.6 | 0.07 | - | - | 108 |
| 11 | 6 | 14 | Tb | 6 | 0.5 | 25 | 65.8 | 14.9 | 0.05 | - | - | 108 |
| 12 | 6 | 14 | Tb | 8 | 1 | 25 | 52.5 | 25.4 | 0.62 | 7.9 | 27.4 | 108 |
| 13 | 6 | 14 | Tb | 8 | 0.5 | 25 | 44.2 | 24.8 | 2.46 | 7.5 | 77.2 | 108 |
| 14 | 6 | 14 | Tb | 10 | 2 | 25 | 43 | 27 | 0.57 | 9.5 | 28.7 | 108 |
| 15 | 6 | 14 | Tb | 10 | 1 | 25 | 36 | 27 | 1.79 | 9 | 71.2 | 108 |
| 16 | 6 | 14 | Tb | 10 | 0.5 | 25 | 38.1 | 25 | 2.66 | 9 | 82.6 | 108 |
| 17 | 6 | 14 | Tb | 11 | 2 | 25 | 42.5 | 29 | 0.82 | 10.6 | 43 | 108 |
| 18 | 6 | 14 | Tb | 11 | 1 | 25 | 38.7 | 28 | 2.02 | 10 | 91.5 | 108 |
| 19 | 6 | 14 | Tb | 11 | 0.5 | 25 | 35.9 | 27 | 3.56 | 8.1 | 106 | 108 |
| 20 | 6 | 14 | Tb | 12 | 2 | 25 | 44.5 | 26 | 0.72 | 8 | 24.8 | 108 |
| 21 | 6 | 14 | Tb | 12 | 1 | 25 | 40.2 | 29 | 1.82 | 10.2 | 65.3 | 108 |
| 22 | 6 | 14 | Tb | 12 | 0.5 | 25 | 37.6 | 25 | 3.36 | 9 | 121 | 108 |
| 23* | 6 | 14 | Tb | 10 | 2 | 25 | 55 | 24 | 0.2 | - | - | 127 |
| 24* | 6 | 14 | Tb | 10 | 1.5 | 25 | 49 | 22 | 0.21 | - | - | 127 |
| 25* | 6 | 14 | Tb | 10 | 1 | 25 | 40 | 25 | 0.8 | 4.5 | 18 | 127 |
| 26* | 6 | 14 | Tb | 10 | 0.5 | 25 | 99 | 5 | 0.04 | - | - | 127 |
| 27$^+$ | 6 | 14 | Tb | 8 | 1.5 | 25 | 60 | 41.8 | 0.30 | 12.1 | 22 | 133 |
| 28$^+$ | 6 | 14 | Tb | 12 | 1.5 | 25 | 38.5 | 22 | 0.33 | 1.9 | 10 | 133 |
| 29 | 6 | 14 | Er | 4 | 1.5 | 25 | 99 | 15.2 | 0.03 | - | - | 137 |
| 30 | 6 | 14 | Er | 8 | 1.5 | 25 | 72 | 4.9 | 0.01 | - | - | 137 |
| 31 | 6 | 14 | Er | 12 | 1.5 | 25 | 54 | 6.6 | 0.03 | - | - | 137 |
| 32 | 6 | 14 | Er | 16 | 1.5 | 25 | 19 | 5.4 | 0.1 | - | - | 137 |
| 33 | 6 | 14 | Pr | 12 | 1.5 | 35 | 110 | 27.8 | 0.1 | - | - | 138 |
| 34 | 6 | 14 | Pr | 12 | 0.5 | 35 | 103.4 | 34.3 | 0.1 | - | - | 138 |
| 35 | 6 | 14 | Nd | 8 | 1.5 | 25 | 117 | 38.6 | 0.2 | 13.4 | - | 140 |
| 36 | 6 | 14 | Nd | 12 | 1.5 | 25 | 111 | 32.2 | 0.11 | 6.9 | - | 140 |
| 37 | 6 | 14 | Nd | 16 | 1.5 | 25 | 86 | 25.8 | 0.13 | 6.5 | - | 140 |
| 38 | 6 | 14 | Pt | 15 | 1.5 | 35 | 71 | 7.5 | 0.026 | - | - | 143 |

| | | | | | | | | | | | | |
|---|---|---|---|---|---|---|---|---|---|---|---|---|
| 39 | 6 | 14 | Pt | 30 | 1.5 | 35 | 75 | 8 | 0.2 | - | - | 143 |
| 40 | 6 | 14 | Pt | 40 | 1.5 | 35 | 67 | 25 | 0.2 | - | - | 143 |
| 41 | 6 | 14 | Pt | 40 | 1 | 35 | 65 | 21 | 0.18 | - | - | 143 |
| 42 | 6 | 14 | Pt | 40 | 0.5 | 35 | 62 | 21 | 0.195 | - | - | 143 |
| 43 | 6 | 14 | Pt | 60 | 1.5 | 35 | 31 | 5.5 | 0.032 | - | - | 143 |
| 44 | 0 | 14 | Tb | 4 | 1.5 | 25 | 142.7 | 8.4 | 0.02 | - | - | 147 |
| 45 | 0 | 14 | Tb | 8 | 1.5 | 25 | 90 | 8.7 | 0.03 | - | - | 147 |
| 46 | 0 | 14 | Tb | 12 | 1.5 | 25 | 54.5 | 23 | 0.24 | - | - | 147 |
| 47 | 0 | 22 | Tb | 4 | 1.5 | 25 | 108 | 8.2 | 0.03 | - | - | 147 |
| 48 | 0 | 22 | Tb | 8 | 1.5 | 25 | 50 | 8 | 0.04 | - | - | 147 |
| 49 | 0 | 22 | Tb | 12 | 1.5 | 25 | 38.8 | 13.3 | 0.1 | - | - | 147 |
| 50 | 6 | 14 | Tb | 12 | 1.5 | 15 | 34 | 18.2 | 1.35 | 6.1 | 51 | 156 |
| 51 | 6 | 14 | Tb | 12 | 1.5 | 25 | 39 | 19.8 | 0.96 | 5.9 | 33 | 156 |
| 52 | 6 | 14 | Tb | 12 | 1.5 | 35 | 36.5 | 24.9 | 5.7 | 12.2 | 412 | 156 |
| 53 | 6 | 14 | Tb | 12 | 1.5 | 45 | 38.5 | 25.4 | 4.57 | 12.5 | 284 | 156 |
| 54 | 2 | 14 | Tb | 12 | 1.5 | 35 | 42.1 | 27.3 | 2.16 | 13.7 | 150 | 162 |
| 55 | 4 | 14 | Tb | 12 | 1.5 | 35 | 38.9 | 26.2 | 4.23 | 13.3 | 275 | 162 |
| 56 | **6** | **14** | **Tb** | **12** | **1.5** | **35** | **36.5** | **24.9** | **5.7** | **12.2** | **412** | 162 |
| 57 | 8 | 14 | Tb | 12 | 1.5 | 35 | 40.5 | 28.7 | 3.68 | 16.2 | 345 | 162 |
| **58[@]** | **6** | **14** | **Tb** | **12** | **1.5** | **35** | **36.7** | **24** | **>7** | **11.2** | **521** | **167** |
| 59 | 6 | 14 | Tb/Y | 10/2 | 1.5 | 35 | 49 | 32.5 | 5.43 | 16.2 | 531.5 | 171 |
| 60 | 6 | 14 | Tb/Y | 8/4 | 1.5 | 35 | 56 | 36.6 | 4.57 | 22.1 | 489.7 | 171 |
| 61 | 6 | 14 | Tb/Y | 6/6 | 1.5 | 35 | 68 | 41 | 3.15 | 27 | 432 | 171 |
| 62 | **6** | **14** | **Tb/Y** | **4/8** | **1.5** | **35** | **81** | **44.7** | **1.5** | **33.8** | **256** | 171 |
| 63 | 6 | 14 | Tb/Y | 2/10 | 1.5 | 35 | 99 | 42.5 | 0.35 | 17.6 | 32.6 | 171 |
| 64 | 6 | 14 | Tb/Y | 0/12 | 1.5 | 35 | 112 | 25 | 0.05 | 1.8 | 2.21 | 171 |
| 65 | 8 | 14 | Tb | 8 | 1.5 | 35 | 50 | 17 | 0.21 | 2.5 | 5 | 180 |
| 66 | 8 | 14 | Tb | 8 | 1 | 35 | 55 | 27.5 | 1.23 | 9.8 | 47 | 180 |
| 67 | 8 | 14 | Tb | 8 | 0.5 | 35 | 62.5 | 30 | 0.63 | 11 | 35 | 180 |
| 68 | 8 | 14 | Tb | 10 | 1.5 | 35 | 56.2 | 21.5 | 1.16 | 8.7 | 62 | 180 |
| 69 | 8 | 14 | Tb | 10 | 1 | 35 | 40 | 25 | 1.8 | 12 | 127 | 180 |
| 70 | **8** | **14** | **Tb** | **10** | **0.5** | **35** | **35.5** | **39** | **5.6**<br>**8.6$_{14T}$** | **29.5** | **700** | 180 |
| 71 | 8 | 14 | Tb | 12 | 1.5 | 35 | 40.6 | 28.7 | 3.66 | 16.1 | 340 | 180 |
| 72 | 8 | 14 | Tb | 12 | 1 | 35 | 41 | 28 | 4.1 | 15 | 408 | 180 |
| 73 | 8 | 14 | Tb | 12 | 0.5 | 35 | 37 | 25.8 | 6.9 | 13.3 | 590 | 180 |
| 74 | 6 | 14 | Dy | 8 | 1.5 | 35 | 58.6 | 24.9 | 0.42 | 6.8 | 18.2 | 193 |
| 75 | 6 | 14 | Dy | 10 | 1.5 | 35 | 43.7 | 24.1 | 0.85 | 9.8 | 38.5 | 193 |
| 76 | 6 | 14 | Dy | 12 | 1.5 | 35 | 39.1 | 21.6 | 1.2 | 7.6 | 48.8 | 193 |
| 77 | 6 | 14 | Dy | 12 | 1 | 35 | 44.1 | 27.2 | 4.1 | 10.5 | 207 | 193 |
| 78 | 6 | 14 | Dy | 12 | 0.5 | 35 | 48.7 | 31.4 | 5.5 | 12.4 | 386 | 193 |
| 79 | 6 | 14 | Dy | 16 | 1.5 | 35 | 29.7 | 10.1 | 0.15 | 1.9 | 3.1 | 193 |

* Heating up to 900K, [+]milled, [@]field annealing in 700K

# 9. Conclusions

The main conclusions related to the Fe-Nb-B-RE alloys in the bulk form, prepared by vacuum suction technique, can be summarized as follows:

1. The phase structure, microstructure and magnetic properties strongly depends on the chemical composition (RE and Nb content) as well as technology parameters (sample diameter and the melting current). The optimal parameters were established: i) Tb as the RE element with the content of 10-12 at. %, ii) Nb content of 6-8 at. %, iii) sample diameter ranged from 0.5 to 1.5 mm and iv) melting current $I$ = 35 A.

2. The alloys reveal hard magnetic properties with a high and ultra-high coercivity depending on the niobium content. Particularly, for the field-annealed $(Fe_{80}Nb_6B_{14})_{0.88}Tb_{0.12}$ alloy, the coercive field measured at room temperature exceeds 7 T which is a unique feature in the case of bulks. A subsequent increase of temperature causes a decrease in $H_c$ but at 550 K, it is still higher than 1 T.

3. The niobium content combined with the specific solidification rate (during casting) are responsible for the observed magnetic hardening effect. The observed phase segregation leads to the formation of grain microstructure with the irregularly shaped dendrites. The optimum, accounting hard magnetic properties, occurs for 6 at.% of the Nb content, for which the dendrites are composed mainly of the $Tb_2Fe_{14}B$ hard magnetic phase, while the regions between the dendrite branches are Nb-rich. Moreover, these inter-dendritic regions break direct magnetic interactions which leads to an introduction of an additional shape and surface anisotropy.

4. The observed submicrometric dendrite branches are a source of some ultra-hard magnetic objects. These objects do not contribute directly to magnetization process (at least up to 7 T), but they cause an exchange anisotropy leading to formation of an asymmetry of the magnetic hysteresis loops. As it was shown, the

proposed field-annealing allows for further improving of the hard magnetic properties.

5. The carried out simulations proved the proposed micro-magnetic picture of the alloys in question. The obtained results, in the frame of the direct Monte Carlo simulations, indicate a significant role of the ultra-hard magnetic objects in the magnetization processes. Moreover, the simulated, in the frame of the random field model, hysteresis loops are in a good agreement with the experimental curves that also confirms the correctness of this approach and the origin of the observed magnetic hardening effect.

6. The partial substitution of Tb by Y leads to the increase in magnetic remanence and the $|BH|_{max}$ parameter. However, with the increase of the Y content the decrease in coercivity is observed.

7. Generally, the examined alloys can be considered as high and ultra-high coercive materials with application potential in the fields of permanent magnets where increasing resistance to external magnetic field is required.

# 10. Bibliography


[1] N. A. Spaldin, *Magnetic materials fundamentals and applications*. Cambridge; New York: Cambridge University Press, 2011.

[2] J. M. D. Coey, *Magnetism and magnetic materials*. Cambridge: Cambridge University Press, 2010.

[3] K. H. J. Buschow and F. R. de Boer, *Physics of magnetism and magnetic materials*. New York: Kluwer Academic/Plenum Publishers, 2003.

[4] M. McHenry, M. A. Willard, and D. E. Laughlin, "Amorphous and nanocrystalline materials for applications as soft magnets," *Prog. Mater. Sci.*, vol. 44, no. 4, pp. 291–433, 1999.

[5] C. M. Hurd, "Varieties of magnetic order in solids," *Contemp. Phys.*, vol. 23, no. 5, pp. 469–493, Sep. 1982.

[6] A. P. Guimarães, *Principles of Nanomagnetism*. Berlin, Heidelberg: Springer Berlin Heidelberg, 2009.

[7] K. A. Gallagher, M. A. Willard, V. N. Zabenkin, D. E. Laughlin, and M. E. McHenry, "Distributed exchange interactions and temperature dependent magnetization in amorphous Fe88−xCoxZr7B4Cu1 alloys," *J. Appl. Phys.*, vol. 85, no. 8, p. 5130, 1999.

[8] M. McHenry and D. E. Laughlin, "Nano-scale materials development for future magnetic applications," *Acta Mater.*, vol. 48, pp. 223–238, 2000.

[9] I. M. L. Billas, J. A. Becker, A. Châtelain, and W. A. de Heer, "Magnetic moments of iron clusters with 25 to 700 atoms and their dependence on temperature," *Phys. Rev. Lett.*, vol. 71, no. 24, pp. 4067–4070, Dec. 1993.

[10] A. Hirt, D. Gerion, I.M.L. Billas, "Thermal properties of ferromagnetic clusters," *Z. Phys. At. Mol. Clust.*, vol. 40, no. 1–4, pp. 160–163, May 1997.

[11] M. Getzlaff, *Fundamentals of magnetism*. Berlin ; New York: Springer, 2008.

[12] F. J. A. den Broeder, W. Hoving, and P. J. H. Bloemen, "Magnetic anisotropy of multilayers," *J. Magn. Magn. Mater.*, vol. 93, pp. 562–570, Feb. 1991.

[13] M. E. Evans and F. Heller, *Environmental magnetism*. San Diego: Academic Press, 2003.

[14] E. C. Stoner and E. P. Wohlfarth, "A mechanism of magnetic hysteresis in heterogeneous alloys," *Philos. Trans. R. Soc. A*, no. 240, pp. 599–642, 1948.

[15] O. Henkel, "Remanenzverhalten und Wechselwirkungen in hartmagnetischen Teilchenkollektiven," *Phys. Status Solidi B*, vol. 7, no. 3, pp. 919–929, 1964.

[16] Q. Chen, B. M. Ma, B. Lu, M. Q. Huang, and D. E. Laughlin, “A study on the exchange coupling of NdFeB-type nanocomposites using Henkel plots,” *J. Appl. Phys.*, vol. 85, no. 8, p. 5917, 1999.

[17] S. Thamm and J. Hesse, “A simple plot indicating interactions between single-domain particles,” *J. Magn. Magn. Mater.*, vol. 154, no. 2, pp. 254–262, Apr. 1996.

[18] S. Thamm and J. Hesse, “The remanence of a Stoner–Wohlfarth particle ensemble as a function of the demagnetisation process,” *J. Magn. Magn. Mater.*, vol. 184, no. 2, pp. 245–255, Apr. 1998.

[19] E. F. Kneller and R. Hawig, “The exchange-spring magnet: a new material principle for permanent magnets,” *IEEE Trans. Magn.*, vol. 27, no. 4, pp. 3588–3560, Jul. 1991.

[20] P. M. S. Monteiro and D. S. Schmool, “Magnetization dynamics in exchange-coupled spring systems with perpendicular anisotropy,” *Phys. Rev. B*, vol. 81, no. 21, Jun. 2010.

[21] H. Kronmüller, “Micromagnetism of hard magnetic nanocrystalline materials,” *Nanostructured Mater.*, vol. 6, no. 1–4, pp. 157–168, Jan. 1995.

[22] Y. Imry and S. Ma, “Random-Field Instability of the Ordered State of Continuous Symmetry,” *Phys. Rev. Lett.*, vol. 35, no. 21, pp. 1399–1401, Nov. 1975.

[23] T. Nattermann and P. Rujan, “Random field and other systems dominated by disorder fluctuations,” *Int. J. Mod. Phys. B*, vol. 03, no. 11, pp. 1597–1654, Nov. 1989.

[24] D. S. Fisher, G. M. Grinstein, and A. Khurana, “Theory of random magnets,” *Phys. Today*, vol. 41, no. 12, pp. 56–67, 1988.

[25] S. Kirkpatrick and D. Sherrington, “Infinite-ranged models of spin-glasses,” *Phys. Rev. B*, vol. 17, no. 11, pp. 4384–4403, Jun. 1978.

[26] R. Alben, J. J. Becker, and M. C. Chi, “Random anisotropy in amorphous ferromagnets,” *J. Appl. Phys.*, vol. 49, no. 3, p. 1653, 1978.

[27] J. D. Patterson, G. R. Gruzalski, and D. J. Sellmyer, “Effect of random anisotropy on magnetic properties of amorphous systems,” *Phys. Rev. B*, vol. 18, no. 3, pp. 1377–1390, Aug. 1978.

[28] C. Jayaprakash and S. Kirkpatrick, “Random anisotropy models in the Ising limit,” *Phys. Rev. B*, vol. 21, no. 9, pp. 4072–4083, May 1980.

[29] A. B. Harris, R. G. Caflisch, and J. R. Banavar, “Random-anisotropy-axis magnet with infinite anisotropy,” *Phys. Rev. B*, vol. 35, no. 10, pp. 4929–4934, Apr. 1987.

[30] B. Derrida and J. Vannimenus, “The random anisotropy axis model in the infinite-range limit,” *J. Phys. C Solid State Phys.*, vol. 13, no. 17, pp. 3261–3269, Jun. 1980.

[31] T. Bitoh, A. Makino, A. Inoue, and T. Masumoto, “Random Anisotropy Model for Nanocrystalline Soft Magnetic Alloys with Grain-Size Distribution,” *Mater. Trans.*, vol. 44, no. 10, pp. 2011–2019, 2003.

[32] G. Herzer, "The Random Anisotropy Model," in *Properties and Applications of Nanocrystalline Alloys from Amorphous Precursors*, vol. 184, B. Idzikowski, P. Švec, and M. Miglierini, Eds. Berlin/Heidelberg: Springer-Verlag, 2005, pp. 15–34.

[33] G. Herzer, "Anisotropies in soft magnetic nanocrystalline alloys," *J. Magn. Magn. Mater.*, vol. 294, no. 2, pp. 99–106, Jul. 2005.

[34] G. Herzer, "Nanocrystalline soft magnetic materials," *Phys. Scr.*, vol. T49A, pp. 307–314, Jan. 1993.

[35] W. M. Saslow and N. C. Koon, "Random-anisotropy model: Monotonic dependence of the coercive field on D/J," *Phys. Rev. B*, vol. 49, no. 5, pp. 3386–3390, Feb. 1994.

[36] R. Street and J. C. Woolley, "A Study of Magnetic Viscosity," *Proc. Phys. Soc. Sect. A*, vol. 62, no. 9, pp. 562–572, Sep. 1949.

[37] N. T. Gorham, R. C. Woodward, T. G. St Pierre, B. D. Terris, and S. Sun, "Apparent magnetic energy-barrier distribution in FePt nanoparticles," *J. Magn. Magn. Mater.*, vol. 295, no. 2, pp. 174–176, Aug. 2005.

[38] T. G. St. Pierre, N. T. Gorham, P. D. Allen, J. L. Costa-Krämer, and K. V. Rao, "Apparent magnetic energy-barrier distribution in horse-spleen ferritin: Evidence for multiple interacting magnetic entities per ferrihydrite nanoparticle," *Phys. Rev. B*, vol. 65, no. 2, Dec. 2001.

[39] G. Ziółkowski, A. Chrobak, N. Randrianantoandro, and G. Chełkowska, "Numerical Analysis of Time Dependent Effects in Bulk Nanocrystalline Hard Magnets," *Solid State Phenom.*, vol. 194, pp. 62–66, Nov. 2012.

[40] A. Chrobak, "Magnetism in disordered materials," *Arch. Mater. Sci. Eng.*, vol. 58, no. 2, 2012.

[41] L. Rutkowski, *Metody i techniki sztucznej inteligencji*. Warszawa: Wydawnictwo Naukowe PWN, 2009.

[42] A. E. Eiben and J. E. Smith, *Introduction to Evolutionary Computing*. Berlin, Heidelberg: Springer Berlin Heidelberg, 2003.

[43] T. Bäck, *Evolutionary algorithms in theory and practice: evolution strategies, evolutionary programming, genetic algorithms*. New York: Oxford University Press, 1996.

[44] D. Ashlock, *Evolutionary computation for modeling and optimization*. New York: Springer, 2006.

[45] J. Kennedy and R. Eberhart, "Particle swarm optimization," 1995, vol. 4, pp. 1942–1948.

[46] M. Mitchell, *An introduction to genetic algorithms*. Cambridge, Mass: MIT Press, 1996.

[47] M. Dorigo and T. Stützle, *Ant colony optimization*. Cambridge, Mass: MIT Press, 2004.

[48] P. J. M. Laarhoven and E. H. L. Aarts, *Simulated Annealing: Theory and Applications*. Dordrecht: Springer, 1987.

[49] M. de S. G. Tsuzuki and T. de C. Martins, *Simulated annealing: strategies, potential uses and advantages*. 2014.

[50] A. Chrobak, M. Karolus, and G. Haneczok, "Preparation of Fe-Based Bulk Amorphous and Nanocrystalline Alloys by Mould Suction Casting Technique," *Solid State Phenom.*, vol. 163, pp. 233–238, Jun. 2010.

[51] S. H. Lim, W. K. Pi, T. H. Noh, H. J. Kim, and I. K. Kang, "Effects of Al on the magnetic properties of nanocrystalline Fe73.5Cu1Nb3Si13.5B9 alloys," *J. Appl. Phys.*, vol. 73, no. 10, p. 6591, 1993.

[52] S. A. Majetich, J. O. Artman, M. E. McHenry, N. T. Nuhfer, and S. W. Staley, "Preparation and properties of carbon-coated magnetic nanocrystallites," *Phys. Rev. B*, vol. 48, no. 22, pp. 16845–16848, Dec. 1993.

[53] C. Steven, *Critical Materials Strategy*. United States Department of Energy, 2011.

[54] A. Oleś, *Metody eksperymentalne fizyki ciała stałego*. Warszawa: Wydawnictwa Naukowo-Techniczne, 1983.

[55] S. Foner, "Versatile and Sensitive Vibrating-Sample Magnetometer," *Rev. Sci. Instrum.*, vol. 30, no. 7, p. 548, 1959.

[56] S. Srinath, "A Review of: 'The SQUID Handbook: Fundamentals and Technology of SQUIDS and SQUID Systems,'" *Mater. Manuf. Process.*, vol. 21, no. 5, pp. 583–583, Aug. 2006.

[57] A. Marx and R. Gross, *Applied Superconductivity: Josephson Effect and Superconducting Electronics*. Garching: Walther-Meißner-Institut, 2005.

[58] Y. Yoshida and G. Langouche, Eds., *Mossbauer spectroscopy: tutorial book*. Berlin ; New York: Springer, 2013.

[59] A. G. Maddock, *Mössbauer spectroscopy: principles and applications*. Chichester: Horwood, 1997.

[60] D. P. E. Dickson and F. J. Berry, Eds., *Mössbauer spectroscopy*. Cambridge: Cambridge University Press, 1986.

[61] J. I. Langford and A. J. C. Wilson, "Scherrer after sixty years: A survey and some new results in the determination of crystallite size," *J. Appl. Crystallogr.*, vol. 11, no. 2, pp. 102–113, Apr. 1978.

[62] B. E. Warren, "The X-ray diffraction methods used in protein studies," *Ann. N. Y. Acad. Sci.*, vol. 41, no. 2, pp. 151–156, May 1941.

[63] B. D. Cullity, *Elements of x-ray diffraction*, 2d ed. Reading, Mass: Addison-Wesley Pub. Co, 1978.

[64] P. J. Eaton and P. West, *Atomic force microscopy*. Oxford ; New York: Oxford University Press, 2010.

[65] G. Höhne, W. Hemminger, and H.-J. Flammersheim, *Differential scanning calorimetry: an introduction for practitioners*, 2nd rev. and enl. ed. Berlin ; New York: Springer, 2003.

[66] V. Kazmiruk, Ed., *Scanning Electron Microscopy*. InTech, 2012.

[67] M. Sagawa, S. Fujimura, N. Togawa, H. Yamamoto, and Y. Matsuura, "New material for permanent magnets on a base of Nd and Fe (invited)," *J. Appl. Phys.*, vol. 55, no. 6, p. 2083, 1984.

[68] J. J. Croat, J. F. Herbst, R. W. Lee, and F. E. Pinkerton, "Pr-Fe and Nd-Fe-based materials: A new class of high-performance permanent magnets (invited)," *J. Appl. Phys.*, vol. 55, no. 6, p. 2078, 1984.

[69] O. Gutfleisch, "Controlling the properties of high energy density permanent magnetic materials by different processing routes," *J. Phys. Appl. Phys.*, vol. 33, no. 17, pp. R157–R172, Sep. 2000.

[70] J. F. Herbst, "R 2 Fe 14 B materials: Intrinsic properties and technological aspects," *Rev. Mod. Phys.*, vol. 63, no. 4, pp. 819–898, Oct. 1991.

[71] L. Zhou, M. K. Miller, P. Lu, L. Ke, R. Skomski, H. Dillon, Q. Xing, A. Palasyuk, M. R. McCartney, D. J. Smith, S. Constantinides, R. W. McCallum, I. E. Anderson, V. Antropov, and M. J. Kramer, "Architecture and magnetism of alnico," *Acta Mater.*, vol. 74, pp. 224–233, Aug. 2014.

[72] N. Randrianantoandro, A. D. Crisan, O. Crisan, J. Marcin, J. Kovac, J. Hanko, J. M. Grenèche, P. Svec, A. Chrobak, and I. Skorvanek, "The influence of microstructure on magnetic properties of nanocrystalline Fe–Pt–Nb–B permanent magnet ribbons," *J. Appl. Phys.*, vol. 108, no. 9, p. 093910, 2010.

[73] L. Li, A. Yan, H. Peng, Y. Luo, J. Yi, and Y. Peng, "Novel exchange-coupled SmFe3/α-Fe nanocomposite magnets fabricated by magnetic annealing," *J. Magn. Magn. Mater.*, vol. 375, pp. 143–147, Feb. 2015.

[74] R. M. Liu, M. Yue, R. Na, Y. W. Deng, D. T. Zhang, W. Q. Liu, and J. X. Zhang, "Ultrahigh coercivity in ternary Tb-Fe-B melt-spun ribbons," *J. Appl. Phys.*, vol. 109, no. 7, p. 07A760, 2011.

[75] J. J. Croat, J. F. Herbst, R. W. Lee, and F. E. Pinkerton, "High-energy product Nd-Fe-B permanent magnets," *Appl. Phys. Lett.*, vol. 44, no. 1, p. 148, 1984.

[76] F. Pinkerton, "Quench rate dependence of the initial magnetization in rapidly solidified neodymium-iron-boron ribbons," *IEEE Trans. Magn.*, vol. 22, no. 5, pp. 922–924, Sep. 1986.

[77] X. H. Tan, H. Xu, Q. Bai, W. J. Zhao, and Y. D. Dong, "Magnetic properties of Fe–Co–Nd–Y–B magnet prepared by suction casting," *J. Non-Cryst. Solids*, vol. 353, no. 4, pp. 410–412, Mar. 2007.

[78] W. Zhang and A. Inoue, "Bulk nanocomposite permanent magnets produced by crystallization of (Fe,Co)–(Nd,Dy)–B bulk glassy alloy," *Appl. Phys. Lett.*, vol. 80, no. 9, p. 1610, 2002.

[79] J. Zhang, K. Lim, Y. Feng, and Y. Li, "Fe–Nd–B-based hard magnets from bulk amorphous precursor," *Scr. Mater.*, vol. 56, no. 11, pp. 943–946, Jun. 2007.

[80] H. Man, H. Xu, H. W. Liu, X. H. Tan, J. C. Peng, and Q. Bai, “Study of microstructure and correlative magnetic property in bulk Fe61Nd10B25Nb4 permanent magnet,” *Mater. Sci. Eng. B*, vol. 177, no. 18, pp. 1655–1659, Nov. 2012.

[81] T. Miyoshi, H. Kanekiyo, and S. Hirosawa, “Effects of Nb addition on structural and magnetic properties of Fe-B/Nd/sub 2/Fe/sub 14/B-based nanocomposite magnets,” *IEEE Trans. Magn.*, vol. 41, no. 10, pp. 3865–3867, Oct. 2005.

[82] Y.-Q. Wu, M. J. Kramer, Z. Chen, B.-M. Ma, D. H. Ping, and K. Hono, “Microstructural control of Nb addition in nanocrystalline hard magnets with different Nd content,” *IEEE Trans. Magn.*, vol. 39, no. 5, pp. 2935–2937, Sep. 2003.

[83] H. Xu, S. Y. Zhang, X. H. Tan, X. L. Hou, J. S. Ni, and M. Yue, “Effect of Nb on the magnetic properties and microstructure for nanocomposite Nd[sub 2]Fe[sub 14]B⁄α-Fe alloys by three-dimensional atom probe,” *J. Appl. Phys.*, vol. 103, no. 7, p. 07E117, 2008.

[84] N. H. Dan, P. T. Thanh, N. H. Yen, N. T. Thanh Huyen, D. D. Thang, and L. T. Hung, “Inducing anisotropy in bulk Nd–Fe–Co–Al–B nanocrystalline alloys by quenching in magnetic field,” *J. Magn. Magn. Mater.*, vol. 324, no. 7, pp. 1435–1439, Apr. 2012.

[85] M. Marinescu, H. Chiriac, and M. Grigoras, “Magnetic properties of bulk nanocomposite permanent magnets based on NdDyFeB alloys with additions,” *J. Magn. Magn. Mater.*, vol. 290–291, pp. 1267–1269, Apr. 2005.

[86] Q. Wu, A. R. Yan, H. L. Ge, P. Y. Zhang, X. K. Hu, and Y. H. Liu, “Synthesis, structure, and magnetic properties of Nd-Y-Fe-Mo-B bulk nanocomposite magnets,” *J. Appl. Phys.*, vol. 109, no. 7, p. 07A739, 2011.

[87] Z. Ahmad, S. Tao, T. Ma, G. Zhao, and M. Yan, “The magnetic, structure and mechanical properties of rapidly solidified (Nd7Y2.5)–(Fe64.5Nb3)–B23 nanocomposite permanent magnet,” *J. Alloys Compd.*, vol. 509, no. 36, pp. 8952–8957, Sep. 2011.

[88] P. Pawlik, “Glass formability of Fe–Co–Pr–Dy–Zr–B alloys and magnetic properties following devitrification,” *Scr. Mater.*, vol. 49, no. 8, pp. 755–760, Oct. 2003.

[89] P. Pawlik, H. A. Davies, W. Kaszuwara, and J. J. Wysłocki, “PrFeCoB-based magnets derived from bulk alloy glass,” *J. Magn. Magn. Mater.*, vol. 290–291, pp. 1243–1246, Apr. 2005.

[90] P. Pawlik, K. Pawlik, H. A. Davies, W. Kaszuwara, and J. J. Wysłocki, “The influence of heat treatment on the microstructure and magnetic properties of (Fe,Co)–Zr–(Pr,Dy)–B- nanocomposite alloys,” *J. Magn. Magn. Mater.*, vol. 316, no. 2, pp. e124–e127, Sep. 2007.

[91] X. Tan, H. Xu, Q. Bai, and Y. Dong, “Fe–Zr–Nd–Y–B permanent magnet derived from crystallization of bulk amorphous alloy,” *Appl. Phys. Lett.*, vol. 91, no. 25, p. 252501, 2007.

[92] X. H. Tan, H. Xu, and S. J. Wu, “Glass forming ability of Fe–Co–Zr–Nd–B alloys and bulk permanent magnets derived from amorphous precursor,” *J. Mater. Sci.*, vol. 45, no. 20, pp. 5543–5546, Oct. 2010.

[93] H. W. Chang, M. F. Shih, C. W. Chang, C. C. Hsieh, Y. K. Fang, W. C. Chang, and A. C. Sun, “Magnetic properties and microstructure of directly quenched Nd[sub 9.5]Fe[sub 75.5−x]M[sub x]B[sub 15] (M=Mo, Nb, Ta, Ti, V, and Zr; x=0–4) bulk magnets,” *J. Appl. Phys.*, vol. 103, no. 7, p. 07E105, 2008.

[94] P. Pawlik, K. Pawlik, H. A. Davies, W. Kaszuwara, J. J. Wysłocki, N. Harrison, and I. Todd, “Directly quenched bulk nanocrystalline (Pr, Dy)–(Fe, Co)–B–Zr–Ti hard magnets,” *J. Alloys Compd.*, vol. 423, no. 1–2, pp. 99–101, Oct. 2006.

[95] J. M. D. Coey, “Permanent magnets: Plugging the gap,” *Scr. Mater.*, vol. 67, no. 6, pp. 524–529, Sep. 2012.

[96] A. Chrobak, G. Ziółkowski, and N. Randrianantoandro, “Magnetic hardening of Fe–Nb–B–Tb type of bulk nanocrystalline alloys,” *J. Alloys Compd.*, vol. 583, pp. 48–54, Jan. 2014.

[97] A. Chrobak, G. Ziółkowski, N. Randrianantoandro, J. Klimontko, and G. Haneczok, “Phase structure and magnetic properties of Fe–Nb–B–Tb type of bulk nanocrystalline alloys,” *J. Alloys Compd.*, vol. 537, pp. 154–158, Oct. 2012.

[98] T. Kulik, “Nanocrystallization of metallic glasses,” *J. Non-Cryst. Solids*, vol. 287, no. 1–3, pp. 145–161, Jul. 2001.

[99] A. Chrobak, G. Ziółkowski, and N. Randrianantoandro, “Phase Stability of (Fe_{80}Nb_{6}B_{14})_{0.9}Tb_{0.1} Bulk Nanocrystalline Magnet,” *Acta Phys. Pol. A*, vol. 126, no. 1, pp. 176–177, Jul. 2014.

[100] G. Ziółkowski, A. Chrobak, and J. Klimontko, “Phase Structure and Magnetic Properties of Fe-Nb-B-Nd Type of Bulk Nanocrystalline Alloys,” *Solid State Phenom.*, vol. 203–204, pp. 302–305, Jun. 2013.

[101] G. Ziółkowski, A. Chrobak, N. Randrianantoandro, and J. Klimontko, “Phase Structure and Magnetic Properties of Fe-Nb-B-Pt Type of Bulk Nanocrystalline Alloys,” *Acta Phys. Pol. A*, vol. 126, no. 1, pp. 174–175, Jul. 2014.

[102] A. Chrobak, G. Ziółkowski, N. Randrianantoandro, J. Klimontko, D. Chrobak, K. Prusik, and J. Rak, “Ultra-high coercivity of (Fe86−xNbxB14)0.88Tb0.12 bulk nanocrystalline magnets,” *Acta Mater.*, vol. 98, pp. 318–326, Oct. 2015.

[103] J.-S. Wang and R. H. Swendsen, “Cluster Monte Carlo algorithms,” *Phys. Stat. Mech. Its Appl.*, vol. 167, no. 3, pp. 565–579, Sep. 1990.

[104] G. Ziółkowski and A. Chrobak, “Magnetization Processes of Nanoparticles Embedded into Ferromagnetic Matrix,” *Acta Phys. Pol. A*, vol. 127, no. 2, pp. 597–599, Feb. 2015.

[105] A. Chrobak, D. Chrobak, G. Haneczok, P. Kwapuliński, Z. Kwolek, and M. Karolus, “Influence of Nb on the first stage of crystallization in Fe86−xNbxB14 amorphous alloys,” *Mater. Sci. Eng. A*, vol. 382, no. 1–2, pp. 401–406, Sep. 2004.